VELOCITY GRADIENTS ALONG PARTICLE TRAJECTORIES IN TURBULENCE

by

Perry L. Johnson

A dissertation submitted to Johns Hopkins University in conformity with the requirements for the degree of Doctor of Philosophy.

Baltimore, Maryland

July, 2017

Abstract

The creation of large spatial gradients in velocity by turbulent flows has important implications for a number of micro-physical applications that are sensitive to the straining and rotating influences of the immediate fluid environment. Because velocity gradients tend to be dominated by contributions from the smallest scales of motion in turbulence, their statistics enjoy many similarities across a wide range of natural and man-made flows and the canonical case of isotropic turbulence provides a simple flow in which to explore this aspect of turbulence in detail. In this thesis, the dynamics and kinematics of turbulent velocity gradients experienced while following Lagrangian trajectories are explored using fully resolved simulations and new, accurate techniques for inexpensive, reduced order models are developed. In particular, the cumulative stretching of infinitesimal material volumes is quantified statistically using large-deviation theory and compared with the stretching of vorticity. Following this, the dynamics of the velocity gradient itself are modeled using a stochastic approach. While some important terms are represented exactly in the Lagrangian formulation of velocity gradient dynamics, closure approximations are

ABSTRACT

constructed systematically by applying a Lagrangian deformation map to Gaussian field statistics. This model is then extended to arbitrarily high Reynolds numbers using a multiple time scale expansion which faithfully represents energy cascade dynamics and the broad range of timescales present in high Reynolds number flows. It is also demonstrated that this stochastic modeling approach provides an accurate, an inexpensive way to model velocity gradients in coarse-grained simulations of inhomogeneous flows where the small scales of turbulence are not resolved. Finally, the restricted Euler model for Lagrangian velocity gradients is extended to inertial particle trajectories. While the model inherits the restricted Euler finite time singularity, qualitative features of velocity gradients on inertial particle trajectories are correctly predicted. Results point to the possibility for future developments of higher-fidelity models for applications where particle density differs significantly from that of the surrounding fluid.

Primary Reader: Charles Meneveau

Secondary Readers: Dennice Gayme, Gregory Eyink

Acknowledgments

My work in this dissertation was made possible by a first year fellowship from the Whiting School of Engineering at Johns Hopkins University and a three year Graduate Research Fellowship from the National Science Foundation. I would like to extend my most sincere appreciation to Professor Charles Meneveau for his exceptional hospitality and enthusiasm in guiding my research over the past four years. My work in this dissertation benefited tremendously from the Johns Hopkins Turbulence Databases (JHTDB) and also from Lagrangian and inertial trajectory data shared by Luca Biferale and Federico Toschi. Many thanks also to Professors Dennice Gayme and Gregory Eyink for enriching my Ph.D. experience with many engaging technical discussions and to the various other faculty who have enhanced my time at Hopkins, to name a few, Professors Tamer Zaki, Andrea Prosperetti, Anand Gnanadesikan, Joseph Katz, Rajat Mittal, Yanif Ahmad, Randal Burns, and others. It has been my pleasure to work together on shared research interests with postdocs and fellow grad students including Michael Wilczek, Xiang Yang, Theo Drivas, Stephen Hamilton, Chichi Lalescu, Kalin Kanov, and Luis 'Tony' Martinez. I also benefited from

ACKNOWLEDGMENTS

discussions, specific to the topics in this dissertation, with Luca Biferale, Laurent Chevillard, Greg Voth, Alan Kerstein, and Ivan Marusic. Additionally, I would like to thank the many postdocs and fellow grad students within the department who shared the journey (and, in some cases, plenty of their political opinions): in addition to the above, Joel Bretheim, Carl Shapiro, Claire VerHulst, Adrian Thormann, Richard Stevens, Di Yang, Mike Howland, Dan Willen, Michelle Chen, Ismail Hameduddin, Jose-Hugo Elsas, Mohammed Danish, Jasim Saddique, Aditya Aiyer, and many others. Also, the students in the Graduate Christian Fellowship have been a personal encouragement to me, most notably, Jimi Oke, Ethan Naylor, Dan Midgett, Jake Mokris, Jon Millburn, and Liz Kim. Various other members of the community in Baltimore have shared life with me and my wife, of whom I am particularly grateful: Karl and Debbie Dortzbach, Dwight and Maria Schwartz, Djik and Ann Maouyo, Ananda Kumar, Aubrey Bauck, Paul Aiyetan, Karl Johnson, Ping 'Teresa' Yeh, Kris Panico, and of course plenty of others at Faith Christian Fellowship and the other churches in the area. Finally, I remain indebted to my parents (Daryl and Kathy) and brothers (Wes, Casey, Cody) for familial love and the opportunities I have been given in life. Also, I thank my in-laws (Barrett, Dayna, Catelin, Aubrey, Luke, Macy) for putting up with me and being OK with me whisking their daughter/sister off to a faraway land. Most of all, I thank my wife Cara and look forward to many years ahead on our life journey!

Dedication

To the Authority in fluid mechanics, who 'commands even winds and water, and they obey Him,' and to the great challenges which lie before us as caretakers of the turbulent world in which we ourselves are immersed.

Contents

Abstract **ii**

Acknowledgments **iv**

List of Tables **xvi**

List of Figures **xviii**

1 Introduction **1**

1.1 Motivation 1

1.2 Theoretical Framework 4

1.2.1 Universality of Small-Scale Turbulence 4

1.2.2 A Lagrangian View 5

1.3 Outline 6

2 Background Concepts and Tools **10**

2.1 Cumulative Stretching by the Velocity Gradient 11

CONTENTS

2.1.1 Finite Time Lyapunov Exponents 11

2.1.2 Lagrangian Coherent Structures 14

2.1.3 Large-Deviation Statistics 19

2.1.4 Large Deviation Theory for a Sum of Independent and Identically Distributed Variables 20

2.1.5 Large Deviation Theory for Continuous Time Integrals 21

2.1.6 Large Deviation Theory for Finite Time Lyapunov Exponents 23

2.1.7 Generalized Lyapunov Exponents 27

2.1.8 Material Lines and Vorticity Stretching 29

2.2 Stochastic Models for Lagrangian Velocity Gradient Evolution 32

2.2.1 Governing Equations 32

2.2.2 Restricted Euler Model 34

2.2.3 The Stochastic Approach 35

2.2.4 An Overview of Closures for the Stochastic Approach 38

2.2.5 Recent Fluid Deformation Closure 38

2.2.6 Gaussian Fields Closure 42

2.3 Large-Eddy Simulations (LES) 44

2.3.1 LES Equations 45

2.3.2 Modeling of Sub-grid Physics in LES 46

2.3.3 Dissipation and Velocity Gradients in LES 47

2.4 Inertial Particles 49

2.5 Numerical Databases 51
2.5.1 Isotropic Turbulence 51
2.5.2 Turbulent Channel Flow 53

3 Large Deviation Statistics of Finite-Time Lyapunov Exponents in Isotropic Turbulence 54

3.1 Numerical Simulations 56
3.1.1 Isotropic Turbulence Databases from DNS 56
3.1.2 Tracking Fluid Volume Deformations 56
3.2 Measuring the Cramér Function 57
3.2.1 Histogram Method 57
3.2.2 Legendre Transform Method 60
3.3 Joint Statistics of FTLE's 71
3.3.1 Joint-Cramér Functions 71
3.3.2 Cramér Function for the Ratio of FTLEs 76
3.4 The Effect of Rotation on Lagrangian Deformation 77
3.5 Conclusions 81

4 Large Deviation Statistics of Vorticity Stretching in Isotropic Turbulence 87

4.1 An Analog of the FTLE for Vorticity Stretching 89
4.1.1 Lagrangian Vorticity Evolution 89

4.1.2 Material Lines and Finite-Time Lyapunov Exponents 92

4.1.3 Vorticity 93

4.2 Numerical Methods 96

4.3 The Cramér Function for Vorticity Stretching 97

4.3.1 Legendre Transform Method 97

4.3.2 Comparison with FTLE Spectrum 102

4.3.3 Comparison with Strain-Rate Eigenvalue Statistics 106

4.4 A Model Kramers-Moyal Equation for the Vorticity Magnitude 107

4.4.1 PDF Closure Using Conditional Means 108

4.4.2 Analogy with Polymers 110

4.4.3 Modeling Approximations 112

4.4.4 Kramers-Moyal Coefficients 116

4.4.5 Results Using a Parabolic Cramér Function 119

4.5 Conclusions 123

5 Material Deformation and Vorticity Stretching in Turbulent Channel Flow 126

5.1 Analysis Tools for a Channel Flow 128

5.1.1 Velocity Gradient Statistics in Channel Flow 128

5.1.2 Various Lyapunov Exponents 132

5.1.3 Large-Deviation Statistics 136
5.2 Numerical Methods 136
5.2.1 Lagrangian Particles 137
5.2.2 Particle Tracking on a Parallel Database 138
5.2.3 Other Considerations for Lagrangian Trajectories in a Channel Flow 139
5.3 Results 141
5.3.1 Local Lyapunov Exponents 142
5.3.2 Strain-Rate Eigenvalues 146
5.3.3 Alignment with Strain-Rate Eigenvectors 149
5.3.4 Cramér Functions 154
5.4 Conclusions 159

6 An Improved Stochastic Model for Lagrangian Velocity Gradients 162

6.1 Recent Deformation of Gaussian Fields Mapping Closure 164
6.1.1 Overview 164
6.1.2 Model Details 166
6.1.3 The Resulting Model 169
6.1.4 Parameters and Constraints 170
6.2 Numerical Methods 172
6.2.1 Stochastic Differential Equation Solver 172
6.2.2 Direct Numerical Simulation Database 173

6.3 Results 173
6.3.1 Longitudinal and Transverse Components 173
6.3.2 Isotropic Relations 176
6.3.3 Enstrophy and Dissipation 177
6.3.4 Vorticity and Strain-Rate 178
6.3.5 Dynamics in the Q-R Plane 181
6.3.6 Correlation Coefficients 187
6.3.7 Computational Cost 189
6.4 Conclusions 190

7 High Reynolds Numbers and Intermittency in a Stochastic Model for Lagrangian Velocity Gradients 192

7.1 Constructing a Stochastic Model for High Reynolds Numbers 194
7.1.1 Relevant Background 194
7.1.2 Single-level Model 194
7.1.3 Coarse-Grained (Two-level) Model 196
7.1.4 Extension to Arbitrary Number of Levels 198
7.1.5 Unsteady Dissipation Constraint 199
7.1.6 Final Form of the Proposed Model 200
7.2 Numerical Implementation 201
7.3 Results 201
7.4 Conclusions 208

8 Coupling Stochastic Models for Lagrangian Velocity Gradients with Large-eddy Simulations 210

8.1 Modeling Framework 211

8.1.1 Lagrangian Velocity Gradients 212

8.1.2 Lagrangian Trajectories 214

8.1.3 Sub-Kolmogorov Droplet Model 216

8.2 Computational Setup 219

8.2.1 Problem Statement 219

8.2.2 Direct Numerical Simulation 223

8.2.3 Large-eddy Simulation 226

8.2.4 Stochastic Differential Equations 229

8.3 Results 231

8.3.1 Particle Dispersion Statistics 231

8.3.2 Velocity Gradient Statistics 233

8.3.3 Droplet Deformation Statistics 241

8.4 Summary and Conclusions 249

9 A Restricted Euler Model for Velocity Gradients on Inertial Trajectories 254

9.1 Model Construction 256

9.2 Results 259

9.3 Analysis 263

9.4 Conclusions 265

10 Summary and Conclusions **267**

A Comparison of two alternate FTLE definitions **276**

A.1 Two-Dimensions 277

A.2 Three-Dimensions, Volume-Preserving 280

B Lyapunov Exponent Code Validation **286**

B.1 Validation: Lorenz System 287

B.2 Convergence of Lyapunov Exponents 290

C Derivation of Finite-Size Effects **293**

C.1 Marginal PDFs 293

C.2 Joint PDFs 295

D Derivation for Ratio of FTLEs **298**

E Kramers-Moyal Solution for Linear Relaxation **302**

F Isotropic Tensorial Stochastic Forcing for Symmetric and Anti-Symmetric Components **306**

G Analytical Calculation of γ for the Gaussian Fields Representation of the Conditional Pressure Hessian **310**

H Gaussian Fields Approximation for the Conditional Hessian of the Velocity Gradient **315**

I Determination of δ for RDGF **319**

J Yoshizawa and Smagorinsky Coefficients **323**

K Dissipation Rates in the Filtered DNS **327**

Bibliography **330**

Vita **368**

List of Tables

2.1 Numerical details for isotropic turbulence datasets used in this dissertation. 52
2.2 Numerical details for the channel flow dataset used in this dissertation.[190] 53

3.1 Skewness and excess kurtosis of the cumulative deformation statistics in HIT, compared to statistics generated from two independent Gaussian variables. 70
3.2 Lyapunov spectra with and without Ω_{ij} compared with the perfect alignment case. 81

4.1 Comparison of first four cumulants for the vorticity stretching with those of the first two FTLEs. The asterisk denotes that the value is corrected for finite integration time effects, see chapter 3 for more details. 106

5.1 Minimum and width of the Cramér functions for channel flow and isotropic turbulence, along with coefficients for skewness and excess kurtosis (which decay as $T \to \infty$.) 158

6.1 Numerical details for simulations used in this chapter. 173
6.2 Skewness and kurtosis values for longitudinal and transverse velocity gradient components from each model compared with DNS. 176
6.3 Results for competing models in terms of reproducing known isotropic relations. 177
6.4 Various mean values for strain-rate and vorticity measures. 181
6.5 Correlation coefficients for three models with DNS results at $Re_\lambda = 430$. 189

8.1 Parameters for the turbulent channel flow case considered in this chapter. 220
8.2 Methods used for calculating trajectories $\mathbf{X}$, sub-grid production Π, and velocity gradients $\mathbf{A}$ for the four cases considered in this chapter. 221
8.3 Parameters for the DNS, filtered DNS, and LES simulation databases used in this chapter. 224

LIST OF TABLES

B.1 Three sets of parameters for which comparison is made with previous numerical results for Lyapunov exponents. 288
B.2 Validation results for the Lyapunov exponents of the Lorenz system. . 289

List of Figures

2.1 Colored images of non-dimensionalized FTLE field, $\gamma_1\tau_\eta$, with integration time of $t/\tau_\eta = 8(\text{left}), 16(\text{center}), 32(\text{right})$. Figures on the top row are of a 10η-by-10η slice, while figures on the bottom row are zoomed into a 2η-by-2η subregion. The data is from a small subset of the isotropic turbulence dataset from Direct Numerical Simulation, described in §3.1. 18

2.2 Sketch of fluid and inertial particle trajectories. In this dissertation, we consider the time history of fluid velocity gradients, $A_{ij}(t)$, along these trajectories. 49

3.1 Cramér functions computed directly from normalized histograms using (a) Eq. (3.2) without the first-order correction and (b) Eq. (3.4) with the first-order shift term. Legend gives integration time in t/τ_η units. 59

3.2 Cramér functions of (a) the maximal FTLE, γ_1, and (b) the minimal FTLE γ_3. The blue dashed and black solid lines are computed directly from normalized histograms at integration times of $30\tau_\eta$ and $45\tau_\eta$ using Eq. (3.4) with the first-order shift term, while the thick solid red lines show results obtained from the moments via the Legendre transform method, see §3.2.2 below. 60

3.3 Example linear curve fits for (a) $\ln\langle\exp(q\gamma_1 t)\rangle$ and (b) $\ln\langle\exp(q\gamma_3 t)\rangle$. In both plots, the values of q are spaced evenly between the stated limits, with curves for higher q values on top of curves with lower q values. 61

3.4 The three generalized Lyapunov exponents as constructed from linear regression analysis. Solid lines show results from different trajectory ensembles computed (containing 64k trajectories each) from the JHTDB data and the dashed lines show results from the iCFD data (containing 3.2k trajectories). 62

3.5 The three marginal Cramér functions constructed via Legendre transform from the GLE. Solid lines show results from different trajectory ensembles computed (containing 64k trajectories each) from the JHTDB data and the dashed lines show results from the iCFD data (containing 3.2k trajectories). 66
3.6 Proxies for the Cramér function created artificially by constructing FTLE spectrum realizations from two independent normally-distributed variables with zero mean equal variance using the incompressibility constraint $\gamma_1 + \gamma_2 + \gamma_3 = 0$. 68
3.7 Example curve fits for (a) $\ln\langle\exp(q\gamma_1 t - q\gamma_3 t)\rangle$ and (b) $\ln\langle\exp(q\gamma_1 t + q\gamma_3 t)\rangle$ used for determining the asymptotic slopes in constructing the two-dimensional GLE $L_{1,3}(q_1, q_2)$. For plot (a), we set $q = q_1 = -q_2$ and show curve fits for evenly-spaced q values, and in plot (b), we set $q = q_1 = q_2$ and show curve fits for evenly-spaced q values. 73
3.8 (a) Contour map of the two-dimensional generalized Lyapunov exponent $L_{1,3}(q_1, q_2)$ as constructed from linear regression analysis, with points having uncertainty beyond a specified threshold removed. (b) The joint-Cramér function $S(\gamma_1, \gamma_3)$ as constructed from the double Legendre transform of the two-dimensional generalized Lyapunov exponent. 75
3.9 The Cramér function $S(r^*)$ for the FTLE ratio $r^* = \gamma_2/\gamma_1$ constructed via Eq. (3.21), "LT", compared with approximations constructed from histogram-generated PDFs of r^* with $S(r^*) \approx -\frac{1}{t}\ln p(r^*, t)$ at two different integration times, $30\tau_\eta$ and $45\tau_\eta$. 78
3.10 Comparison of the three marginal Cramér functions (a) $S(\gamma_1)$, (b) $S(\gamma_2)$, and (c) $S(\gamma_3)$ for deformation tensors integrated using the full velocity gradient tensor, A_{ij} (blue solid lines), and using only the strain-rate, S_{ij} (red dashed lines), and perfect alignment between Cauchy-Green and instantaneous strain rate eigen-frames (green dotted lines). Each plot contains multiple blue lines, indicating the statistical spread from different ensembles of 64k particles each. 85
3.11 The (a) 2D GLE, $L_{1,3}(q_1, q_2)$, and (b) joint-Cramér function, $S(\gamma_1, \gamma_3)$, constructed using only the strain rate tensor to integrate fluid particle deformation along the Lagrangian trajectories. Note that part (b) of this figure is zoomed out compared to part (b) of Fig. 3.8. 86
3.12 The Cramér function for the PDF of $r^* = \gamma_2/\gamma_1$ constructed using the full velocity gradient tensor, A_{ij} (solid line), and only the strain rate tensor, S_{ij} (dotted line). 86

4.1 The cumulant-generating function for the cumulative vorticity stretching, $\Gamma_\omega = \gamma_\omega T$, for (a) $q = -1.6, -1.4, -1.2, -1.0, -0.8, -0.6, -0.4, -0.2$, and (b) $q = 0, 0.2, 0.4, 0.6, 0.8, 1.0$. Symbols represent numerical values from the dataset and dashed-lines represent linear curve-fits for the $30\tau_\eta < T < 45\tau_\eta$ range. 98
4.2 The generalized Lyapunov exponents for the vorticity stretching from five different $64k$ Lagrangian particle ensembles. The dashed line represents a parabolic curve fit in the region of $q = 0$. 99
4.3 The Cramér function for the vorticity stretching from five different $64k$ Lagrangian particle ensembles. The differences between the five different ensembles illustrate the extent of uncertainty from statistical convergence. The symbol g is used for the probability space variable of γ_ω and both axes are non-dimensionalized by the Kolmogorov timescale τ_η. The gray vertical line indicates $\gamma_\omega = 0$. The dashed line represents a parabolic curve fit to the Cramér function near the minimum. . . . 101
4.4 Comparison of the Cramér function for vorticity stretching with the marginal Cramér functions for the finite-time Lyapunov exponents. Each Cramér function was measured from five separate ensembles of $64k$ Lagrangian particles each in order to demonstrate the level of statistical convergence uncertainty. The symbol g is used for the probability space variable of γ and both axes are non-dimensionalized by the Kolmogorov timescale τ_η. The gray vertical line indicates $\gamma = 0$. . 104
4.5 Comparison of the Cramér function for vorticity stretching with the hypothetical Cramér functions if perfect alignment with the largest or second-largest strain-rate eigenvalues was maintained throughout the dynamics. Note that five separate ensemble measurements of the vorticity Cramér function are shown as five different continuous lines, qualitatively showing the statistical convergence error. 107
4.6 (a) The conditional mean, Eq. (4.30), as computed indirectly from the strain-rate using Eq. (4.24). Also shown is a power-law curve fit of the form, Eq. (4.32) for the interval $2 < |\omega|\tau_\eta < 6$, with $A = 0.129$, $n = 1.462$. (b) The conditional coefficient of variation (standard deviation/mean) of the relaxation term. 115
4.7 Plot of $-\log\left(\xi^{1-\frac{\lambda}{\Delta}} p_{\omega^2\tau_\eta^2}(\xi)\right)$ against $\xi^{(n-1)/2}$, for which the model successfully predicts a linear relationship. In this plot, $n = 1.462$, $\lambda = 0.100/\tau_\eta$, $\Delta = 0.122/\tau_\eta$. 121
4.8 Comparison of enstrophy PDF, normalized by Kolmogorov timescale τ_η, from truncated Kramers-Moyal model with JHTDB DNS-generated statistics using (a) pre-determined model parameters, $A = 0.129$, $n = 1.462$, $\lambda = 0.100/\tau_\eta$, $\Delta = 0.122/\tau_\eta$, and (b) adjusting only $A = 0.174$ to give excellent agreement with DNS enstrophy PDF. 122

5.1 Kolmogorov timescale (left), and Taylor-scale Reynolds number (right) as a function of distance from the wall. Dashed lines indicate values calculated with only turbulent dissipation, while continuous lines indicate values using both turbulent and mean flow dissipation. 132
5.2 Schematic showing the mediator synchronization and task-parallel algorithms for parallel processing of Lagrangian trajectories in the JHTDB. Mediator synchronization is on the left, and the task-parallel is on the right 139
5.3 The minimum time step, as a function of wall distance, at which a particle in the database may leave the domain by violating the no-penetration condition. The worst-case scenario is a particle leaving the domain from $y^+ \approx 3$ with a timestep of $\Delta t = 2.6\text{e-}2$, which is four times the database storage timestep. 141
5.4 The average instantaneous Lyapunov exponents, $\langle \widehat{S}_{(ii)} \rangle$, for $i = 1, 2, 3, \omega$, as a function of wall distance (continuous lines), (a) normalized by bulk Kolmogorov timescale, and (b) normalized by local Kolmogorov timescale, with dashed lines representing $|\lambda_i| \tau_\eta$ from homogeneous isotropic turbulence. 143
5.5 PDFs of instantaneous Lyapunov exponents normalized by local Kolmogorov timescale in the core of the channel, i.e. conditioned on $y^+ > 100$. Continuous lines with open symbols represent channel flow results while dotted lines with filled symbols represent isotropic turbulence results. Squares (left): $\widehat{S}_{11}$, circles (left): $\widehat{S}_{22}$, triangles (left): $\widehat{S}_{33}$, diamonds (right): $\widehat{S}_{\omega}$. 145
5.6 Average strain-rate eigenvalues as a function of wall distance (continuous lines), (a) normalized by bulk Kolmogorov timescale, and (b) normalized by local Kolmogorov timescale, with dashed lines representing results from homogeneous isotropic turbulence. 148
5.7 PDFs of strain-rate eigenvalues normalized by local Kolmogorov timescale in the core of the channel (continuous lines with open symbols), i.e. conditioned on $y^+ > 100$. Dotted lines with filled symbols represent results from homogeneous isotropic turbulence. Squares: Λ_1, circles: Λ_2, triangles: Λ_3. 149
5.8 Averages of $\cos^2(\theta_{ij})$ as a function of y^+, where θ_{ij} represents the angle between the Cauchy-Green eigenvector associated with its i^{th} largest eigenvalue and the strain-rate eigenvector associated with its j^{th} largest eigenvalue. Continuous lines represent results for (a) most extensive FTLE direction ($i = 1$), (b) intermediate FTLE direction ($i = 2$), (c) most compressive FTLE direction ($i = 3$), (d) vorticity vector direction ($i = \omega$). Dashed lines represent results from homogeneous isotropic turbulence. 150

5.9 PDFs of $\cos(\theta_{ij})$ in the core of the channel, i.e. conditioned on $y^+ > 100$. Continuous lines represent (a) most extensive FTLE direction ($i = 1$), (b) intermediate FTLE direction ($i = 2$), (c) most compressive FTLE direction ($i = 3$), (d) vorticity unit vector. Dashed lines represent results from homogeneous isotropic turbulence. Squares: $j = 1$, circles: $j = 2$, triangles: $j = 3$. 155
5.10 The Cramér functions of the three Lyapunov exponents and vorticity for the channel flow (continuous lines with open symbols) compared to those from isotropic turbulence (dotted lines with filled symbols). Squares: γ_1, circles: γ_2, triangles: γ_3, diamonds: γ_ω. 156
5.11 The Cramér function for the maximal finite-time Lyapunov exponent in a channel flow at $Re_\tau = 180$ (dashed line with plus symbols, from[42]) and $Re_\tau = 1000$ (continuous lines with open symbols) compared to those from isotropic turbulence (dotted lines with filled symbols). . . 159

6.1 Schematic illustrating the main elements of the RDGF model for the conditional pressure Hessian. The viscous Laplacian model is constructed analogously. 165
6.2 Sample trajectories of (a) longitudinal and (b) transverse velocity gradient components from the RDGF mapping closure. Three different trajectories are shown, represented by three different colours. 174
6.3 Single component PDFs for longitudinal (a-c) and transverse (d-f) velocity components. Three models are compared: (a,d) RFD, (b,e) EGF, (c,f) RDGF mapping closure. Solid gray line denotes Gaussian, dashed line shows DNS results at $Re_\lambda = 430$, dotted line shows DNS at $Re_\lambda = 160$, and solid line with markers shows the model result. . . 175
6.4 PDFs of dissipation (a-c) and enstrophy (d-f) normalized by their mean values for RFD (a,d), EGF (b,e), RDGF (c,f). Solid lines with symbols indicate model results, and DNS results are shown with dashed ($Re_\lambda = 430$) and dotted ($Re_\lambda = 160$) lines. 179
6.5 Probability distribution functions for the cosine of the angle between vorticity and the strain-rate eigenvectors: (a) RFD, (b) EGF, (c) RDGF. (d) Probability density functions for s^*, as defined in (6.18), for the three models compared with DNS results and Gaussian field statistics. 180
6.6 Logarithmically scaled joint-probability density function for the invariants Q and R as given by (a) RFD, (b) EGF, (c) RDGF, and (d) DNS. 182
6.7 Thick lines with arrows represent "streamlines" in the QR-plane due to the deviatoric part of the pressure Hessian. Thin lines represent contours for the velocity magnitude in the QR-plane. Results are as given by (a) RFD, (b) EGF, (c) RDGF mapping closure, and (d) DNS. 185

6.8 Thick lines with arrows represent streamlines in the QR-plane due to the viscous Laplacian. Thin lines represent contours for the velocity magnitude in the QR-plane, non-dimensionalized by powers of $\langle S_{ij}S_{ij}\rangle$. Results are as given by (a) RFD, (b) EGF, (c) RDGF, and (d) DNS. 186

7.1 A sample A_{11} signal from three adjacent levels of the same trajectory in a three-level model. Top: coarsest level, $n = 1$; middle: next-coarsest level, $n = 2$; Bottom: fully resolved velocity gradient, $n = N = 3$. . . 202
7.2 Probability density functions of A_{11} (left) and A_{12} (right) for $N = 1$, 2, 3, 4, and 5 (colored solid lines) compared with DNS data at $Re_\lambda = 430$ (dotted line). Also shown is a model with $N_{\text{eff}} = 1.85$ (dashed line). . 203
7.3 Skewness (left) and flatness (right) factor of velocity gradient components as a function of Re_λ compared with DNS data. Filled circles (A_{11} skewness and flatness) and squares (A_{12} flatness) represent the results of the multi-level model. DNS data from chapter 6 (□,○); 230 (△); and a compilation of experimental data from Ref. 1 (+). Smaller filled symbols represent the multi-level model with non-integer N_{eff}. . 203
7.4 Schematic showing the phenomenological construction of the dissipation mixing leading to the equation (7.7). The dissipation rate at the second level used for defining $\tau_2(t)$ is mixed between a fraction γ of the total energy dissipation rate transferred from the first level (and fluctuating in time on each individual trajectory) and a fraction $1-\gamma$ of the total energy dissipation rate from 'direct' injection (constant in time and over all trajectories) which lowers the effective intermittency. 205
7.5 Scaling exponents $\alpha(m)$ from the multiple-time scale RDGF model with ratio $\beta = 10$ (filled red circles with error bars), compared with log-normal $\mu = 0.2$ (dashed magenta line) and $\mu = 0.25$ (dot-dashed green line), She-Leveque[224] (continuous blue line), p-model[223] with $p_1 = 0.7$ (black dotted line), and DNS data from Refs. 230 (▽), 38 (△), and 231 (□), as well as experimental data from Ref. 232 (▷). The RDGF model with $\beta = 6$ is shown as well (filled green circles with error bars), illustrating the effect of changing β on the predicted scaling exponents. 206
7.6 Probability density functions of alignment of vorticity vector with the j^{th} strain-rate eigenvector ordered by decreasing eigenvalues (left): Λ_1, circles; Λ_2, triangles; Λ_3, squares; and of s^* (right). Dashed lines indicate DNS results from Ref. 77 at $Re_\lambda = 430$ and solid lines indicate model results that are the same for any N. 207
7.7 Joint PDFs in RQ invariant space from the multilevel RDGF stochastic model with $\beta = 10$ and $N_{\text{eff}} = 1.85$ (left) and from DNS of Ref. 77 at $Re_\lambda = 430$ (right). Logarithmically-spaced iso-contours shown are: 10^1, 10^0, 10^{-1}, 10^{-2}, 10^{-3}. 208

8.1 Snapshots of streamwise velocity on a plane parallel to the wall at the center of the channel from the DNS (left), fDNS (center), LES (right). 222
8.2 Mean velocity (left) and Reynolds stress tensor component (right) profiles for DNS (continuous lines) and filtered DNS (symbols). For the Reynolds stress components: $\langle u'^2\rangle_E$ ($\circ$), $\langle v'^2\rangle_E$ ($\triangledown$), $\langle w'^2\rangle_E$ ($\triangle$), and $\langle u'v'\rangle_E$ ($\square$). 225
8.3 Mean velocity (left) and Reynolds stress tensor component (right) profiles for DNS (continuous lines) and LES (symbols). For the Reynolds stress components: $\langle u'^2\rangle$ ($\circ$), $\langle v'^2\rangle$ ($\triangledown$), $\langle w'^2\rangle$ ($\triangle$), and $\langle u'v'\rangle$ ($\square$). . . 227
8.4 On the left, Kolmogorov timescales $\tau_\eta = \sqrt{\nu/\langle\epsilon|y\rangle_E}$ from DNS ($-$), LES-RDGF ($\circ$), and LES-NM ($\triangle$). On the right, the Smagorinsky coefficient prescribed for fDNS-RDGF ($-$), i.e. (K.1), and $\langle C_s|y\rangle_E$ as computed by the LES with the scale-dependent Lagrangian dynamic formulation ($\circ$). 229
8.5 Sample time histories of wall-normal location (top) and transverse velocity component (middle) and deformation magnitude parameter D (bottom) from the DNS (left) and LES-RDGF (right) results for 6 independent Lagrangian trajectories. The droplets shown are have $Ca = 1.0$ and $\hat{\mu} = 1.0$. 232
8.6 Distribution of particles at different times after being released from the centerline at $t = 0$. Continuous lines show the distributions from DNS while symbols show the results from LES with stochastic model for sub-grid velocity. Left: $t = 0.26$ ($\square$), $t = 0.78$ ($\circ$), $t = 1.56$ ($\triangle$), $t = 2.34$ ($\triangledown$). Right: $t = 2.6$ ($\square$), $t = 7.8$ ($\circ$), $t = 15.6$ ($\triangle$), $t = 23.4$ ($\triangledown$). 233
8.7 Probability distribution functions for dissipation (left) and enstrophy (right) using an ensemble of all particle locations at each time for $0 < t < L_t$, excluding $y^+ < 100$. The continuous black line indicates LES-RDGF results compared with DNS (red dashed line) and LES-NM results (black dotted line). 235
8.8 Probability distribution functions for alignment cosine between vorticity and strain-rate eigenvectors (left) and topology indicator $s^* = -3\sqrt{6}\Lambda_1\Lambda_2\Lambda_3/(\Lambda_1^2+\Lambda_2^2+\Lambda_3^2)^{3/2}$ (right) using an ensemble of all particle locations at each time for $0 < t < L_t$, excluding $y^+ < 100$. The continuous lines indicate LES-RDGF results compared with DNS (dashed lines) and LES-NM results (dotted lines). On the left, colors indicate the eigenvectors associated with largest eigenvalue (blue), intermediate eigenvalue (green), smallest eigenvalue (red). 236
8.9 Logarithmically-spaced contours of the joint probability density function for the second and third invariants of the velocity gradient tensor along the particle trajectories, excluding $y^+ < 100$. The results of DNS (left) are compared with LES-RDGF model results (right). 237

8.10 Kolmogorov timescale $\tau_\eta = \sqrt{\nu/\langle\epsilon\rangle_L}$ with averaging over the particle ensemble as a function of time after release from the centerline. The DNS results (dashed red) are compared with fDNS-RDGF (continuous gray) and LES-RDGF (continuous black). 238
8.11 Kolmogorov timescales as a function of wall distance for Eulerian averaging (gray) and particle ensemble averaging at time $t = 23.4$ (black). Continuous lines indicate DNS results and symbols ($\circ$) indicate RDGF results. Left: fDNS-RDGF (*a priori*) compared with DNS. Right: LES-RDGF (*a posteriori*) compared with DNS. 239
8.12 At $t = 23.4$, the PDF of D (left) and conditional average $\langle D|y\rangle_L$ (right) for the droplet ensemble. Droplet with location $y^+ < 100$ are removed from the ensemble for these plots. The DNS results (red dashed lines) are compared with fDNS-RDGF (gray lines), LES-RDGF (black lines), and LES-NM (black dotted lines). 243
8.13 Left: the PDF of the shape parameter s_d^* at $t = 23.4$ for the ensemble of droplets, exclude those with $y^+ < 100$. Right: the PDFs of alignment cosines between the σ_1 singular vector of the droplet deformation tensor and the three eigenvectors of the strain rate tensor (blue: Λ_1, green: Λ_2, red:Λ_3) as well as the vorticity vector (black). In both, the continuous lines indicate LES-RDGF results, the dashed lines show DNS results, and the dotted lines are results from the LES-NM case. 244
8.14 The deformation magnitude ($0 < D < 1$) and shape parameter ($-1 < s_d^* < 1$) averaged over the particle ensemble as a function of time for $Ca = 0.25$ (black), 0.5 (magenta), 1.0 (blue), 2.0 (green), 4.0 (red). Dashed lines show DNS results while continuous lines show results from the *a posteriori* LES simulation. Arrows indicate the direction of increasing Ca. 245
8.15 Probability density functions for droplet deformation magnitude (left) and shape parameter (right) near the end of the simulation, $t = 23.4$. On the left, the range of Ca in Figure 8.14 is shown, while on the right, a reduced set $Ca = 0.25$, 1.0, 4.0 is shown. Continuous lines indicate LES-RDGF results while dashed lines show DNS results. Arrows indicate the direction of increasing Ca. 247
8.16 Conditional means for deformation magnitude conditioned on wall-normal distance (left) and shape parameter conditioned on deformation magnitude near the end of the simulation, $t = 23.4$. The same range of Ca from Figure 8.15 is shown. Arrows indicate the direction of increasing Ca. 248

8.17 Comparison of deformation for oil droplet cases for Ca = 5e-3 (without dispersants) and $Ca = 2$ (with dispersants). Top left: time history of ensemble averaged deformation magnitude after release from channel centerline at $t = 0$. Top right: Average deformation magnitude conditioned on wall distance at $t = 23.4$. Bottom left: PDF of deformation magnitude at $t = 23.4$. Bottom right: PDF of droplet shape parameter at $t = 23.4$. 250

9.1 Sketch outlining the features of the RQ invariant space, including representative local flow topology cubes. The Vieillefosse tail (dashed line) represents the boundary between real and complex eigenvalues of the velocity gradient tensor. 259

9.2 Restricted Euler streamlines (top) and DNS-computed joint-PDF iso-contours (bottom) for Lagrangian trajectories (left), heavy particle trajectories with $\beta = 0$, $St = 0.3, \alpha = 1.8\sqrt{\nu/\langle\epsilon\rangle}$ (center), and light particle trajectories with $\beta = 3$, $St = 0.1, \alpha = -1.2\sqrt{\nu/\langle\epsilon\rangle}$ (right). The timescale $|\alpha|$ is used to normalize the axes on the streamline plots, while $\sqrt{2\nu/\langle\epsilon\rangle}$ is used to normalize the axes for the DNS results, where $\langle\epsilon\rangle$ is the average turbulent dissipation rate from the simulation. The red circles show fixed points of the RQ dynamics, providing a visual connection between the two normalizations. The DNS data is from a pseudo-spectral simulation performed at $Re_\lambda = 185$ with a grid resolution of 512^3.[188] The PDF iso-contours are spaced logarithmically with levels 10^z, $z = 1, 0, -1, -2, -3, -4$. 260

A.1 Comparison of Cramér functions for two FTLE definitions. 285

B.1 Variation of computed Lyapunov exponent of the Lorenz system ($\sigma = 10$, $\beta = \frac{8}{3}$, $\rho = 28$) with the curve fit range used for the generalized Lyapunov exponent. Open symbols represent the three identical runs with $20,000$ trajectories and the 'x' markers represent one of the run with only 2000 trajectories. The last symbols (at $t = 175\tau$) represent the results reported in Table B.2 compared to literature (dotted lines). 290

B.2 The trend of maximal LE with increasing time of curve fit range from the iCFD Lagrangian database. The length of the time used for each curve fit range is varied from $5\tau_\eta < t < 50\tau_\eta$. 292

G.1 Integrand in (G.7) plotted in normalized variables $\hat{r} = \frac{r}{\gamma_2\eta}$ with $\gamma_2 \approx 13.312$

K.1 On the left, Kolmogorov timescales from DNS (lines) and fDNS (symbols) constructed using sub-grid production $\tau_\eta = \sqrt{\nu/\langle \Pi | y \rangle_E}$ (- -,△) and using dissipation rate $\tau_\eta = \sqrt{\nu/\langle \epsilon | y \rangle_E}$ (−,○). On the right, the non-equilibrium correction used for matching the DNS dissipation rate in the fDNS case. 329

Chapter 1

Introduction

1.1 Motivation

From the tumbling and colliding of ice crystals and droplets in clouds, to the stressing and damaging of red blood cells downstream of an artificial heart value, to the motility and nutrient uptake of phytoplankton in the ocean, fluid turbulence can have a profound impact on the microscopic world embedded in a wide variety of macroscopic environments. The nonlinear and nonlocal behavior of incompressible turbulent flows gives rise to complex, chaotic dynamics across a wide range of strongly coupled scales which, to a large extent, continues to defy the ongoing efforts of scientists and engineers to develop accurate models based on first principles.

The statistics of velocity gradients in isotropic turbulence are of both practical and theoretical importance in the study of turbulent flows.[1,2] In a wide variety of

scientific and engineering applications, including those mentioned above, the micro-physical details of an object of study occur on scales comparable to or smaller than the smallest length scales of turbulent motions, the Kolmogorov scale. The Kolmogorov scale is given by $\eta = \nu^{3/4}\langle\epsilon\rangle^{-1/4}$, where ν is the kinematic viscosity of the fluid and $\langle\epsilon\rangle$ is the mean energy dissipation rate of the flow per unit mass. For sufficiently small objects (e.g. particles or droplets in a flow) and features (e.g. thin flame fronts) in a turbulent environment, the flow in the immediate vicinity of a point $\mathbf{x}_0$ can be well-approximated by a linearized description, $u_i(\mathbf{x}, t) \approx u_i(\mathbf{x}_0, t) + (x_j - x_{0,j})A_{ij}(\mathbf{x}_0, t)$, where $A_{ij} = \partial u_i/\partial x_j$ is the velocity gradient tensor having 9 components. In an incompressible flow, the trace of $\mathbf{A}$ vanishes due to the solenoidal constraint on the velocity field, leaving 8 degrees of freedom. The velocity gradient tensor describes both the local straining and rotating behavior of the fluid, given by the strain-rate tensor $S_{ij} = \frac{1}{2}(A_{ij} + A_{ji})$ and rotation-rate tensor $\Omega_{ij} = \frac{1}{2}(A_{ij} - A_{ji})$ respectively (the rotation-rate tensor, being anti-symmetric, can be more compactly expressed by the vorticity $\omega_i = -\epsilon_{ijk}\Omega_{jk}$). Thus, the velocity gradient tensor describes the action of the fluid flow to rotate, stretch, deform, and re-orient small embedded objects and features. As such, the velocity gradient in turbulence is relevant to quite a number of micro-physical applications, for instance: polymer stretching and relaxation,[3–6] deformation and breakup of droplets, bubbles, and aggregates,[7–11] rigid particle rotation and orientation,[12–14] heat and mass transfer,[15,16] the damaging of red blood cells,[17–20] local extinction events in turbulent flamelets,[21,22] and preferential

clustering of inertial particles.[23,24]

In addition to the velocity gradient, the *coarse-grained* or *perceived* velocity gradient has been used to explore scale-dependent properties of small-scale turbulence.[25–28] The coarse-grained velocity gradient, obtained by applying a spatial low-pass filter to the velocity gradient field, shares many dynamical and kinematical features in common with its fully-resolved counterpart and can be used to capture dynamics at scales much larger than the Kolmogorov length scale. This broadens the range of application beyond objects and features smaller than η to physics across a much wider range of length scales.

Meanwhile, from a theoretical perspective, the statistics of velocity gradients and increments in isotropic turbulence are key ingredients in exploring internal intermittency and multi-fractality, e.g. the tendency of the dissipation rate to cluster into relatively small, intermittent, sub-regions of the flow.[29–33] The phenomenon of small-scale intermittency represents a long-standing challenge to developing a theory for fluid turbulence that is based on first principles, i.e. derivable from the Navier-Stokes equations.[34,35] The manifestation of intermittency is that fluctuations in velocity gradients or increments become more extreme and violent,[1,36] exhibiting longer (fatter) tails in their probability distribution, with increasing Reynolds number or shrinking observation length scale. While this phenomenon represents a key aspect of turbulent theory, it also touches on the practical aspects discussed above. Such extreme events can affect phenomena ranging from flame extinction, droplet breakup and heavy par-

ticle clustering in turbulent flows.

1.2 Theoretical Framework

1.2.1 Universality of Small-Scale Turbulence

Because velocity gradients are dominated by contributions of small-scale motions near the Kolmogorov length scale, Kolmogorov's 1941 hypotheses[37] imply (approximately) universal isotropic behavior for velocity gradients at high Reynolds numbers far enough from solid boundaries, even for very anisotropic turbulent flows. This idea of universal properties of small-scale turbulence has been an important theme in turbulence research ever since. As a result, the small-scale structure of turbulence, including velocity gradients, has broad relevance across various types of flows.[1] While much of the modern understanding of small-scale turbulence dynamics has its roots in the similarity hypotheses of Kolmogorov,[37] the refined similarity hypothesis[29,30] further implies (possible) dependence on the Reynolds number, i.e., through intermittency effects. Subsequent refinements such as the multifractal view[32,33] have often focused on more precise understanding of small-scale intermittency. These advances in turbulence theory have been built on the idea of (approximate) universality at small scales for high Reynolds number turbulence. Indeed, velocity gradient statistics have been found to have such universal behavior for different flows.[38] In the end, the hypothesis of approximate local isotropy at sufficiently high Reynolds number[37]

provides an important framework for exploring universality of small-scale statistics, including velocity gradients.

In exploring the behavior of velocity gradient along trajectories traced through time in a homogeneous turbulent field, statistical stationarity is helpful for enabling straightforward analysis by maintaining constant in time bulk properties (i.e., removing effects of turbulence decay). To maintain statistical stationarity in homogeneous isotropic turbulence, it is necessary to introduce an artificial forcing term for injection of turbulent kinetic energy. The forcing is performed at large scales, which presumably have a negligible effect on small-scale dynamics such as velocity gradients at high Reynolds numbers. Therefore, this dissertation makes heavy use of forced isotropic turbulence as a canonical turbulent flow exhibiting the essential small-scale behaviors relevant to a wide range of anisotropic flow applications.

1.2.2 A Lagrangian View

Much of the early work on turbulence focused on Eulerian descriptions of the flow and of intermittency, but this dissertation will take the Lagrangian view. It is now well accepted that the dynamics of turbulence, including velocity gradients, can often be better understood in a Lagrangian frame following the flow.[39,40] Also, in many practical situations, the velocity gradient along Lagrangian or inertial particle paths determines the dynamics of sub-Kolmogorov scale objects immersed in turbulent flows, such as the deformation and break-up of bubbles and immiscible

drops,[8,9,41] the stretching of polymers,[5,6,42] the rotation rate and nutrient uptake of small swimming organisms,[14–16,43,44] and hemolysis in red-blood cells,[17,18,45] among other applications.

In recent years, considerable progress has been made by studying small-scale turbulence in the Lagrangian frame.[40,46] For example, Ref. 47 studied the deformation of volume elements in isotropic turbulence simulations finding that the deformation of spherical fluid elements into ellipsoids tends to produce a strong stretching and strong compressing direction, with the third direction stretched slightly. The energy cascade has been posed in the Lagrangian frame[48,49] and Lagrangian anomalous scaling for Lagrangian structure functions have been studied extensively and relationships to Eulerian descriptors have been established.[46,50–53] While analysis methods for dynamical systems are often impractical because of the high-dimensionality of turbulent flows,[34] tools such as finite-time Lyapunov exponents are useful in the Lagrangian frame for studying chaotic advection[54] and coherent structures.[55–58]

1.3 Outline

A more detailed discussion of the necessary background material is given next in chapter 2. Following that, the main work presented in this dissertation is comprised of two parts. In chapters 3 through 5, fully-resolved simulations are used to explore the intricate physics of stretching and rotation in turbulent flows. Chapter 3 explores

how incompressible fluid particles are deformed by exponential stretching along one direction balanced by exponential compression in another. In addition to marginal statistics for exponential stretching/compression in various directions, joint statistics are also considered to elucidate the interplay between stretching and compression by the strain rate tensor in turbulent flows. The removal of vorticity effects from the deformation process is also studied, showing that vorticity tends to decorrelate the alignment between the deformed fluid ellipsoid and the eigenvectors of the strain rate, keeping actual stretching rates much lower than in the case of perfect alignment. The material presented in chapter 3 is also published in Ref. 59. In chapter 4, the relationship between material fluid deformation and vorticity stretching is explored within the same statistical framework by inventing a measure of cumulative vorticity stretching analogous to those used for material deformation. This approach facilitates, for example, a careful comparison between the stretching of vorticity and infinitesimal material lines in isotropic turbulence using large-deviation theory. It also motivates a stochastic model for vorticity inspired by previous models of polymer stretching-relaxation dynamics. The statistical equilibrium of the vorticity model is solved analytically, giving results in good agreement with known trends. The material presented in chapter 4 is also published in Ref. 60. While chapters 3 and 4 explore these physics in homogeneous isotropic turbulence, chapter 5 considers both material deformation and vorticity stretching in an inhomogeneous turbulent flow, namely, a turbulent channel flow. In particular, instantaneous deformation rates are

localized as a function of wall distance and shown to have statistics mirroring those of isotropic turbulence above 100 viscous units from the wall, in strong support of the local isotropy hypothesis even at a quite low local Reynolds number. The effect of the spatial inhomogeneity of dissipation rate on the Lagrangian deformation statistics is also explored and compared with a previous study at a lower Reynolds number. The material presented in chapter 5 is also published in Ref. 61.

In the second part of the dissertation, chapters 6 through 9, various low-dimensional models for the dynamics of velocity gradients along Lagrangian and inertial particles are considered. Chapter 6 introduces a novel statistical closure technique using a short-time deformation map on Gaussian field statistics to generate the necessary closures, resulting in a robust stochastic model accurately capturing many of the features of low-to-moderate Reynolds number isotropic turbulence. The material presented in chapter 6 is also published in Ref. 62. In chapter 7, this stochastic model is expanded into a multiple time scale model which accurately reproduces intermittency scaling exponents, providing a fresh view on the dynamics of intermittency in turbulence. The material presented in chapter 7 is under consideration for publication as Ref. 63. Chapter 8 demonstrates the utility of the stochastic velocity gradient models for inhomogeneous turbulent flows by coupling them with LES. This opens the door to more efficient evaluation of the influence of a turbulent environment on a wide range of micro-physical applications using standard high performance computing techniques in conjunction with the velocity gradient models developed in this dissertation. The

material presented in chapter 8 is under consideration for publication as Ref. 64. Chapter 9 extends the restricted Euler model for velocity gradients from Lagrangian to general inertial trajectories. While the resulting model suffers the same drawbacks as the original restricted Euler, it also has many of the promising features and qualitative agreement with observations that under-gird the success of the stochastic models of previous sections. The material presented in chapter 9 is also published in Ref. 65. Finally, chapter 10 summarizes the main findings and draws conclusions, providing an outlook for future work.

Chapter 2

Background Concepts and Tools

This chapter introduces in more detail the concepts and tools used throughout this dissertation to explore the topic at hand. All the requisite background material is presented in this chapter, since many of the concepts are needed in multiple chapters throughout the thesis. First, §2.1 introduces the background concepts for chapters 3 through 5, such as finite time Lyapunov exponents and large-deviation statistics. Then, §2.2 lays out the stochastic formulation for modeling Lagrangian velocity gradients and reviews previous closure approaches which inform the work in chapters 6 through 8. Further introductory remarks about large-eddy simulations needed for chapter 8 are given in §2.3. In §2.4, the main concepts for treating inertial particle trajectories in chapter 9 are reviewed. Finally, the numerical datasets used throughout the dissertation for exploring physical phenomena and testing closures are detailed in §2.5.

2.1 Cumulative Stretching by the Velocity Gradient

2.1.1 Finite Time Lyapunov Exponents

Turbulence in the Lagrangian frame has been studied by exploiting analogies with dynamical systems.[54] In particular, the tendency of closely spaced fluid particle trajectories to diverge exponentially (as long as their separation distance does not exceed the viscous dissipative range), as well as the cumulative deformation of infinitesimally small fluid volumes along the trajectories, can be conveniently described by Lyapunov exponents (LE).[54,66] The largest positive Lyapunov exponent represents the average strength of the exponential growth rate. Moreover, fluctuations in the rate of growth are characterized by the finite-time Lyapunov exponents (FTLE).[67,68]

A fluid particle trajectory $\mathbf{x}(\mathbf{X}, t)$ can be defined as a mapping from an initial location $\mathbf{X}$ at time t_0 to a location $\mathbf{x}$ at a later time t, that is

$$\mathcal{T}_{t_0,t} : \mathbf{X} \in \mathbb{R}^3 \mapsto \mathbf{x} \in \mathbb{R}^3. \tag{2.1}$$

The trajectory evolves according to

$$\frac{dx_i}{dt} = u_i(\mathbf{x}, t), \qquad x_i(\mathbf{X}, t_0) = X_i, \tag{2.2}$$

where the velocity vector field $u_i(\mathbf{x}, t)$ is the solution to the incompressible Navier-Stokes (INS) equations

$$\frac{\partial u_j}{\partial x_j} = 0, \qquad \frac{\partial u_i}{\partial t} + u_j \frac{\partial u_i}{\partial x_j} = -\frac{1}{\rho}\frac{\partial p}{\partial x_i} + \nu \frac{\partial^2 u_i}{\partial x_j \partial x_j} + f_i, \tag{2.3}$$

with appropriate boundary conditions, where $p(\mathbf{x}, t)$ is the pressure, ρ is the fluid density, and $f_i(\mathbf{x}, t)$ represents any additional forcing terms.

An infinitesimal fluid particle following such a trajectory experiences deformation due to the local velocity gradient. The gradient of Eq. (2.2) with respect to initial positions yields

$$\frac{dD_{ij}}{dt} = A_{ik} D_{kj}, \qquad D_{ij}(\mathbf{X}, t_0) = \delta_{ij}, \tag{2.4}$$

which describes the evolution of the deformation tensor $D_{ij} = \partial x_i / \partial X_j$ along a trajectory. Here, $A_{ik} = \partial u_i / \partial x_k$ is the velocity gradient tensor, whose Lagrangian evolution is described by the gradient of Eq. (2.3) and has been studied in some depth.[69] The dynamics of A_{ij} itself will be considered later.

The singular values, $\sigma_i(\mathbf{X}, t)$, of the deformation tensor (square-roots of the eigenvalues for the Cauchy-Green tensor $C_{ij} = D_{ik} D_{jk}$) provide the magnitude of semi-axes for the ellipse resulting from the action of D_{ij} on a unit sphere. The finite-time Lyapunov exponents (FTLE) are defined as the exponential growth rate of these singular values:

$$\gamma_i(\mathbf{X}, t) = \frac{1}{t - t_0} \ln(\sigma_i(\mathbf{X}, t)). \tag{2.5}$$

The complete set of finite-time Lyapunov exponents $\{\gamma_1, \gamma_2, \gamma_3\}$ is composed of the three FTLEs in decreasing order, i.e. $\gamma_1 \geq \gamma_2 \geq \gamma_3$. Because of incompressibility, the velocity gradient is traceless and the deformation tensor has unity determinant (is volume-preserving) for all time. Therefore, the product of the singular values is unity $\sigma_1\sigma_2\sigma_3 = 1$ and the sum of the three FTLEs is zero $\gamma_1 + \gamma_2 + \gamma_3 = 0$. In this way, it is seen that $\gamma_1 \geq 0$ and $\gamma_3 \leq 0$ with equality in either one of these relations only if $\gamma_1 = \gamma_2 = \gamma_3 = 0$.

The Lyapunov exponents (LE) are defined as the infinite time limit of the FTLE

$$\lambda_i = \lim_{t\to\infty} \gamma_i(\mathbf{X}, t) = \lim_{t\to\infty} \frac{1}{t - t_0} \ln(\sigma_i(\mathbf{X}, t)). \tag{2.6}$$

With an appropriate ergodic assumption, the LEs are independent of the initial position $\mathbf{X}$ and equal to the ensemble-averaged or volume-averaged FTLEs:

$$\lambda_i = \langle \gamma_i \rangle = \frac{1}{t - t_0} \langle \ln(\sigma_i) \rangle. \tag{2.7}$$

A positive maximal LE, λ_1, is generally used as an indicator of chaotic Lagrangian behavior, because small disturbances in initial conditions with almost any orientation grow exponentially.

The maximal LE, λ_1, can alternatively be defined as

$$\lambda_1 = \limsup_{t\to\infty} \frac{1}{t - t_0} \ln\left(\frac{|\mathbf{r}(\mathbf{X}, t)|}{|\mathbf{r}(\mathbf{X}, t_0)|}\right), \tag{2.8}$$

where $r_i(\mathbf{X}, t)$ is an infinitesimal displacement vector evolving according to

$$\frac{dr_i}{dt} = A_{ij} r_j \tag{2.9}$$

along the trajectory. The second LE, λ_2, can be similarly defined by projecting the vector $\mathbf{r}$ into a subspace orthogonal to the maximal stretching direction. Further, the minimal LE, λ_3, can similarly be found by projecting $\mathbf{r}$ into the subspace orthogonal to both of the larger two stretching directions. This alternative view is the basis for the Gram-Schmidt orthonormalization-based procedure used for computing the Lyapunov spectrum, discussed later. A subtle difference between these two definitions of Lyapunov exponents relevant to chapter 3 is discussed in Appendix A.

2.1.2 Lagrangian Coherent Structures

In the past two decades, FTLEs have been used in attempt to define coherent flow structures in complex flows. In contrast to common Eulerian definitions of coherent structures,[70] Ref. 56 built on the insight of Ref. 55 to define Lagrangian coherent structures (LCS) in fluid flows as the locally most attracting or repelling material surfaces (material curves in 2D), which therefore create coherent trajectory patterns in their vicinity over a finite time interval of interest. Ref. 71 introduced a simple technique for elucidating hyperbolic (i.e., repelling and attracting) LCS in terms of ridges of the largest FTLE in forward and backward time, respectively. Since then,

much work has focused on mathematical refinements to the definition of LCS, leading to geodesic and variational approaches to LCS. Such refinements have introduced parabolic (jet-core surfaces) and elliptic (vortex surfaces) LCSs in addition to the hyperbolic LCSs (repelling and attracting surfaces) in the original definition. See Ref. 58 for a comprehensive review.

Although this more refined mathematical treatment of LCS theory has been developed in recent years,[58,72] the FTLE field remains the popular method for visualization of hyberbolic LCS. The simplest and most popular numerical method for elucidating hyperbolic LCS from velocity field data $\mathbf{u}(\mathbf{x}, t)$ is through the association of LCS with ridges of locally maximized FTLEs.[73] Repelling manifolds are roughly defined as having a local maximum in the $\gamma_1(\mathbf{X}, t; t_0)$ field for a given integration time $t - t_0 > 0$. These represent regions where neighboring particle trajectories are diverging most rapidly. In contrast, attracting manifolds have a local maximum in the leading FTLE when the integration is performed backward in time, thus indicating a minimum in the $\gamma_3(\mathbf{X}, t; t_0)$ field for a given integration time $t-t_0 < 0$. Attracting manifolds, then, are those regions in which neighboring trajectories are converging most rapidly. Experience has shown that such ridges in the FTLE fields usually become well-defined and sharply peaked for appropriate integration times, allowing for clarity in the practical application of the above definitions. A physical meaning often attributed to hyperbolic LCS is that of a coherent barrier to mixing in the fluid following the local fluid trajectory.[74] In other words, hyperbolic LCS are often seen as boundaries between

two regions of fluid that do not interact/mix. A critique of the common practice of equating FTLE ridges (computed over moving time windows) with LCSs is given in Ref. 72.

Studies using LCS[56–58,71,75,76] have focused on flow visualizations and identification of different regions of the flow, such as coherent barriers to mixing, etc. Typical visualizations of LCS using FTLEs display a rich structure of striated structures with more and thinner bundles of striations appearing at increasing times. The computational method used for extracting the FTLE field for the purpose of constructing LCS releases fluid particles on a densely-packed grid at time t_0. The particles are then traced using Eq. (2.2) with the known velocity field data (from experiment or direct numerical simulation of the Navier-Stokes equations). The Cauchy-Green tensor is obtained using finite-differencing on the grid of initial conditions and Eq. (2.5) is used to define the FTLE field. In this way, no velocity gradients are needed as would be the case if Eq. (2.4) were used and the resulting numerical method relates more closely with finite-size Lyapunov exponents (FSLE). This approach is helpful in reducing computation time and also noise,[57] since the gradient operator amplifies noise in the velocity field, which is particularly troublesome for experimental results.

We now briefly demonstrate LCS in the context of small-scale turbulence to briefly explore qualitative features of FTLE fields before proceeding to quantitative statistical studies in chapters 3 through 5. Instead of the typical method outlined in the previous paragraph, we construct the FTLE field by integrating Eq. (2.4) as described later

in §3.1.2 using a uniform grid of points for initial conditions. We compute FTLEs in three-dimensional space on a two-dimensional slice from a Direct Numerical Simulation database of isotropic turbulence (from the Johns Hopkins Turbulence Databases, JHTDB,[77] described later in more detail in §2.5.1). The same method for the computation of FTLEs as described later (in §3.1.2) is used here so that the results here correspond directly to the statistical results in chapter 3. The two-dimensional grid of initial conditions is 100x100 with a size of 10η in each direction. Ref. 74 pointed out that this method not as efficient as the method in the previous paragraph for the task of elucidating FTLE ridges because for long integration times, the ridges become very fine and it becomes less likely that a grid point lies on the ridge. This is the reason for using such a fine grid for our present purposes.

Figure 2.1 shows the FTLE field computed for varying values of (forward) integration time $t - t_0$ for a fixed region in the JHTDB isotropic turbulence database. As integration time increases, the overall topology of the FTLE ridges remains qualitatively the same, but the ridges themselves become finer-grained and more striations appear. Thus the process of increasing integration time reveals more and more detailed structure of the FTLE field on finer and finer scales, eventually on much smaller scales than the smallest dynamically relevant scale, η. In chapters 3 through 5, we shall be concerned with the statistical distribution of such fine-scale structures, e.g. the PDF of FTLEs.

The results and insights arising from studies using LCS as a flow visualization

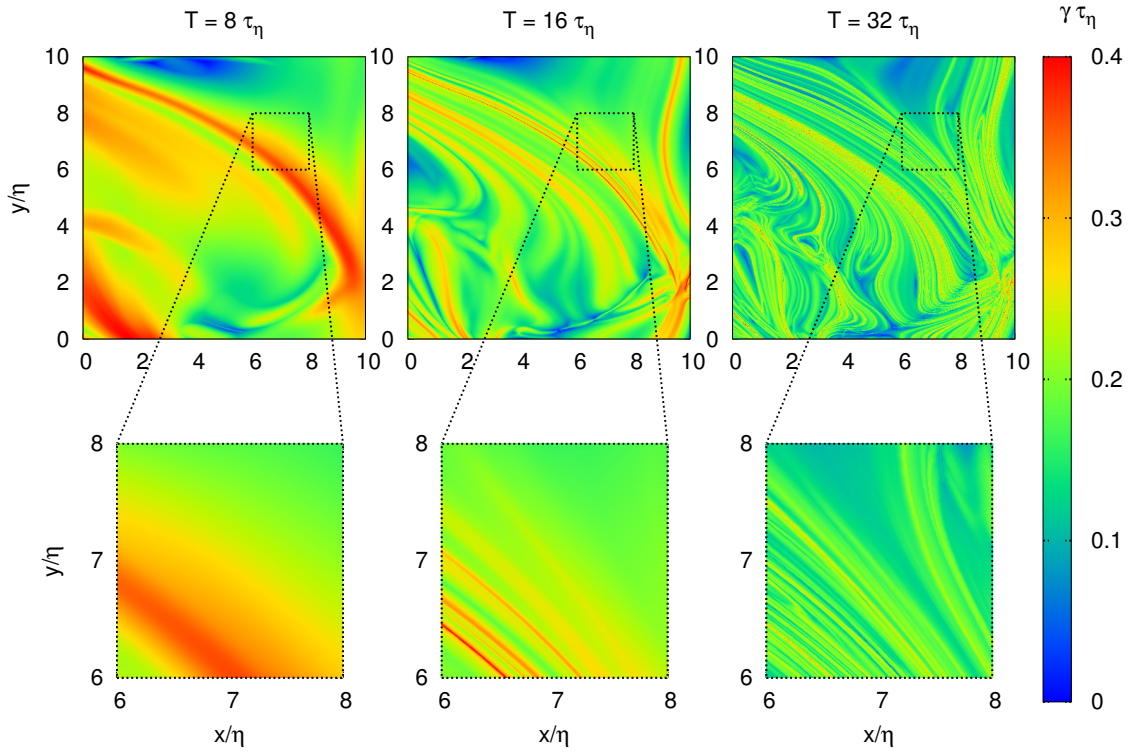

Figure 2.1: Colored images of non-dimensionalized FTLE field, $\gamma_1\tau_\eta$, with integration time of $t/\tau_\eta = 8(\text{left}), 16(\text{center}), 32(\text{right})$. Figures on the top row are of a 10η-by-10η slice, while figures on the bottom row are zoomed into a 2η-by-2η subregion. The data is from a small subset of the isotropic turbulence dataset from Direct Numerical Simulation, described in §3.1.

tool have been mostly qualitative in nature. To complement such studies, one is also interested in a more quantitative, statistical characterization of the resulting striated structures. Specifically, a statistical description of these structures must capture at the very least the probability density distribution of these structures, and how these depend on time. Describing accurately the *statistics* of FTLEs in fluid flows could lead to quantitative tools that allow for more precise use of LCS

as a diagnostic tool of important flow processes such as mixing and deformation of particles advected by the flow. For example, quantification of statistical behavior of the FTLEs of fluid particles is important for examining the physical mechanism of polymer drag reduction,[5,6,42] which occurs through the interaction of velocity gradient stretching of long polymer chains and their relaxation back toward the equilibrium state. Additionally, Ref. 9 showed that the large deviation formalism for FTLEs of fluid particle trajectories is useful in studying the deformation behavior of sub-Kolmogorov-scale droplets subjected to turbulent flows.

2.1.3 Large-Deviation Statistics

As it turns out, the basic structure of FTLEs resulting from successive applications of fluid deformations leading to fluctuating exponential growth rates has implications for the time dependence of their probability distribution functions. These too are expected to follow exponential dependence on time. The relevant formalism is called the large deviation formalism and is traceable to Cramer's work.[78] The large deviation formalism has been applied to a number fields of statistical physics, and within the study of turbulence it underlies the multifractal interpretation of the energy cascade.[34] It turns out that the statistics of FTLEs are also amenable to the large deviation formalism,[68,79] where it describes the behavior of FTLE probability density functions (PDFs) in the (thermodynamic) limit of long times ($t \to \infty$).

2.1.4 Large Deviation Theory for a Sum of Independent and Identically Distributed Variables

For a sequence of N independent and identically distributed (i.i.d.) random variables, x_i $(i = 1, 2, ..N)$, the law of large numbers ensures that the estimator for the mean

$$y_N = \frac{1}{N} \sum_{i=1}^{N} x_i, \tag{2.10}$$

is an unbiased estimator and converges to the true mean,

$$\lim_{N \to \infty} y_N = \langle x \rangle. \tag{2.11}$$

Further, Cramér's theorem states that, for large N, the probability of large deviations from the true mean decreases exponentially with increasing N, proportional to a rate function S,

$$p_y(\eta) \sim \exp(-NS(\eta)). \tag{2.12}$$

or

$$p_Y(\xi, N) \sim \exp\left[-NS\left(\frac{\xi}{N}\right)\right], \tag{2.13}$$

where $Y_N = \sum_{i=1}^{N} x_i$, is the sum of i.i.d. variables. The rate function S is sometimes also called the entropy or Cramér function in various contexts.[42, 79, 80] The Cramér

function essentially quantifies the self-similar collapse of the PDF of $y_N = \frac{Y_N}{N}$ to a Dirac delta-function at $\langle x \rangle$.

The justification of the large-deviation formalism depends on the additivity of cumulants (cumulant-generating functions) for independent variables, as well as the fact that identically distributed variables share the same cumulant-generating function. With these properties, the cumulants of the sum, Y_N, are equal to N times the cumulants of the independent variables, x_i. The validity of Eq. (2.13) thus hinges on the linear growth of the cumulants of Y_N with N.

2.1.5 Large Deviation Theory for Continuous Time Integrals

The large-deviation formalism can be extended to applications with the integration over a continuous variable with finite correlation time, $Y(T) = \int_0^T x(t)dt$. Here, the integral can be thought of as a sum of many integrals over sub-intervals, $[t_i, t_i + \Delta t)$, of the full integration interval $[0, T)$, each sub-integral being over a sufficiently large interval that it is independent of the others (and identically distributed assuming stationarity of $x(t)$). In this case, the probability density function of the integral becomes,

$$p_Y(\xi, T) \sim \exp\left[-TS_y\left(\frac{\xi}{T}\right)\right], \qquad \text{in the limit} \quad T \to \infty. \tag{2.14}$$

The validity of Eq. (2.14) hinges on the linear growth of the cumulants of $Y(T)$ with increasing integration time, T.

The preceding discussion provides an informal expectation for a large deviation principle to hold. In fact, the application of a large-deviation principle has been extended rigorously well beyond the case of sums of i.i.d. variables. The Gärtner-Ellis theorem[81,82] gives the existence of a scaled cumulant-generating function, see §2.1.7 as a criterion for the applicability of a large deviation principle. Furthermore, Donsker and Varadhan have provided a rigorous basis for large-deviation statistics of general Markovian systems.[83–86]

To date, the large-deviation formalism has found many fruitful applications within the study of turbulent flows. It forms the basis for the multifractal theory in three-dimensional turbulence,[32–34,87,88] where the singularity spectrum $f(\alpha)$ is related to the Cramér function. Large-deviation statistics have been used to digest the results of shell models[89,90] and also to introduce a variational action principle for the behavior of Navier-Stokes flows.[91,92] It has also been used for passive scalar advection,[93] the stretching of polymers,[5,6,42,94] the clustering of inertial particles,[79,95] droplet deformation,[9] and other applications reviewed by Ref. 39. Furthermore, it is important for developments in the statistical mechanical description of two-dimensional turbulence.[96–99] Meanwhile, the large-deviation statistics of FTLEs in two-dimensional turbulence and the impact on vorticity increments was explored.[100] Additionally, the bistability of two-dimensional flows has been investigated using large-deviation

statistics.[101,102]

2.1.6 Large Deviation Theory for Finite Time Lyapunov Exponents

The applicability of large-deviation statistics to FTLEs can be observed one of two ways. First, using the definition of the FTLEs in terms of singular values in Eq. (2.5), with singular value decomposition,

$$D_{ij} = U_{ik}\Sigma_{k\ell}V_{j\ell}, \tag{2.15}$$

we can utilize the evolution equation for the singular values,[103]

$$\frac{d\ln\sigma_i}{dt} = \hat{S}_{(ii)}, \qquad \hat{S}_{ij} = U_{ki}S_{k\ell}U_{\ell j}, \tag{2.16}$$

where $\hat{S}_{(ii)}$ is i^{th} diagonal element from the strain-rate tensor rotated into the reference frame of the deformation tensor, given by the unitary matrix $\mathbf{U}$. Integrating this expression along a trajectory and employing Eq. (2.5) yields

$$\gamma_i(t) = \frac{1}{t-t_0}\int_{t_0}^{t}\hat{S}_{(ii)}d\tau, \tag{2.17}$$

meaning that the FTLE can be viewed as the time-average of the quantity $\hat{S}_{(ii)}$ along the trajectory. In view of the rapidly decreasing correlation for the strain-rate tensor along a Lagrangian path,[49] we can break this integral into many sub-intervals, with the length of the sub-intervals sufficient to make each sub-integral close to statistically independent. With this step, the FTLE, γ_i, can be seen as an average of i.i.d. variables, with the mean given by the Lyapunov exponent, λ_i. Further discussion of this definition in the context of inhomogeneous flows is given in §5.1.2.

The second way to see the applicability of large-deviation statistics is to consider the material line vector evolution, Eq. (2.9). Decomposing the material line vector into a magnitude and normal vector, $r_i = |\mathbf{r}|n_i$, the evolution of the magnitude is

$$\frac{d\ln|r|}{dt} = n_i S_{ij} n_j, \tag{2.18}$$

in direct analogy to Eq. (2.16). Then following from Eq. (2.8), given that the material line aligns with the first Lyapunov direction for long time, we can write the FTLE as

$$\gamma_1(t) = \frac{1}{t-t_0}\int_{t_0}^{t} \ln\left(\frac{|\mathbf{r}(t)|}{|\mathbf{r}(t_0)|}\right) = \frac{1}{t-t_0}\int_{t_0}^{t} n_i S_{ij} n_j d\tau. \tag{2.19}$$

Some slight differences between equations (2.17) with $i = 1$ and (2.19) are elucidated in Appendix A. The same arguments from the previous paragraph can be applied here as well with the same result: the largest FTLE, γ_1, can be viewed as an average

of i.i.d. variables, with the mean being the Lyapunov exponent, λ_1. Extension to the rest of the Lyapunov spectrum can be provided by projecting material lines into orthogonal subspaces, as done in the Gram-Schmidt orthogonalization procedure.

In this way, the original theorem for i.i.d. variables can be heuristically extended to FTLEs,[34] which can be regarded as estimators for the Lyapunov exponents. Thus, the large deviation form for the probability density function of an FTLE field is given by

$$p(\gamma_i, t) \sim \exp(-tS(\gamma_i)), \tag{2.20}$$

where $S(\gamma_i)$ is the Cramér function for the i^{th} largest FTLE.

Ref. 79 measured the Cramér function of the maximal FTLE for isotropic turbulence for three Reynolds numbers (up to $Re_\lambda = 185$). They found that the maximal LE is about $\lambda_1\tau_\eta \approx 0.14$ (where τ_η is the Kolmogorov time scale) and that this value decreased slowly with increasing Reynolds number, while the width of the Cramér function increased. They also found that the second LE (λ_2) was positive with the ratio $\lambda_2/\lambda_1 = 0.28$ and pointed out that $\lambda_2 \neq 0$ is an indication of the irreversibility embedded in the Navier-Stokes equations. Then, they compared their Cramér function to the maximal FTLE for fluid particles with that for heavy particles. Later, Ref. 41 compared their Cramér function to that of lighter particles and discussed its application to bubble dynamics. Ref. 42 measured Cramér functions for FTLEs at various wall-normal locations from a turbulent channel flow simulation. They showed that, due to the fact that fluid particle trajectories sample from all wall-normal locations

when a long enough time interval, the Cramér functions from trajectories ending at different wall-normal distances collapsed onto one curve. They fit the Cramér function with a fourth-order polynomial for use in their study of polymer extensions.

To date, the Cramér function formalism has been applied to turbulence to characterize the strongest expansion, i.e. the maximal Lyapunov exponent. A more complete statistical description of LEs and FTLEs is desirable that also describes the deformations in the other directions. For three-dimensional incompressible turbulent flow, two more LEs and FTLEs exist, the minimal one being always negative while the intermediate one can be of either sign. Considering joint probability density functions for two different FTLEs (γ_i, γ_j), we extend the large deviation form to

$$p(\gamma_i, \gamma_j, t) \sim \exp(-tS(\gamma_i, \gamma_j)), \tag{2.21}$$

where we shall refer to $S(\gamma_i, \gamma_j)$ as the joint-Cramér function. Because incompressibility imposes the constraint $\gamma_1 + \gamma_2 + \gamma_3 = 0$, joint-statistics with just two of the three FTLEs is sufficient for a full description of their behavior.[47] Further, it has been effectively shown that the Kraichnan model of turbulence, with velocity statistics Gaussian in space and delta-correlated in time,[104] predicts a paraboloidal joint-Cramér function (joint-Gaussian statistics) for the FTLE.[93,105] In chapter 3, we characterize the full FTLE spectrum, including joint statistics, using Cramér functions in isotropic turbulence using fully resolved simulations. The Cramér functions for channel flow are

also considered in chapter 5. These analyses make use of the generalized Lyapunov exponent, which is described next.

2.1.7 Generalized Lyapunov Exponents

A complementary view of the probability density distribution of a random variable is given by its moments. In this context the generalized Lyapunov exponent (GLE) is defined as[68]

$$L_i(q) = \lim_{t\to\infty} \frac{1}{t} \ln\langle \exp(q\gamma_i t)\rangle = \lim_{t\to\infty} \frac{1}{t} \ln\langle \sigma_i^q\rangle, \tag{2.22}$$

where $\langle\cdot\rangle$ signifies ensemble averaging over Lagrangian trajectories in isotropic turbulence. It bears striking resemblance to, and effectively operates like, a cumulant generating function. In fact, in the general theory of large deviations, $L_i(q)$ is referred to as a scaled cumulant generating function (SCGF), the existence of which is sufficient for proving the existence of a large deviation principle.[81,82] It can be easily shown that

$$\left.\frac{dL_i}{dq}\right|_{q=0} = \langle\gamma_i\rangle = \lambda_i. \tag{2.23}$$

When the large deviation form of the probability density function for the FTLE, Eq. (2.20), is substituted into the definition of the ensemble average and the resulting integration is performed via the method of steepest descent, it is shown that the GLE

is related to the Cramér function by a Legendre transform,[68]

$$L_i(q) = \sup_{\gamma_i} \{\gamma_i q - S(\gamma_i)\}, \qquad q = \frac{dS}{d\gamma_i}. \tag{2.24}$$

Similarly, we introduce a two-dimensional GLE as

$$L_{i,j}(q_1, q_2) = \lim_{t\to\infty} \frac{1}{t} \ln\langle \exp(q_1\gamma_i t + q_2\gamma_j t)\rangle = \lim_{t\to\infty} \frac{1}{t} \ln\langle \sigma_i^{q_1}\sigma_j^{q_2}\rangle, \tag{2.25}$$

such that

$$\left.\frac{\partial L_{i,j}}{\partial q_1}\right|_{q_1=q_2=0} = \langle\gamma_i\rangle = \lambda_i, \qquad \left.\frac{\partial L_{i,j}}{\partial q_2}\right|_{q_1=q_2=0} = \langle\gamma_j\rangle = \lambda_j. \tag{2.26}$$

Then, evaluating the mean FTLE using the form of the probability density function specified by Eq. (2.21) with the method steepest descent shows the two-dimensional GLE to be related to the joint-Cramér function by a double Legendre transform,

$$L_{i,j}(q_1, q_2) = \sup_{\gamma_i,\gamma_j} \{\gamma_i q_1 + \gamma_j q_2 - S(\gamma_i, \gamma_j)\}, \qquad q_1 = \frac{\partial S}{\partial \gamma_i}, \qquad q_2 = \frac{\partial S}{\partial \gamma_j}. \tag{2.27}$$

A similar generalization to joint statistics and moments was introduced before in the context of multiple multifractal dissipation fields in turbulence.[106] Care must be taken when applying the forward and inverse Legendre transform method in practice: moments must be statistically well converged to enable accurate measurements of the

exponents.

2.1.8 Material Lines and Vorticity Stretching

An intrinsic quality of turbulence is that it is rotational.[107] The curl of Navier-Stokes, (2.3), gives an equation for the vorticity, $\omega_i = \epsilon_{ijk}\frac{\partial u_k}{\partial x_j}$,

$$\frac{\partial \omega_i}{\partial t} + u_j \frac{\partial \omega_i}{\partial x_j} = \omega_j \frac{\partial u_i}{\partial x_j} + \nu \frac{\partial^2 \omega_i}{\partial x_j \partial x_j} + \epsilon_{ijk}\frac{\partial f_k}{\partial x_j}, \tag{2.28}$$

where ϵ_{ijk} is the Levi-Cevita alternating tensor. The anti-symmetric part of the velocity gradient is directly related to the vorticity by $\Omega_{ij} = -\frac{1}{2}\epsilon_{ijk}\omega_k$ and $\omega_i = -\epsilon_{ijk}\Omega_{jk}$, so that $\Omega_{ij}\omega_j = 0$. Considering low-wavenumber forcing and sufficiently high Reynolds number, the curl of the forcing can be neglected.

One can arrive at an equation for enstrophy, $\frac{1}{2}\omega_i\omega_i$, by multiplying (2.28) by ω_i. It is seen, then, that $\omega_i A_{ij}\omega_j = \omega_i S_{ij}\omega_j$ emerges as an important source term in the enstrophy equation. This production of enstrophy by the straining of existing vorticity, $\omega_i S_{ij}\omega_j$, is often discussed in tandem with the idea of the cascade of energy to small scales[107] and can be related to the negative velocity derivative skewness[108] representing inter-scale transfer of energy. For this reason, the structure and statistics of enstrophy and other vorticity-related measures have also been studied extensively.[109–119]

Visualization of vorticity magnitude iso-surfaces in high-resolution simulations

has revealed the ubiquitous presence of tube-shaped regions of concentrated high-vorticity,[109,118,120–123] confirming earlier experimental evidence.[124] Coarse-graining at various filter-widths reveals a hierarchy of vorticity tubes, smaller tubes spirally-wrapped within larger ones,[125] once again suggesting the importance of multi-scale vorticity interactions in the turbulence energy cascade. The vortex tube picture has formed the basis for a number of simplified models of small-scale turbulence.[126–131]

Meneveau and Sreenivasan[33] and Bershadskii et al.[132] proposed a stretched-exponential fit to the tails of the dissipation and enstrophy probability density function (PDF) based on experimental data, with exponent 0.5. Later numerical results, with access to more computational resources, confirmed that a stretched-exponential provides a good fit to the both dissipation and enstrophy PDFs, but with exponent closer to 0.25.[133]

Along Lagrangian trajectories in turbulence, the velocity gradient tensor determines the deformation and rotation of infinitesimal fluid elements as well as the stretching and tilting of vorticity. These two processes are mathematically similar for an inviscid flow,[134] but key differences exist for finite viscosity,[135] such as the viscous tilting effect on vorticity.[119] A key universal observation from DNS and experiment in this context is that the enstrophy production term, $\omega_i S_{ij} \omega_j$, is positive on average, meaning that enstrophy production by stretching is more prevalent than enstrophy destruction by contraction. While Taylor[134] attributed this to the stretching of material lines by invoking an equality between material deformation and vortic-

ity stretching in inviscid flow, important differences such as those mentioned above have been identified and investigated.[116,117,119,135] These differences are manifest in the tendency of vorticity to align with the strain-rate eigenvector associated with the second-largest eigenvalue,[111] while material lines tend to align slightly toward the eigenvector associated with the largest eigenvalue.[136] As a result Ref. 116 showed that vorticity stretching is on average smaller than material line stretching.

In chapter 4, we adapt the tools used for material deformation in the previous chapters to analyze the kinematics of vorticity stretching in isotropic turbulence by introducing a novel concept: an FTLE-like quantity for the vorticity vector. This facilitates a direct comparison of material deformation and vorticity stretching statistics as two different measures of cumulative action of the strain-rate tensor. With this approach, we will attempt to explain the stretched exponential behavior using statistical properties of the vorticity stretching as described by the large deviation formalism. Chapter 5 further extends this analysis of vorticity stretching to turbulent channel flow.

2.2 Stochastic Models for Lagrangian Velocity Gradient Evolution

2.2.1 Governing Equations

The gradient of the incompressible Navier-Stokes equations, (2.3), gives the evolution equation for velocity gradient tensor, $A_{ij} = \frac{\partial u_i}{\partial x_j}$,

$$\frac{dA_{ij}}{dt} = -A_{ik}A_{kj} - P_{ij} + \nu\nabla^2 A_{ij} + f_{ij}, \tag{2.29}$$

where $\frac{d}{dt} = \frac{\partial}{\partial t} + u_k\frac{\partial}{\partial x_k}$ represents the material derivative, $P_{ij} = \frac{\partial^2 p}{\partial x_i \partial x_j}$ is the symmetric pressure Hessian tensor, and f_{ij} is the gradient of the forcing. The first term on the right-hand side is the non-linear self-amplification term, which includes important physics such as vorticity stretching, which is explored in chapter 4.

The incompressibility constraint, i.e. that the velocity gradient tensor should be trace-free, can be incorporated by evaluating the trace of the velocity gradient evolution equation, which yields the pressure Poisson equation, $P_{kk} = 2Q$, where $Q \equiv -\frac{1}{2}A_{k\ell}A_{\ell k}$. Solving the pressure Poisson equation and twice taking the gradient leads to,[113]

$$P_{ij}(\mathbf{x}, t) = \frac{2}{3}Q(\mathbf{x}, t)\delta_{ij} + \iiint_{P.V.} \frac{Q(\mathbf{x}+\mathbf{r})}{2\pi r^3}\left(\delta_{ij} - 3\frac{r_i r_j}{r^2}\right) d\mathbf{r}. \tag{2.30}$$

The isotropic part of the pressure Hessian is local and closed, while the deviatoric part of the pressure Hessian, $P_{ij}^{(d)}$, is non-local and depends on the structure of the surrounding flow. Decomposition into isotropic and deviatoric parts gives

$$\frac{dA_{ij}}{dt} = -\left(A_{ik}A_{kj} + \frac{2}{3}Q\delta_{ij}\right) - P_{ij}^{(d)} + \nu\nabla^2 A_{ij} + f_{ij}. \tag{2.31}$$

This tensor equation represents 9 differential equations for the 9 components of the velocity gradient tensor, of which 8 are independent.

The velocity gradient tensor can be written as a sum of symmetric and anti-symmetric parts, $A_{ij} = S_{ij} + \Omega_{ij}$, where $S_{ij} = \frac{1}{2}(A_{ij} + A_{ji})$ is the strain-rate tensor and $\Omega_{ij} = \frac{1}{2}(A_{ij} - A_{ji})$ is the rotation rate tensor, which can be related to the vorticity, $\omega_i = -\epsilon_{ijk}\Omega_{jk}$. Using this decomposition on the Lagrangian evolution equation,[114]

$$\begin{aligned}\frac{dS_{ij}}{dt} = &-\left(S_{ik}S_{kj} - \frac{1}{3}S_{k\ell}S_{k\ell}\delta_{ij}\right) - \left(\Omega_{ik}\Omega_{kj} - \frac{1}{3}\Omega_{ik}\Omega_{kj}\delta_{ij}\right) \\ &-P_{ij}^{(d)} + \nu\nabla^2 S_{ij} + f_{ij}^{(s)},\end{aligned} \tag{2.32}$$

$$\frac{d\Omega_{ij}}{dt} = -\left(S_{ik}\Omega_{kj} + \Omega_{ik}S_{kj}\right) + \nu\nabla^2\Omega_{ij} + f_{ij}^{(a)}, \tag{2.33}$$

where $f_{ij}^{(s)} = \frac{1}{2}(f_{ij} + f_{ji})$ and $f_{ij}^{(a)} = \frac{1}{2}(f_{ij} - f_{ji})$, are the symmetric and anti-symmetric parts of the forcing, respectively. Note that (2.33) is simply a rewriting of (2.28) in terms of the rotation rate tensor. In this way, we can separately view the evolution of the vorticity and the strain-rate, although the strong coupling in the

non-linear term is evident.

2.2.2 Restricted Euler Model

Viewing (2.31) as a 9 component dynamical system for the time evolution of A_{ij}, the self-amplification term $\mathbf{A}^2$ is closed, as is the isotropic part of the pressure Hessian $\nabla^2 p = -\mathrm{tr}\mathbf{A}^2$. Neglecting the gradient of the forcing, the evolution of velocity gradients along Lagrangian paths contains two unclosed terms requiring models: the deviatoric part of the pressure Hessian and the viscous Laplacian. These two terms require information from neighboring Lagrangian trajectories. Removal of these two terms results in the restricted Euler equation,[137–139]

$$\frac{dA_{ij}}{dt} = -A_{ik}A_{kj} + \frac{1}{3}A_{k\ell}A_{\ell k}\delta_{ij}, \tag{2.34}$$

which has the property of leading to a finite-time singularity. The term driving the singularity is the quadratic self-amplification of velocity gradients that is kinematic in nature. The unclosed terms are evidently responsible for opposing the restricted Euler singularity. A number of studies have shed some light on the dynamics of velocity gradients along Lagrangian paths, exploring invariant spaces and the unclosed terms.[114,140–143]

The restricted Euler model, despite its finite-time singularity, is interesting to study in its own right. The restricted Euler system can be projected to just two

degrees of freedom and was shown to display important features seen in turbulent flows, such as the preferential alignment of the vorticity vector in the direction of the eigenvector associated with the median eigenvalue of the strain-rate,[109,111] negative skewness in longitudinal velocity gradients, as well as the tendency to produce extreme velocity gradient events,[69] which are clustered near an invariant manifold of the restricted Euler dynamics known as the Vieillefosse tail. This qualitative success from such a simple model (neglecting unknown terms) is what generated interest and motivated further work on stochastic closures to be discussed next. In fact, much of the success seen in the stochastic models is simply due to the formulation in terms of (2.31) which capture the self-stretching of the velocity gradient exactly from the governing equations. The addition of a linear relaxation term eliminates the singularity for some initial conditions, but not for all.[144]

2.2.3 The Stochastic Approach

In order to model the Lagrangian evolution of the velocity gradient, a stochastic representation is taken.[145–147] The main idea is to split the unclosed terms into conditional means and fluctuations about these means, e.g., $P_{ij} = \langle P_{ij}|\mathbf{A}\rangle + P'_{ij}$. The conditional means can be closed through statistical approximations, while the fluctuations are modeled using Gaussian white noise. The resulting Langevin equation

is,

$$dA_{ij} = \left[-\left(A_{ik}A_{kj} + \frac{2}{3}Q\delta_{ij} \right) - \left\langle P_{ij}^{(d)} \middle| \mathbf{A} \right\rangle + \left\langle \nu\nabla^2 A_{ij} \middle| \mathbf{A} \right\rangle \right] dt + dF_{ij}, \tag{2.35}$$

which provides a model for the Lagrangian velocity gradient dynamics provided the two conditional averages and the stochastic noise term can be specified. The stochastic forcing term, $dF_{ij} = b_{ijk\ell}dW_{kl}$, is built on a tensorial Wiener process, $\langle dW_{ij} \rangle = 0$, $\langle dW_{ij}dW_{k\ell} \rangle = \delta_{ik}\delta_{j\ell}dt$, with diffusion tensor $d_{ijk\ell} = b_{ijmn}b_{k\ell mn}$. This forcing term includes contributions both from large-scale forcing, i.e., for forced isotropic turbulence, and from fluctuations in the unclosed terms away from their conditional means, i.e., the 'neighboring eddy' interpretation of Ref. 148, though the latter may be expected to be the dominant effect.

Furthermore, this tensorial stochastic ODE can be decomposed into symmetric and anti-symmetric components, as in (2.32) and (2.33),

$$\begin{aligned} dS_{ij} = \Bigg[&-\left(S_{ik}S_{kj} - \frac{1}{3}S_{k\ell}S_{k\ell}\delta_{ij} \right) - \left(\Omega_{ik}\Omega_{kj} - \frac{1}{3}\Omega_{ik}\Omega_{kj}\delta_{ij} \right) \\ &- \left\langle P_{ij}^{(d)} \middle| \mathbf{S}, \mathbf{\Omega} \right\rangle + \left\langle \nu\nabla^2 S_{ij} \middle| \mathbf{S}, \mathbf{\Omega} \right\rangle \Bigg] dt + dF_{ij}^{(s)}, \end{aligned} \tag{2.36}$$

$$d\Omega_{ij} = \left[-\left(S_{ik}\Omega_{kj} + \Omega_{ik}S_{kj} \right) + \left\langle \nu\nabla^2 \Omega_{ij} \middle| \mathbf{S}, \mathbf{\Omega} \right\rangle \right] dt + dF_{ij}^{(a)}. \tag{2.37}$$

In this system, Ω_{ij} has three independent variables with the requirement to remain anti-symmetric and S_{ij} has five independent variables with the requirement to re-

main symmetric and trace-free. The symmetric and anti-symmetric stochastic forcing terms, in this view, can be chosen independent of each other and obeying these constraints. The details of the stochastic forcing term are given in Appendix F.

The stochastic modeling approach produces the evolution equation for the single-time probability density function (PDF) for the velocity gradient tensor,

$$\begin{aligned}\frac{\partial f(\mathcal{A};t)}{\partial t} &= -\frac{\partial}{\partial \mathcal{A}_{ij}}\left(\left[-\left(\mathcal{A}_{ik}\mathcal{A}_{kj}+\frac{2}{3}\mathcal{Q}\delta_{ij}\right)-\left\langle P_{ij}^{(d)}\middle|\,\mathcal{A}\right\rangle+\left\langle \nu\nabla^2 A_{ij}\middle|\,\mathcal{A}\right\rangle\right]f(\mathcal{A};t)\right)\\ &\quad+\frac{1}{2}d_{ijk\ell}\frac{\partial^2 f(\mathcal{A};t)}{\partial \mathcal{A}_{ij}\partial \mathcal{A}_{k\ell}}.\end{aligned} \tag{2.38}$$

This Fokker-Planck equation for the PDF evolution matches that which can be constructed from (2.31), by adding stochastic forcing to represent the fluctuation of the unclosed terms.

Constructing a fully-specified stochastic model for the Lagrangian velocity gradient, then, requires specification of the two conditional averages: $\left\langle P_{ij}^{(d)}\middle|\,\mathcal{A}\right\rangle$ and $\langle \nu\nabla^2 A_{ij}|\,\mathcal{A}\rangle$. These statistical objects, in general, are quite complex, as can be appreciated by the experimental work of Ref. 143. A number of attempts, however, have been made to prescribe closures essentially having the form of (2.35), which will be reviewed next.

2.2.4 An Overview of Closures for the Stochastic Approach

Stochastic closures date back to Ref. 145, which introduced a model for the pressure Hessian and viscous Laplacian designed to reproduce log-normal statistics for the pseudo-dissipation by construction. Ref. 149 constructed a non-linear relaxation model for the viscous Laplacian using the trace of the inverse Cauchy-Green tensor, neglecting the deviatoric part of the pressure Hessian. More recent developments include the Recent Fluid Deformation (RFD) closure[146,148] and the Enhanced Gaussian Fields (EGF) closure,[147] both of which are reviewed in more detail in the following subsections.

2.2.5 Recent Fluid Deformation Closure

The central idea in the RFD closure approach[148] is to introduce a coordinate mapping based on material volume deformation in the recent Lagrangian history. Defining a Lagrangian trajectory as a map, (2.1), the Lagrangian trajectory evolves according to (2.2). The local fluid deformation map can be described by the deformation tensor, $D_{ij} = \partial x_i / \partial X_j$, which evolved according to (2.4). The general solution to this equation involves the time-ordered exponential, but approximating that the velocity

gradient is constant for short time,

$$\mathbf{D}(\mathbf{x},t;\mathbf{X},t_0) \approx \exp\left[\mathbf{A}(\mathbf{x},t)(t-t_0)\right]. \tag{2.39}$$

Instead of directly attempting to close the conditional averages in (2.35), first the approximate fluid deformation tensor is used to strain the coordinate system,

$$\langle P_{ij} | \mathbf{A} \rangle = \left\langle \frac{\partial^2 p}{\partial x_i \partial x_j} \middle| \mathbf{A} \right\rangle \approx \frac{\partial X_k}{\partial x_i} \left\langle \frac{\partial^2 p}{\partial X_k \partial X_\ell} \middle| \mathbf{A} \right\rangle \frac{\partial X_\ell}{\partial x_j} = D_{ki}^{-1} \left\langle \widetilde{P}_{k\ell} \middle| \mathbf{A} \right\rangle D_{\ell j}^{-1}, \tag{2.40}$$

where $\widetilde{P}_{ij}$ represents an approximation for the pressure Hessian at a previous time along the Lagrangian path and $D_{ij}^{-1} = \partial X_i/\partial x_j \approx \left(\exp\left[-\mathbf{A}(\mathbf{x},t)(t-t_0)\right]\right)_{ij}$. This is akin to assuming the pressure is approximately constant along pathlines for a short time (in the sense of conditional averages on $\mathbf{A}$), so that the changes in the conditional pressure Hessian are due entirely to the relative movement of neighboring fluid trajectories induced by the local velocity gradient. In this way, the closure of the conditional pressure Hessian requires the specification of initial conditions of the pressure Hessian upstream along the Lagrangian path.

The strongest assumption in the RFD model comes next, in assuming the initial condition for the mapping, i.e. the upstream conditional pressure Hessian, to be an isotropic tensor,

$$\left\langle \widetilde{P}_{ij} \middle| \mathbf{A} \right\rangle \approx \frac{1}{3} \left\langle \widetilde{P}_{kk} \middle| \mathbf{A} \right\rangle \delta_{ij}, \tag{2.41}$$

which gives

$$\langle P_{ij} | \mathbf{A} \rangle \approx \frac{1}{3} C_{ij}^{-1} \left\langle \widetilde{P}_{kk} \middle| \mathbf{A} \right\rangle . \tag{2.42}$$

where $C_{ij}^{-1} = D_{ki}^{-1} D_{kj}^{-1}$ is the inverse of the left Cauchy-Green tensor. The trace of (2.42),

$$2Q = \langle P_{kk} | \mathbf{A} \rangle \approx \frac{1}{3} C_{kk}^{-1} \left\langle \widetilde{P}_{\ell\ell} \middle| \mathbf{A} \right\rangle , \tag{2.43}$$

upon substitution, allows for the final form,

$$\langle P_{ij} | \mathbf{A} \rangle \approx 2Q \frac{C_{ij}^{-1}}{C_{kk}^{-1}}. \tag{2.44}$$

This form of the conditional pressure Hessian is appealing due to its simplicity and the intuition that the statistical bias of the pressure Hessian is related to the recent deformation of fluid particles by the velocity gradient tensor. However, as will be recalled later, even isotropic Gaussian velocity fields contain anisotropic contributions for the conditional pressure Hessian, highlighting a crucial limitation to (2.41) above.

The RFD model treats the viscous Laplacian in the same way,

$$\left\langle \nu \nabla^2 A_{ij} \middle| \mathbf{A} \right\rangle \approx \nu \frac{\partial X_p}{\partial x_k} \left\langle \frac{\partial A_{ij}}{\partial X_p \partial X_q} \middle| \mathbf{A} \right\rangle \frac{\partial X_q}{\partial x_k} = \nu D_{pk}^{-1} \left\langle \frac{\partial A_{ij}}{\partial X_p \partial X_q} \middle| \mathbf{A} \right\rangle D_{qk}^{-1}, \tag{2.45}$$

and assumes that the conditional Hessian of the velocity gradient tensor is likewise

an isotropic tensor,

$$\left\langle \frac{\partial A_{ij}}{\partial X_k \partial X_\ell} \middle| \mathbf{A} \right\rangle = \frac{1}{3} \left\langle \nabla^2_{\mathbf{X}} A_{ij} \middle| \mathbf{A} \right\rangle \delta_{k\ell}, \tag{2.46}$$

which yields,

$$\left\langle \nu \nabla^2 A_{ij} \middle| \mathbf{A} \right\rangle \approx \frac{C^{-1}_{kk}}{3} \nu \left\langle \nabla^2_{\mathbf{X}} A_{ij} \middle| \mathbf{A} \right\rangle. \tag{2.47}$$

Then taking a linear relaxation model[144] for the initial upstream conditions of the conditional viscous Laplacian,

$$\left\langle \nu \nabla^2 A_{ij} \middle| \mathbf{A} \right\rangle \approx -\frac{C^{-1}_{kk}}{3} \frac{A_{ij}}{T}. \tag{2.48}$$

In this way, the RFD closure provides a physically motivated mechanistic approach to introduce non-linearity in the viscous Laplacian term, which is helpful in removing the finite-time singularity (the Cauchy-Green tensor is exponential rather than linear). Ref. 148 and Ref. 146 argue that the proper relaxation timescale, T, for the viscous Laplacian is the integral timescale, and that the proper timescale for the recent deformation tensor is the Kolmogorov timescale, $t - t_0 = \tau_\eta$. In this way, the model introduces $Re_\lambda \sim (T/\tau_\eta)$ effects. Indeed, certain intermittency trends are reproduced by this model[148] at moderate Re_λ, but continuing to increase Re_λ beyond a certain threshold leads to increasingly unphysical results.[150] Nonetheless, the RFD closure provides a model that reproduces many of the known trends of velocity

gradient statistics at moderate Re_λ, and continues to be useful for studying velocity gradient statistics.[151]

2.2.6 Gaussian Fields Closure

Ref. 147 took a different approach to closing the conditional averages. They assumed that the *velocity* field has joint-Gaussian N-point PDFs with prescribed spectral (two-point) statistics (the pressure field constructed from such a velocity field is not Gaussian). They computed the conditional averages using this approximation by employing the characteristic functional of a Gaussian velocity field and obtaining an exact analytical result for the conditional pressure Hessian for a Gaussian velocity field

$$\begin{aligned}\left\langle P_{ij}^{(d)} \middle| \mathbf{A} \right\rangle_{\text{Gaussian}} &= \alpha\left(S_{ik}S_{kj} - \frac{1}{3}S_{k\ell}S_{\ell k}\delta_{ij}\right) + \beta\left(\Omega_{ik}\Omega_{kj} - \frac{1}{3}\Omega_{k\ell}\Omega_{\ell k}\delta_{ij}\right) \\ &\quad +\gamma\left(S_{ik}\Omega_{kj} - \Omega_{ik}S_{kj}\right) \end{aligned} \tag{2.49}$$

where

$$\alpha = -\frac{2}{7}, \qquad \beta = -\frac{2}{5}, \qquad \gamma = \frac{6}{25} + \frac{16}{75f''(0)^2}\int \frac{f'(r)f'''(r)}{r}dr, \tag{2.50}$$

with $f(r)$ specifying the longitudinal velocity correlation function in isotropic turbulence. In this expression, α and β are independent of Re_λ while γ is expected to have

weak Re_λ-dependence through the integral of the correlation function derivatives. Using a model spectrum at $Re_\lambda = 430$, a numerical result of $\gamma \approx 0.08$ was obtained.[147] As noted by Ref. 147, the form of equation (2.49) is a linear combination of the three possible symmetric, traceless tensors for general non-Gaussian fields. That is, (2.49) is quite general and is only specific to Gaussian fields when α, β, and γ are assumed independent of invariants of $\mathbf{A}$ and chosen specifically by (2.50).

Furthermore, the conditional viscous Laplacian could also be computed for Gaussian fields,[147]

$$\left\langle \nu\nabla^2 A_{ij} \middle| \mathbf{A} \right\rangle_{\text{Gaussian}} = \delta A_{ij}, \quad \text{where} \quad \delta = \nu\frac{7}{3}\frac{f^{(4)}(0)}{f''(0)}. \tag{2.51}$$

Note that $\delta < 0$ for realistic correlation functions, meaning that the Gaussian approximation leads to a linear damping model as in Ref. 144 for the viscous Laplacian. Numerical evaluation using a model spectrum at $Re_\lambda = 430$ gave the result $\delta \approx -0.65/\tau_\eta$. Using the above Gaussian-derived functional form but invoking in addition the balance of enstrophy production and dissipation with its relationship to skewness, Ref. 147 related the coefficient δ to the velocity derivative skewness, $\mathcal{S} = \left\langle (\partial u_1/\partial x_1)^3 \right\rangle / \left\langle (\partial u_1/\partial x_1)^2 \right\rangle^{3/2}$,

$$\delta = \frac{7}{6\sqrt{15}}\frac{\mathcal{S}}{\tau_\eta}, \tag{2.52}$$

a result which gave much better agreement with values estimated from DNS at

$Re_\lambda = 430$, namely $\delta \approx -0.15/\tau_\eta$, when using realistic values for the skewness (non-zero, i.e. non-Gaussian). Because the original Gaussian closure led to a singularity when integrated numerically, the authors considered an alternative model in which the functional form of the Gaussian closure was retained but the coefficients were empirically obtained by estimating them from DNS results: $\alpha = -0.61,\ \beta = -0.65,\ \gamma = 0.14,\ \delta = -0.15/\tau_\eta$.

With these empirically-adjusted coefficients, statistical stationarity was achieved and many of the known trends for velocity gradient statistics were reproduced with this approach termed the Enhanced Gaussian Fields (EGF) closure.

2.3 Large-Eddy Simulations (LES)

The goal of large-eddy simulations (LES) is to accurately capture the coarse-grained dynamics of high Reynolds number turbulent flows[152] with arbitrarily complex geometries. In doing so, a large majority of the turbulent kinetic energy and flow-specific large-scale features may be resolved at a small fraction of the cost of direct numerical simulations (DNS) by replacing the fine-scale details of the flow with a sub-grid scale (SGS) model for their effect on the resolved dynamics.[153,154] While such an approach has, in many cases, proven successful for simulating high Reynolds number turbulence, many applications require a more detailed representation of the fine-scale properties of the flow. Examples include particle dispersion,[155]

preferential concentration of inertial particles,[23,24] rotation and orientation dynamics of rigid particles and fibers,[12–14] break-up and coalescence of aggregates, drops, and bubbles,[7–11] micro-organism motility and nutrient uptake,[15,16,156] flow-induced hemolysis,[17–20] polymer stretching-relaxation dynamics,[3–6] and strain-rate quenching of turbulent premixed flames.[22,157]

2.3.1 LES Equations

Large-eddy simulations (LES) represent an attempt to simulate the evolution of a filtered velocity field,[158]

$$\widetilde{u}_i(\mathbf{x}) = \iiint G(\mathbf{r};\Delta) u_i(\mathbf{x}+\mathbf{r}) d^3r, \tag{2.53}$$

defined using a filter kernel $G(\mathbf{r};\Delta)$ with width Δ. The LES equations are derived by applying the filtering operation, (2.53), to the INS equations, (2.3),

$$\partial_t \widetilde{u}_i + \widetilde{u}_j \partial_j \widetilde{u}_i = -\partial_i \widetilde{p} + \nu \nabla^2 \widetilde{u}_i - \partial_j \sigma_{ij}, \tag{2.54}$$

where $\sigma_{ij} = \widetilde{u_i u_j} - \widetilde{u}_i \widetilde{u}_j$ is the sub-grid stress (SGS) tensor which requires a closure model.[152] For chapter 8, we consider the popular, broad class of Smagorinsky models based on the eddy viscosity approximation for the deviatoric stress σ^d_{ij}, with length

scale Δ and inverse time scale $|\widetilde{S}| = \sqrt{2\widetilde{S}_{ij}\widetilde{S}_{ij}}$,[159]

$$\sigma_{ij}^{d} = -2(C_s\Delta)^2|\widetilde{S}|\widetilde{S}_{ij}, \tag{2.55}$$

where C_s is the Smagorinsky coefficient. This coefficient may be specified as a prescribed model parameter,[153] or determined dynamically using information from the resolved flow field.[160]

2.3.2 Modeling of Sub-grid Physics in LES

While improvements for SGS modeling of LES have been an important topic of research for the past three decades, some focus is now shifting toward how micro-physical processes such as those mentioned above might be accurately dealt with in the context of LES, where the relevant small-scale turbulence dynamics are simply not resolved. For instance, there has been work on modeling unresolved velocity fluctuations for studying dispersion and other particle statistics such as inertial particle clustering.[161–166] However, many of the aforementioned micro-physical applications are strongly affected by the gradient of the velocity field (or coarse-grained gradient depending on the scale of the physics involved), which has not received much attention in LES modeling contexts. A notable exception is the work of Ref. 167, which coupled the tensorial Ornstein-Uhlenbeck (OU) model of Ref. 13 to an LES of isotropic turbulence. In that case, the limitations of the OU model, most notably

the assumption of Gaussian statistics, in faithfully representing turbulent velocity gradient dynamics severely limited the resulting accuracy. The dynamics of velocity gradients in turbulence are highly non-Gaussian[168,169] with significant spatio-temporal complexity. These highly non-trivial dynamics can have important consequences for a wide range of micro-physical applications where turbulence can play a role. The dynamics of velocity gradients provide not only a rich description of the local flow conditions[69] but are also of theoretical interest to better understand phenomena such as intermittency[38,170] and Lagrangian chaos.[54,66]

2.3.3 Dissipation and Velocity Gradients in LES

When considering the large-scale kinetic energy equation derived from (2.54), energy is dissipated from the filtered field in two ways: (i) resolved molecular dissipation, $\nu|\widetilde{S}|^2$, and (ii) transfer of energy to unresolved scales, $\Pi = -\sigma_{ij}\widetilde{S}_{ij}$. When using a Smagorinsky model, this so-called SGS production becomes $\Pi = (C_s\Delta)^2|\widetilde{S}|^3$, and is positive (no backscatter) as long as C_s^2 remains positive.

The goal of LES is to resolve the most energetic motions of the flow. In fact, some consider the defining quality of an LES to be the resolution of a certain percentage (e.g. 80%) of the flow's turbulent kinetic energy.[108] Away from walls, this goal can often be achieved with cost relatively independent of Reynolds number since most of the energy resides in the largest decade (or so) of length scales. However, when velocity gradients are important to the application at hand, the situation becomes

more difficult.

Consider a turbulent flow with Hölder exponents $h(\mathbf{x}, t)$, that is, the velocity increments at length ℓ locally scale as $\delta u(\ell) \sim \ell^h$ in the inertial range of scales (this scaling can also be done in a global sense for L_p norms using Besov exponents[171]). The fully resolved velocity gradient scales as $|\mathbf{A}| \sim \delta u(\eta)/\eta \sim \eta^{h-1}$, where $\eta = \nu^{3/4}\langle\epsilon\rangle^{-1/4}$ is the Kolmogorov length scale. Further, the filtered velocity gradient scales as $|\widetilde{\mathbf{A}}| \sim \delta u(\Delta)/\Delta \sim \Delta^{h-1}$. Thus, the percent of resolved velocity gradient can be estimated roughly as

$$\frac{|\widetilde{\mathbf{A}}|}{|\mathbf{A}|} \sim \left(\frac{\eta}{\Delta}\right)^{1-h}, \tag{2.56}$$

which becomes very small for $\Delta \ll \eta$ when $h < 1$ (the similarity arguments of Kolmogorov in 1941 (K41)[37] and the phenomenologies that have emerged from that work lead to the approximation $h \approx \frac{1}{3}$). According to (2.56), to resolve a certain fraction of the velocity gradient as the Reynolds number is increased, the grid resolution ($\sim \Delta$) must increase proportional to η, which leads to DNS-like scaling of the computation cost. At high Reynolds numbers, direct resolution of velocity gradients becomes prohibitively expensive and further modeling effort is needed. Therefore, while the average value of the magnitude of velocity gradients in a turbulent flow can be approximated from LES according to $|\mathbf{A}| \sim \sqrt{\Pi/\nu}$, the velocity gradient's tensorial structure, dynamical evolution, and increasing intermittency at smaller scales cannot easily be predicted in LES. A model for computing these details of the velocity gradient tensor within LES is developed in chapter 8.

2.4 Inertial Particles

Small particles embedded in a turbulent flow have interesting behaviors when the particle density, ρ_p, is different from the density of the surrounding fluid, ρ_f. For example, within a certain parameter range, heavy particles tend to cluster in regions where the strain-rate is higher than the rotation-rate,[23,24,172,173] while the opposite is true of lighter particles[41] such as bubbles[174,175] and oil droplets.[176] This clustering effect[95,177] can enhance collision rates.[178–182] The rate of clustering can be related to the surrounding fluid's velocity gradient structure experienced by particles along their trajectories.[23,95] Other important aspects of multi-phase flows in various applications, such as particle rotation and orientation,[13,14,44] droplet or bubble deformation,[9,183] and nutrient uptake[15,16] similarly depend on the local velocity gradient structure.

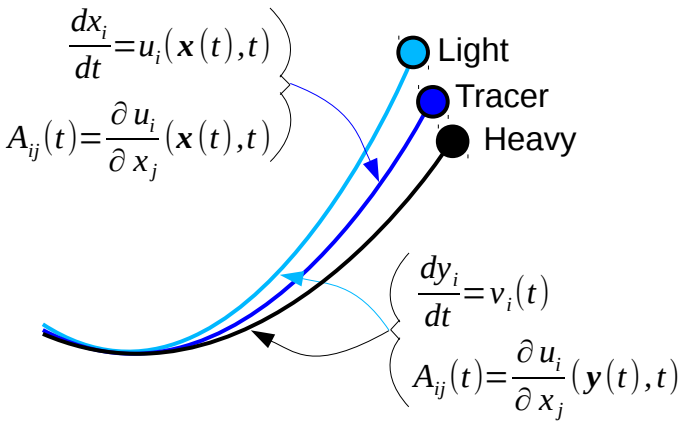

Figure 2.2: Sketch of fluid and inertial particle trajectories. In this dissertation, we consider the time history of fluid velocity gradients, $A_{ij}(t)$, along these trajectories.

As illustrated in Figure 2.2, while small fluid tracer particles, i.e. with $\rho_p = \rho_f$,

follow Lagrangian trajectories, (2.2), inertial particle trajectories evolve following the particle velocity $\mathbf{v}(t)$ according to $dy_i/dt = v_i(t)$, where $y_i(t)$ is the inertial particle position and, in general, $v_i(t) \neq u_i(\mathbf{y}, t)$. When the particle radius $a \ll \eta = \nu^{3/4}\langle\epsilon\rangle^{-1/4}$ (η is the Kolmogorov length scale, where ν is kinematic viscosity of the surrounding fluid and $\langle\epsilon\rangle$ is the average dissipation rate of the fluid flow) and $Re_a = a|\mathbf{v}-\mathbf{u}|/\nu \ll 1$ (particle Reynolds number), the dynamical equation of the inertial particle trajectory[184] in the absence of gravitational settling can be simplified to,[23,95]

$$\frac{dv_i}{dt} = \beta\frac{Du_i}{Dt} + \frac{u_i - v_i}{\tau_p}, \tag{2.57}$$

where $\beta = 3\rho_f/(2\rho_p + \rho_f)$ is the added mass parameter and $\tau_p = a^2/3\nu\beta$ is the relaxation time for the trajectory of a spherical particle of radius a. When discussing inertial particle trajectories, the Lagrangian time derivative will be given the special notation $D/Dt = \partial/\partial t + u_k\partial/\partial x_k$ to denote the lack of inertial effects. For small Stokes number based on the Kolmogorov timescale ($\tau_\eta = \nu^{1/2}\langle\epsilon\rangle^{-1/2}$), $St = \tau_p/\tau_\eta \ll 1$, Ref. 23 constructed a perturbation solution to linear order in St which yields the following approximation,

$$v_i = u_i - (1-\beta)\tau_p\frac{Du_i}{Dt}. \tag{2.58}$$

This solution admits an interpretation in terms of a particle velocity field, $v_i(\mathbf{x}, t)$, such that the velocity of a particle at location $y_i(t)$ can be approximated by $v_i(t) = v_i(\mathbf{y}(t), t)$. In this way, the particle's time derivative can be interpreted as $d/dt =$

$\partial/\partial t + v_k \partial/\partial x_k$. While at finite Stokes number the particle velocity field could be multi-valued as two particles can have different velocities at the same point, the linear perturbation expansion for $St \ll 1$ gives a single-valued particle velocity field. Since this velocity field has non-zero divergence, it can describe clustering effects due to particle inertia. In chapter 9, this approximation will be used to extend the restricted Euler model introduced in §2.2.2 to include inertial particle effects – a first step toward modeling the time history of velocity gradients experienced by inertial particles in a turbulent flow.

2.5 Numerical Databases

2.5.1 Isotropic Turbulence

The main source of isotropic turbulence data in this dissertation is a 1024^3-node DNS that is publicly available at the Johns Hopkins Turbulence Databases (JHTDB).[77,185] The computational domain is a $2\pi^3$ box with periodic boundaries. The incompressible Navier-Stokes equations with low wavenumber forcing, Eq. (2.3), are solved using a pseudo-spectral method with $k_{max}\eta \approx 1.4$ and a 2^{nd}-order Adams-Bashforth method for time advancement with de-aliasing via a $2\sqrt{2}/3$ truncation and random phase shift.[186] The main parameters of the simulation are given in Table 2.1. The velocity and pressure field data are stored on a database and publicly accessible through a web-services interface with server-side routines for computing Lagrangian

trajectories and velocity gradients. The total simulation time stored is approximately 45 Kolmogorov time scales (τ_η) with the velocity field data provided at a time step of $\Delta t \approx \tau_\eta/22$ (10 times the simulation time step). After the studies performed for this dissertation, the isotropic dataset has been extended in time to include about 225 Kolmogorov time scale of continuous integration.

Using the velocity field data from the JHTDB, the built-in function for calculating Lagrangian trajectories from Eq. (2.2) uses a 2^{nd}-order predictor-corrector method.[187] Once the trajectories are calculated, the velocity gradients are computed at each point using a 4^{th}-order central finite-difference method with 4^{th}-order Lagrange interpolation.

Table 2.1: Numerical details for isotropic turbulence datasets used in this dissertation.

Database	N	Re_λ	ϵ	ν	η	τ_η	Δt (saved)	T
JHTDB[77,185]	1024^3	433	0.928	1.85e-04	2.87e-03	0.045	2e-03	2.048
iCFD[188]	2048^3	420	0.88	3.5e-04	2.6e-03	0.02	1.15e-03	5.428

To facilitate comparisons useful for chapter 3, see Appendix B.2, data from a second simulation were used. This simulation, from the iCFD database, is described in Ref. 188 and Table 2.1 gives some representative parameters. This simulation likewise uses a pseudo-spectral method in space with a 2^{nd}-order Adams-Bashforth method for time advancement. The Reynolds number was very close to that of the JHTDB data, allowing for close comparison between the two datasets. Particle trajectories and velocity gradients were calculated during the simulation, having the advantages of spectral differentiation methods for the velocity gradient calculations rather than

the less accurate finite differencing. The velocity gradient data is stored with a time step of about $\Delta t \approx \tau_\eta/17$ over a time interval of about $270\tau_\eta$ for 3184 trajectories.

2.5.2 Turbulent Channel Flow

The channel flow dataset from JHTDB used throughout this dissertation, particularly in chapters 5 and 8, was generated from a DNS of Navier-Stokes using a pseudo-spectral method in the plane parallel to the walls and a seventh-order B-splines collocation method in the wall-normal direction.[189,190] For the simulation, the Navier-Stokes equations were formulated in wall-normal, velocity-vorticity form.[191] Pressure was computed through solving the pressure Poisson equation only when writing to disk, which was every 5 timesteps for 4000 snapshots, enough for about one domain flow-through time. The simulation domain size was $8\pi \times 2 \times 3\pi$ with a resolution of $2048 \times 512 \times 1536$ in the streamwise (x), wall-normal (y), and spanwise (z) directions respectively. Time advancement was done with a third-order low-storage Runge-Kutta method and 2/3 truncation was performed for de-aliasing.[192] A constant pressure gradient was enforced to drive the flow at $Re_\tau = \frac{u_* h}{\nu} = 1000$ ($Re_{bulk} = \frac{2hU_{\text{bulk}}}{\nu} = 40,000$) with near unity bulk velocity. Table 2.2 includes further details about the channel flow simulation.

Table 2.2: Numerical details for the channel flow dataset used in this dissertation.[190]

N_x	N_y	N_z	Re_τ	dp/dx	ν	u_*	U_{bulk}	Δx^+	Δz^+	Δt
2048	512	1536	1000	−2.5e-3	5e-5	5e-2	1.00	12.3	6.1	1.3e-3

Chapter 3

Large Deviation Statistics of Finite-Time Lyapunov Exponents in Isotropic Turbulence

In this chapter, the kinematic consequences of turbulent velocity gradients are considered in the Lagrangian frame, particularly with respect to the deforming, stretching, and rotating action of the local fluid environment. Understanding the way turbulence acts to deform fluid elements is fundamental to the way in which turbulence can impact immersed deformable particles such as drops, bubbles, or aggregates. While previous studies have focused primarily only on the most extensive direction of stretching (largest Lyapunov exponent), we study the full 3-dimensional behavior of stretching in turbulence, which is important for considering the behavior of such

3-dimensional objects in turbulence. In some situations, such as viscous droplets, the relative influence of strain-rate and vorticity on micro-physical dynamics can be dramatically varied by application-specified parameters. This fact highlights also the importance of studying separately the impact of vorticity and strain-rate on material volume behavior. The results in this chapter provide a fundamental building block for understanding the complex behavior of deformable particles in turbulent flows.

In §3.1, some numerical details are given of how FTLEs are evaluated based on Lagrangian tracking of fluid deformations. In §3.2 we compare two methods to obtain the Cramér function, one based on histograms and the other on moments. For the former, a finite size correction method is formulated which accelerates convergence towards asymptotic behavior (some technical details are also presented in Appendix C). Then in §3.3, the formalism is extended and applied to joint distributions to characterize simultaneously the statistics of two FTLEs, fully specifying the Lyapunov spectrum. Also we introduce a Cramér function for the ratio of two FTLEs. In §3.4 we examine the importance of rotation (vorticity) on the FTLEs and show that rotation severely curtails the successive straining arising from the symmetric part of the velocity gradient tensor. Conclusions of the study are summarized in §3.5. The content of this chapter is published in Ref. 59.

3.1 Numerical Simulations

3.1.1 Isotropic Turbulence Databases from DNS

For this study, ensembles of $20,000$ Lagrangian trajectories were used to compute the relevant statistical quantities from the JHTDB isotropic dataset. The $2\pi^3$ domain was subdivided into $1,000$ boxes of size $(\pi/5)^3$. Within each box, 20 particle trajectories were initialized at random positions, selected from a uniform spatial distribution along each coordinate. This approach ensures a quite uniform yet random coverage of the domain.

3.1.2 Tracking Fluid Volume Deformations

The fluid volume deformation D_{ij} along each trajectory was simulated using Eq. (2.4), which is equivalent to simulating Eq. (2.9) for three orthogonal displacement vectors r_i (the vectors being the columns of D_{ij}). Each deformation tensor was initialized to the identity tensor δ_{ij} and, in keeping with the method of Ref. 193, were periodically orthonormalized using the modified Gram-Schmidt method to avoid numerical overflow and precision issues.[194]

The governing ordinary differential equation, Eq. (2.4), was advanced in time using the matrix exponential, which is the exact solution for a constant velocity

gradient:

$$D_{ij}(t + \Delta t) = \exp(A_{ik}(t)\Delta t)D_{kj}(t). \tag{3.1}$$

The time step used and total simulation time interval were the same as those of the simulation storage time step discussed above. The Gram-Schmidt orthonormalization was performed every ten time steps. A sensitivity study showed that the FTLE results were very insensitive to the periodicity of the orthonormalization in this range. The Gram-Schmidt process splits the deformation tensor into an orthonormal tensor Q_{ij} which preserves the directional information of the deformation and an upper triangular matrix R_{ij} whose diagonal elements provide the stretching (or contraction) information for the time segment since the last Gram-Schmidt step. The deformation tensor was then re-initialized to the Q_{ij} tensor and the diagonal elements of R_{ij} were stored for reconstructing the FTLEs at the end of the simulation.

3.2 Measuring the Cramér Function

3.2.1 Histogram Method

For numerical calculation, at a given finite FTLE integration time, the Cramér function can be estimated by

$$S(\gamma_i) \approx -\frac{1}{t - t_0} \ln p(\gamma_i, t), \tag{3.2}$$

which is obtained by directly inverting Eq. (2.20). Of course, this equation is obtained only from a statement of proportionality that holds directly only for $t \to \infty$. For a finite time computation, additional correction terms could be important (we recall that in the multifractal formalism such a correction was shown to be important in the direct evaluation of the singularity spectrum[195]). The first-order correction is simply the requirement of a normalized PDF. For this, we introduce a normalization factor $N_i(t)$, which is a function of time such that $\int_{-\infty}^{\infty} p(\gamma_i, t) d\gamma_i = 1$, resulting in,

$$p(\gamma_i, t) \approx N_i(t) \exp(-tS(\gamma_i)). \tag{3.3}$$

Inverting (3.3) gives an approximation for the Cramér function with first-order correction,

$$S(\gamma_i) \approx -\frac{1}{t - t_0} \ln p(\gamma_i, t) + C_i(t), \qquad C_i(t) = -\frac{1}{t - t_0} \ln N_i(t). \tag{3.4}$$

An approximation for the specific form of $C_i(t)$, which provides a time-dependent shift to the Cramér function, is given in Appendix C.1. Therefore, the normalized marginal PDF for one of the FTLEs $p(\gamma_i, t)$ can be constructed from a histogram at a given integration time and Eq. (3.2) or Eq. (3.4) is applied to approximate the Cramér function, with the latter expected to give more rapid collapse as integration time increases. Figure 3.1 compares the Cramér function results for the maximal FTLE γ_1 obtained from the histograms using these two equations for four different integration

times. The shift term does well in collapsing the four curve from different integration times, especially near the minima, which are now very close to the expected $S_{min} = 0$.

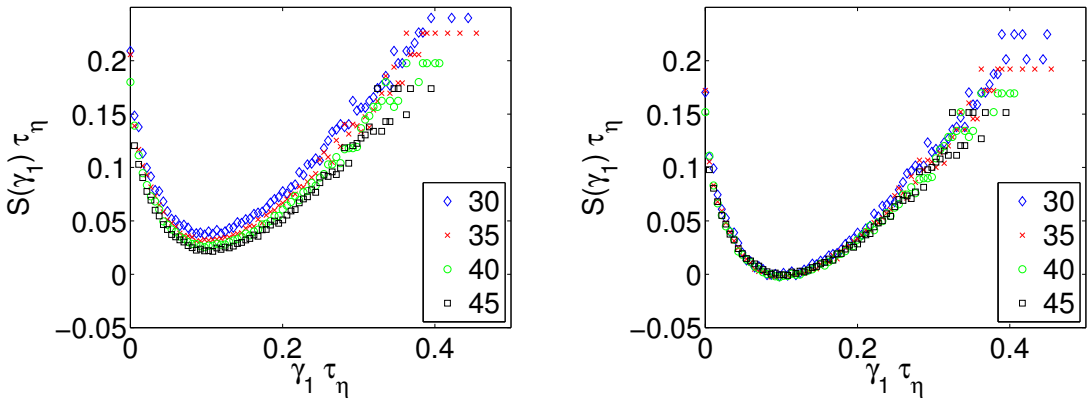

Figure 3.1: Cramér functions computed directly from normalized histograms using (a) Eq. (3.2) without the first-order correction and (b) Eq. (3.4) with the first-order shift term. Legend gives integration time in t/τ_η units.

While the shift term from normalization considerations provides considerable improvement in the collapse of the Cramér function approximated using the histogram method, there are still clear signs that a converged result has not been obtained for an integration time of $t = 45\tau_\eta$. Figure 3.2 shows the histograms used for constructing the Cramér functions and highlights the convergence behavior by showing two different integration times of $t = 30\tau_\eta$ and $t = 45\tau_\eta$. It is apparent that as the integration time increases, the Cramér function width is increasing. Less apparent in the figure is the increase of λ_1, the location of the Cramér function's minimum. This provides motivation for exploring other means of generating the Cramér function from the results of the fluid particle deformation simulations.

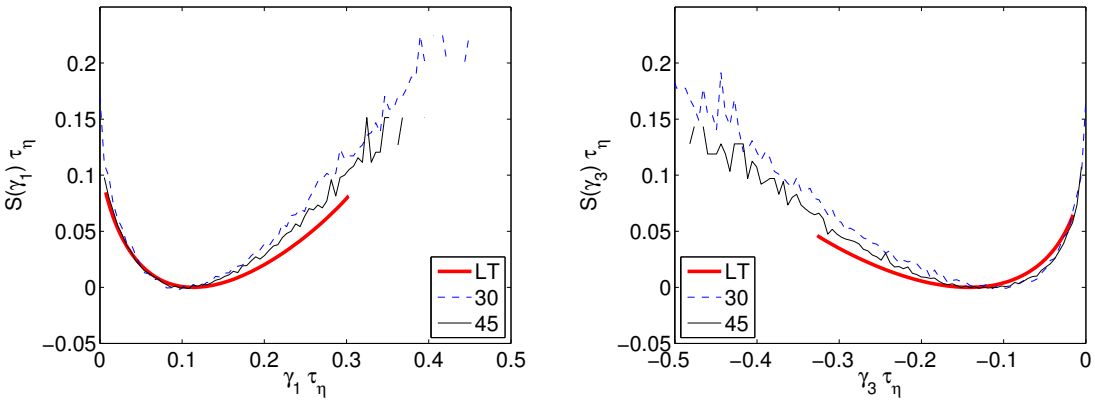

Figure 3.2: Cramér functions of (a) the maximal FTLE, γ_1, and (b) the minimal FTLE γ_3. The blue dashed and black solid lines are computed directly from normalized histograms at integration times of $30\tau_\eta$ and $45\tau_\eta$ using Eq. (3.4) with the first-order shift term, while the thick solid red lines show results obtained from the moments via the Legendre transform method, see §3.2.2 below.

3.2.2 Legendre Transform Method

The generalized Lyapunov exponents $L_i(q)$ are computed using the fact that, for $t \to \infty$,

$$\ln\langle \exp(q\gamma_i t)\rangle \sim L_i(q)t. \tag{3.5}$$

Therefore, the generalized Lyapunov exponents can be constructed by plotting $\ln\langle \exp(q\gamma_i t)\rangle$ versus time for a range of q values and using linear regression analysis over a suitable time interval to determine the slope. As shown in Figure 3.3, the plots appear to display a clear asymptotic linear trend in the data. In this case, the range of acceptable curve fits used to reconstruct the Cramér function was about $-3 < q < 0.5$. This figure is representative of the quality of curve fits obtained for all three Lyapunov

exponents.

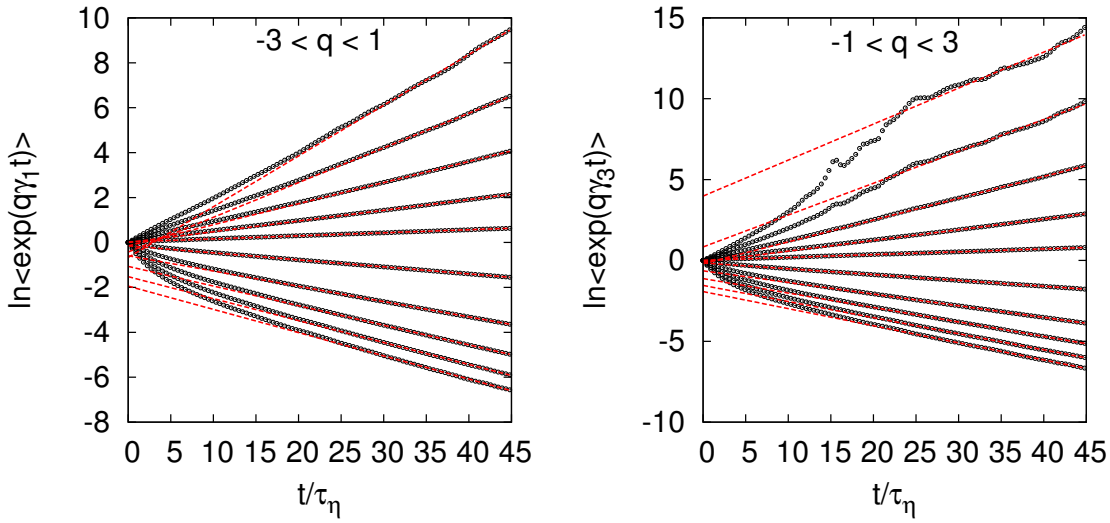

(a) (b)

Figure 3.3: Example linear curve fits for (a) $\ln\langle\exp(q\gamma_1 t)\rangle$ and (b) $\ln\langle\exp(q\gamma_3 t)\rangle$. In both plots, the values of q are spaced evenly between the stated limits, with curves for higher q values on top of curves with lower q values.

The linear regression analysis was performed for $-3 < q < 3$ with spacing $\Delta q = 0.02$. Only the last third of the time interval, i.e. $30\tau_\eta < t < 45\tau_\eta$, is used for the linear regression analysis. The slopes as a function of q provided the $L_i(q)$ results. Along with the slope, the 95% confidence interval was computed based on the standard error in the regression analysis. Slopes with errors above a specified threshold were removed from the results. The resulting GLEs are shown in Fig. 3.4, non-dimensionalized using the Kolmogorov time scale τ_η, and compared with iCFD results for the same integration time ($45\tau_\eta$).

Finally, the inverse Legendre transform was performed on the generalized Lya-

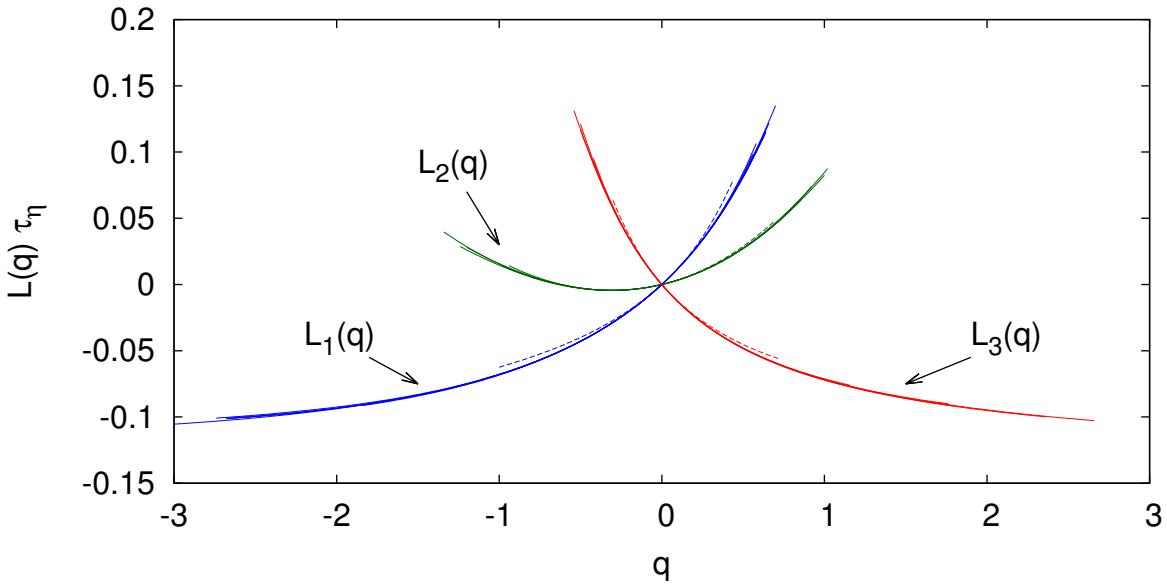

Figure 3.4: The three generalized Lyapunov exponents as constructed from linear regression analysis. Solid lines show results from different trajectory ensembles computed (containing 64k trajectories each) from the JHTDB data and the dashed lines show results from the iCFD data (containing 3.2k trajectories).

punov curves to construct the Cramér functions. For this, Eq. (2.24) was inverted so that, for each $L_i(q)$ data point, the corresponding FTLE was found via

$$\gamma_i = \frac{dL_i}{dq} \tag{3.6}$$

which was computed using 2^{nd}-order central finite-differencing. Then the Cramér function was computed from

$$S(\gamma_i) = q\gamma_i - L_i(q) \tag{3.7}$$

on a point-by-point basis. Note that this method assumes a certain regularity for inverting the Legendre transform, speicfically, that the Cramér function is convex. Therefore, this method technically constructs the convex hull of the Cramér function.

The resulting Cramér functions are shown in Fig. 3.5. The results from the Legendre transform method provide smoother curves because the linear curve fitting procedure smooths out noise from finite sample effects. This is especially notable in the tails of the Cramér function, but it is important to note that this does not mean that the Legendre transform method circumvents the convergence difficulties of accurately measuring statistics of rare events. While the curves are smooth in the tails, there is still increased statistical error in these regions, as seen from the spread in the curves generated from different ensembles in Fig. 3.5. Nonetheless, the Legendre transform method circumvents some of the convergence effects plaguing the direct histogram method (e.g., the Legendre transform method requires no finite-size correction) and is therefore favored for the remainder of this chapter. To compare the Legendre transform method to that based on PDFs, in Fig. 3.2 we show as a thick solid red lines the results from the Legendre transform method. As can be seen the results of the histogram method appear to be converging toward the results of the Legendre transform method. Further validation of the Legendre transform method and error estimates from remaining convergence issues are briefly discussed in Appendix B.

Because this method for construction returns the convex hull of the Cramér func-

tion, regions of $S(\gamma) \sim a\gamma + b$ (for any a and b values) cannot be represented explicitly by this method with finite-differencing used for the inverse transform because they would map to a single point/kink on the generalized Lyapunov exponent.

Note that the function $S(\gamma_1)$ is only defined for $\gamma_1 \geq 0$ and $S(\gamma_3)$ is only defined for $\gamma_3 \leq 0$, which is a requirement of incompressibility. The respective minimum point for each Cramér function occurs at the location where the FTLE equals the LE, i.e. $S(\lambda_i) = 0$. With this observation, the Lyapunov spectrum for the JHTDB simulation is found to be $\{\lambda_1, \lambda_2, \lambda_3\}\tau_\eta = \{0.114, 0.029, -0.143\}$. It is of interest to note that the ratio between the LEs is close to $\lambda_1 : \lambda_2 : \lambda_3 \approx 3.9 : 1 : -4.9$. The middle Lyapunov exponent λ_2 is positive but significantly smaller than the maximal LE λ_1, in qualitative agreement with the observations of Ref. 47.

For comparison, consider the hypothetical scenario in which the strain-rate eigen-frame is, at every point in time along a Lagrangian trajectory, artificially rotated so as to align with the eigen-frame of the Cauchy-Green tensor. In this scenario, γ_1 is always stretched by $\Lambda_1 > 0$ (the largest strain-rate eigenvalue), γ_2 is always stretched or compressed by Λ_2 (the middle strain-rate eigenvalue), and γ_3 is always compressed by $\Lambda_3 < 0$ (the smallest strain-rate eigenvalue). Therefore, under the ergodic assumption, each of the three FTLE values approach their respective mean eigenvalues from the strain-rate tensor for long time. The result is that the Lyapunov spectrum would be given by the mean of the strain-rate eigenvalue spectrum. The same effect could also be achieved by artificially rotating the Cauchy-Green tensor

at every point in time to align with the eigen-frame of the strain-rate tensor. We refer to this scenario as one with perfect alignment between the Cauchy-Green and strain-rate tensors. Monin and Yaglom[196] argued that the tilting of the Cauchy-Green tensor by the strain-rate tensor toward the its eigen-frame leads to perfect alignment and realization of the above equality between the Lyapunov exponents and mean strain-rate eigenvalues.

The spectrum of mean eigenvalues of the strain-rate tensor for the JHTDB simulation is $\{\langle\Lambda_1\rangle, \langle\Lambda_2\rangle, \langle\Lambda_3\rangle\}\tau_\eta = \{0.358, 0.083, -0.441\}$, which forms a ratio of $\langle\Lambda_1\rangle : \langle\Lambda_2\rangle : \langle\Lambda_3\rangle \approx 4.3 : 1 : -5.3$. This is close to the ratio of approximately 4 : 1 : -5 first identified by Ref. 111 at a lower Reynolds number also for the strain-rate eigenvalues. Notably, the largest FTLE, λ_1, is about one-third of the largest average strain-rate eigenvalue, $\langle\Lambda_1\rangle$, confirming the observations of Ref. 47 that perfect alignment between the Cauchy-Green tensor and the strain-rate tensor is not nearly achieved. The ratio of FTLEs favors a positive λ_2 slightly more than the ratio of strain-rate eigenvalues favors a positive middle eigenvalue.

There are two physical effects preventing perfect alignment between the deformation tensor and the strain-rate tensor.[47] First, the vorticity acts to rotate the deformation tensor along the Lagrangian trajectory. Secondly, the principal axes of the strain-rate also rotate and can suddenly switch, which Ref. 47 referred to as non-persistent straining. The extent of the former effect will be directly investigated later in this chapter (§3.4) in terms of large-deviation statistics by removing the action of

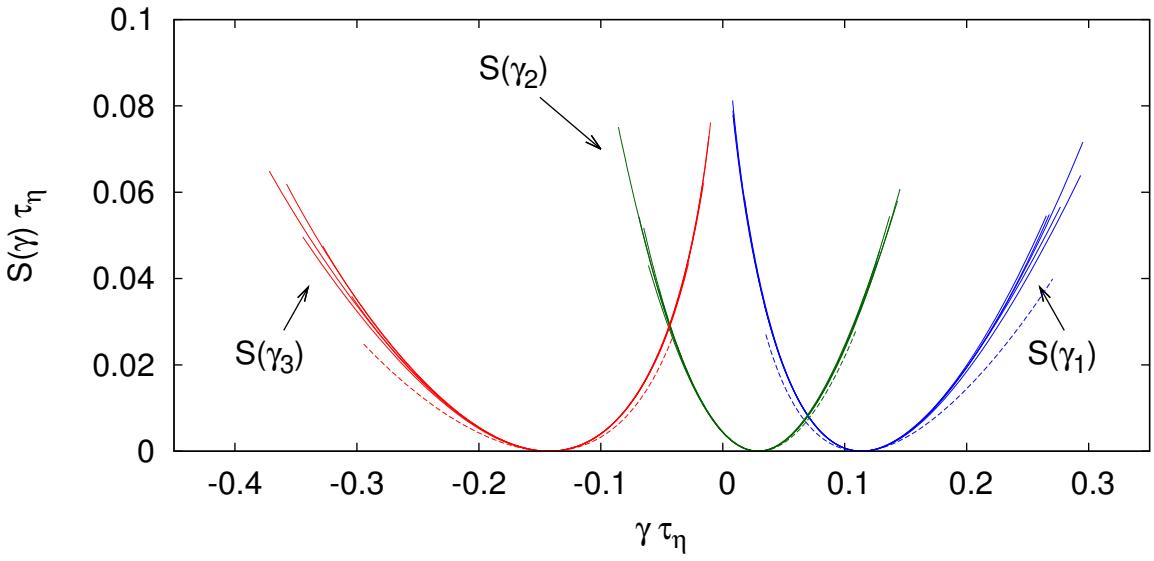

Figure 3.5: The three marginal Cramér functions constructed via Legendre transform from the GLE. Solid lines show results from different trajectory ensembles computed (containing 64k trajectories each) from the JHTDB data and the dashed lines show results from the iCFD data (containing 3.2k trajectories).

the vorticity on the deformation tensor.

In Figure 3.5, the behavior of the Cramér functions near the minimum point is nearly parabolic, but the regions further away from the minimum (tails of the PDFs) deviate significantly from parabolic behavior. For the maximal and minimal FTLE, incompressibility constrains the side of the Cramér function approaching zero, while the strong stretching and contracting events of γ_1 and γ_3, respectively, are less steep, with a $S(\gamma) \sim \gamma^n$ behavior with $n < 2$. The result is that the Cramér functions for γ_1 and γ_3 are highly asymmetric.

This asymmetry highlights the necessity of the large deviation formalism to describe the $t \to \infty$ behavior of the FTLE PDFs, in contrast to the central limit theo-

rem, which leads to a parabolic prediction for the Cramér function. While the middle LE, λ_2, is positive, a significant part of the $S(\gamma_2)$ Cramér function extends to negative FTLE values, indicating that the middle FTLE has a non-negligible probability to be negative for finite times. This is qualitatively consistent with the observations of Ref. 47.

The strong stretching (contracting) tails of the maximal (minimal) FTLE Cramér function indicate higher probability extreme events compared to a Gaussian (parabola). While this may seem to be a signature of intermittency, Gaussian variables with an incompressibility constraint can produce a similar effect. In Fig. 3.6, we demonstrate this by plotting proxies for the three Cramér functions,

$$\hat{S}(\gamma_i) = -\frac{1}{T}\ln\left(\hat{p}(\gamma_i, T)\right), \tag{3.8}$$

where T is an arbitrary parameter and the probability density functions $\hat{p}(\gamma_i)$ are constructed from histograms of ensembles with

$$\gamma_1 = \max\{X, Y, -(X+Y)\}, \qquad \gamma_3 = \min\{X, Y, -(X+Y)\}, \qquad \gamma_2 = -(\gamma_1 + \gamma_3), \tag{3.9}$$

where X and Y are independent normally-distributed ensembles with arbitrary variance. The variance of X, Y and the parameter T are adjusted so that the results are on a similar scale to Fig. 3.5. Indeed the Cramér functions for the maximal and minimal FTLEs show the same qualitative behavior as seen in Fig. 3.5 with only the

incompressibility constraint. We conclude that it is not necessary to invoke intermittency to explain the deviations from symmetric parabolic (unconstrained Gaussian) behavior because the incompressibility constraint appears to be sufficient to explain the observed trends. The primary qualitative differences between isotropic turbulence in Fig. 3.5 and Gaussian-generated volume-preserving FTLE statistics in Fig. 3.6 is the behavior of the middle FTLE, $S(\gamma_2)$, which is more parabolic (Gaussian) and shifted from the origin (bias toward $\gamma_2 > 0$) in isotropic turbulence.

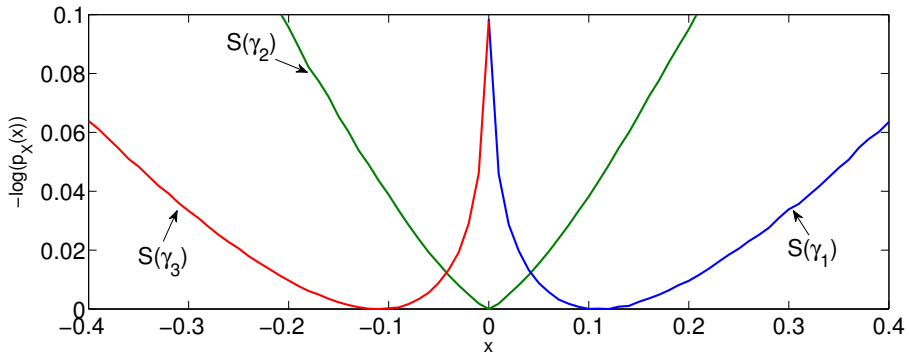

Figure 3.6: Proxies for the Cramér function created artificially by constructing FTLE spectrum realizations from two independent normally-distributed variables with zero mean equal variance using the incompressibility constraint $\gamma_1 + \gamma_2 + \gamma_3 = 0$.

In order to quantify the relative deviation of the marginal Cramér functions from unconstrained Gaussian statistics, we can consider the skewness and kurtosis of the distributions arising from them. From Eq. (2.22) we can recognize that in the long time limit, the generalized Lyapunov exponent is related to the cumulant-generating

function for the cumulative deformation $\Gamma_i = \gamma_i T = \int_{t_0}^{t_0+T} \hat{S}_{(ii)} dt$ (see Eq. (2.17)),

$$L(q)T \overset{T\to\infty}{=} \ln \langle \exp(\Gamma q) \rangle . \tag{3.10}$$

In this way, we can extract cumulants, κ_n, by differentiation at the origin of the generalized Lyapunov exponents for each of the three FTLEs. The skewness and excess kurtosis of the cumulative deformation are given by

$$\mathcal{S} = \frac{\kappa_3}{\kappa_2^{3/2}} = \frac{L'''(0)T}{(L''(0)T)^{3/2}} = \frac{L'''(0)\tau_\eta}{(L''(0)\tau_\eta)^{3/2}} \left(\frac{T}{\tau_\eta}\right)^{-1/2}, \tag{3.11}$$

$$\mathcal{K} - 3 = \frac{\kappa_4}{\kappa_2^2} = \frac{L^{(4)}(0)T}{(L''(0)T)^2} = \frac{L^{(4)}(0)\tau_\eta}{(L''(0)\tau_\eta)^2} \left(\frac{T}{\tau_\eta}\right)^{-1}. \tag{3.12}$$

The skewness and excess kurtosis both approach zero for long time, but the above relations give the leading-order asymptotic expression of their long-time behavior. The rate at which they approach zero is characterized by derivatives at the origin. The first four derivatives of $L(q)$ were measured for each FTLE at the origin $q = 0$ from a fourth-order polynomial curve-fit to the measured functions from the isotropic dataset. The results are tabulated in Table 3.1, averaged over the results from 5 independent ensembles. For comparison, the skewness and kurtosis of the proxy PDFs generated by the maximum/median/minimum of two independent Gaussian variables was measured and listed in Table 3.1 using the for the parameter T the value which gave similar scaling in Fig. 3.6 to Fig. 3.5.

This table shows that the proxy FTLE distributions of γ_1 and γ_3 are able to qualitatively mimic the deviation of the skewness and kurtosis from Gaussian values seen in the isotropic turbulence FTLEs. For isotropic turbulence, the middle FTLE, γ_2, has a distribution much closer to Gaussian than the other two FTLEs, in that its skewness and excess kurtosis are closer to zero at any given integration time. Meanwhile, the proxy FTLE distribution of γ_2 shows exactly zero skewness, but excess kurtosis comparable to that of the other two FTLEs.

Table 3.1: Skewness and excess kurtosis of the cumulative deformation statistics in HIT, compared to statistics generated from two independent Gaussian variables.

	HIT FTLEs (Fig. 3.5)			Proxy FTLEs (Fig. 3.6)		
	Γ_1	Γ_2	Γ_3	Γ_1	Γ_2	Γ_3
$\mathcal{S}\sqrt{\frac{T}{\tau_\eta}}$	4.8	0.93	-4.7	6.7	0.00	-6.7
$(\mathcal{K}-3)\,\frac{T}{\tau_\eta}$	30	2.7	22	62	47	62

The iCFD results for the Legendre transform-generated Cramér functions are shown by dotted lines in Fig. 3.5. These results from iCFD use an integration time of $45\tau_\eta$ so as to facilitate direct comparison with the JHTDB data. The effects of this finite integration time are explored in Appendix B.2. The Lyapunov spectrum for the two datasets are almost identical. The Cramér functions do show some discrepancy in the highly positive (negative) regions of the γ_1 (γ_3) distribution. In these regions, the iCFD Cramér functions betray a higher probability of highly deformed particles. This is likely due to the differences in how the velocity gradients are calculated along the trajectories. For the iCFD data, the trajectories were calculated along with the simulation, and therefore had access to spectral differentiation and interpolation

for computing velocity gradients. The JHTDB data is stored in physical space and the trajectories are calculated after the simulation. Velocity gradients are computed along the trajectories using 4^{th} order finite-differencing with 4^{th} order Lagrange interpolation. Thus, the JHTDB calculations likely reflect an under-estimated velocity gradient for large (intermittent) stretching events. Another possible contribution to this discrepancy is that the iCFD simulations were computed with higher spatial resolution.

3.3 Joint Statistics of FTLE's

In this section, we measure the joint distribution of two FTLEs, and also characterize the ratio of these two FTLEs. Once two of the three FTLEs $(\gamma_1, \gamma_2, \gamma_3)$ are specified, the third is fixed by the incompressibility relationship $\gamma_1 + \gamma_2 + \gamma_3 = 0$.

3.3.1 Joint-Cramér Functions

The joint-Cramér function $S(\gamma_i, \gamma_j)$ provides a full characterization of the joint-statistics of the three FTLEs. Similar to the marginal Cramér functions discussed above, it can be simply reconstructed from a histogram of simulated particle deformations by inverting Eq. (2.21) to obtain

$$S(\gamma_i, \gamma_j) \approx -\frac{1}{t - t_0} \ln(p(\gamma_i, \gamma_j, t)). \tag{3.13}$$

Similarly to the case of the marginal Cramér functions, a first-order correction to this asymptotic formulation is relatively easy to obtain by enforcing normalization of the PDF at every time with a normalization constant $N(t)$

$$\iint_{-\infty}^{\infty} p(\gamma_i, \gamma_j) d\gamma_i d\gamma_j = 1, \qquad p(\gamma_i, \gamma_j, t) \approx N(t) \exp(-tS(\gamma_i, \gamma_j)), \tag{3.14}$$

which leads to a better approximation of the Cramér function from finite time intervals

$$S(\gamma_i, \gamma_j) \approx -\frac{1}{t - t_0} \ln(p(\gamma_i, \gamma_j, t)) + C(t), \qquad C(t) = -\frac{1}{t - t_0} \ln N(t). \tag{3.15}$$

Appendix C.2 derives an approximation for $C(t)$, which simply provides a time-dependent shift for the Cramér function. Unlike the single variable case, the joint-histogram method becomes quickly prohibitive in terms of the number of trajectories necessary in the ensemble for statistical convergence. For this reason, along with the previously discussed motivations, the Legendre transform method is preferred for constructing the joint-Cramér function.

Rearranging the definition of the two-dimensional GLE, Eq. (2.25), in the $t \to \infty$ limit,

$$\ln\langle \exp(q_1 \gamma_i t + q_2 \gamma_j t) \rangle \sim L_{i,j}(q_1, q_2) t, \tag{3.16}$$

therefore a plot of $\ln\langle \exp(q_1 \gamma_i t + q_2 \gamma_j t) \rangle$ versus time should reveal linear behavior after some time has past if the GLE exists. In this case, linear regression can again be used

to determine the asymptotic slope of this function, as well as its uncertainty level. The slopes are evaluated for q_1 and q_2 values on a regular grid from $-3 < q_1, q_2 < 3$ with uniform spacing $\Delta q = 0.02$. Resulting slopes from cases with uncertainty based on the 95% confidence interval of the linear regression higher than a specified threshold are removed from the data. Example curve fits are shown in Fig. 3.7. Contours of the resulting GLE are shown in Fig. 3.8(a).

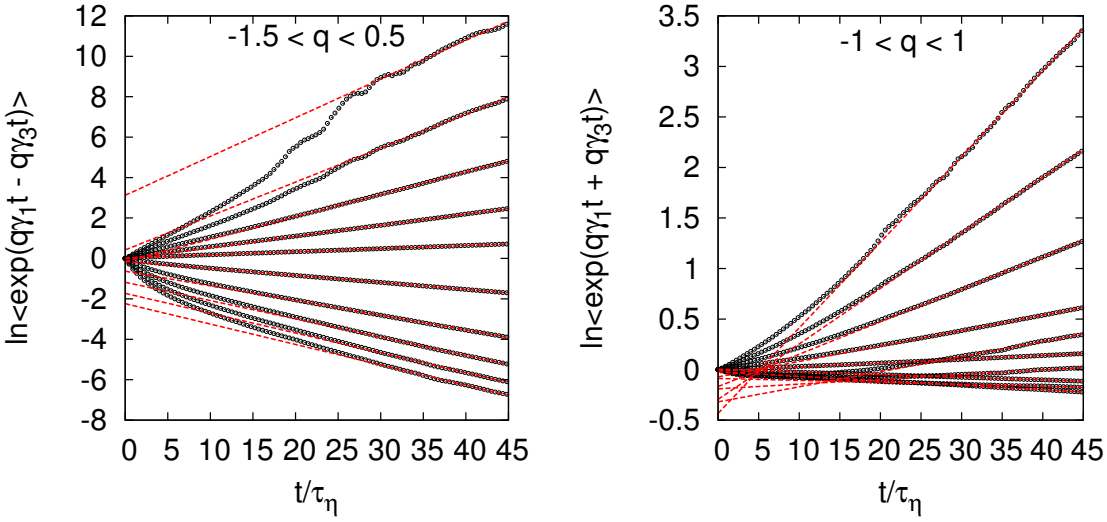

(a) (b)

Figure 3.7: Example curve fits for (a) $\ln\langle\exp(q\gamma_1 t - q\gamma_3 t)\rangle$ and (b) $\ln\langle\exp(q\gamma_1 t + q\gamma_3 t)\rangle$ used for determining the asymptotic slopes in constructing the two-dimensional GLE $L_{1,3}(q_1, q_2)$. For plot (a), we set $q = q_1 = -q_2$ and show curve fits for evenly-spaced q values, and in plot (b), we set $q = q_1 = q_2$ and show curve fits for evenly-spaced q values.

To construct the joint-Cramér function from the two-dimensional GLE, a double Legendre transform is required. Specifically, Eq. (2.27) is inverted so that, each point

in the q-space is mapped to a location in γ-space given by

$$\gamma_i = \frac{\partial L_{i,j}}{\partial q_1}, \qquad \gamma_j = \frac{\partial L_{i,j}}{\partial q_2}. \tag{3.17}$$

Then the value of the joint-Cramér function is given by

$$S(\gamma_i, \gamma_j) = q_1\gamma_i + q_2\gamma_j - L_{i,j}(q_1, q_2). \tag{3.18}$$

The resulting joint-Cramér function is shown in Fig. 3.8. As constrained by the large deviation formalism, the minimum point of the joint-Cramér function (where it is equal to zero) is equivalent to the minima of the two marginal Cramér functions $S(\gamma_1)$ and $S(\gamma_3)$. Near this minimum, the contours of the joint-Cramér function are approximately elliptical, reflecting a joint-Gaussian behavior of the PDFs in keeping with the central limit theorem. Further away from the minimum, the contour lines deviate significantly from ellipses, indicating a departure from central limit theorem validity.

A dotted black line indicates the $\gamma_1 = -\gamma_3$ situation in which the middle FTLE vanishes. Reversible dynamics would require the minimum of the joint-Cramér function to lie somewhere along this $\gamma_2 = 0$ line. Below and to the left of this line, we have $\gamma_2 > 0$, indicating two extension directions and a single contracting direction. Above and to the right, we have $\gamma_2 < 0$ and hence two contracting directions with a single extension direction.

The constraints of incompressibility, namely that $-\frac{1}{2}\gamma_3 \leq \gamma_1 \leq -2\gamma_3$, are plotted in the figure with solid black lines. These represent the boundaries of possible states for an incompressible fluid (volume preserving dynamics). On the left, the boundary at $\gamma_1 = -\frac{1}{2}\gamma_3$ represents two equally strong expansion directions with the third contracting direction. Thus, fluid volumes here form a 'disk' or 'pancake' like morphology. The other boundary, on the right at $\gamma_1 = -2\gamma_3$ indicates two equally contracting directions with a single extensive direction. Fluid volumes here acquire a 'pencil' or 'cigar' like form.

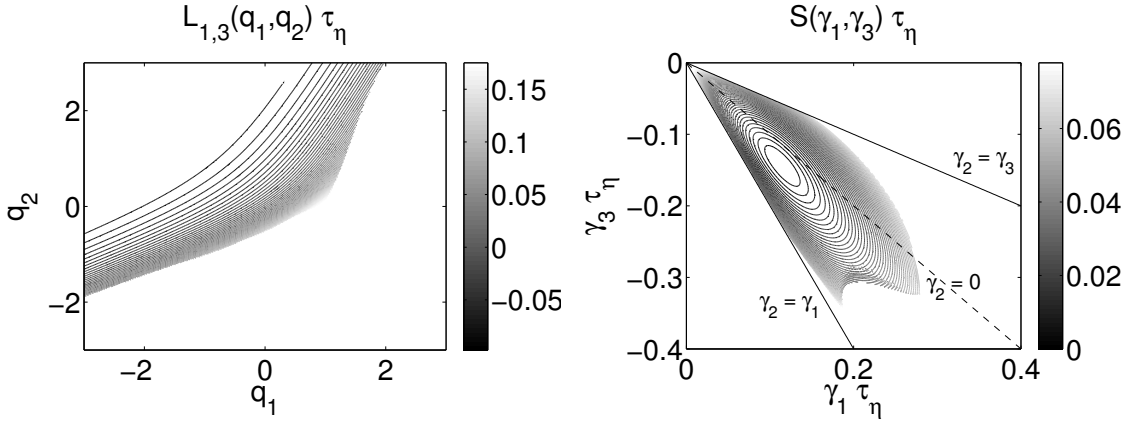

Figure 3.8: (a) Contour map of the two-dimensional generalized Lyapunov exponent $L_{1,3}(q_1, q_2)$ as constructed from linear regression analysis, with points having uncertainty beyond a specified threshold removed. (b) The joint-Cramér function $S(\gamma_1, \gamma_3)$ as constructed from the double Legendre transform of the two-dimensional generalized Lyapunov exponent.

The joint-Cramér function in Fig. 3.8 highlights the clear bias toward two positive FTLEs with a third negative one. This is true for both weakly stretched particles (closer to the origin, upper left of the figure) and particles experiencing strong stretch-

ing events (further from the origin, lower right of the figure).

Near the minimum of the joint Cramér function, a quadratic truncation of the Taylor series expansion is reasonably accurate, see Eq. (C.11). This amounts to using a Gaussian approximation to the PDF, i.e. the central-limit theorem. Approximating the second derivatives at the origin using a curve fit to the data in Fig. 3.8 within a radius 0.01 of the minimum yields

$$S(\gamma_1,\gamma_3)\tau_\eta \approx 9.6(\gamma_1\tau_\eta - 0.114)^2 + 11(\gamma_1\tau_\eta - 0.114)(\gamma_3\tau_\eta + 0.143) + 5.2(\gamma_3\tau_\eta + 0.143)^2. \tag{3.19}$$

The correlation coefficient, Eq. (C.15), for this approximation is $\rho_{13} \approx -0.8$. Such parameterization may be useful but its approximate character must be recalled, especially the fact that it looses validity at the tails.

3.3.2 Cramér Function for the Ratio of FTLEs

In the previous sections, the large deviation form of the marginal and joint-PDFs for the FTLEs has been shown. It is of interest also to explore the behavior of the PDF for ratio of FTLEs in the $t \to \infty$ limit. For this, we define a quantity

$$r^*(\mathbf{X},t) = \frac{\gamma_2(\mathbf{X},t)}{\gamma_1(\mathbf{X},t)} = -1 - \frac{\gamma_3(\mathbf{X},t)}{\gamma_1(\mathbf{X},t)}, \tag{3.20}$$

which is similar to quantities whose PDFs have been previously studied for eigenvalues of the instantaneous strain-rate tensor.[111,197] The ratio r^* ranges from $-0.5 \leq r^* \leq 1$. The steps shown in Appendix D lead to a large-deviation form for the PDF of r^*

$$p(r^*, t) = N^*(t) \exp\left(-tS(r^*)\right), \qquad S(r^*) = S(\overline{\gamma}_1, -(1+r^*)\overline{\gamma}_1), \tag{3.21}$$

where $\overline{\gamma}_1$ denotes the FTLE value which minimizes $S(\gamma_1, \gamma_3)$ along the line of constant r^*, i.e. $\gamma_3 = -(1+r^*)\gamma_1$. In this way, we recover a large deviation form for the PDF of r^*, with a Cramér function that can be easily evaluated from the joint-Cramér function.

The results for this analysis are shown in Fig. 3.9 along with histogram method results. The histogram method appears to be converging slowly to the curve from generated using Eq. (3.21) with the joint-Cramér function from the Legendre transform method shown in Fig. 3.8. The minimum of the $S(r^*)$ is near 0.25, exactly as can be found from the marginal Cramér functions.

3.4 The Effect of Rotation on Lagrangian Deformation

It is also of interest to study the behavior of the infinitesimal fluid volume deformations if only the strain-rate $S_{ij} = \frac{1}{2}(A_{ij} + A_{ji})$ is used in place of the velocity

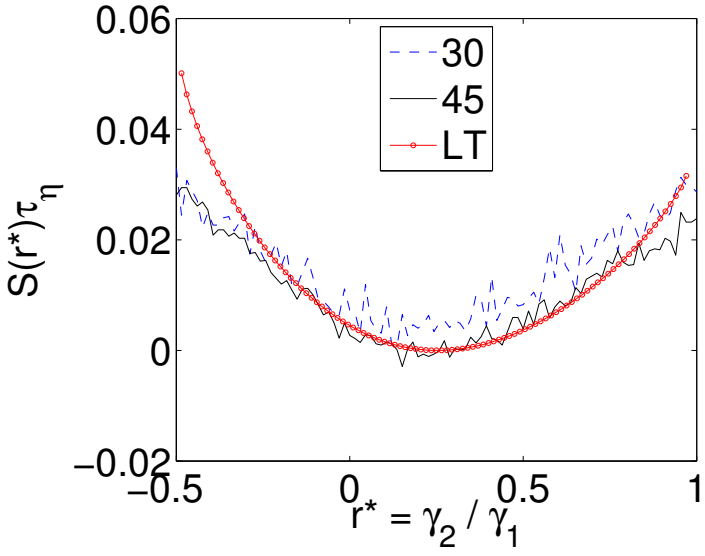

Figure 3.9: The Cramér function $S(r^*)$ for the FTLE ratio $r^* = \gamma_2/\gamma_1$ constructed via Eq. (3.21), "LT", compared with approximations constructed from histogram-generated PDFs of r^* with $S(r^*) \approx -\frac{1}{t}\ln p(r^*, t)$ at two different integration times, $30\tau_\eta$ and $45\tau_\eta$.

gradient tensor in Eq. (2.4). Such information could be useful, for example, when studying droplet deformation with a viscosity ratio different from unity. In this case, the evolution of the morphology tensor (analogous to the Cauchy-Green tensor) can be influenced by the rotation rate and strain rate with varying weight.[9] While the present analysis does not represent a physical realization of deformations in a fluid flow, it is presented here to highlight the effects of rotation on the cumulative Lagrangian deformations. To examine the extreme case where this effect is completely eliminated, we integrate

$$\frac{dD_{ij}}{dt} = S_{ik}D_{kj}. \tag{3.22}$$

Evaluating the Cramér functions for particle deformations evolved using Eq. (3.22) instead of Eq. (2.4) allows insight into the effects of particle rotation, $\Omega_{ij} = \frac{1}{2}(A_{ij} - A_{ji})$, by examining the results of its absence.

For this analysis, we have eliminated the role of the rotation tensor in re-aligning the Cauchy-Green tensor while the strain-rate stretches and compresses it along its principal axes. We have not, however, removed the rotation of the principal axes of the strain-rate in the evolution of the velocity gradient tensor along the trajectory.[69] For the perfect alignment of the Cauchy-Green and strain-rate eigen-frames, both of these effects must be removed. In fact, the Lyapunov exponents become the average values of the strain-rate tensor eigenvalues. The case of complete elimination of both rotation (even on strain-rate tensor realignment) and non-persistent straining thus provides an upper bound for the magnitudes of the Lyapunov exponents, since in that case the Cauchy-Green tensor aligns perfectly with the strain-rate tensor.

The same analysis as in the previous section is performed, except with the substitution of Eq. (3.22) for Eq. (2.4) when the deformation tensor is numerically integrated along each trajectory. Figure 3.10 compares the marginal Cramér functions $S(\gamma_1)$, $S(\gamma_2)$, and $S(\gamma_3)$ constructed from trajectories using only the strain-rate (i.e., artificially neglecting the vorticity) against the results from the previous section using the full velocity gradient tensor. Also shown in this figure are the marginal Cramér functions which result from artificially enforcing perfect alignment between the Cauchy-Green and strain-rate tensors.

The primary effect of neglecting rotation rate effects on the Cauchy-Green tensor is a dramatic increase in the FTLEs throughout the distribution. The minimum point for each of the curves, indicating the set of three Lyapunov exponents, shows the each of the LEs have been approximately doubled. The shape of the Cramér functions, in terms of deviations from parabolic behavior caused by incompressibility and rare extreme events remains qualitatively similar, but the width increases in the case with no rotational effect, indicating more intermittency. The set of LEs is found to be $\{\lambda_1, \lambda_2, \lambda_3\}\tau_\eta = \{0.195, 0.073, -0.268\}$ which is close to the ratio $\lambda_1 : \lambda_2 : \lambda_3 = 2.7 : 1 : -3.7$. It is apparent that the middle LE, λ_2, has increased proportionally more than the other two and the peak/average r^* value for $t \to \infty$ has increased from about $\frac{1}{4}$ to near $\frac{3}{8}$.

Even with this increase, the strain-rate-only Lyapunov exponents remain about half of those computed from perfect alignment. In the perfect alignment case, the Lyapunov spectrum becomes $\{\lambda_1, \lambda_2, \lambda_3\}\tau_\eta = \{\langle\Lambda_1\rangle, \langle\Lambda_2\rangle, \langle\Lambda_3\rangle\}\tau_\eta = \{0.361, 0.083, -0.444\}$, where Λ_i represents the i^{th} eigenvalue of the strain-rate tensor in decreasing order. The ratios of the Lyapunov exponents return approximately to those of the full A_{ij} case, $\lambda_1 : \lambda_2 : \lambda_3 = 4.3 : 1 : -5.3$: Table 3.2 summarizes the results in this chapter for the Lyapunov spectrum. The uncertainty due to integration time convergence is the dominant error in these results, and is discussed in Appendix B.2.

The joint-Cramér function, $S(\gamma_1, \gamma_3)$, is shown in Fig. 3.11 for fluid deformations using only the strain rate tensor. The minimum of the Cramér function has shifted

Table 3.2: Lyapunov spectra with and without Ω_{ij} compared with the perfect alignment case.

Case	$\lambda_1\tau_\eta$	$\lambda_2\tau_\eta$	$\lambda_3\tau_\eta$	λ_2/λ_1
Full A_{ij}	0.114	0.029	-0.143	0.254
Only S_{ij}	0.195	0.073	-0.268	0.374
Perfect Alignment	0.361	0.083	-0.444	0.230

away from the dotted $\gamma_2 = 0$ line, indicating that the second stretching direction is now on average closer in magnitude to the first, creating fluid particles more closely resembling 'disk' or 'pancake' type morphologies. The contours lines again resemble ellipses near the minimum in line with central limit theorem behavior. The bias toward positive γ_2 is again consistent for both weakly and strongly stretched particles.

Finally, the Cramér function for the ratio of FTLEs $r^* = \gamma_2/\gamma_1$ is constructed using only S_{ij} instead of A_{ij} and shown in Fig. 3.12. This plot highlights the increase in peak/average r^* value when the rotation tensor is neglected. It also appears that the Cramér function is narrower for the S_{ij}-only deformations, indicating an r^* PDF that more quickly converges to its $t \to \infty$ expectation value of $r^* \to \lambda_2/\lambda_1$.

3.5 Conclusions

In this chapter, we have presented a statistical characterization of FTLEs as a complement to their studies in the context of Lagrangian Coherent Structures. It was recalled that the Cramér function provides a natural formalism to describe these statistics. As time progresses, the PDFs of FTLEs changes, becoming ever closer to a delta function around the overall LE. However, a logarithmic rescaling of the PDF

the Cramér function, rapidly tends to a time-independent distribution. In this chapter the Cramér function was computed for finite-time Lyapunov exponents (FTLE) of Lagrangian particle trajectories. While a finite-time correction based on the normalization of the FTLE PDF helps to accelerate the collapse of the Cramér function estimations with increasing integration time, the moment-based calculation of the Cramér function using a Legendre transform of the generalized Lyapunov exponent was shown to more naturally correct for these effects. The shape of the Cramér functions for γ_1 and γ_3 reflects significant deviations from central-limit theorem behavior while the γ_2 Cramér function was closer to parabolic. The ratio of Lyapunov exponents for Lagrangian particles was found to be $\lambda_1 : \lambda_2 : \lambda_3 \approx 4 : 1 : -5$.

Errors due to finite-differencing and interpolation in physical space (as opposed to the higher spectral accuracy in the original DNS), as evaluated by comparison to the iCFD database, do not appear to affect the Lyapunov exponents, but do appear to have a non-negligible effect on the tails of the Cramér functions. Furthermore, the error in the results due to finite-integration time was explored by comparing to results from the iCFD database at various integration times, showing that the JHTDB results shown here could be underpredicting the Lyapunov exponents by about $10 - 15\%$.

The formalism was generalized to joint statistics, to provide a fuller description of the FTLEs. The joint-Cramér function for γ_1 and γ_3 was constructed using a double Legendre transform of the two-dimensional generalized Lyapunov exponents. The bias toward positive γ_2 was seen to hold for all magnitudes of stretching. While

the joint-Cramér function was approximately a paraboloidal near its minimum, it deviated significantly due to the same effects as the marginal Cramér functions: incompressibility constraints and rare extreme events associated with intermittency. An extension of the large-deviation theory for FTLEs gave a method for constructing a Cramér function for the ratio of FTLEs, $r^* = \gamma_2/\gamma_1$, from the joint-Cramér function. This Cramér function characterizes the long-time behavior of the PDF of r^*.

The maximal Lyapunov exponent (i.e. the minimum of the Cramér function $S(\gamma_1)$), is about one third of the average maximal strain-rate eigenvalue Λ_1, which reflects significant de-correlating effects preventing alignment between Cauchy-Green and strain-rate eigen-frames. Such effects include the action of vorticity, the pressure Hessian, and viscous terms in rotating the strain-rate eigen-frame, as well as the action of vorticity in rotating the Cauchy-Green eigen-frame. To eliminate the latter of these effects, the above results were compared to those of FTLEs resulting from deformation by the strain-rate tensor only (symmetric part of the velocity gradient tensor). When using only the strain-rate, the values of λ_1 and λ_3 approximately doubled, confirming the intuition that the deformation of a fluid volume is significantly more efficient when the particle does not rotate. The ratio of Lyapunov exponents was also altered to about $\lambda_1 : \lambda_2 : \lambda_3 \approx 8 : 3 : -11$, indicating that the middle Lyapunov exponent has an even stronger tendency to be positive when only the strain-rate is used. Even without the vorticity rotating the Cauchy-Green eigen-frame, the stretching rates remained considerable less than the mean strain-rate eigenvalues, confirming that the rotation

of the strain-rate eigen-frame by vorticity, pressure and viscous effects is equally important in preventing alignment. Indeed, simply considering strain-rate statistics leads to a considerable over-prediction of turbulent stretching of sub-Kolmogorov scale elements.

It is hoped that the insights gained from this description may be useful in various applications where cumulative deformations by turbulence is important. Prior applications to polymer and droplet dynamics have already been summarized before. Turbulent combustion represents another area where such information may prove useful. We recall that most existing combustion models that aim at relating flame-front deformations use statistical characterizations of the instantaneous strain-rates (see e.g. a model for flamelet quenching[157]). More relevant is the cumulative deformation over a period of time. Also, it often matters whether the cumulative deformation occurs along 2 directions, or all three. This information is conveniently encapsulated in the joint Cramér function $S(\gamma_1, \gamma_3)$ which we have determined for isotropic turbulence.

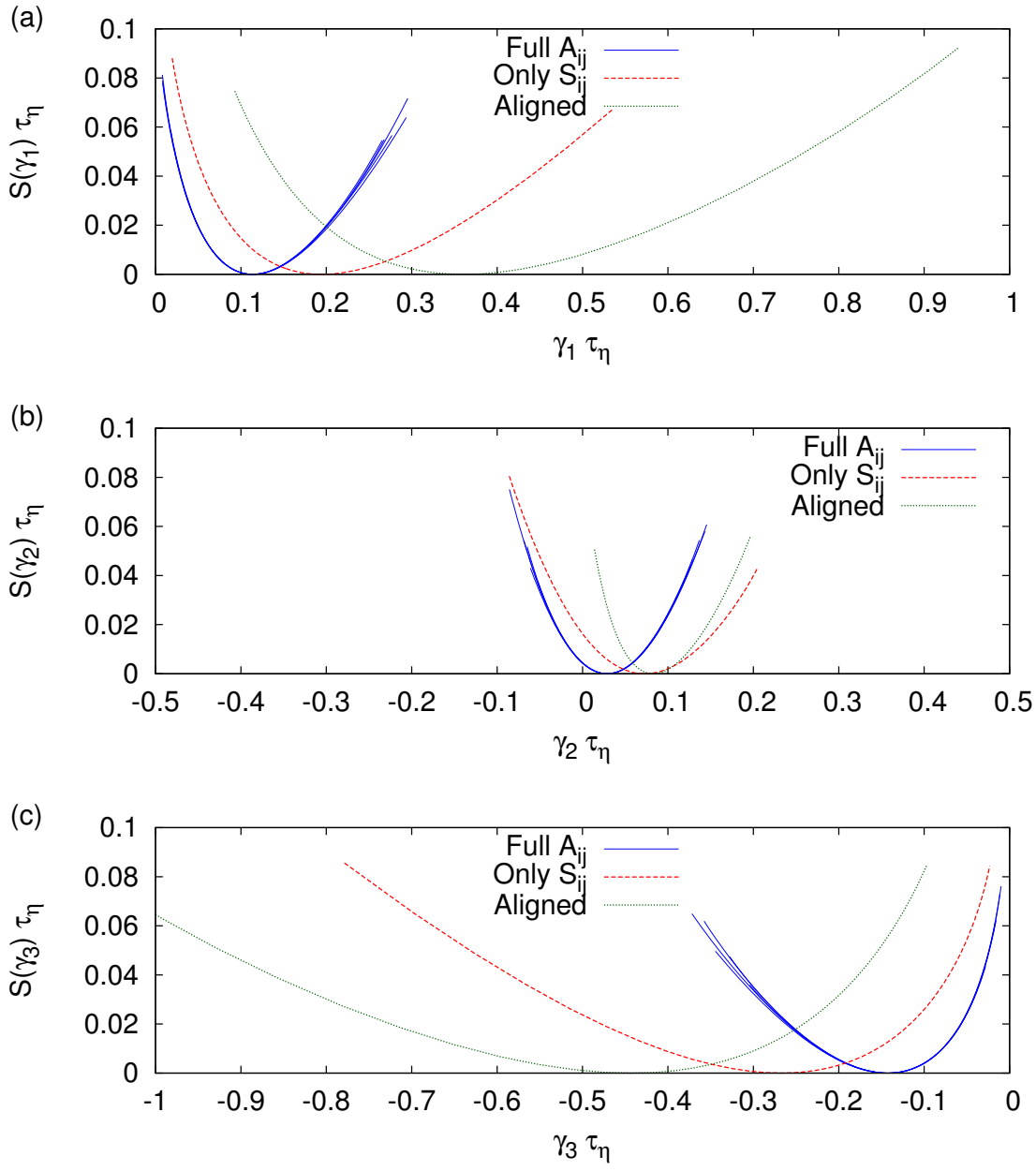

Figure 3.10: Comparison of the three marginal Cramér functions (a) $S(\gamma_1)$, (b) $S(\gamma_2)$, and (c) $S(\gamma_3)$ for deformation tensors integrated using the full velocity gradient tensor, A_{ij} (blue solid lines), and using only the strain-rate, S_{ij} (red dashed lines), and perfect alignment between Cauchy-Green and instantaneous strain rate eigen-frames (green dotted lines). Each plot contains multiple blue lines, indicating the statistical spread from different ensembles of 64k particles each.

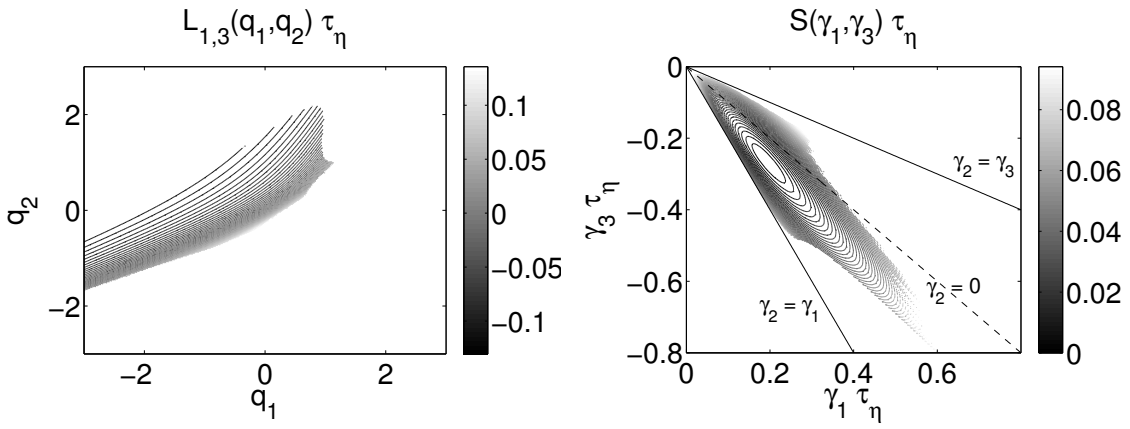

Figure 3.11: The (a) 2D GLE, $L_{1,3}(q_1, q_2)$, and (b) joint-Cramér function, $S(\gamma_1, \gamma_3)$, constructed using only the strain rate tensor to integrate fluid particle deformation along the Lagrangian trajectories. Note that part (b) of this figure is zoomed out compared to part (b) of Fig. 3.8.

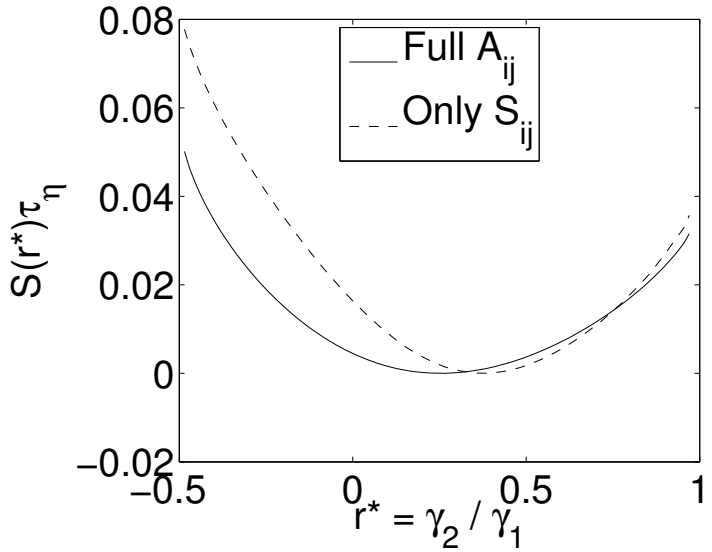

Figure 3.12: The Cramér function for the PDF of $r^* = \gamma_2/\gamma_1$ constructed using the full velocity gradient tensor, A_{ij} (solid line), and only the strain rate tensor, S_{ij} (dotted line).

Chapter 4

Large Deviation Statistics of Vorticity Stretching in Isotropic Turbulence

The production of enstrophy in three-dimensional isotropic turbulence is accomplished by the vorticity stretching mechanism, which strongly resembles the mechanism for the stretching of material lines in turbulence, though important differences can be identified. A useful concept in the study of material line stretching is the finite-time Lyapunov exponent (FTLE) of Lagrangian trajectories, which can be interpreted as the cumulative stretching of material lines along a Lagrangian path. As the statistics of FTLEs follow a large-deviation principle, it is of interest to investigate the application of large-deviation statistics to the cumulative stretching of vorticity

along Lagrangian paths.

In this chapter, we seek to characterize the statistics of the vorticity stretching term by looking at *cumulative* stretching along a Lagrangian path using the large deviation formalism. This characterization allows direct comparison with previous results for material deformation from chapter 3 in order to clarify similarities and differences between the two processes. Specifically, the Cramér function provides an efficient description of the asymptotic evolution of the cumulative stretching probability density function (PDF). This description enables a more detailed statistical comparison between vorticity stretching and material line stretching in turbulence. Additionally, the details of this statistical characterization can be incorporated into an approximate stochastic model for predicting features of the equilibrium distribution function of enstrophy using some existing approaches from polymer stretching studies.[5,6]

Background on vorticity stretching and material lines stretching is reviewed in §4.1, leading up to the definition of a novel quantity, γ_ω, which measures the exponential stretching rate for vorticity in the same way the FTLE characterizes material line stretching. The details for the direct numerical simulation dataset and evaluation of Lagrangian statistics are given in §4.2. In §4.3, the results of the statistical analysis are shown and discussed in terms of the Cramér function for vorticity stretching. Particular attention is paid to the relationship to material line deformation and strain-rate eigenvalue statistics. Using the Cramér function for vorticity stretching

and statistical observations of diffusion, a stochastic model is constructed for the Lagrangian vorticity evolution in §4.4, allowing for the prediction of the vorticity magnitude PDF in stationary isotropic turbulence. Following that, §4.5 delineates conclusions drawn from the results in the previous sections. The content of this chapter is published in Ref. 60.

4.1 An Analog of the FTLE for Vorticity Stretching

4.1.1 Lagrangian Vorticity Evolution

Following Lagrangian trajectories, $x_i(t)$, given by (2.2), the vorticity evolution is

$$\frac{d\omega_i}{dt} = S_{ij}\omega_j + \nu\frac{\partial^2\omega_i}{\partial x_j \partial x_j}. \tag{4.1}$$

Consider the decomposition of the vorticity vector, $\omega_i = \omega\widehat{\omega}_i$, where $\omega = \sqrt{\omega_i\omega_i}$ is the vorticity magnitude and $\widehat{\omega}_i = \frac{\omega_i}{\omega}$ is the unit vector associated with the vorticity orientation. With this decomposition, the Lagrangian evolution for vorticity magnitude can be written as

$$\frac{d\omega}{dt} = \widehat{\omega}_i S_{ij}\widehat{\omega}_j\omega + \nu\widehat{\omega}_i\frac{\partial^2\omega_i}{\partial x_j \partial x_j}. \tag{4.2}$$

It is interesting, then, to consider this in terms of the logarithm of vorticity magnitude,

$$\frac{d\ln\omega}{dt} = \widehat{\omega}_i S_{ij} \widehat{\omega}_j + \nu \frac{\widehat{\omega}_i}{\omega} \frac{\partial^2 \omega_i}{\partial x_j \partial x_j}. \tag{4.3}$$

The first term on the right-hand side, $\widehat{\omega}_i S_{ij} \widehat{\omega}_j$, represents vorticity stretching (enstrophy production) by the strain-rate tensor. This chapter will focus primarily on this term, using the large-deviation formalism to represent its statistics. The second term represents the effect of viscous forces, preventing the unbounded growth in vorticity magnitude at finite ν.

Complementing Eq. (4.3) for the vorticity magnitude is the equation for the evolution of the vorticity orientation,

$$\frac{d\widehat{\omega}_i}{dt} = \left(\delta_{ik} - \widehat{\omega}_i \widehat{\omega}_k\right) S_{kj} \widehat{\omega}_j + \nu \left[\left(\delta_{ik} - \widehat{\omega}_i \widehat{\omega}_k\right) \frac{\partial^2 \widehat{\omega}_k}{\partial x_j \partial x_j} + 2 \frac{\partial \widehat{\omega}_i}{\partial x_j} \frac{\partial \ln\omega}{\partial x_j} \right]. \tag{4.4}$$

The first term on the right-hand side represents the rotation/re-alignment of the vorticity due to the strain-rate tensor. This term shows that the strain rate acts to rotate the vorticity toward alignment with the strain-rate eigenvector associated with the largest eigenvalue. Such an alignment is not observed in single-time statistics due to the lack of persistent straining,[47] i.e. the vorticity never "catches up" with the strain-rate. However, allowing for a time lag, it has been observed that the vorticity shows statistical bias toward aligning with the eigenvector of the largest eigenvalue of the strain-rate tensor at a previous time along the Lagrangian path.[198,199]

The second term on the right-hand side represents the viscous-tilting effect.[119] In this form, we see that the viscous tilting has contributions from the Laplacian of the vorticity unit vector (projected normal to the unit vector) and from the vorticity curvature tensor,[200] $\frac{\partial \widehat{\omega}_i}{\partial x_j}$, acting on the gradient of $\ln \omega$. The vorticity tilting effect is responsible for the difference in Lagrangian evolution between vorticity and infinitesimal material lines that are initialized in alignment with the local vorticity.[116]

The focus of this chapter is on the statistics of the vorticity stretching term in (4.3), $\widehat{\omega}_i S_{ij} \widehat{\omega}_j$, so as to focus on the properties of the strain-rate tensor and its alignment with vorticity. The eigenframe of the strain-rate tensor is useful to clarify the connection between the magnitude of the vorticity stretching term and the vorticity orientation dynamics. In this frame it is seen that,[135]

$$\widehat{\omega}_i S_{ij} \widehat{\omega}_j = \sum_{i=1}^{3} \Lambda_i \cos^2(\theta_i), \tag{4.5}$$

where Λ_i is the i^{th} eigenvalue of the strain-rate tensor and θ_i is the angle between the vorticity vector and the eigenvector associated with the i^{th} eigenvalue of the strain-rate tensor. Thus, the vorticity stretching can be viewed as a weighted average of the three strain-rate eigenvalues, where the weight of a given eigenvalue is determined by how closely its eigenvector aligns with the vorticity vector being stretched. In this chapter, we consider the statistics of the cumulative vorticity stretching along a Lagrangian path using the large deviation formalism.

4.1.2 Material Lines and Finite-Time Lyapunov Exponents

As discussed in §2.1.1, an infinitesimal material line evolves as

$$\frac{dr_i}{dt} = A_{ij} r_j, \tag{4.6}$$

along a Lagrangian path. Performing the same decomposition as with the vorticity above, $r_i = r\widehat{r}_i$, this can be decomposed into an equation for the magnitude and an equation for the orientation,

$$\frac{d\ln r}{dt} = \widehat{r}_i S_{ij} \widehat{r}_j, \qquad \frac{d\widehat{r}_i}{dt} = (\delta_{ik} - \widehat{r}_i \widehat{r}_k) S_{kj} \widehat{r}_j + \Omega_{ij} \widehat{r}_i. \tag{4.7}$$

For material lines, integrating the first part of Eq. (4.7) results in

$$\Gamma(T) = \ln\left(\frac{r(T)}{r(0)}\right) = \int_0^T \widehat{r}_i S_{ij} \widehat{r}_j dt. \tag{4.8}$$

Furthermore, given the finite correlation time of the strain-rate along Lagrangian paths[49,201] proportional to the Kolmogorov time-scale τ_η, and given the passive nature of the material line (i.e. S_{ij} does not depend on r), the application of the large-deviation formalism is quite straight-forward. In this case, the finite-time Lyapunov

exponent (FTLE),[67,68,202] is intimately related to this result,

$$\gamma(T) \equiv \frac{1}{T} \ln \left(\frac{r(T)}{r(0)} \right) = \frac{1}{T} \int_0^T \widehat{r}_i S_{ij} \widehat{r}_j dt. \tag{4.9}$$

Accordingly, the PDF of FTLEs evolves as

$$p_\gamma(g, T) \sim \exp\left(-T S_\gamma(g)\right), \tag{4.10}$$

where g is the sample space variable for the FTLE. Cramér functions, $S_\gamma()$, of the largest FTLE have been computed by Bec et al.[79] and for the entire FTLE spectrum (including for joint-statistics) in chapter 3 for the case of isotropic turbulence. Recall that Appendix A discusses the distinction between $\gamma(T)$ for material lines and $\gamma_1(T)$ from the singular values of the material deformation tensor.

4.1.3 Vorticity

Seeing that a large-deviation principle has been shown for cumulative material deformation along Lagrangian paths, it is interesting to seek one also for cumulative Lagrangian vorticity stretching. A large-deviation principle for vorticity stretching would allow a more detailed comparison with material line stretching in terms of the Cramér function, which describes the self-similar behavior of the cumulative stretching PDF along Lagrangian paths. The existence of a large-deviation principle in the

case of Lagrangian material deformation provides a strong rationale for expecting one to hold in the case of Lagrangian vorticity stretching, although a rigorous proof is not available and so it must be shown empirically. The first task in this chapter is to verify that the cumulative vorticity stretching term indeed behaves in such a way as to support the application of the large deviation formalism. Secondly, we seek to determine the integration time T needed to allow for such behavior to take hold.

As already stated, this chapter seeks to study only the vorticity stretching term in the vorticity evolution equation, without considering any details of the viscous term. Thus neglecting the viscous term, we define an increment of $\ln \omega$,

$$\Gamma_\omega(T) \equiv \Delta_T(\ln \omega) = \ln\left(\frac{\omega(T)}{\omega(0)}\right) = \int_0^T \widehat{\omega}_i S_{ij} \widehat{\omega}_j dt, \tag{4.11}$$

such that there is an analog to the FTLE for the vorticity stretching,

$$\gamma_\omega(T) \equiv \frac{\Gamma_\omega(T)}{T} = \frac{1}{T} \ln\left(\frac{\omega(T)}{\omega(0)}\right) = \frac{1}{T} \int_0^T \widehat{\omega}_i S_{ij} \widehat{\omega}_j dt. \tag{4.12}$$

Because the viscous term has been discarded, comparison of statistical behavior between γ_ω and that of the FTLEs, especially the largest FTLE γ_1, allows for an exploration of the differences between the stretching of vorticity and material lines by strain-rates in turbulence.

A useful quantity is the scaled cumulant-generating function (which is analogous

to the generalized Lyapunov exponent[68]),

$$L_{\gamma_\omega}(q) = \lim_{T\to\infty} \frac{1}{T} \ln \left\langle \exp\left(q\gamma_\omega T\right)\right\rangle , \tag{4.13}$$

which exists only if the cumulant-generating function for $\Gamma_\omega(T)$ grows linearly in time. If this cumulant-generating function, $\ln \left\langle \exp\left(q\gamma_\omega T\right)\right\rangle$, can be shown to grow linearly with time, the slope as a function of q gives the generalized Lyapunov exponent, $L(q)$. Furthermore, casting the PDF in the form of Eq. (4.10) to compute the ensemble average in Eq. (4.13), and using steepest-descent integration in the $T \to \infty$ limit, it results that $L(q)$ is the Legendre transform of S_{γ_ω},

$$L_{\gamma_\omega}(q) = \sup_g \left[qg - S_{\gamma_\omega}(g)\right] . \tag{4.14}$$

For the present purposes, the linear growth of the cumulant-generating function (i.e. the existence of $L_{\gamma_\omega}(q)$) is considered sufficient evidence that the PDF of γ_ω behaves according to Eq. (4.10). Direct numerical simulations of forced isotropic turbulence in a periodic domain can be used to test the hypothesis that the vorticity stretching term should behave in this way.

4.2 Numerical Methods

In this section, the numerical methods applied in this study are briefly introduced. This study uses a direct numerical simulation dataset for gathering statistics for isotropic turbulence, and performs Lagrangian particle tracking with velocity gradient extraction to evaluate important terms for the vorticity evolution equation.

The Johns Hopkins Turbulence Databases (JHTDB) isotropic dataset[77,185] is used for the turbulence statistics reported in this chapter. For this chapter, ensembles of 64k particles were tracked using the 2^{nd} order predictor-corrector method with cubic Hermite interpolation in time and 6^{th} order Lagrange interpolation in space. As in chapter 3, for the initial distribution of particles, the $(2\pi)^3$ domain was divided into 1000 cubes of equal size $(\pi/5)^3$. Within each sub-cube, 64 particle trajectories were initialized at random positions, selected from a uniform spatial distribution along each coordinate. In this way, a uniform coverage of the domain was ensured within a randomized initialization procedure. Predictor-corrector steps were taken with a time-step of $\frac{1}{5}^{th}$ of the storage time step.

At each time step, velocity gradients were extracted from the dataset using 4^{th} order finite-differencing with 4^{th} order Lagrangian interpolation in space and cubic Hermite interpolation in time. The cumulative vorticity stretching along each trajectory, Eq. (4.11), was computed using the midpoint rule for numerical integration.

4.3 The Cramér Function for Vorticity Stretching

In this section, the method for constructing the Cramér function from the Lagrangian vorticity stretching data is presented. The resulting Cramér function for vorticity stretching in isotropic turbulence is shown.

4.3.1 Legendre Transform Method

In chapter 3, we compared two methods for constructing the Cramér function for material deformation: (i) histogram-based construction of the PDF and finite-size compensation via vertical shift of the Cramér function, (ii) moment-based construction of the generalized Lyapunov exponent with (inverse) Legendre transform to construct the Cramér function. The Legendre transform method proved superior in that case and is adopted here. Another advantage of this method is the explicit evaluation of the cumulant-generating function, which is useful for verifying the applicability of the large-deviation formalism to vorticity stretching. Below, the method is briefly outlined before presenting results.

The first step in the moment-based method for constructing the Cramér function is to compute the generalized Lyapunov exponent, $L_{\gamma_\omega}(q)$, given by Eq. (4.13). To construct $L_{\gamma_\omega}(q)$, the cumulant-generating function, $\ln\langle\exp(q\gamma_\omega T)\rangle$, is calculated as a function of q and T. The applicability of the large-deviation formalism requires

the results to asymptotically ($T \to \infty$) grow linearly with integration time. The cumulant-generating function is plotted for sample values of $-1 < q < 1$ as a function of integration time in Fig. 4.1. In this range, the linear growth in time is a striking feature of the results.

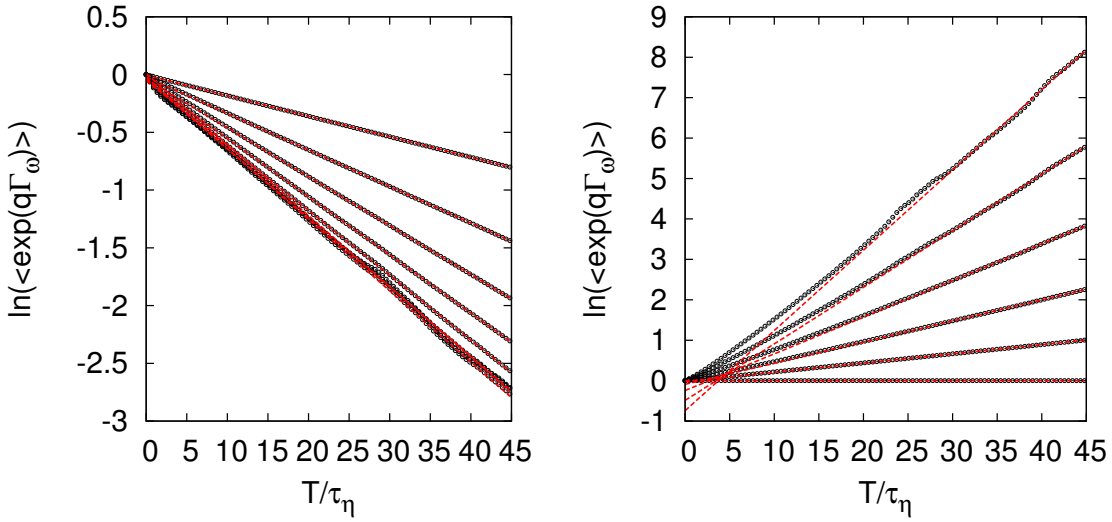

Figure 4.1: The cumulant-generating function for the cumulative vorticity stretching, $\Gamma_\omega = \gamma_\omega T$, for (a) $q = -1.6, -1.4, -1.2, -1.0, -0.8, -0.6, -0.4, -0.2$, and (b) $q = 0, 0.2, 0.4, 0.6, 0.8, 1.0$. Symbols represent numerical values from the dataset and dashed-lines represent linear curve-fits for the $30\tau_\eta < T < 45\tau_\eta$ range.

On the basis of the evidence shown in Fig. 4.1, it is concluded that the required behavior for the applicability of the large-deviation formalism is seen for vorticity stretching, even at relatively small integration times $\sim 30\tau_\eta$. The slopes of the curve fits (shown as dotted lines in Fig. 4.1) then represent the generalized Lyapunov exponent at a given q. Using a linear regression procedure for $-3 < q < 3$ with uniform discretization of $\Delta q = 0.02$, the generalized Lyapunov exponent is constructed and

shown in Fig. 4.2 for five different ensembles of $64k$ particles each. The linear regression was performed only on the interval $30\tau_\eta < T < 45\tau_\eta$. A specified threshold on the 95% confidence interval, computed from the standard error of the regression analysis, was used to determine the range over which the curve fits were reliable. Points with standard error above this threshold were removed.

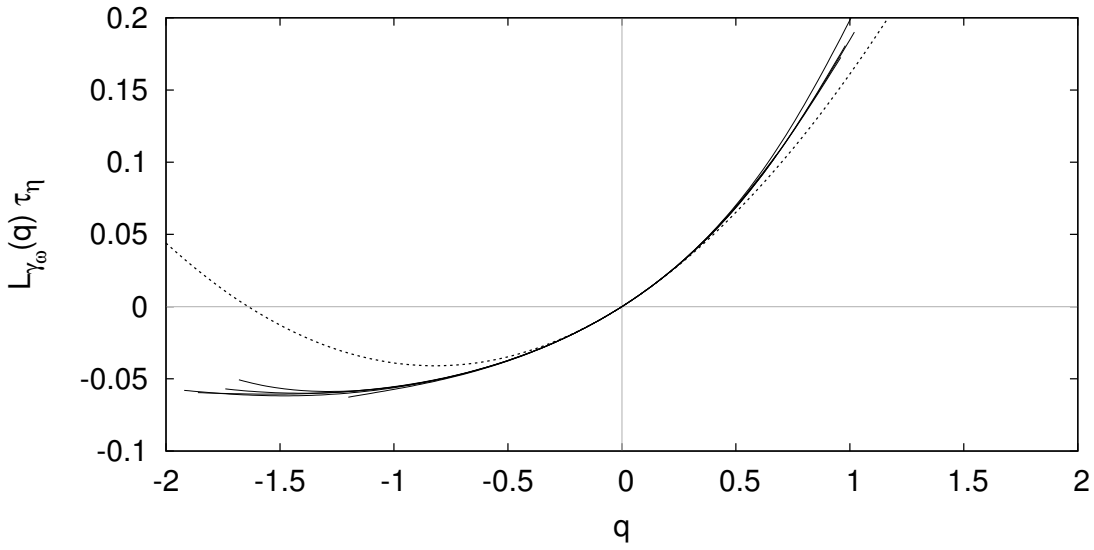

Figure 4.2: The generalized Lyapunov exponents for the vorticity stretching from five different $64k$ Lagrangian particle ensembles. The dashed line represents a parabolic curve fit in the region of $q = 0$.

The spread of the five curves in this figure, especially noticeable in the tails, is indicative of the statistical convergence error. The curves pass through the origin as expected and near the origin can be approximated by a truncated Taylor expansion,[68]

$$L_{\gamma_\omega}(q) \approx \lambda_\omega q + \frac{1}{2}\Delta_\omega q^2. \tag{4.15}$$

The slope at the origin, $L'_{\gamma_\omega}(0) = \lambda_\omega = \langle \widehat{\omega}_i S_{ij} \widehat{\omega}_j \rangle \approx 0.100/\tau_\eta$, represents the average vorticity stretching and is analogous to the Lyapunov exponent of Lagrangian trajectories in the context of material line stretching. The curvature at the origin, $L''_{\gamma_\omega}(0) = \Delta_\omega \approx 0.122/\tau_\eta$, gives a measure of the strength of fluctuations in cumulative stretching about the mean. This parabolic approximation is shown in Fig. 4.2 as a dashed line.

As given by Eq. (4.14), the generalized Lyapunov exponent is the Legendre transform of the Cramér function. For a known generalized Lyapunov exponent, the inverse Legendre transform can be used to recover the (convex hull of the) Cramér function,

$$S_{\gamma_\omega}(g) = \sup_q \left[gq - L_{\gamma_\omega}(q) \right]. \tag{4.16}$$

The inverse Legendre transform is performed numerically, for a given g-q pair,

$$g = L'_{\gamma_\omega}(q), \qquad S_{\gamma_\omega}(g) = qL'_{\gamma_\omega}(q) - L_{\gamma_\omega}(q), \tag{4.17}$$

using second-order central differencing for the derivative of the generalized Lyapunov exponent.

Figure 4.3 shows the resulting Cramér function for the vorticity stretching term. The minimum of the Cramér function is $S_{\gamma_\omega}(\lambda_\omega) = 0$. A truncated Taylor expansion

about the minimum gives a parabola,

$$S_{\gamma_\omega}(g) \approx \frac{(g-\lambda_\omega)^2}{2\Delta_\omega}, \tag{4.18}$$

which is the Legendre transform of the parabolic generalized Lyapunov exponent given in Eq. (4.15). The dashed line in Fig. 4.3 shows this approximation. Substitution of Eq. (4.18) into Eq. (4.10) yields Gaussian statistics, that is, the Gaussian toward which the central-limit theorem predicts that the PDF is approaching for $T \to \infty$.

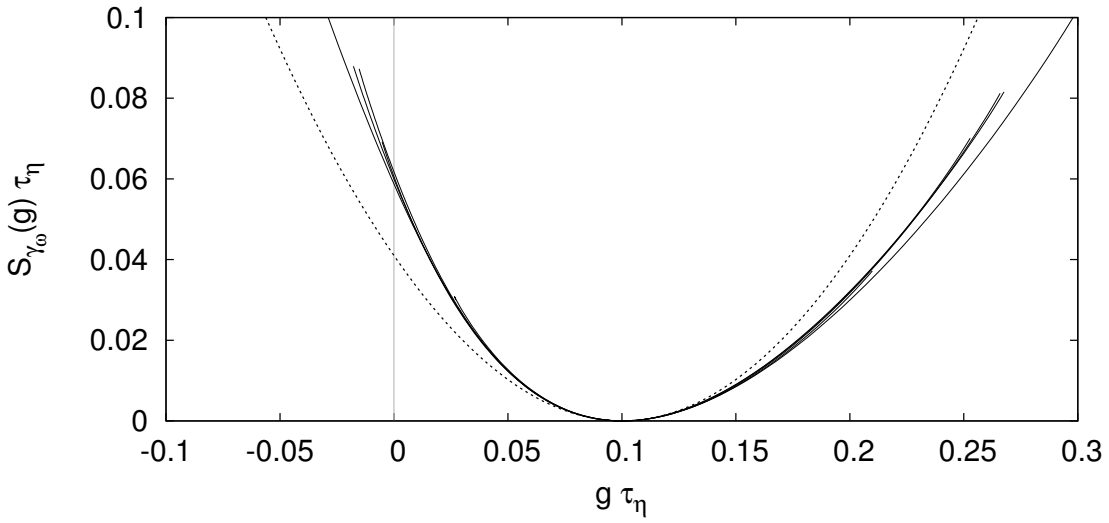

Figure 4.3: The Cramér function for the vorticity stretching from five different $64k$ Lagrangian particle ensembles. The differences between the five different ensembles illustrate the extent of uncertainty from statistical convergence. The symbol g is used for the probability space variable of γ_ω and both axes are non-dimensionalized by the Kolmogorov timescale τ_η. The gray vertical line indicates $\gamma_\omega = 0$. The dashed line represents a parabolic curve fit to the Cramér function near the minimum.

4.3.2 Comparison with FTLE Spectrum

In §4.1, an analogy was drawn between the behavior of vorticity along Lagrangian trajectory and the behavior of material lines. Specifically in the context of large deviation statistics, the quantity γ_ω was introduced to quantify the cumulative stretching of vorticity by the strain-rate tensor along Lagrangian paths. This quantity is directly analogous to the finite-time Lyapunov exponents (FTLE) of Lagrangian trajectories, γ_i with $i = 1, 2, 3$, which characterize the cumulative deformation of a fluid volume by the strain-rate tensor. Specifically, γ_1 can be used to investigate material line stretching and $\gamma_1 + \gamma_2$ for material surface area stretching. It is of interest, therefore, to compare the large deviation statistics of cumulative vorticity stretching with those of the FTLEs as a way of exploring similarities and differences in vorticity and material line behavior in turbulence.

It is known that vorticity tends to align most readily with the strain-rate eigenvector corresponding to the intermediate eigenvalue,[111] Λ_2, while material lines tend to align more with the eigenvector corresponding to the largest eigenvalue,[116] Λ_1. As a result, the mean material line stretching, $\langle \widehat{r}_i S_{ij} \widehat{r}_j \rangle$, is larger than the mean vorticity stretching, $\langle \widehat{\omega}_i S_{ij} \widehat{\omega}_j \rangle$.

For material lines, the first term in Eq. (4.7), $(\delta_{ik} - \widehat{r}_i \widehat{r}_k) S_{kj} \widehat{r}_j$, shows that the strain-rate tends to tilt material lines in the direction of the strongest strain. Perfect alignment does not occur, in fact, because of the impact of vorticity on the material line, $\Omega_{ij} \widehat{r}_j$, and the fact that the strain-rate eigenvectors are moving targets, being

themselves rotated by the vorticity and non-local pressure Hessian.[203] For vorticity, Eq. (4.4), the $\Omega_{ij}\widehat{\omega}_j$ term vanishes and is replaced by the viscous tilting terms. The tendency of the strain-rate to rotate vorticity toward its largest eigenvalue remains. A vital difference is the active feedback that the vorticity has on the strain-rate evolution (as opposed to passive material lines). This appears to be the key ingredient in the vorticity's alignment bias toward the second largest eigenvalue.[116]

The ratio of Lyapunov exponents (the average stretching of mutually orthogonal material lines) in isotropic turbulence is approximately $\lambda_1 : \lambda_2 : \lambda_3 \approx 4 : 1 : -5$.[59,79] In Fig. 4.4, the Cramér function for cumulative vorticity stretching is compared with the Cramér functions for the Lyapunov spectrum (see chapter 3 for details). Bec et al.[79] reported a leading Lyapunov exponent of $\lambda_1\tau_\eta \approx 0.14$ while chapter 3 found $\lambda_1\tau_\eta \approx 0.125$ after correcting for finite integration time effects (with S_{γ_1} evaluated up to $45\tau_\eta$ it is slightly lower, i.e. $\lambda_1\tau_\eta \approx 0.114$, as shown in Fig. 4.4). For vorticity, the present results show mean stretching, $\lambda_\omega\tau_\eta = \langle\widehat{\omega}_i S_{ij}\widehat{\omega}_j\rangle = 0.10$, which is significantly lower than that of the mean stretching for material lines. Guala et al.[116] measured $\langle\widehat{\omega}_i S_{ij}\widehat{\omega}_j\rangle$ and $\langle\widehat{r}_i S_{ij}\widehat{r}_j\rangle$ for short evolution times up to $6\tau_\eta$, concluding that the material lines had significantly stronger stretching. Indeed, this is easy to understand, since the vorticity tends to preferentially align with the second-largest strain-rate eigenvalue, while material lines tend to tilt towards the largest one. However, here it is shown that the mean vorticity stretching rate greatly exceeds that of the second-largest FTLE, and is much closer to λ_1 than $\lambda_2 \approx 0.03/\tau_\eta$.

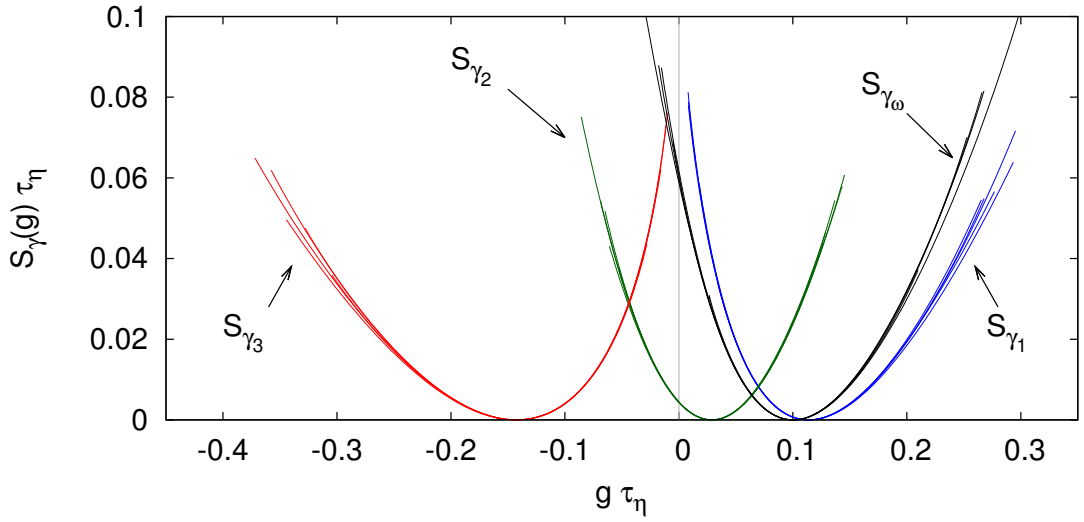

Figure 4.4: Comparison of the Cramér function for vorticity stretching with the marginal Cramér functions for the finite-time Lyapunov exponents. Each Cramér function was measured from five separate ensembles of $64k$ Lagrangian particles each in order to demonstrate the level of statistical convergence uncertainty. The symbol g is used for the probability space variable of γ and both axes are non-dimensionalized by the Kolmogorov timescale τ_η. The gray vertical line indicates $\gamma = 0$.

The width of the Cramér function of cumulative vorticity stretching is visually very similar to that of the largest FTLE. To quantify the behavior of these Cramér functions, the derivatives of the generalized Lyapunov exponent at the origin are used. As apparent from the relation of Eq. (4.13) to the cumulant-generating function of $\Gamma = \gamma T$, these derivatives represent the growth rate of cumulants, e.g. of the integrated vorticity stretching, $\Gamma_\omega = \int_0^T \widehat{\omega}_i S_{ij} \widehat{\omega}_i dt$. In addition to mean, $\lambda T = L'(0)T$, and variance, $\Delta T = L''(0)T$, the deviation from Gaussian statistics can be quantified

by the skewness,

$$\mathcal{S} = \frac{L'''(0)T}{(L''(0)T)^{3/2}} = \frac{L'''(0)\tau_\eta}{(L''(0)\tau_\eta)^{3/2}} \left(\frac{T}{\tau_\eta}\right)^{-1/2}, \tag{4.19}$$

and excess kurtosis,

$$\mathcal{K} - 3 = \frac{L^{(4)}(0)T}{(L''(0)T)^2} = \frac{L^{(4)}(0)\tau_\eta}{(L''(0)\tau_\eta)^2} \left(\frac{T}{\tau_\eta}\right)^{-1}. \tag{4.20}$$

Note that, in agreement with the central-limit theorem, the skewness and excess kurtosis (and all higher-order cumulants) are decaying to zero at $T \to \infty$. The large-deviation formalism gives a means for computing the rate at which they decay. Table 4.1 shows these cumulant values for three of the curves in Fig. 4.4. The derivatives were evaluated using fourth-order polynomial curve fits to $L(q)$ near $q = 0$ and averaged over each of the five ensembles. It is apparent from this analysis that the cumulative vorticity stretching statistics behave more similarly to γ_1 than γ_2. The cumulative vorticity stretching and largest FTLE have much larger deviations from Gaussian statistics (skewness and excess kurtosis) than the second-largest FTLE for a given integration time.

Physically speaking, the intermediate FTLE, γ_2, can be thought of as the cumulative stretching of material lines constrained to be perpendicular to the most stretched material line. Perhaps the most intuitive feel for the significance of γ_2 is to think of cumulative material surface area stretching as $\gamma_1 + \gamma_2$. The similarity between γ_ω and

Table 4.1: Comparison of first four cumulants for the vorticity stretching with those of the first two FTLEs. The asterisk denotes that the value is corrected for finite integration time effects, see chapter 3 for more details.

	$\lambda\tau_\eta$	$\Delta\tau_\eta$	$\mathcal{S}\left(\frac{T}{\tau_\eta}\right)^{1/2}$	$(\mathcal{K}-3)\left(\frac{T}{\tau_\eta}\right)$
γ_1	0.125^*	0.145	4.8	30
γ_ω	0.100	0.122	3.6	18
γ_2	0.029	0.098	0.93	2.7

γ_1 is *relative* to the comparison of γ_ω with γ_2 in a statistical sense and should not be seen to overshadow the important differences between vorticity stretching and material line stretching but only to put them in perspective. For example, while vorticity stretching is on average less than material line stretching, it is still much greater than the average stretching in the plane perpendicular to material lines.

4.3.3 Comparison with Strain-Rate Eigenvalue Statistics

In order to emphasize the effect of preferential alignment of vorticity with the second-largest strain-rate eigenvalue, a Cramér function can be constructed for a vector always in perfect alignment with a given strain-rate eigenvalue. This artificial Cramér function does not reflect any physical dynamics, but rather the hypothetical dynamics of vorticity magnitude if perfect alignment with any of the eigenvectors was maintained. Two such Cramér functions, one for the largest eigenvalue Λ_1 and one for the second-largest eigenvalue Λ_2, are plotted in Fig. 4.5 alongside the Cramér

function for cumulative vorticity stretching. It is clear that the Cramér function for vorticity stretching is much closer to that of perfect alignment with Λ_2 rather than Λ_1, which is consistent with the observed preferential alignment of the vorticity vector.

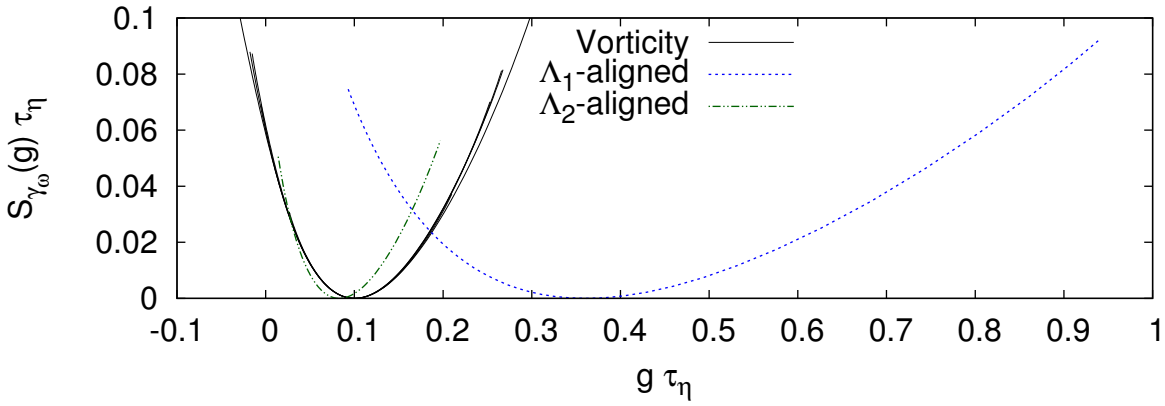

Figure 4.5: Comparison of the Cramér function for vorticity stretching with the hypothetical Cramér functions if perfect alignment with the largest or second-largest strain-rate eigenvalues was maintained throughout the dynamics. Note that five separate ensemble measurements of the vorticity Cramér function are shown as five different continuous lines, qualitatively showing the statistical convergence error.

4.4 A Model Kramers-Moyal Equation for the Vorticity Magnitude

In this section, an application of the above statistical characterization of vorticity stretching to a model for the vorticity magnitude PDF is described. Some of the assumptions of the model are justified by appealing to results from DNS of forced isotropic turbulence. The vorticity magnitude PDF is defined for a statistical en-

semble of Lagrangian trajectories, so that the Lagrangian evolution of the vorticity described in the previous sections is the relevant dynamical input to the statistical equations. In addition, the free parameters of the model are prescribed using statistics from DNS. While progress in solving the full model has so far proved difficult, the results of the model for a parabolized Cramér function are presented.

4.4.1 PDF Closure Using Conditional Means

The goal of this section is to model the statistics of vorticity magnitude using Eq. (4.3). To appreciate this goal, first consider the direct approach to constructing the evolution equation for the PDF. Following a similar procedure as Wilczek and Friedrich[168] (i.e. following Lundgren,[204] Monin,[205] and Novikov[206] with closure introduced through conditional means), the PDF of $\ln\omega$ can be written in terms of the fine-grained PDF,

$$p_{\ln\omega}(\chi,t) = \langle\delta(\ln\omega(t)-\chi)\rangle\,. \tag{4.21}$$

Differentiating in time and using conditional mean closure,

$$\frac{\partial p_{\ln\omega}}{\partial t} = -\frac{\partial}{\partial\chi}\left\langle\frac{d\ln\omega}{dt}\delta(\ln\omega(t)-\chi)\right\rangle = -\frac{\partial}{\partial\chi}\left(\left\langle\frac{d\ln\omega}{dt}\middle|\ln\omega=\chi\right\rangle p_{\ln\omega}\right), \tag{4.22}$$

and substituting Eq. (4.3) on the right-hand side yields,

$$\frac{\partial p_{\ln\omega}}{\partial t} = -\frac{\partial}{\partial\chi}\left[\left(\langle\widehat{\omega}_i S_{ij}\widehat{\omega}_j|\ln\omega=\chi\rangle + \nu\left\langle\frac{\widehat{\omega}_i}{\omega}\frac{\partial^2\omega_i}{\partial x_j\partial x_j}\middle|\ln\omega=\chi\right\rangle\right)p_{\ln\omega}\right]. \tag{4.23}$$

Solving for the stationary PDF, $\frac{\partial p_{\ln\omega}}{\partial t} = 0$, the constant of integration vanishes due to $p_{\ln\omega} \to 0$ as $\ln\omega \to \infty$, resulting in the requirement,

$$\langle \widehat{\omega}_i S_{ij} \widehat{\omega}_j | \ln\omega = \chi \rangle = -\frac{\nu}{\omega} \left\langle \widehat{\omega}_i \frac{\partial^2 \omega_i}{\partial x_j \partial x_j} \middle| \ln\omega = \chi \right\rangle . \tag{4.24}$$

That is, the conditional mean stretching must equal the conditional mean viscous relaxation at every point in probability space for $\ln\omega$. While this is a helpful constraint on the conditional means, it provides no prescription for finding the stationary distribution $p_{\ln\omega}$.

A useful manipulation of the above equation for finding the stationary PDF is found by invoking the fact that for homogeneous turbulence, the vorticity PDF is independent of spatial coordinates, so its Laplacian is zero,[168]

$$\begin{aligned} 0 &= \frac{\partial^2 p_{\ln\omega}}{\partial x_j \partial x_j} \\ &= -\frac{\partial}{\partial\chi}\left(\left\langle \frac{\partial^2 \ln\omega}{\partial x_j \partial x_j} \middle| \ln\omega = \chi \right\rangle p_{\ln\omega} \right) + \frac{\partial^2}{\partial\chi^2}\left(\left\langle \frac{\partial \ln\omega}{\partial x_j}\frac{\partial \ln\omega}{\partial x_j} \middle| \ln\omega = \chi \right\rangle p_{\ln\omega} \right). \end{aligned} \tag{4.25}$$

With the help of Eqs. (4.3) and (4.25), the evolution equation for $p_{\ln\omega}$, Eq. (4.23), can be rewritten as

$$\begin{aligned} \frac{\partial p_{\ln\omega}}{\partial t} = -\frac{\partial}{\partial\chi}\left[\left(\langle \widehat{\omega}_i S_{ij} \widehat{\omega}_j | \ln\omega = \chi \rangle + \nu \left\langle \frac{\partial \ln\omega}{\partial x_j}\frac{\partial \ln\omega}{\partial x_j} - \frac{\partial \widehat{\omega}_i}{\partial x_j}\frac{\partial \widehat{\omega}_i}{\partial x_j} \middle| \ln\omega = \chi \right\rangle \right) p_{\ln\omega} \right] \\ - \nu \frac{\partial^2}{\partial\chi^2}\left(\left\langle \frac{\partial \ln\omega}{\partial x_j}\frac{\partial \ln\omega}{\partial x_j} \middle| \ln\omega = \chi \right\rangle p_{\ln\omega} \right). \end{aligned} \tag{4.26}$$

Indeed, this expression is analogous to one obtained by Wilczek and Friedrich[168] for a single component of the vorticity. Wilczek and Friedrich[168] solved their equation and numerically evaluated two conditional averages from DNS, showing that such an approach can exactly reconstruct the PDF for a single component of vorticity. The present goal is to introduce a model which incorporates the statistical information from the Cramér function of vorticity stretching to reconstruct the vorticity magnitude PDF.

4.4.2 Analogy with Polymers

We first invoke an analogy between vorticity stretching and polymer stretching in turbulence. Representing the polymer with a bead-spring model, with vector ρ_i signifying the displacement between the two ends of the polymer, the polymer equation along a Lagrangian path is modelled with

$$\frac{d\rho_i}{dt} = A_{ij}\rho_j - f(|\rho|)\frac{\rho_i}{|\rho|}, \tag{4.27}$$

where $f(|\rho|)$ represents the elastic restoration force of the polymer.[6] For the Oldroyd-B model, the restoration force is that of a linear spring, $f(|\rho|) = \frac{|\rho|}{\tau_p}$, where τ_p is the relaxation time of the polymer.[5,6] The Oldroyd-B model allows infinite extension of the polymer, and therefore a popular extension is the non-linear FENE-P model.[3]

Using the decomposition $\rho_i = \rho\widehat{\rho}_i$, the equations become,

$$\frac{d\ln\rho}{dt} = \widehat{\rho}_i S_{ij}\widehat{\rho}_j - \frac{f(\rho)}{\rho}, \qquad \frac{d\widehat{\rho}_i}{dt} = (\delta_{ik} - \widehat{\rho}_i\widehat{\rho}_k)S_{kj}\widehat{\rho}_j + \Omega_{ij}\widehat{\rho}_j. \tag{4.28}$$

These equations resemble those of the material line, Eq. (4.7), except that they now contain a relaxation term to prevent unbounded growth of the polymer.

Comparison with Eqs. (4.3) and (4.4) reveals three differences between the evolution equations for polymers and vorticity. First, while both the vorticity and polymer stretching are resisted by a second term that acts to prevent unbounded growth, the relaxation term in the polymer length equation is due to the properties of the polymer, whereas the viscous term in the vorticity equation is a function of the flow in the neighborhood of the point (and therefore, much more challenging to model). Second, there is no viscous tilting in the equation for the polymer orientation evolution, because the polymer relaxation always acts along the polymer axis. Third, the polymer can be rotated by the vorticity, whereas the vorticity cannot rotate itself: $\Omega_{ij}\widehat{\omega}_j = 0$.

Perhaps the most important difference, however, is not obvious in this comparison: how the vorticity and polymers affect the strain-rate that is stretching them. Both the vorticity and polymers can have a back-reaction on the flow, though the details of the two-way coupling vary. However, especially below the coil-stretch transition, the polymer can be approximately modelled as a passive entity.[5,6] There is no similar regime for the vorticity in which a passive treatment is a good approximation.

For polymers, under the assumption that the polymer has negligible influence on the flow (i.e. on S_{ij}), the integration of the first part of Eq. (4.28) gives

$$\ln\left(\frac{\rho(T)}{\rho(0)}\right) = \int_0^T \left(\widehat{\rho}_i S_{ij} \widehat{\rho}_j - \frac{f(\rho)}{\rho}\right) dt. \tag{4.29}$$

Because the orientation of the polymer, Eq. (4.28), follows the same equation as the orientation of the material line, Eq. (4.7), the statistics of $\widehat{\rho}_i S_{ij} \widehat{\rho}_j$ are identical in these cases, and the Cramér function for material lines can be directly used. For this reason, the large-deviation formalism has been found useful for studying polymer length distributions.[5,6,42]

4.4.3 Modeling Approximations

The qualitative resemblance of vorticity stretching statistics to material line stretching in Fig. 4.4, despite the fact that the vorticity plays an active role in turbulent dynamics, motivates the attempt to model and approximate the vorticity as a passive vector with relaxation. This is the first and most drastic modeling approximation, removing the effect of the vorticity on the strain-rate. Statistically, this effectively removes the dependence of the conditional mean vorticity stretching on the vorticity magnitude, i.e. $\langle \widehat{\omega}_i S_{ij} \widehat{\omega}_j | \ln \omega = \chi \rangle = \langle \widehat{\omega}_i S_{ij} \widehat{\omega}_j \rangle = \lambda$. While this approach does neglect the effect of vorticity/strain-rate coupling which makes the vorticity stretching rate directly dependent on the instantaneous value of vorticity magnitude, the effects

of vorticity/strain-rate coupling on the statistics of vorticity stretching fluctuations are preserved by using the appropriate Cramér function.

With the mean of the vorticity stretching thus fixed as the minimum of the Cramér function, the model is constructed to incorporate the rest of the Cramér function into information about fluctuations in vorticity stretching. To accomplish this, the second modeling approximation proposes an intermediate time-scale, $\tau_S \ll T \ll \tau_\Omega$, at which the vorticity stretching can be modeled as stochastic noise with statistics prescribed by the Cramér function shown previously in this chapter. This approximation can be thought of in the same vein as the Kraichnan ensemble,[104] in which rapid velocity field fluctuations are modeled statistically as white-in-time stochastic terms. Indeed, the auto-correlation for vorticity has been found to be significantly longer than that of the strain-rate along Lagrangian trajectories in isotropic turbulence,[49,201] though perhaps not enough to justify this model.

Finally, the model treats the viscous relaxation as deterministic. In other words, the viscous relaxation term in Eq. (4.2) is modeled as, $\nu\,\widehat{\omega}_i \frac{\partial^2 \omega_i}{\partial x_j \partial x_j}\Big|_{\omega=w} \approx -f(w)$, where $f(w)$ is a deterministic function. In particular, the deterministic relaxation is set to be equal to the conditional mean given a particular value of the vorticity magnitude,

$$f(w) = -\nu \left\langle \widehat{\omega}_i \frac{\partial^2 \omega_i}{\partial x_j \partial x_j} \middle| \omega = w \right\rangle. \tag{4.30}$$

With this model for the relaxation, the vorticity evolution along a Lagrangian path

in dimensionless form, from Eq. (4.3), becomes,

$$\frac{d\ln(\omega\tau_\eta)}{d\,(t/\tau_\eta)} = \widehat{\omega}_i S_{ij} \tau_\eta \widehat{\omega}_j - \frac{f(\omega)\tau_\eta^2}{\omega\tau_\eta}, \tag{4.31}$$

which is identical to Eq. (4.28) for the polymer length. The difference between vorticity and polymer length, however, is the difference in the relaxation functions.

Such a function can be measured from DNS results of forced isotropic turbulence. We note that it is possible to measure the right-hand side of Eq. (4.30) directly, or indirectly using Eq. (4.24). Because evaluation of these statistics from the JHTDB isotropic dataset utilizes finite-differences in physical space (as opposed to spectral differentiation), it is preferable to measure the conditional mean of the viscous term indirectly using Eq. (4.24). The indirect calculation requires only first derivatives of the velocity field (i.e. the strain-rate) while the direct calculation requires third derivatives of the velocity field (i.e. Laplacian of vorticity).

Figure 4.6 shows the results as computed from the JHTDB isotropic dataset, using $\widehat{\omega}_i S_{ij} \widehat{\omega}_j$ computed at 100 million points using an 8^{th}-order finite difference. The scatter in the conditional mean at large $\omega\tau_\eta$ is due to lack of statistical convergence. It is found that a power law functional form for the deterministic relaxation function,

$$f(\omega)\tau_\eta^2 = A\ (\omega\tau_\eta)^n, \tag{4.32}$$

provides an excellent fit to the numerical results. The best fit of this form is shown in

Fig. 4.6a, with $A = 0.129$, $n = 1.462$ (we remark that this fitted value is very close to 3/2). Figure 4.6b shows the conditional coefficient of variance (conditional standard deviation divided by conditional mean) for the viscous relaxation term. For increasing vorticity magnitude, the conditional coefficient of variance decreases toward zero, meaning that the viscous relaxation behaves increasingly like a deterministic variable for large vorticity magnitudes (the tail of the PDF). This helps to justify one of the modelling approximations.

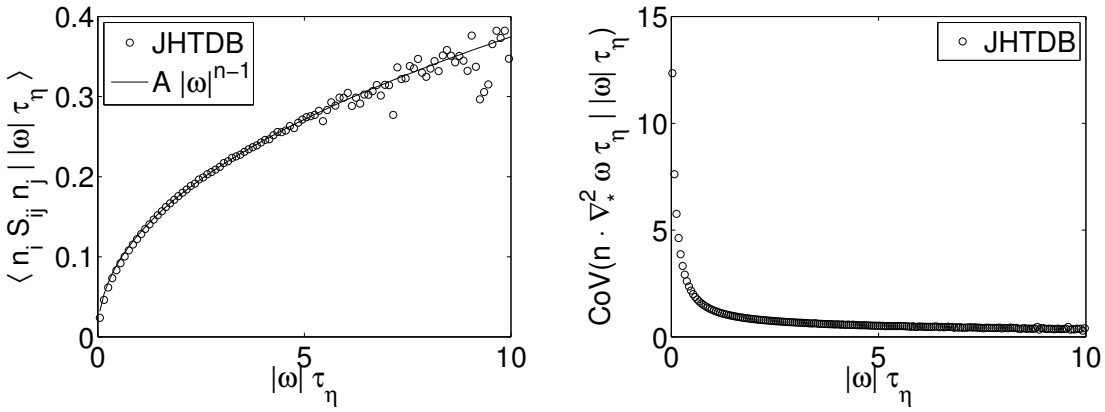

Figure 4.6: (a) The conditional mean, Eq. (4.30), as computed indirectly from the strain-rate using Eq. (4.24). Also shown is a power-law curve fit of the form, Eq. (4.32) for the interval $2 < |\omega|\tau_\eta < 6$, with $A = 0.129$, $n = 1.462$. (b) The conditional coefficient of variation (standard deviation/mean) of the relaxation term.

With these modeling assumptions, we have a stochastic model for the Lagrangian vorticity magnitude, here given in dimensionless form,

$$d\ln(\omega\tau_\eta) = \{\lambda\tau_\eta - A\ \exp[(n-1)\ln(\omega\tau_\eta)]\}\frac{dt}{\tau_\eta} + d\mathcal{W}, \tag{4.33}$$

where $d\mathcal{W}$ represents a stochastic forcing term with zero mean and increment statistics in agreement with the large-deviation statistics of the vorticity stretching fluctuations. Approximating the vorticity stretching Cramér function as a parabola, the statistics become Gaussian and $d\mathcal{W} = \sqrt{\Delta\tau_\eta}dW$, where Δ is the width of the Cramér function and dW represents a Wiener process.

4.4.4 Kramers-Moyal Coefficients

The above model is a Markovian stochastic model, for which we seek a PDF evolution equation in the form of the Kramers-Moyal equation for $p_{\ln\omega}(\chi, T)$, (see Pope[108] Appendix J),

$$\frac{\partial p_{\ln\omega}}{\partial T} = \sum_{m=1}^{\infty} \frac{(-1)^m}{m!} \frac{\partial^m}{\partial \chi^m} \left(B_m p_{\ln\omega}\right), \tag{4.34}$$

where the Kramers-Moyal coefficients are given by,

$$B_m(\chi) = \lim_{T\to 0} \frac{1}{T} \left\langle \Delta_T (\ln\omega)^m | \ln\omega = \chi \right\rangle, \tag{4.35}$$

and where the increment of $\ln\omega$ is

$$\Delta_T(\ln\omega) = \ln\omega(t+T) - \ln\omega(t). \tag{4.36}$$

Applying this approach to Lagrangian vorticity evolution, it is clear from Eq.

(4.31) that the vorticity increments are given by

$$\Delta_T(\ln\omega) = \int_t^{t+T} \left[\widehat{\omega}_i S_{ij} \widehat{\omega}_j - \widetilde{f}(\ln\omega)\right] dt', \tag{4.37}$$

where $\widetilde{f}(\ln\omega) = \frac{f(\omega)}{\omega}$. Due to the modeling assumption on the relaxation term, it gives a non-zero contribution only to the first coefficient,

$$B_1(\chi) = \lambda - \widetilde{f}(\chi). \tag{4.38}$$

For $m \geq 2$, only the vorticity stretching fluctuations from our model contribute to the Kramers-Moyal coefficients. Due to the model assumptions, we consider the $T \to 0$ limit in Eq. (4.35) to be effectively $\frac{T}{\tau_S} \to 0$,

$$B_m(\chi) = \lim_{T/\tau_S \to 0} \frac{1}{T} \left\langle \Gamma_\omega(T)^m | \ln\omega = \chi \right\rangle, \tag{4.39}$$

where Γ_ω is given by Eq. (4.11). The application of large-deviation statistics requires the $T \to \infty$ limit, which can be interpreted in this framework as $\frac{T}{\tau_\Omega} \to \infty$. In this limit of large integration time, where the large-deviation formalism is applicable, it is clear from Eq. (4.13) that the cumulant-generating function of Γ is given by

$$L_{\gamma_\omega}(q)T = \ln\langle \exp(q\Gamma_\omega)\rangle, \tag{4.40}$$

so that the moment-generating function is,

$$\exp(L_{\gamma_\omega}(q)T) = \langle \exp(q\Gamma_\omega) \rangle. \tag{4.41}$$

The moments, $\langle \Gamma_\omega(T)^m \rangle$, necessary to find the Kramers-Moyal coefficients can be computed via differentiation of the moment-generating function at the origin. For $m \geq 2$, by construction, the model gives constant coefficients. From Eq. (4.39), using the moment-generating function one obtains,

$$B_m(\chi) = \lim_{T/\tau_S \to 0} \frac{1}{T} \frac{d^m}{dq^m} \exp(L_{\gamma_\omega}(q)T)\bigg|_{q=0} = L^{(m)}_{\gamma_\omega}(0). \tag{4.42}$$

Thus, the Kramers-Moyal coefficients are given by the derivatives of the generalized Lyapunov exponent at the origin. Note that $\lambda_\omega = L'_{\gamma_\omega}(0)$ is the contribution to the $m = 1$ coefficient as shown above. The Kramers-Moyal equation for $p_{\ln\omega}(\chi, T)$ based on the model is given by

$$\frac{\partial p_{\ln\omega}}{\partial T} = -\frac{\partial}{\partial \chi}\left[(\lambda_\omega - \widetilde{f}(\chi))p_{\ln\omega}\right] + \sum_{m=2}^{\infty} \frac{(-1)^m}{m!} L^{(m)}_{\gamma_\omega}(0) \frac{\partial^m p_{\ln\omega}}{\partial \chi^m}. \tag{4.43}$$

The stationary distribution can be found by setting the time-derivative to zero,

$$0 = -\frac{d}{d\chi}\left[(\lambda_\omega - \widetilde{f}(\chi))p_{\ln\omega}\right] + \sum_{m=2}^{\infty} \frac{(-1)^m}{m!} L^{(m)}_{\gamma_\omega}(0) \frac{d^m p_{\ln\omega}}{d\chi^m}. \tag{4.44}$$

In general, this is an infinite-order ODE with variable coefficients, making analytical progress difficult. For the case of linear relaxation, the coefficients become constant, i.e. $f(\chi) = \frac{1}{\tau}$, making some analytical progress possible. Appendix E shows that the solution to the Kramers-Moyal equation gives a power-law for the tail of the stationary PDF of vorticity magnitude when linear relaxation is considered, in agreement with the stationary distribution derived by Ref.[5] for polymer lengths with linear relaxation. Nonetheless, seeing from Fig. 4.6 that this is not the case, another means of simplification to enable analytical progress is sought.

4.4.5 Results Using a Parabolic Cramér Function

Following Ref.,[6] an approximation can be obtained by representing the Cramér function as a parabola, i.e. Gaussian statistics, Eq. (4.18). This amounts to truncating the Kramers-Moyal expansion at second-order, since all higher cumulants are zero for Gaussian statistics. In this case, the first two cumulants, λ_ω and Δ_ω, fully characterize the statistics and the stationary PDF must satisfy,

$$0 = -\frac{d}{d\chi}\left[(\lambda\tau_\eta - \widetilde{f}(\chi))p_{\ln\omega\tau_\eta}\right] + \frac{\Delta_\omega\tau_\eta}{2}\frac{d^2 p_{\ln\omega\tau_\eta}}{d\chi^2}. \tag{4.45}$$

This truncation of the Kramers-Moyal equation at second-order reduces to a Fokker-Planck equation.

The solution has the form,

$$p_{\ln \omega\tau_\eta}(\chi) = C \exp\left(\frac{2\lambda_\omega}{\Delta_\omega}\chi - \frac{2}{\Delta_\omega \tau_\eta}\int^{\chi} \widetilde{f}(x)dx\right), \tag{4.46}$$

with $\widetilde{f}(\chi) = A\exp[(n-1)\chi]$,

$$p_{\ln \omega\tau_\eta}(\chi) = C \exp\left(\frac{2\lambda_\omega}{\Delta_\omega}\chi - \frac{2A}{(n-1)\Delta_\omega \tau_\eta}\exp[(n-1)\chi]\right), \tag{4.47}$$

and after change of variables to vorticity magnitude,

$$p_{\omega\tau_\eta}(w) = Cw^{-1+\frac{2\lambda}{\Delta}} \exp\left(-\frac{2A}{(n-1)\Delta_\omega \tau_\eta}w^{n-1}\right), \tag{4.48}$$

and enstrophy,

$$p_{\omega^2\tau_\eta^2}(\xi) = C'\xi^{-1+\frac{\lambda}{\Delta}} \exp\left(-\frac{2A}{(n-1)\Delta_\omega \tau_\eta}\xi^{(n-1)/2}\right). \tag{4.49}$$

Therefore, the parabolic Cramér function approximation to the Kramers-Moyal model gives a stretched exponential for the stationary PDF of enstrophy in isotropic turbulence. As discussed in the development of the model, it is only designed for applicability in the tails of the PDF, therefore the interpretation of this result is that the model gives stretched-exponential tails with a power-law correction. In fact, the power-law correction with exponent $-1+\frac{\lambda}{\Delta} \approx -0.18$ is quite small and has very little

effect on the following plots.

A first test of the model PDF is to test the proposed relationship, derived from Eq. (4.49),

$$-\log\left(\xi^{1-\frac{\lambda}{\Delta}} p_{\omega^2\tau_\eta^2}(\xi)\right) = \frac{2A}{(n-1)\Delta_\omega \tau_\eta}\xi^{(n-1)/2} - \log C', \tag{4.50}$$

by observation of a linear relationship on a plot of $-\log\left(\xi^{1-\frac{\lambda}{\Delta}} p_{\omega^2\tau_\eta^2}(\xi)\right)$ against $\xi^{(n-1)/2}$. The result, shown in Fig. 4.7, indicates the success of the model, particularly in predicting the exponent $(n-1)/2 = 0.231$ (again, suggestive of 1/4).

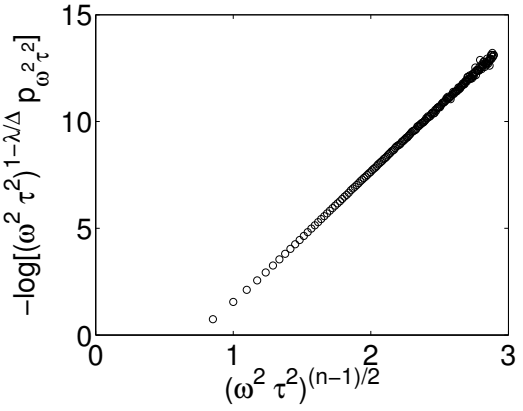

Figure 4.7: Plot of $-\log\left(\xi^{1-\frac{\lambda}{\Delta}} p_{\omega^2\tau_\eta^2}(\xi)\right)$ against $\xi^{(n-1)/2}$, for which the model successfully predicts a linear relationship. In this plot, $n = 1.462$, $\lambda = 0.100/\tau_\eta$, $\Delta = 0.122/\tau_\eta$.

The slope in Fig. 4.7 is the pre-factor $\frac{2A}{(n-1)\Delta_\omega\tau_\eta}$, for which there was found to be a 35% difference between the DNS PDF and the model PDF, as illustrated in Fig. 4.8. Figure 4.8a compares Eq. (4.49) with the observed enstrophy PDF from the isotropic DNS. The model is fully specified up to a (normalization) coefficient

by the values previously determined: $A = 0.129$, $n = 1.462$, $\lambda_\omega \tau_\eta = 0.100$, and $\Delta_\omega \tau_\eta = 0.122$. The exponent $(n-1)/2 = 0.231$ is in agreement with the values found by Ref.[133] However, from inspecting the figure, the tail of the PDF is evidently too heavy, suggesting that the coefficient $\frac{2A}{(n-1)\Delta_\omega \tau_\eta}$ is too small. Indeed, increasing the viscous relaxation coefficient A by 35% leads to very good agreement with the DNS statistics, as shown in Fig. 4.8.

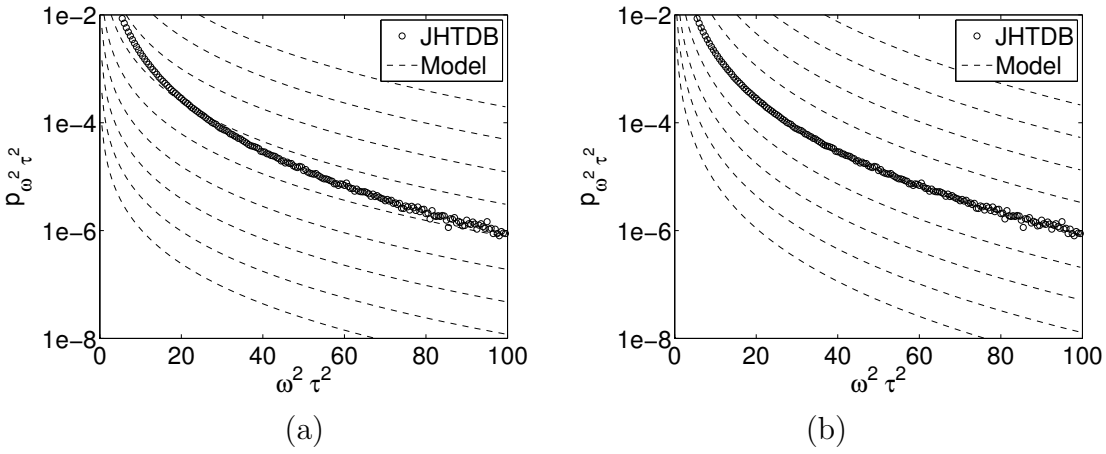

Figure 4.8: Comparison of enstrophy PDF, normalized by Kolmogorov timescale τ_η, from truncated Kramers-Moyal model with JHTDB DNS-generated statistics using (a) pre-determined model parameters, $A = 0.129$, $n = 1.462$, $\lambda = 0.100/\tau_\eta$, $\Delta = 0.122/\tau_\eta$, and (b) adjusting only $A = 0.174$ to give excellent agreement with DNS enstrophy PDF.

The success outlined in Fig. 4.7 emphasizes the utility of the modeling approach. Before any DNS data is used, the stochastic model predicts a stretched exponential form (with small power-law correction) that has become common in fitting enstrophy PDFs. Then, once the DNS data in introduced in terms of λ and Δ from the Cramér function of cumulative vorticity stretching and n from power-law fit to the conditional

mean of the viscous Laplacian, Fig. 4.7 shows that the model also predicts an accurate exponent, $(n-1)/2$. On the other hand, Fig. 4.8 provides a caveat, that the parameter A determined from the DNS needs extra adjustment for full agreement with the PDF from DNS.

Pawula's theorem[207] warns against truncation of the Kramers-Moyal equation at higher than second-order, this being similar in nature to cumulant-discard approximations. Indeed, numerical calculations (not shown) of the Kramers-Moyal model truncated after the fourth-order term resulted in negative probabilities. Therefore, while the truncation of the Kramers-Moyal expansion at second-order is less than ideal, better options are not apparent.

4.5 Conclusions

The growth of infinitesimal material lines in isotropic turbulence is commonly described by the cumulative stretching by the strain-rate along Lagrangian trajectories, i.e. finite-time Lyapunov exponents, whose statistical behavior is governed by a large deviation principle. The evolution of vorticity along Lagrangian paths is similar to that of material lines, with important caveats, such as the two-way coupling between strain-rate and vorticity. In this chapter, it is hypothesized that the cumulative vorticity stretching $\int \frac{\omega_i S_{ij} \omega_j}{\omega^2} dt$ along Lagrangian paths also has a large deviation principle governing the asymptotic evolution of its PDF. This is confirmed by noting the linear

growth of the cumulant-generating function for large enough integration times. As a result, the large-deviation formalism is available to describe the statistical behavior of cumulative vorticity stretching and provides a more in-depth way to compare the statistics of vorticity stretching with material line stretching.

The Cramér function of vorticity stretching was computed from isotropic DNS at $Re_\lambda = 433$ from the Johns Hopkins Turbulence Databases (JHTDB). The Cramér function for vorticity stretching confirmed that the mean vorticity stretching is less than the mean material line stretching, as was previously known. In addition to this fact, other characteristics of the Cramér functions were compared, giving a comparison between cumulative vorticity stretching and FTLE statistics. The mean, variance, skewness and excess kurtosis of the cumulative vorticity stretching, γ_ω, was shown to fall in between the maximal and intermediate FTLEs, γ_1 and γ_2 respectively. Overall, the statistics of γ_ω were shown to be more similar to γ_1 than γ_2, which helps put the differences between vorticity stretching and material line stretching in perspective. In particular, the Cramér function for γ_ω showed that cumulative vorticity stretching PDFs display the same non-Gaussian tendencies as for γ_1; both of these distributions indicate more probable large positive fluctuations than negative. In the case of γ_1, this is caused at least in part by the incompressibility constraint that prevents $\gamma_1 < 0$ occurrences by definition. It is interesting to note that no such constraint exists for the vorticity stretching.

In the final section, a stochastic model using information from the vorticity stretch-

ing Cramér function was proposed for the logarithm of vorticity magnitude in high vorticity regions (i.e. in the tail of the enstrophy PDF). The model gives a stretched-exponential with small power-law correction for the tail of the enstrophy PDF. When parameters from the Cramér function and conditional statistics measured from DNS are used, the stretched exponential matches well with exponent $n \approx 3/2$, but the pre-factor A is seen to be too low by about 35%. This is most likely indicative of the modeling error involved in assuming a separation of time-scales between strain-rate stretching and viscous relaxation effects.

Chapter 5

Material Deformation and Vorticity Stretching in Turbulent Channel Flow

The statistical properties of turbulent fluid deformation and vorticity stretching have been primarily studied in the context of homogeneous isotropic turbulence.[9,41,47,59,60,79,111,116,119,208–210] Velocity gradients being essentially dominated by contributions from the smallest scales in turbulence, it follows from the hypothesis of local isotropy that the statistics of fluid deformation and vorticity stretching in regions of turbulent flows with high enough local Reynolds number and far enough from solid boundaries should be similar to those of isotropic turbulence, which have been studied in some detail. It is of interest, therefore, to investigate the details of

material deformation and vorticity stretching in anisotropic flows with solid boundaries. For instance, it is interesting to investigate the extent to which locally isotropic behavior can be observed in stretching statistics at locations far enough from the wall and how such statistics deviate from local isotropy near the wall.

In addition to the statistics of material deformation and vorticity stretching rates at a particular instant in time, it is also important to consider the statistics of cumulative deformation along Lagrangian paths, i.e., finite-time Lyapunov exponents (FTLE). Even in an inhomogeneous flow such as a channel flow, these cumulative statistics are expected to have a large-deviation principle,[5] given a long enough time for trajectories to sample across the width of the channel sufficiently, assuming ergodicity. Therefore, the long time behavior of the probability density functions (PDF) also may be summarized by a Cramér function[42,79] similar to those in chapters 3 and 4, even in a channel flow. Investigation along these lines may provide insight for a wide range of phenomena in wall-bounded flows including polymer-induced drag reduction,[3,4,42] the kinematics of Lagrangian coherent structures,[57,58,71] and the deformation of immiscible droplets and bubbles.[8,9,41]

The chapter is organized as follows. First, the relevant mathematical tools for quantifying the statistics of velocity gradients, material deformation and vortex stretching are developed in §5.1. Then, §5.2 briefly details the development of the task-parallel Lagrangian tracking algorithm for the channel database. Analysis results are given in §5.3 for instantaneous statistics as a function of wall distance as well as

cumulative statistics for the whole channel. When possible, comparison is made with statistics from isotropic turbulence to highlight similarities and differences. Conclusions are provided in §5.4. The material shown in this chapter is also published in Ref. 61.

5.1 Analysis Tools for a Channel Flow

5.1.1 Velocity Gradient Statistics in Channel Flow

In a turbulent channel flow, the statistics are only non-homogeneous in the wall-normal direction. Kinetic energy is dissipated by both the mean flow and turbulent fluctuations: $\langle\epsilon\rangle(y) = 2\nu\left(\langle S_{ij}\rangle\langle S_{ij}\rangle + \langle S'_{ij}S'_{ij}\rangle\right)$, where angle brackets denote ensemble averaging and S_{ij} is the strain-rate tensor. However, energy dissipation by the mean flow becomes negligible for $y^+ \gg 1$, i.e. in the log-layer and core of the channel. At a given friction Reynolds number, the scale separation between large energetic motions and small dissipative motions increases with wall distance.[211] The typical magnitude of turbulent velocity gradients at a given distance from the wall is characterized by the Kolmogorov timescale,

$$\tau'_\eta(y) = \sqrt{\frac{\nu}{\langle\epsilon\rangle_{\text{turb}}}} = \frac{1}{\sqrt{2\langle S'_{ij}S'_{ij}\rangle}}. \tag{5.1}$$

For a typical magnitude of total velocity gradients (mean + fluctuating), the Kolmogorov timescale can be generalized to include the mean strain-rate,

$$\tau_\eta(y) = \sqrt{\frac{\nu}{\langle\epsilon\rangle}} = \frac{1}{\sqrt{2\left(\langle S_{ij}\rangle\langle S_{ij}\rangle + \langle S'_{ij}S'_{ij}\rangle\right)}}. \tag{5.2}$$

It will be argued that this more inclusive timescale is useful in the channel flow because the mean flow is also able to perform stretching in addition to the turbulent fluctuations, especially in the viscous sublayer and buffer region. Near the wall, i.e. $y^+ \sim 1$, this definition of Kolmogorov scale becomes $\tau_\eta \sim \tau_{\text{viscous}}$, where $\tau_{\text{viscous}} = \frac{\nu}{u_*^2}$ is the viscous timescale while it equals the traditional Kolmogorov timescale when the mean strain-rate becomes negligible (i.e., at $y^+ \gg 1$). Assuming an approximate balance between production and dissipation in the logarithmic region, where $-\langle u'v'\rangle \approx u_*^2$ and $\frac{\partial\langle u\rangle}{dy} \approx \frac{u_*}{\kappa y}$, then $\tau_\eta(y) \sim \sqrt{y^+}\tau_{\text{viscous}}$. At the centerline of the channel, the mean strain-rate exactly vanishes and dissipation is done only by the turbulent fluctuations. Extrapolating the scaling law from the logarithmic region, the timescale at the center of the channel is $\tau_{\eta,c} \sim Re_\tau^{1/2}\tau_{\text{viscous}}$. For the remainder of this chapter, we refer to this generalized Kolmogorov timescale simply as the Kolmogorov timescale.

To quantify the average strain-rate magnitude available over the whole channel,

a bulk Kolmogorov timescale can be defined according to,

$$\tau_{\eta,\text{bulk}} = \sqrt{\frac{2h\nu}{\mathcal{E}}}, \qquad \mathcal{E} = \int_{-h}^{h} \langle \epsilon \rangle dy. \tag{5.3}$$

This timescale has a physical basis, since $\rho\mathcal{E} = -\frac{\dot{m}}{\rho}\frac{dp}{dx}$ represents the pumping power needed to force the channel flow at mass flow rate $\dot{m} = \rho \int_{-h}^{h} \langle u_1 \rangle dy = 2h\rho U_{\text{bulk}}$. We thus can write $\tau_{\eta,\text{bulk}} = \sqrt{\frac{h\nu}{u_*^2 U_{\text{bulk}}}} = (\frac{1}{2}C_f)^{1/4} Re_\tau^{1/2} \tau_{\text{viscous}}$.

The separation of scales between large-scale (more flow-dependent) and small-scale (more universal) turbulent motions is quantified in isotropic turbulence by the Taylor-scale Reynolds number, $Re_\lambda = \frac{\sqrt{\langle u_1'^2 \rangle}}{\nu\sqrt{|f''(0)|}}$, where $f(r) = \langle u_1'(\mathbf{x}) u_1'(\mathbf{x} + r\mathbf{e}_1) \rangle / \langle u_1'^2 \rangle$ is the longitudinal correlation function. For the channel flow, it is useful to characterize the separation of scales at a given height from the wall, which can be accomplished using the Taylor-scale Reynolds number expressed in terms of kinetic energy and mean dissipation rate,

$$Re_\lambda(y) = \frac{2\sqrt{15}}{3} \frac{k}{\sqrt{\nu \langle \epsilon \rangle}}, \tag{5.4}$$

where $k(y) = \frac{1}{2}\langle u_i' u_i' \rangle$ is the turbulent kinetic energy at a given wall distance.

Figure 5.1 shows the generalized Kolmogorov timescale and Taylor-scale Reynolds number as a function of wall distance as computed from the JHTDB channel flow dataset at $Re_\tau = 1000$ (details in §5.2). In both sub-figures, the values are alternatively calculated using only the dissipation of turbulent fluctuations, i.e. without the mean flow dissipation, and plotted as a dashed line. Above $y^+ \approx 50$, the dif-

ference between the two is negligible, signaling that practically all the dissipation is accomplished by the turbulent fluctuations (mean strain-rate is negligible).

The Kolmogorov timescale is plotted on a log-log scale and displays an approximate power-law region where $\tau_\eta \sim y^n$, where $n \sim 0.5$, close to the theoretical prediction assuming local balance between production and dissipation of kinetic energy. The velocity gradient magnitudes ($\sim \tau_\eta^{-1}$) are highest near the wall and decay monotonically to the lowest magnitudes at the center of the channel ($y^+ = 1000$). With highest fluid deformation rates occuring nearest to the wall, we may naïvely expect the Lyapunov exponents to be largest in magnitude nearest the wall as well; something that will be checked in §5.3.

In the fully turbulent region of the channel flow ($y^+ > 50$), the Taylor-scale Reynolds number is between 50 and 90. The peak Reynolds number occurs near $y^+ = 400$ rather than at the center of the channel. In this light, there is only moderate scale-separation in the fully turbulent region. With such moderate Reynolds numbers, it is of interest to compare stretching statistics in the fully turbulent region of the channel to those of isotropic turbulence, i.e. to test the hypothesis of local isotropy in the context of stretching statistics. Approaching the wall, Re_λ vanishes due to vanishing turbulent kinetic energy.

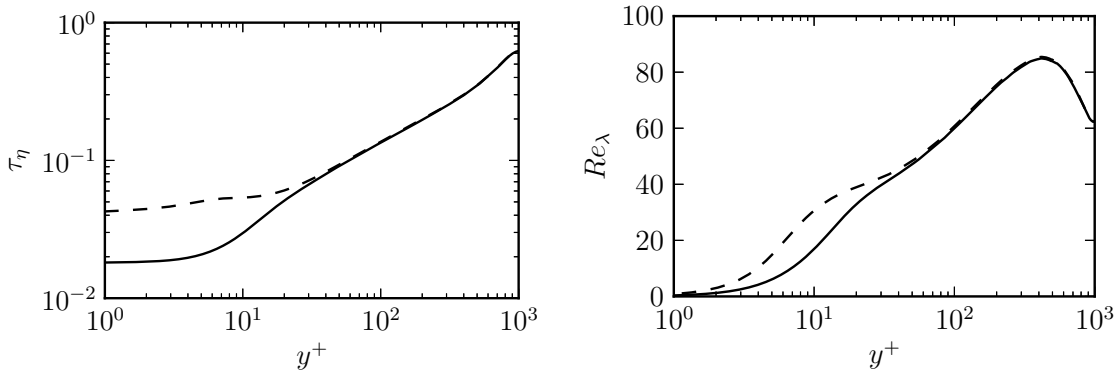

Figure 5.1: Kolmogorov timescale (left), and Taylor-scale Reynolds number (right) as a function of distance from the wall. Dashed lines indicate values calculated with only turbulent dissipation, while continuous lines indicate values using both turbulent and mean flow dissipation.

5.1.2 Various Lyapunov Exponents

The basic background of Lyapunov exponents and finite-time Lyapunov exponents has been given in §2.1.1. Here, we consider these concepts again in order to develop tools for exploring the spatial dependence of material element deformation and vorticity stretching in an inhomogeneous flow.

While the strain-rate, S_{ij}, gives the instantaneous rate of fluid deformation, the *cumulative* deformation of fluid particles is described by the finite-time Lyapunov exponents of the Lagrangian map, (2.1). The evolution in time of Lagrangian map is given by (2.2). As discussed in §2.1.1 The geometry of an infinitesimal fluid element centered at $\mathbf{x}(t)$ can be described by the deformation tensor, $D_{ij} = \partial x_i / \partial X_j$, which is the sensitivity of the trajectory to initial position. The evolution equation for the deformation tensor is given by 2.4, and a singular value decomposition (SVD),

$D_{ij} = U_{ik}\Sigma_{k\ell}V_{j\ell}$, is useful for separates the deformation tensor into its magnitude (represented by the diagonal matrix $\mathbf{\Sigma}$) and direction (columns of the unitary matrix $\mathbf{U}$). This is equivalent to an eigenvalue decomposition of the (left) Cauchy-Green tensor, $C_{ij} = D_{ik}D_{jk} = U_{ik}\Sigma^2_{k\ell}U_{j\ell}$. The singular values, σ_i, give the ratio fluid stretching along its associated Lyapunov vector, thus by definition $\sigma_i(t_0) = 1$. In an incompressible flow, the volume of the fluid element must be preserved, i.e. $\sigma_1\sigma_2\sigma_3 = 1$ for all t. The singular value decomposition of (2.4) results in evolution equations for the singular values and their associated (forward) singular vectors,[103]

$$\frac{d\ln\sigma_i}{dt} = \widehat{S}_{(ii)}, \qquad U_{ki}\frac{dU_{kj}}{dt} = \begin{cases} \left(\frac{1+\frac{\sigma_j}{\sigma_i}}{1-\frac{\sigma_j}{\sigma_i}}\right)\widehat{S}_{ij} + \widehat{\Omega}_{ij} & i \neq j \\ 0 & i = j \end{cases}, \tag{5.5}$$

where the hat denotes rotation to the Lyapunov reference frame, e.g. $\widehat{S}_{ij} = U_{ki}S_{k\ell}U_{\ell j}$. Repeated indices in parentheses are not summed. The singular values grow exponentially in time according to $\widehat{S}_{(ii)}$, i.e. the longitudinal velocity gradient along the direction of the i^{th} singular vector. For this reason, we refer to $\widehat{S}_{(ii)}$ as an instantaneous Lyapunov exponent (ILE). The ILE contains some Lagrangian memory from the alignment of the deformation tensor, $\mathbf{U}$. The statistical alignment of Lyapunov vectors and strain-rate eigenvectors plays a key role in determining cumulative fluid particle deformation along with the strain-rate eigenvalues themselves, Λ_i. For instance, in the eigenframe of the strain-rate tensor, $\widehat{S}_{(ii)} = \cos^2(\theta_{ij})\Lambda_j$, where θ_{ij} is the angle between the i^{th} eigenvector of the Cauchy-Green tensor and the j^{th} eigenvector

of the strain-rate tensor.

Finite-time Lyapunov exponents (FTLE), as previously introduced, are simply the time-average of the ILE over a certain interval along a Lagrangian path,

$$\gamma_i(T;\mathbf{X},t_0) = \frac{1}{T}\ln\sigma_i(t_0+T;\mathbf{X},t_0) = \frac{1}{T}\int_{t_0}^{t_0+T}\widehat{S}_{(ii)}(\mathbf{x}(t'),t')dt', \tag{5.6}$$

Assuming ergodicity in homogeneous flows, the FTLEs converge for $T\to\infty$ to the Lyapunov exponents (LE), $\lambda_i = \langle\widehat{S}_{(ii)}\rangle = \langle\gamma_i\rangle$, with probability one. Similarly in this limit, the singular vectors of the deformation tensor (eigenvectors of the left Cauchy-Green tensor) converge to the Lyapunov vectors.

In a channel flow, however, the statistics involving finite-time Lyapunov exponents naturally depend on wall distance. For this reason, statistics of FTLEs can be difficult to obtain in a localized manner in a channel flow, given that they naturally require integration over trajectories that move toward and away from the wall. Nonetheless, the mean of FTLE distributions can be easily localized to a particular y^+ location by averaging ILEs conditioned on wall distance. In this way, the local Lyapunov exponents (LLE), $\langle\widehat{S}_{(ii)}|y\rangle$, represent the average stretching rates undergone by a material element (or vorticity) given that the current location of its trajectory is at that wall distance. The LLE quantities are in some sense related to traditional Lyapunov exponents in an ergodic system, but with a localization using conditional averaging.

Given the similarity between the equations for material line and vorticity stretching discussed in detail in chapter 4, the definitions for ILE and LLE can be easily extended to also cover vorticity stretching in a channel flow. The vorticity analog to the ILE is simply the normalized vorticity stretch rate, $\frac{d\ln\omega}{dt} = \widehat{\omega}_i S_{ij} \widehat{\omega}_j = \widehat{S}_\omega$. As covered in chapter 4, the analog to the FTLE are given by the time-average of the vorticity ILE along the trajectory,

$$\gamma_\omega(T; \mathbf{X}, t_0) = \frac{1}{T} \ln \omega(t_0 + T; \mathbf{X}, t_0) = \frac{1}{T} \int_{t_0}^{t_0+T} \widehat{S}_\omega(\mathbf{x}(t'), t') dt. \tag{5.7}$$

Again, an ergodic assumption for homogeneous flows means that the $T \to \infty$ limit converges to an analog of the Lyapunov exponent for vorticity stretching, $\lambda_\omega = \langle \widehat{S}_\omega \rangle = \langle \gamma_\omega \rangle$. Finally, the local Lyapunov exponent can be generalized to vorticity, $\langle \widehat{S}_\omega | y \rangle$.

As with fluid deformation, the alignment between vorticity and strain-rate eigenvectors plays a key role alongside strain-rate eigenvalue statistics in determining vorticity stretching statistics. For instance, the instantaneous vorticity stretching rate can be decomposed as $\widehat{S}_\omega = \cos^2(\theta_{\omega,j})\Lambda_j$, where $\theta_{\omega,j}$ represents the angle between the vorticity and the j^{th} eigenvector of the strain-rate tensor. The instantaneous statistics of $\widehat{S}_\omega$ and $\widehat{S}_{(ii)}$ as well as their finite time averages γ_ω and γ_i are useful for comparing vorticity stretching statistics with those of fluid element deformation.

5.1.3 Large-Deviation Statistics

In homogeneous isotropic turbulence, the probability density functions (PDF) of γ_i and γ_ω have been shown to follow a large-deviation principle, $p_{\gamma_i}(g,T) \sim \exp(-TS_i(g))$, for $T \to \infty$ by Ref. 79 and in chapters 3 and 4. At sufficiently long integration times allowing for particles to mix thoroughly in the wall-normal direction, the lack of statistical homogeneity in this direction is not an obstacle for the existence of a large-deviation principle. Indeed, Bagheri et al.[42] showed for a channel flow with $Re_\tau = 180$ that PDFs for γ_1 collapse self-similarly to a Cramér function that is independent of wall-normal location at the end of the trajectory. The predicted power-law PDFs for the polymer stretch were also observed. As in the previous chapters, proving the existence of a large deviation principle[81,82] and constructing the Cramér function can be done simultaneously using the generalized Lyapunov exponent (GLE),[68] also known as the scaled cumulant generating function (SCGF).

5.2 Numerical Methods

In this section, the numerical methods used for this study are briefly summarized. Although this chapter focuses mainly on channel flow results, frequent comparison with isotropic turbulence is made. Direct numerical simulation data for both channel flow and isotropic turbulence are obtained from the JHTDB. In order to obtain the

necessary Lagrangian particle paths, the JHTDB Lagrangian tracking algorithm was extended to work in the channel flow dataset. This extension is briefly summarized with discussion of particle tracking concerns unique to the channel dataset.

5.2.1 Lagrangian Particles

This study makes use of both the channel flow and isotropic turbulence datasets from the JHTDB.[77,185] For the results in this study, ensembles of $43,200$ particles were advanced through the entire database time with sixth-order spatial interpolation and a timestep of $\Delta t = 0.0013$, i.e., the simulation timestep. For initialization, the domain was split into 432 sub-domains of size $\frac{\pi}{3} \times 1 \times \frac{\pi}{3}$. In each sub-domain 100 particles were placed randomly according to a uniform distribution. Every 5 particle timesteps (each database storage timestep), the velocity gradient was retrieved from the database using fourth-order finite-differencing and fourth-order Lagrangian interpolation in space. Chapter 3 briefly explored the effect of simulation resolution as well as finite-differencing on stretching statistics in isotropic turbulence, finding that low-order statistical quantities can be accurately obtained with the resolution and finite-differencing used here in both channel and isotropic datasets.

An important aspect of this study was the ability to compute Lagrangian trajectories from the Eulerian databases. This functionality was previously implemented in the JHTDB only for the unbounded flows via the *getPosition* function, which uses a second-order predictor-corrector method for time advancement with user choice of

fourth-, sixth-, and eighth-order Lagrangian interpolation in space and piecewise cubic Hermitian interpolation in time.[187] Kanov and Burns[212] developed an asynchronous task-parallel algorithm for improving the query response time compared with other parallel methods. For this study, we extended the Lagrangian tracking capabilities to the channel dataset with the task-parallel approach.

5.2.2 Particle Tracking on a Parallel Database

Initially, the *getPosition* function was implemented using a Mediator Synchronization approach. In this approach, a mediator (in this case the web server) accepts a batch of particle positions, and determines which database contains their velocities. Upon completion of this task, the mediator spawns a process in each particle's respective database to advect each particle for the given integration step. Once complete, the new positions are returned to the mediator and the mediator must wait for all particles to complete for each integration step. After each step, the particles are reassigned to their new database location based on each particle's new position. This will be either the same database or a different one depending upon whether the particle crossed a database boundary. While this approach works, two other methods of particle tracing were experimented with, data-parallel, and task-parallel.

The task parallel method works differently from the mediator synchronization approach in that the mediator is not responsible for tracking each particle at every integration step. Instead, the mediator performs the initial placement of particles

based on their respective positions in the database, and then the database performs each integration step upon advecting each particle. This allows for particles computation to remain on the server in which the particle is placed. The only concern with this approach is when a particle crosses a server boundary, the original server is still responsible for follow-on integration steps. However during testing this issue did not outweigh the speed gained from allowing each particle to advance asynchronously at each integration, thus making this the preferred approach.

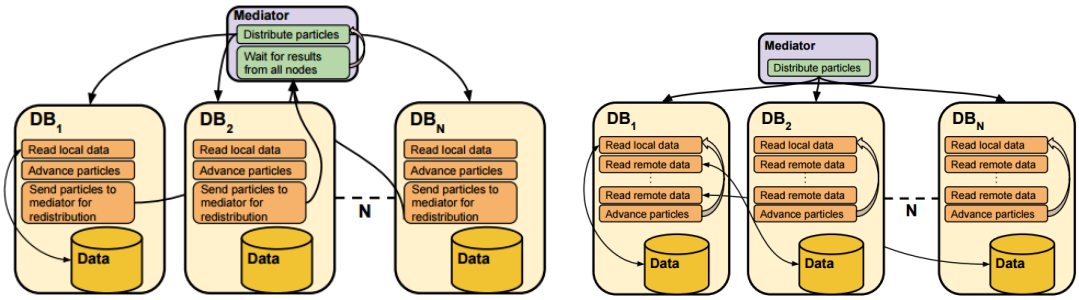

Figure 5.2: Schematic showing the mediator synchronization and task-parallel algorithms for parallel processing of Lagrangian trajectories in the JHTDB. Mediator synchronization is on the left, and the task-parallel is on the right

5.2.3 Other Considerations for Lagrangian Trajectories in a Channel Flow

Because the simulation was computed and stored in the database on a moving grid with velocity 0.45 in the streamwise direction, this had to be taken into account within the particle tracking calculation. At the beginning of a *getPosition* query,

$0.45t_{\text{start}}$ is subtracted from the physical x-position of the particle, moving it from the physical location to the grid location. Then, throughout the particle tracking calculation, 0.45 is subtracted from the streamwise velocity component. Finally, at the conclusion of the calculation, $0.45t_{\text{end}}$ is added back to the grid position to recover the physical position of the particle. Periodic wrapping in x and z is used to keep the particle always somewhere in the domain.

One additional consideration when implementing the Lagrangian path procedure in the channel dataset was the numerical (but not physical!) possibility that Lagrangian particles could travel through the walls at $y = \pm 1$. If the particles moves outside the domain ($|y| > 1$) during the predictor phase, then zero velocity is applied for the corrector step and hence half of the predictor velocity is used when actually advancing the particle. In this way, for a particle at distance y from the wall, the maximum time step allowed for which the particle remains in the domain is $\Delta t_{max} = \frac{2y}{v(y)}$, where $v(y)$ is the wall-normal velocity from the predictor step (possibly the result of interpolation). In order to determine the maximum time step that can be taken with such a scheme without worrying about particles violating the no-penetration condition, the database was scanned to obtain the maximum velocity toward the wall at each y grid location.

The results are shown in Figure 5.3. Using every 100^{th} timestep, each grid location was tested up to $y^+ = 30$. To find the minimum timestep at which a particle could leave the domain, the range of y^+ values searched was narrowed and every 10^{th}

timestep was searched. Finally, the minimum wall normal location from this result was searched over the entire database. The result is that the minimum timestep at which a particle could pass through the wall was found to be four times the database storage timestep and twenty times the simulation timestep. It is recommended that a timestep at least as small as the storage timestep be used, therefore, the current numerial method is deemed sufficient for preventing particles from violating the non-penetration condition at the wall.

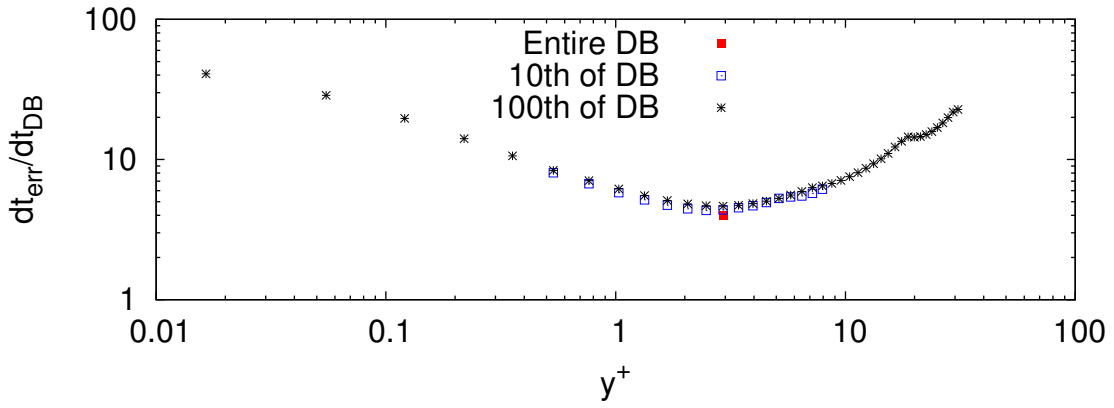

Figure 5.3: The minimum time step, as a function of wall distance, at which a particle in the database may leave the domain by violating the no-penetration condition. The worst-case scenario is a particle leaving the domain from $y^+ \approx 3$ with a timestep of $\Delta t =$ 2.6e-2, which is four times the database storage timestep.

5.3 Results

In this section, the DNS results concerning the statistics of material deformation and vorticity stretching in a channel flow at $Re_\tau = 1000$ are explored. Compar-

isons with isotropic turbulence at $Re_\lambda = 430$ are used when applicable. In addition to exploring the dependence of Lyapunov exponents on wall distance, the factors contributing to these trends, such as strain rate eigenvalues and alignment between Cauchy-Green and strain rate eigenvectors, are shown to provide additional insight.

5.3.1 Local Lyapunov Exponents

In order to characterize the mean stretching of material elements and vorticity as a function of wall distance, Figure 5.4 presents LLE normalized by bulk and local Kolmogorov timescales. In Figure 5.4a, the LLE are normalized by the bulk Kolmogorov timescale, which is constant across the channel. LLE magnitudes are plotted so that all results fit on a log-log plot. For most of the channel only $\langle \widehat{S}_{33}|y\rangle$ is negative, while all others are positive. The instantaneous stretching of the maximal singular value, $\langle \widehat{S}_{11}|y\rangle$, has a peak between $10 \leq y^+ \leq 20$, signifying that the maximum stretching of material lines occurs in the buffer layer, on average. The other two Lyapunov exponents, $\langle \widehat{S}_{22}|y\rangle$ and $\langle \widehat{S}_{33}|y\rangle$, likewise have peak magnitudes in the buffer layer. The vorticity stretching LLE, $\langle \widehat{S}_{\omega}|y\rangle$, has its peak further from the wall, near $30 \leq y^+ \leq 50$. This occurs because, while vorticity stretching is close in magnitude to material line stretching throughout the channel, it drops off more quickly approaching the wall through the buffer layer. The value of $\langle \widehat{S}_{22}|y\rangle$, meanwhile, drops off precipitously approaching the wall in the viscous sublayer and even becomes slightly negative below $y^+ = 3$, indicating that material deformation

becomes mostly two-dimensional.

Figure 5.4b normalizes the local Lyapunov exponents using the local Kolmogorov timescale, which increases monotonically with wall distance (see Figure 5.1). By rescaling with local strain rate averages, the Lyapunov exponent represents something like an efficiency of stretching accomplished per unit available strain rate (dissipation). This allows direct comparison with isotropic turbulence, indicated by dashed lines in Figure 5.4b. For $y^+ > 100$, there is excellent agreement between the Lyapunov exponents of channel flow and isotropic turbulence. This shows that, above 100 viscous units from the wall, the variation of LLEs (including for vorticity stretching) with wall distance can be accurately predicted from Kolmogorov's hypothesis of local isotropy, given knowledge only of the y-dependence of the Kolmogorov timescale, even though the Re_λ is not large.

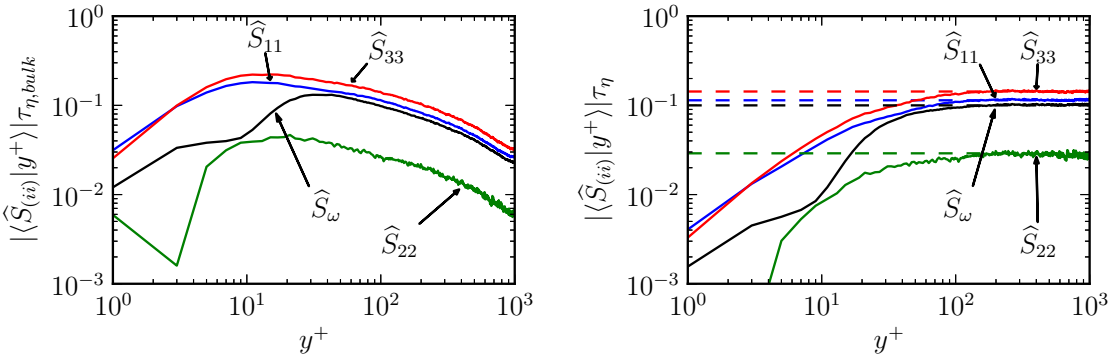

Figure 5.4: The average instantaneous Lyapunov exponents, $\langle\widehat{S}_{(ii)}\rangle$, for $i = 1, 2, 3, \omega$, as a function of wall distance (continuous lines), (a) normalized by bulk Kolmogorov timescale, and (b) normalized by local Kolmogorov timescale, with dashed lines representing $|\lambda_i|\tau_\eta$ from homogeneous isotropic turbulence.

Seeing from Figure 5.4b that the LLE values are constant above $y^+ = 100$ when normalized by the local Kolmogorov timescale and equal to the values in isotropic turbulence, it is of interest to compare the entire distribution of $\widehat{S}_{(ii)}\tau_\eta$. Figure 5.5 shows the PDF of $\widehat{S}_{(ii)}\tau_\eta$ created from histograms binned along Lagrangian trajectories according to the Kolmogorov timescale of the current wall distance. The result is compared to the PDF of instantaneous Lyapunov exponents in homogeneous isotropic turbulence (dotted lines). It is immediately clear that the entire distributions are quite similar. The isotropic flow does have a higher Re_λ, thus is expected to have higher intermittency in velocity derivative statistics, which is evidenced by slightly wider tails for the isotropic data in Figure 5.5. Grid resolution is another factor to consider when comparing the tails of these distributions, however, as chapter 3 showed that resolution and finite-differencing can significantly influence the statistics of larger fluctuations in fluid stretching. Nonetheless, comparing the cores of these distributions, this figure represents more detailed evidence that the local isotropy hypothesis is sufficient for describing the material deformation and vorticity stretching statistics above $y^+ = 100$.

Returning to Figure 5.4b, the stretching efficiency per unit dissipation, $\langle \widehat{S}_{(ii)}|y\rangle\tau_\eta$, drops significantly approaching the wall. Near the wall, the combination of decreasing stretching efficiency per unit dissipation with increasing available dissipation causes the maximal stretching, $\langle \widehat{S}_{(ii)}|y\rangle\tau_{\eta,\mathrm{bulk}}$, to occur in the buffer layer in Figure 5.4a. In order to explore the causes of this loss in stretching efficiency near the wall, it is useful

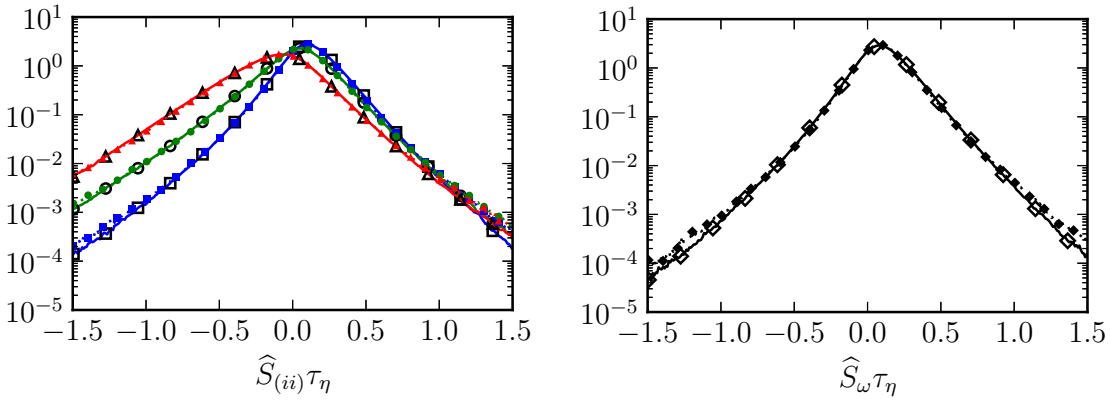

Figure 5.5: PDFs of instantaneous Lyapunov exponents normalized by local Kolmogorov timescale in the core of the channel, i.e. conditioned on $y^+ > 100$. Continuous lines with open symbols represent channel flow results while dotted lines with filled symbols represent isotropic turbulence results. Squares (left): $\widehat{S}_{11}$, circles (left): $\widehat{S}_{22}$, triangles (left): $\widehat{S}_{33}$, diamonds (right): $\widehat{S}_\omega$.

to employ the following decomposition:

$$\widehat{S}_{(ii)} = \sum_{j=1}^{3} \Lambda_j \cos^2 \theta_{ij}, \tag{5.8}$$

which is obtained by taking the eigenframe of the strain-rate tensor, where Λ_j represents the j^{th} eigenvalue of the strain-rate tensor and θ_{ij} represents the angle between the eigenvector of the Cauchy-Green tensor associated with its i^{th} eigenvalue and the strain-rate eigenvector associated with its j^{th} eigenvalue. Here, eigenvalues are sorted in decreasing order. Note that we can also take $i = \omega$, where then $\theta_{\omega j}$ indicates angles between the vorticity vector and strain-rate eigenvectors. From this decomposition, it is clear that statistics of the ILEs at each wall-normal location are a function jointly of strain-rate eigenvalue statistics and alignment statistics. That is, the Lyapunov

exponent can be written as,

$$\langle \widehat{S}_{(ii)}|y\rangle = \sum_{j=1}^{3}\langle \Lambda_j \cos^2\theta_{ij}|y\rangle. \tag{5.9}$$

Although statistical independence of Λ_j and θ_{ij} is neither expected nor observed, thus $\langle \Lambda_j \cos^2\theta_{ij}|y\rangle \neq \langle \Lambda_j|y\rangle\langle \cos^2\theta_{ij}|y\rangle$, it is nonetheless instructive to explore $\langle \Lambda_j|y\rangle$ and $\langle \cos^2\theta_{ij}|y\rangle$ separately as a function of wall distance. Partly justifying this separation, it was found that correlation coefficients between the strain-rate eigenvalues and alignment angles were quite small, $\sim \pm 0.1$.

5.3.2 Strain-Rate Eigenvalues

The first ingredient in fluid element deformation and vorticity stretching statistics is the strain-rate magnitude statistics, characterized most effectively by its eigenvalues. It is first worth noting that by definition, at every wall-normal location,

$$\sum_{i=1}^{3}\langle \Lambda_i^2|y\rangle \tau_\eta^2 = \frac{1}{2}. \tag{5.10}$$

Further, $\langle \Lambda_i^2\rangle = \langle \Lambda_i\rangle^2 + \langle \Lambda'^2\rangle$, so that $\langle \Lambda_i\rangle^2 \leq \langle \Lambda_i^2\rangle$, where equality holds only in the absence of fluctuations. Therefore, we conclude that

$$\sum_{i=1}^{3}\left(\langle \Lambda_i|y\rangle \tau_\eta\right)^2 \leq \frac{1}{2}. \tag{5.11}$$

Larger variance of Λ_i fluctuations tends to decrease the left-hand side.

Figure 5.6a shows the mean strain-rate eigenvalues as a function of wall distance, with constant-in-space normalization by $\tau_{\eta,\text{bulk}}$. The maximal and minimal eigenvalues reach their peak magnitude at the wall, decreasing monotonically to the center of the channel. The intermediate eigenvalue, however, reaches its maximum in the buffer layer, since the flow in the viscous sublayer tends to resemble unsteady two-dimensional shear flow. The drop off in Λ_2 near the wall is accompanied by equal magnitudes for Λ_1 and Λ_3 (opposite signs).

The mean strain-rate eigenvalues are rescaled with the local Kolmogorov timescale in Figure 5.6b. Here, the dashed lines show the values from the isotropic dataset. As with the Lyapunov exponent above, the mean strain-rate eigenvalues collapse to the isotropic values for $y^+ > 100$ when normalized this way. Thus, the hypothesis of local isotropy provides a good platform for describing the mean strain-rate eigenvalues' dependence on wall distance above 100 viscous units. The magnitude of the minimal strain-rate eigenvalue, which is always negative, remains approximately constant across the entire channel under this normalization. Meanwhile, the two-dimensional nature of the flow near the wall causes the intermediate strain-rate eigenvalue to vanish. To compensate, the maximal strain-rate eigenvalue, which is always positive, increases in magnitude near the wall and becomes equal in magnitude to the minimal eigenvalue. The Kolmogorov timescale is an effective characterization of strain-rate magnitude available for deforming fluid elements or stretching vorticity. While align-

ment with the strain-rate eigenvector corresponding to its intermediate eigenvalue is beneficial for stretching over most of the channel (i.e. because $\lambda_2 > 0$), near the wall such alignment provides very little stretching.

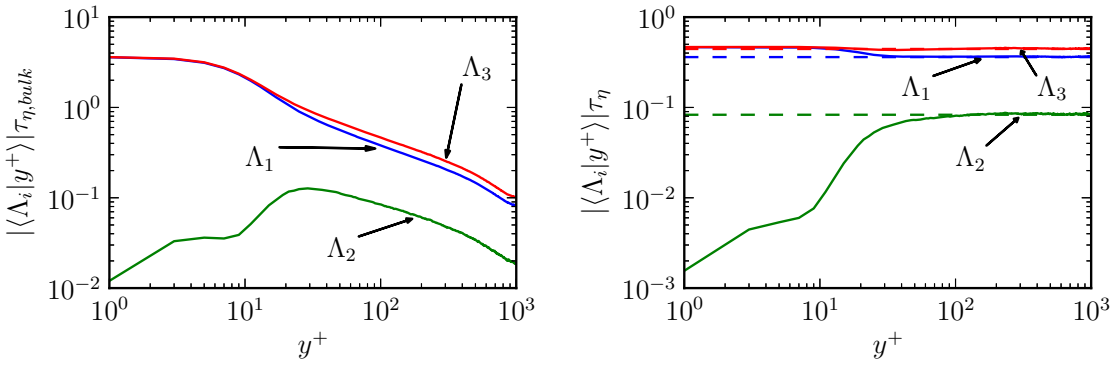

Figure 5.6: Average strain-rate eigenvalues as a function of wall distance (continuous lines), (a) normalized by bulk Kolmogorov timescale, and (b) normalized by local Kolmogorov timescale, with dashed lines representing results from homogeneous isotropic turbulence.

Since Figure 5.6b shows that the mean strain-rate eigenvalues are constant for $y^+ > 100$, it is of interest to pursue the entire PDF of strain-rate eigenvalues in this region when normalized by the local Kolmogorov timescale. The resulting distribution (continuous lines) is compared with the strain-rate eigenvalue PDFs from isotropic turbulence (dotted lines) in Figure 5.7. The comparison is quite good, although the PDFs from the isotropic simulation have slightly wider tails due to their higher Re_λ. Therefore, the hypothesis of local isotropy for strain-rate eigenvalue statistics gains further support.

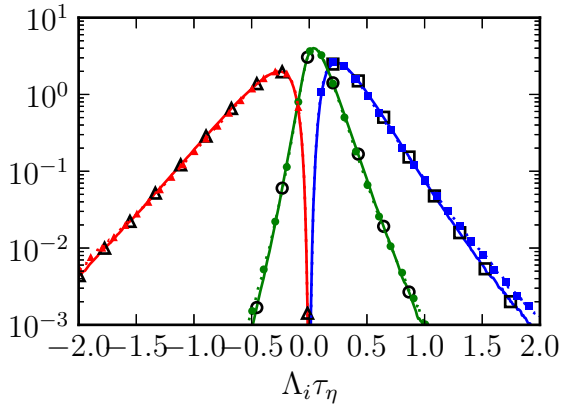

Figure 5.7: PDFs of strain-rate eigenvalues normalized by local Kolmogorov timescale in the core of the channel (continuous lines with open symbols), i.e. conditioned on $y^+ > 100$. Dotted lines with filled symbols represent results from homogeneous isotropic turbulence. Squares: Λ_1, circles: Λ_2, triangles: Λ_3.

5.3.3 Alignment with Strain-Rate Eigenvectors

The statistics of alignment between strain-rate eigenvectors and Cauchy-Green eigenvectors (or vorticity vectors) are of importance in determining the efficiency at which a turbulent flow stretches fluid elements (or vorticity) per unit dissipation. The average weights assigned to alignments between strain-rate and Cauchy-Green eigenvectors are given by $\langle \cos^2 \theta_{ij} | y \rangle$, as discussed above. Figure 5.8 presents, as a function of wall distance, all the components of this tensor with $i = 1, 2, 3, \omega$ and $j = 1, 2, 3$.

The eigenvector associated with the largest eigenvalue of the Cauchy-Green tensor ($i = 1$) represents the asymptotic alignment direction of material lines. Its mean alignment with strain-rate eigenvectors for different wall distances in the channel

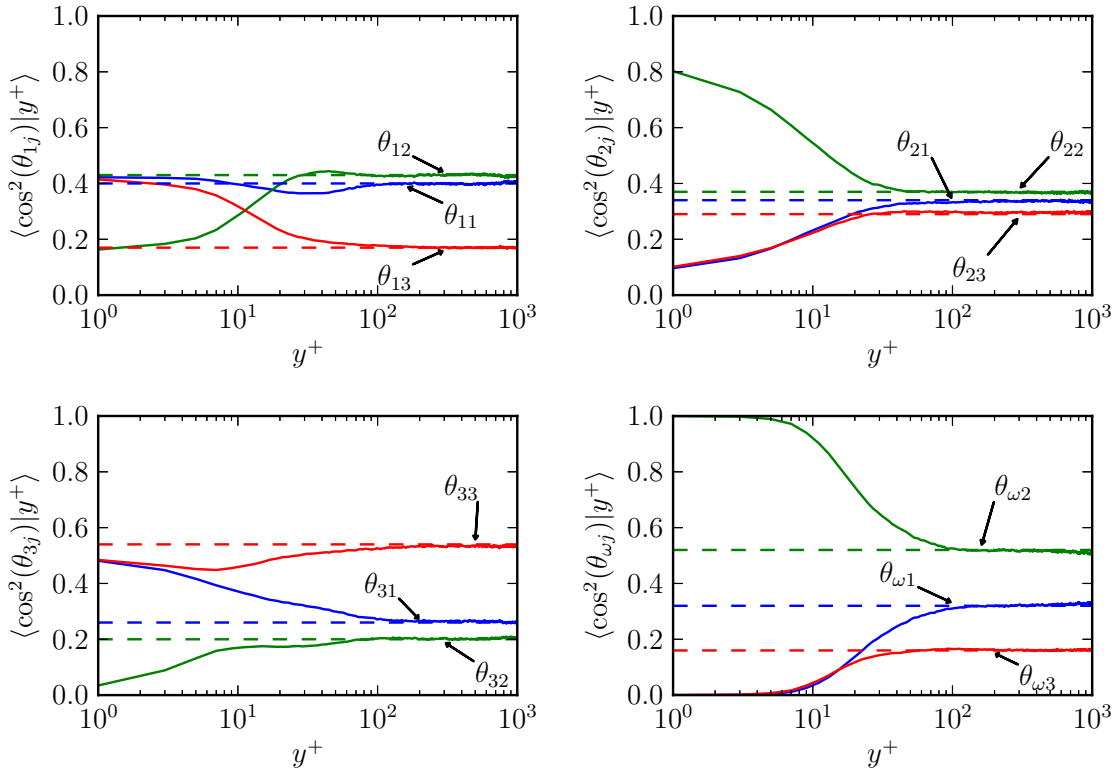

Figure 5.8: Averages of $\cos^2(\theta_{ij})$ as a function of y^+, where θ_{ij} represents the angle between the Cauchy-Green eigenvector associated with its i^{th} largest eigenvalue and the strain-rate eigenvector associated with its j^{th} largest eigenvalue. Continuous lines represent results for (a) most extensive FTLE direction ($i = 1$), (b) intermediate FTLE direction ($i = 2$), (c) most compressive FTLE direction ($i = 3$), (d) vorticity vector direction ($i = \omega$). Dashed lines represent results from homogeneous isotropic turbulence.

flow is shown in Figure 5.8a compared with isotropic turbulence alignments. As with previous observations in this chapter, the mean alignment collapses to the isotropic values for $y^+ > 100$, indicating agreement with local isotropy assumptions. In the isotropic turbulence regime, the material line asymptotically aligns more closely with the strain-rate eigenvectors associated with the largest two eigenvalues, with slight preference for the intermediate eigenvalue. Meanwhile, it tends to align more orthog-

onally with the strain-rate eigenvector of the minimal eigenvalue (contracting direction). This bias in alignment allows for net stretching, since it experiences better alignment with the expanding eigenvectors than the contracting ones. The situation changes approaching the wall, however. Alignment with the largest strain-rate eigenvalue remains fairly steady, dipping slightly between $10 < y^+ < 100$ but rising above the isotropic value within 10 viscous units of the wall. Alignment with the intermediate eigenvalue of the strain-rate tensor drops dramatically within 30 viscous units of the wall after a slight maximum between $30 < y^+ < 100$. The loss of alignment with the intermediate eigenvalue is replaced by more alignment with the contracting strain-rate eigenvalue. Approaching the wall, the alignment of material lines is equal with the Λ_1 and Λ_3 strain-rate eigenvectors. In this way, the stretching done by alignment with the expanding direction is statistically canceled by equal alignment and magnitude of the contracting direction. This increased alignment with the Λ_3 direction is the cause for the decreased mean stretching efficiency, $\lambda_1\tau_\eta$, near the wall noticed in Figure 5.4b.

The mean alignments of the eigenvector for the intermediate Lyapunov exponent ($i = 2$) similarly collapse to isotropic values above $y^+ = 100$. This eigenvector shows the lowest level of bias in aligning with each of the three strain-rate eigenvectors, with a slight preference for the eigenvector of Λ_2 and against the eigenvector of Λ_3. Near the wall, however, it becomes strongly biased toward alignment with the Λ_2 eigenvalue, which is itself vanishing. Alignments with the Λ_1 and Λ_3 eigenvectors

decrease significantly and become equal. The drop in $\lambda_2\tau_\eta$ near the wall in Figure 5.4b is mostly a result of the drop in $\langle\Lambda_2\rangle$ due to the increasingly two-dimensional nature of the near wall flow.

The eigenvector of the minimal Lyapunov exponent ($i = 3$) also statistically mirrors the strain-rate eigenvalue alignments of isotropic turbulence for $y^+ > 100$. In this region, its preferential alignment with the contracting eigenvalue preserves the $\lambda_3 < 0$ relationship. Approaching the wall, however, this eigenvector's increasing alignment with the Λ_1 direction coupled with a slight decrease in alignment with Λ_3 effectively decreases the magnitude of $\lambda_3\tau_\eta$ as well, as seen in Figure 5.4b. The tendency toward contraction by Λ_3 becomes statistically canceled with more tendency toward stretching by Λ_1.

The vorticity vector shows the most exaggerated behavior, moving from its well-known alignment with the Λ_2 direction at $y^+ > 100$, toward the two-dimensional shear flow behavior in the viscous sublayer, where vorticity is perpendicular to the non-zero strain-rate eigenvalues. The drop off in Λ_2 approaching the wall, along with the vorticity's dramatically increasing alignment with the Λ_2 direction, is responsible for the drop in vorticity stretching efficiency $\lambda_\omega\tau_\eta$ approaching the wall.

The following picture thus emerges. For $y^+ > 100$, alignment and strain-rate statistics mirror those of isotropic turbulence. In the viscous sublayer, $y^+ < 5$, the flow becomes like an unsteady two-dimensional shear flow. In this regime, the Cauchy-Green tensor is relatively un-stretched out of the shear plane (typically, the

transverse direction). Thus, the λ_1 and λ_3 Cauchy-Green eigenvectors lie in the plane of the shear, while the vorticity is perpendicular to this plane. As a result, the vorticity directly opposes the efforts of the strain-rate tensor to tilt the λ_1 Cauchy-Green eigenvector toward the Λ_1 strain-rate eigenvector (and likewise λ_3 toward Λ_3). The stalemate that emerges results in statistically equal alignment of the λ_1 and λ_3 eigenvectors with stretching and contracting directions of the strain-rate tensor, which are approximately equal in magnitude. The λ_2 Cauchy-Green eigenvector aligns preferentially out of the shear plane (and with the vorticity vector) and thus experiences little stretching or contraction. In this limit, all three Lyapunov exponents effectively vanish and fluid elements are not stretched exponentially. In between these two limits, $5 < y^+ < 100$, the DNS results indicate a primarily monotonic interpolation in alignment statistics, though some non-monotonic behavior is seen, for instance, in Figure 5.8. Due to less optimal alignment statistics, buffer layer turbulence is evidently less efficient at material deformation and vorticity stretching compared with the locally isotropic turbulence seen at higher y^+, due to less favorable alignment statistics seen in that region. These alignment statistics which are less favorable in the buffer layer compared to isotropic turbulence could be due to the strong background shear (although not as influential as in the two-dimensional regime seen in the viscous layer) as well as the decrease in local Reynolds number and the increased influence of coherent structures on velocity gradient statistics. Of course, the strain-rate magnitudes in the buffer layer are much higher than in the core of the channel, so that the maximal

deformation and stretching still occurs there.

Finally, Figure 5.9 compares the full PDF of these alignments for $y^+ > 100$. As with the LLEs and strain-rate eigenvalues, its is true with the alignment statistics as well that the entire PDF matches that of isotropic turbulence. In fact, many of the lines in Figure 5.9 are indistinguishable. This figure completes the compelling evidence given in this chapter that, above $y^+ = 100$, channel flow turbulence deforms fluid elements and stretches vorticity in a manner fully consistent with the hypothesis of local isotropy, even at relatively modest Reynolds numbers.

5.3.4 Cramér Functions

For long integration time, assuming ergodic and mixing properties, the FTLEs along Lagrangian paths all converge to $\lim_{T\to\infty} \gamma_i(T) = \lambda_i$. The distribution of FTLEs in this limit collapses toward a Dirac delta function according to the self-similar shape dictated by the Cramér function, $p_{\gamma_i}(g) \sim \exp\left(-TS_{\gamma_i}(g)\right)$. The Cramér functions for $i = 1, 2, 3, \omega$ are constructed using the Legendre transform of the SCGF introduced in §5.1.3. The SCGF, $L_{\gamma_i}(q)$, is computed numerically via linear regression fit to $\ln\langle\exp\left(q\gamma_i T\right)\rangle$ as a function of T for different values of q. The derivative of the SCGF can also be calculated by linear fit to $\frac{\langle\gamma_i T\exp(q\gamma_i T)\rangle}{\langle\exp(q\gamma_i T)\rangle}$. The Cramér function is then computed via Legendre transform, $S(g) = qL'(q) - L(q)$ with $g = L'(q)$.

Figure 5.10 presents the Cramér functions for the three FTLEs as well as for vorticity stretching in the channel flow (continuous lines) compared with those of

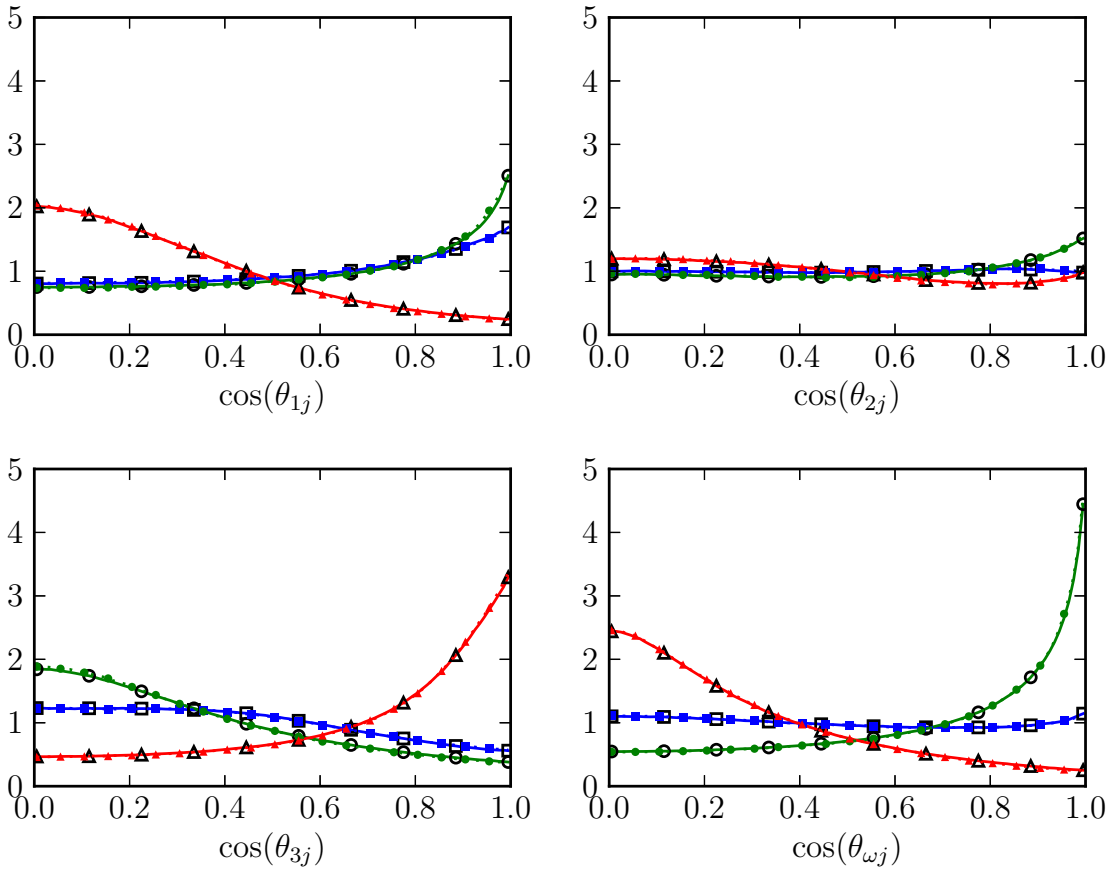

Figure 5.9: PDFs of $\cos(\theta_{ij})$ in the core of the channel, i.e. conditioned on $y^+ > 100$. Continuous lines represent (a) most extensive FTLE direction ($i = 1$), (b) intermediate FTLE direction ($i = 2$), (c) most compressive FTLE direction ($i = 3$), (d) vorticity unit vector. Dashed lines represent results from homogeneous isotropic turbulence. Squares: $j = 1$, circles: $j = 2$, triangles: $j = 3$.

isotropic turbulence (dashed lines). Immediately evident is that the minima of the channel flow Cramér functions, which indicate the mean values λ_i, are closer to the origin than their isotropic counterparts. In fact, these mean values are tabulated in the first column of Table 5.1. Each volume-averaged Lyapunov exponent, normalized by volume-averaged dissipation rate, is approximately half as large as its counterpart

from isotropic turbulence. The cumulative stretching accomplished by velocity gradients along Lagrangian paths in channel flow is less efficient per unit dissipation than is isotropic turbulence. While the turbulent stretching statistics are indistinguishable from those of isotropic turbulence in the core of the channel ($y^+ > 100$), it was clear that the alignment statistics in the buffer region and viscous sublayer are less favorable. As a result, in the locations of highest available strain-rates, the alignment efficiency dropped dramatically below the values from isotropic turbulence. Nonetheless, the channel flow maintains approximately the same ratio between Lyapunov exponents because all are decreased proportionally.

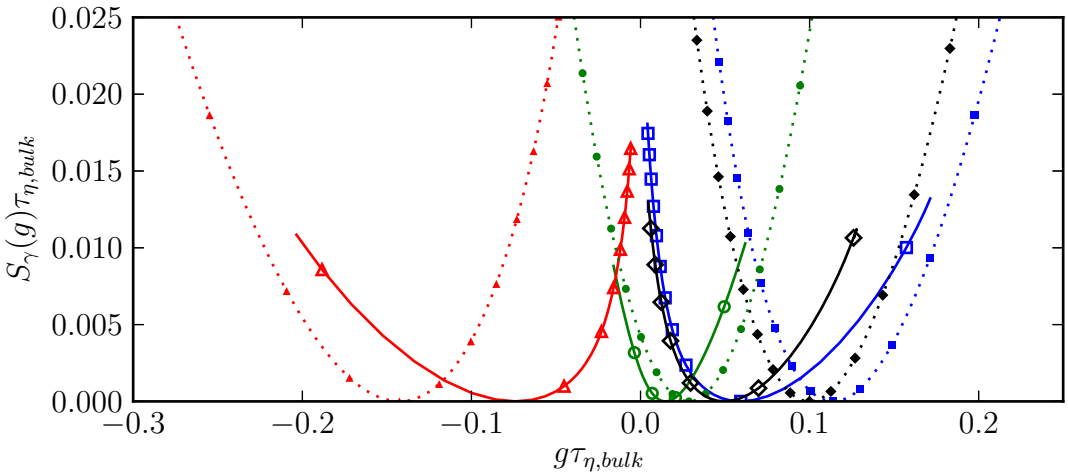

Figure 5.10: The Cramér functions of the three Lyapunov exponents and vorticity for the channel flow (continuous lines with open symbols) compared to those from isotropic turbulence (dotted lines with filled symbols). Squares: γ_1, circles: γ_2, triangles: γ_3, diamonds: γ_ω.

The shape of the Cramér functions can be characterized by looking at the behavior of cumulants in the $T \to \infty$ limit.[59] Since the existence of the SCGF indicates

the asymptotically linear growth of the cumulant generating function in time, the cumulants themselves likewise grow linearly. For instance, the variance of the FTLE distribution grows like $\Delta_i T$, where $\Delta_i = L''_{\gamma_i}(0)$ represents the width of the Cramér function. Furthermore, the third and fourth cumulants grow like $L'''(0)T$ and $L^{(4)}(0)T$ respectively, thus the skewness and excess kurtosis decrease in time as $\mathcal{S}_i = \frac{L'''_{\gamma_i}(0)}{L''_{\gamma_i}(0)^{3/2}\sqrt{T}}$ and $\mathcal{K}_i - 3 = \frac{L^{(4)}_{\gamma_i}(0)}{L''(0)^2 T}$ in accordance with the central limit theorem. These measures are summarized in Table 5.1 for both the channel flow and isotropic turbulence Cramér functions.

While the channel flow Cramér functions show a mean FTLE 50% below that of isotropic turbulence, the width of the Cramér functions for γ_1, γ_3, and γ_ω are about twice as large, indicating larger fluctuations in cumulative stretching. Furthermore, the channel flow displays much larger skewness and kurtosis values, with negative skewness for the negative FTLE and positive skewness for the positive ones. This statistical behavior reflects the influence of wall-normal movement of Lagrangian paths in causing the FTLEs to fluctuate more violently, particularly in creating rare events of large stretching and deformation when a particle advects into the high strain-rate region near the wall (and only occasionally will see beneficial alignments there). Such events appear not to cause as much fluctuations in γ_2, perhaps because they occur near the wall where the flow behaves more two-dimensionally.

Finally, to briefly explore the influence of Re_τ, Figure 5.11 compares the Cramér function for the maximal FTLE from the channel flow simulation of Bagheri et

Table 5.1: Minimum and width of the Cramér functions for channel flow and isotropic turbulence, along with coefficients for skewness and excess kurtosis (which decay as $T \to \infty$.)

Channel	$\lambda_i \tau_\eta$	$\Delta_i \tau_\eta$	$\mathcal{S}_i \sqrt{\frac{T}{\tau_\eta}}$	$(\mathcal{K}_i - 3)\left(\frac{T}{\tau_\eta}\right)$
$i = 1$	0.059	0.34	13.9	95
$i = 2$	0.014	0.07	10.9	263
$i = 3$	-0.073	0.53	-14.0	107
$i = \omega$	0.049	0.21	12.2	63
HIT	$\lambda_i \tau_\eta$	$\Delta_i \tau_\eta$	$\mathcal{S}_i \sqrt{\frac{T}{\tau_\eta}}$	$(\mathcal{K}_i - 3)\left(\frac{T}{\tau_\eta}\right)$
$i = 1$	0.114	0.15	4.6	29
$i = 2$	0.029	0.10	0.9	3
$i = 3$	-0.143	0.26	-4.5	24
$i = \omega$	0.100	0.12	3.5	19

al.[42] at $Re_\tau = 180$. Because they presented their results in terms of the timescale $\tau_L = h/U_{center}$, their fourth-order polynomial fit to the Cramér function was carefully rescaled in terms of $\tau_{\eta,bulk}$ using data from their paper. The mean stretching at $Re_\tau = 180$ is $\lambda_1 \tau_{\eta,bulk} = 0.036$, which is 30% of that seen in isotropic turbulence, even lower than the $Re_{\tau,bulk} = 1000$ case. The width of the Cramér function (variance of FTLE fluctuations) is also much smaller for $Re_\tau = 180$, which likely reflects the lower fluctuations due to wall-normal sweeping. As argued in section §5.1.1, the range of strain-rate magnitudes in the channel flow scales as $\tau_{\eta,center}/\tau_{\eta,wall} \sim Re_\tau^{1/2}$, meaning that the stretching can fluctuate more violently with increasing Reynolds number simply by wall-normal migration.

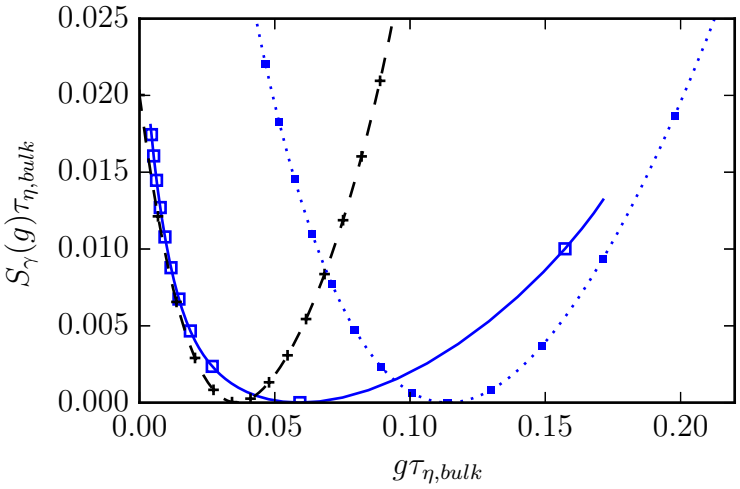

Figure 5.11: The Cramér function for the maximal finite-time Lyapunov exponent in a channel flow at $Re_\tau = 180$ (dashed line with plus symbols, from[42]) and $Re_\tau = 1000$ (continuous lines with open symbols) compared to those from isotropic turbulence (dotted lines with filled symbols).

5.4 Conclusions

In this chapter, the deformation of fluid elements and stretching of vorticity are explored in a channel flow at $Re_\tau = 1000$ using both instantaneous and finite-time Lyapunov exponents. The Lagrangian paths are extracted from an Eulerian DNS database by adapting the task-parallel approach previously used for isotropic turbulence to the channel flow. It has been verified empirically based on the data that no particles can cross into the wall as long as an appropriate Lagrangian time-step is used. When averaged conditionally on wall-normal location, the instantaneous Lyapunov exponents have a maximum in the buffer layer and approach zero at the wall. Their behavior for $y^+ > 100$ is dictated only by the local value of τ_η with magni-

tudes equal to those of homogeneous isotropic turbulence (equal stretching per unit dissipation). For $y^+ < 100$, however, the strain-rate becomes less efficient than in isotropic turbulence in stretching fluid elements and vorticity, where alignments between Cauchy-Green and strain-rate eigenvalues become less favorable for sustained stretching. In this viscous sublayer, the alignment and stretching statistics betray the characteristics of two-dimensional unsteady shear flow, which is particularly poor at producing exponential stretching and deformation. In the buffer layer, the alignments are still less efficient for stretching than isotropic turbulence, though the flow topology is much more complex than in the viscous sublayer.

The probability density functions of instantaneous Lyapunov exponents, strain-rate eigenvalues, and alignments between Cauchy-Green and strain-rate eigenvalues all mimic those of isotropic turbulence when conditioned on $y^+ > 100$ and scaled according to the dissipation rate averaged conditionally on wall-normal location. Together, these provide strong support for the ability of the local isotropy hypothesis to describe quantities important in fluid element deformation and vorticity stretching in this region. The observed success of local isotropy is notable, since the large scale fluctuations in the channel are highly anisotropic and the scale separation is relatively moderate ($Re_\lambda \sim 80$) in the core. The contributions of strain-rate and alignment statistics were explored separately in considering the departure from locally isotropic behavior near the wall.

The Cramér functions for finite-time Lyapunov exponents, describing cumulative

deformation along Lagrangian paths, reflect the less efficient stretching near the wall when compared with those of isotropic turbulence. Per unit dissipation, the channel flow at $Re_\tau = 1000$ provides about 50% of the stretching compared to isotropic turbulence, while ratios between the Lyapunov exponents remain about the same as isotropic turbulence. This occurs because the maximum local stretching occurs in the buffer layer, where alignments between Cauchy-Green and strain-rate eigenvectors are not as propitious. The generation of large fluctuations in FTLEs by wall-normal movement of trajectories is reflected in increased Cramér function width, skewness, and excess kurtosis values compared to isotropic turbulence. An exception to this observation is γ_2 which actually tends to fluctuate less, perhaps due to its faster drop-off near the wall as the flow becomes more two-dimensional.

While local isotropy is successful in describing the cumulative deformation behavior above $y^+ = 100$, and the viscous sublayer tends toward the behavior of unsteady two-dimensional shear flow, the intermediate behavior of the buffer layer is less straightforward. For instance, approaching the wall in the buffer layer, the mean vorticity stretching drops off sooner than the fluid element deformation. Description of this region is difficult because the influential anisotropic coherent structures are also responsible for dissipation and stretching.

Chapter 6

An Improved Stochastic Model for Lagrangian Velocity Gradients

Having considered the kinematics of stretching and rotation as dictated by the velocity gradient in the previous three chapters, the dynamical equations determining the velocity gradient are now considered. In particular, modeling techniques for simulating velocity gradients at a tiny fraction of the cost of DNS are sought. In this chapter, a new closure for low-dimensional stochastic modeling of velocity gradients is introduced and compared with previous approaches. Later chapters will build on this chapter to explore intermittency, large-eddy simulations, and inertial particle effects.

Previous stochastic models for the Lagrangian velocity gradient evolution have been reviewed in §2.2. In that section, it was pointed out that the RFD closure provided a robust model, but the underlying assumptions were perhaps too strong,

i.e., using isotropic tensors for the upstream closure before performing the short-time deformation map. Further, we saw from the GF and EGF closures that Gaussian approximations can be constructed for the unclosed terms. In this chapter, we construct a model based on a new approach using the above insights. The approach is based on the idea that the Gaussian fields closure, while insufficient to prevent the singularity on its own, can provide a short-time deformation mapping procedure with a better initial condition than the isotropic tensors used by the RFD approach.

The new stochastic model is thus called the Recent Deformation of Gaussian Fields (RDGF) model. In the sense of this nomenclature, the term 'Gaussian fields' is used to refer to the Gaussian velocity field along with its associated (non-Gaussian) pressure field. For the pressure Hessian, the recent deformation mapping is applied to the pressure field derived from Gaussian velocity field.

The novel stochastic closure model based on a recent deformations of Gaussian fields is introduced and explained in §6.1. After a brief explanation in §6.2 of numerical methods for the stochastic ODEs and for the DNS data to which results are compared, an examination of results is given in §6.3. The results of the new model are compared alongside RFD and EGF results with DNS data, and afterward appropriate conclusions are drawn. The works shown in this chapter is published in Ref. 62.

6.1 Recent Deformation of Gaussian Fields Mapping Closure

This section introduces the RDGF closure for the pressure Hessian and viscous Laplacian terms in the Lagrangian stochastic evolution equation for the velocity gradient tensor.

6.1.1 Overview

As summarized before, a strong assumption underlying the RFD approximation was the assumption that the initial upstream condition of the conditional pressure Hessian (and viscous Laplacian) are isotropic tensors. Here we relax this strong assumption and instead assume that the upstream conditional pressure Hessian is that of an isotropic Gaussian velocity field. In this way, (2.41) is modified as follows

$$\left\langle \widetilde{P}_{ij} \middle| \mathbf{A} \right\rangle \approx \frac{1}{3} \left\langle \widetilde{P}_{kk} \middle| \mathbf{A} \right\rangle \delta_{ij} + \left\langle \widetilde{P}_{ij}^{(d)} \middle| \mathbf{A} \right\rangle_{\text{Gaussian}}, \tag{6.1}$$

where the latter term is evaluated using (2.49). Similarly for the viscous term, the conditional Hessian of the upstream velocity gradient is no longer assumed isotropic, and (2.46) is modified to include the anisotropic contributions from the Gaussian closure. The same mapping as in the RFD model is applied to convert the upstream initial conditions to the resulting closure. Figure 6.1 illustrates the overall procedure

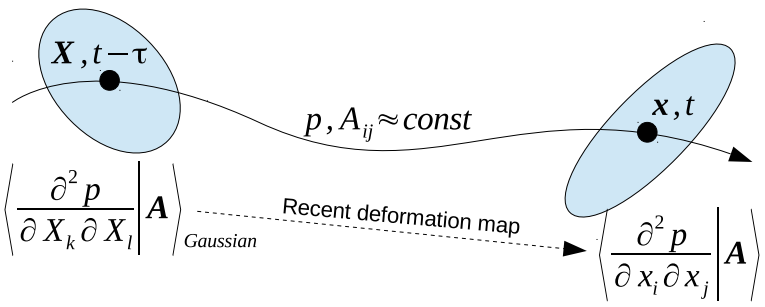

Figure 6.1: Schematic illustrating the main elements of the RDGF model for the conditional pressure Hessian. The viscous Laplacian model is constructed analogously.

for constructing the model for the pressure Hessian. A similar procedure is used for the viscous Laplacian.

The underlying phenomenology of the RDGF model is that approximate turbulence statistics can be developed efficiently by a mapping of Gaussian statistics. This motivation is similar to the spatial distortion applied to Gaussian evaluations of conditional means for scalar Laplacian terms used in the mapping closures,[213–215] as well as the multiscale turnover Lagrangian map (MTLM) procedure of Ref. 216 to generate non-Gaussian synthetic turbulence fields. It should be noted that, despite some similarity, many important and technical details differ between the present approach and these previous works.

The linear diffusion model of Ref. 144 forms the basis on which all three models considered in detail here: RFD, EGF, and RDGF. The linear diffusion model follows the same assumptions of the restricted Euler model (i.e., it ignores the deviatoric part of the pressure Hessian), but adds a linear relaxation term to model the viscous

damping of velocity gradients. The RFD model adds the additional effect of recent fluid deformation in biasing the statistics of the pressure Hessians and viscous Laplacian. On the other hand, the EGF model computes the deviatoric part of the pressure Hessian (and the linear viscous diffusion coefficient) by approximating the turbulent velocity field as a Gaussian velocity field, an approximation with well-known limitations. The RDGF model uses the Gaussian approximation but only as an initial condition for the recent fluid deformation map.

6.1.2 Model Details

The model for the unclosed terms along the Lagrangian path at point $\mathbf{x}$ (time t) involves applying the Gaussian fields approximation at the upstream point $\mathbf{X}$ (time $t-\tau$). For the deviatoric part of the pressure Hessian, using (2.49),

$$\begin{aligned}\left\langle \widetilde{P}_{ij}^{(d)} \middle| \mathbf{A} \right\rangle_{\text{Gaussian}} &= -\frac{2}{7}\left(S_{ik}S_{kj} - \frac{1}{3}S_{k\ell}S_{\ell k}\delta_{ij}\right) - \frac{2}{5}\left(\Omega_{ik}\Omega_{kj} - \frac{1}{3}\Omega_{k\ell}\Omega_{\ell k}\delta_{ij}\right) \\ &\quad +\gamma\left(S_{ik}\Omega_{kj} - \Omega_{ik}S_{kj}\right), \end{aligned} \tag{6.2}$$

where (2.50) provides the numerical values of the parameters for Gaussian fields. In Appendix G, an analytical evaluation of γ using Batchelor interpolation for the second-order structure function is presented.[217] The result, $\gamma = \frac{86}{1365} \approx 0.063$, does not deviate much from the previous numerical result.[147]

Similarly, the Gaussian fields approximation for the upstream Hessian of the ve-

locity gradient uses the results of Appendix H,

$$\left\langle \nu \frac{\partial^2 A_{ij}}{\partial X_p \partial X_q} \middle| \mathbf{A} \right\rangle_{\text{Gaussian}} = \delta \left[T_{ij}\delta_{pq} + T_{iq}\delta_{jp} + T_{ip}\delta_{jq} - \tfrac{2}{21}\left(S_{jq}\delta_{ip} + S_{jp}\delta_{iq} + S_{pq}\delta_{ij} \right) \right], \tag{6.3}$$

where

$$\delta = \nu \frac{7}{3} \frac{f^{(4)}(0)}{f''(0)}, \qquad T_{ij} = \frac{23}{105} A_{ij} + \frac{2}{105} A_{ji}, \qquad S_{ij} = \frac{1}{2}\left(A_{ij} + A_{ji} \right). \tag{6.4}$$

It can be easily shown that contraction with δ_{pq} recovers (2.51) and contraction with δ_{ij}, δ_{ip}, or δ_{iq} causes the term to vanish in accordance with incompressibility. Following Ref. 147, i.e. (2.52), the enstrophy balance is used to determine δ in Appendix I,

$$\delta = \frac{C_{kk}}{3} \frac{7}{6\sqrt{15}} \frac{\mathcal{S}}{\tau_\eta}, \tag{6.5}$$

where the typical value of $\mathcal{S} = -0.6$ can be used.

Then, the conditional pressure Hessian and velocity gradient Hessian are mapped from $\mathbf{X}$ to $\mathbf{x}$ along the trajectory. The deformation tensor used for the mapping, $D_{ij} = \frac{\partial x_i}{\partial X_j}$, is approximated by assuming that the velocity gradient is constant for the short time span τ, i.e. (2.39). Using (2.40) with the new upstream conditional

pressure Hessian in (6.1),

$$\langle P_{ij} |\, \mathbf{A} \rangle = \frac{1}{3} \left\langle \widetilde{P}_{\ell\ell} \middle|\, \mathbf{A} \right\rangle C_{ij}^{-1} + D_{mi}^{-1} \left\langle \widetilde{P}_{mn}^{(d)} \middle|\, \mathbf{A} \right\rangle_{\text{Gaussian}} D_{nj}^{-1}, \tag{6.6}$$

where (6.2) is substituted for the deviatoric part of the pressure Hesssian. The trace of this equation gives,

$$2Q = \langle P_{kk} |\, \mathbf{A} \rangle = D_{mk}^{-1} \left\langle \widetilde{P}_{mn}^{(d)} \middle|\, \mathbf{A} \right\rangle D_{nk}^{-1} + \frac{1}{3} \left\langle \widetilde{P}_{\ell\ell} \middle|\, \mathbf{A} \right\rangle C_{kk}^{-1}. \tag{6.7}$$

Solving (6.7) for $\left\langle \widetilde{P}_{kk} \middle|\, \mathbf{A} \right\rangle$, and substituting into (6.6), the resulting closure is,

$$\langle P_{ij} |\, \mathbf{A} \rangle = 2Q \frac{C_{ij}^{-1}}{C_{kk}^{-1}} + G_{ij} - \frac{C_{ij}^{-1}}{C_{kk}^{-1}} G_{\ell\ell}, \tag{6.8}$$

where

$$G_{ij} = D_{mi}^{-1} \left\langle \widetilde{P}_{mn}^{(d)} \middle|\, \mathbf{A} \right\rangle_{\text{Gaussian}} D_{nj}^{-1}, \tag{6.9}$$

using (6.2) with (2.50). Similarly for the viscous Laplacian, using (2.45) with the new upstream conditional viscous Hessian (6.3) leads to,

$$\left\langle \nu \nabla^2 A_{ij} \middle|\, \mathbf{A} \right\rangle = \delta \left(T_{ij} C_{kk}^{-1} + 2 T_{ik} B_{kj}^{-1} - \frac{4}{21} B_{ik}^{-1} S_{kj} - \frac{2}{21} B_{k\ell}^{-1} S_{k\ell} \delta_{ij} \right) \tag{6.10}$$

where $B_{ij}^{-1} = D_{ik}^{-1} D_{jk}^{-1}$ is the inverse of the right Cauchy-Green tensor and $\mathbf{T}$ and $\mathbf{S}$ are given in (6.4).

6.1.3 The Resulting Model

The resulting stochastic ODE model for the Lagrangian velocity gradient dynamics is

$$dA_{ij} = \left[-\left(A_{ik}A_{kj} - \frac{C_{ij}^{-1}}{C_{kk}^{-1}}\mathrm{tr}\left(\mathbf{A}^2\right)\right) - \left(G_{ij} - \frac{C_{ij}^{-1}}{C_{kk}^{-1}}\mathrm{tr}\left(\mathbf{G}\right)\right) + V_{ij} \right] dt + b_{ijk\ell}dW_{k\ell}, \tag{6.11}$$

where the contribution of the deviatoric part of the back-in-time pressure Hessian is,

$$\begin{aligned} G_{ij} = D_{mi}^{-1} \Bigg[& -\frac{2}{7}\left(S_{mk}S_{kn} - \frac{1}{3}S_{k\ell}S_{\ell k}\delta_{mn}\right) - \frac{2}{5}\left(\Omega_{mk}\Omega_{kn} - \frac{1}{3}\Omega_{k\ell}\Omega_{\ell k}\delta_{mn}\right) \\ & + \frac{86}{1365}\left(S_{mk}\Omega_{kn} - \Omega_{mk}S_{kn}\right) \Bigg] D_{nj}^{-1}, \end{aligned} \tag{6.12}$$

and the contribution of the viscous Laplacian is,

$$V_{ij} = \frac{7}{6\sqrt{15}}\frac{C_{kk}}{3}\frac{\mathcal{S}}{\tau_\eta}\left(T_{ij}C_{kk}^{-1} + 2T_{ik}B_{kj}^{-1} - \frac{4}{21}B_{ik}^{-1}S_{kj} - \frac{2}{21}B_{k\ell}^{-1}S_{k\ell}\delta_{ij}\right), \tag{6.13}$$

with $\mathcal{S} = -0.6$ and,

$$S_{ij} = \frac{1}{2}\left(A_{ij} + A_{ji}\right), \qquad \Omega_{ij} = \frac{1}{2}\left(A_{ij} - A_{ji}\right), \qquad T_{ij} = \frac{23}{105}A_{ij} + \frac{2}{105}A_{ji}. \tag{6.14}$$

The recent deformation is described by

$$D_{ij}^{-1} = \left[\exp\left(-\mathbf{A}\tau\right)\right]_{ij}, \qquad C_{ij}^{-1} = D_{ki}^{-1}D_{kj}^{-1}, \qquad B_{ij}^{-1} = D_{ik}^{-1}D_{jk}^{-1}, \tag{6.15}$$

and the diffusion coefficient tensor of the stochastic forcing term is

$$b_{ijk\ell} = \frac{1}{2}\sqrt{\frac{D_s}{5}}\left(\delta_{ik}\delta_{j\ell} + \delta_{i\ell}\delta_{jk} - \frac{2}{3}\delta_{ij}\delta_{k\ell}\right) + \frac{1}{2}\sqrt{\frac{D_a}{3}}\left(\delta_{ik}\delta_{j\ell} - \delta_{i\ell}\delta_{jk}\right) \tag{6.16}$$

Note that the present model does *not* use the coefficients estimated from DNS. Instead, the coefficients are derived from the Gaussian field statistics.

In some sense, this model can be seen as a generalization of both RFD and GF closures. To recover the RFD model, first the back-in-time deviatoric component of the pressure Hessian should be removed, $G_{ij} = 0$, i.e. $\alpha = \beta = \gamma = 0$. Then, including only the isotropic part of (6.3) gives $\nu\nabla^2 A_{ij} = \delta\frac{C_{kk}^{-1}}{3}A_{ij}$, and the coefficient should be set to $\delta = -\frac{1}{T}$, where T is the integral timescale. This roughly corresponds to the RFD model at $\frac{\tau_K}{T} = -\frac{7\mathcal{S}}{6\sqrt{15}} \approx 0.18$. To recover the GF model, the deformation tensor should be set to identity, $D_{ij} = \delta_{ij}$.

6.1.4 Parameters and Constraints

The model in Eqs. (6.11)-(6.16) now contains three parameters that have yet to be determined: D_s, D_a, and τ. As discussed in more detail in Appendix F, the stochastic forcing term, $dF_{ij} = b_{ijk\ell}dW_{k\ell}$, can be split into symmetric and anti-symmetric parts, each with its own amplitude. This can be thought of as separately forcing Eqs (2.36) and (2.37). The amplitudes of the symmetric and anti-symmetric stochastic forcing tensors, D_s and D_a, are two parameters that must be set to fully specify the model.

Additionally, the time interval of the mapping, τ, must be set. In keeping with the RFD phenomenology, it is expected that this should be $\tau \sim \mathcal{O}(\tau_\eta)$. The RFD model used $\tau = \tau_K$, where τ_K is an *input* Kolmogorov timescale, but *a posteriori* evaluation at $\frac{\tau_K}{T} = 0.1$ reveals that the actual Kolmogorov timescale produced by the model is $\tau_\eta \approx 2.0\tau_K$. Therefore, the effective time interval was $\tau \approx 0.5\tau_\eta$, based on the actual velocity gradient statistics produced by the model.

The three free parameters can be set by a choice of three constraints. First, without loss of generality, considering the evolution of the dimensionless velocity gradient tensor, $2\langle S_{ij}S_{ij}\rangle = \tau_\eta^{-2}$. This constraint effectively guarantees that the definition of δ in terms of τ_η is consistent. For the other two constraints, it is desirable to pick relationships for isotropic turbulence with analytical derivation, which can be considered *a priori* constraints. It is natural, then, to pick the two Betchov relations,[218] $\langle Q\rangle = \langle R\rangle = 0$. In light of the aforementioned dimensionless form of the equation, the former can be rephrased as $2\langle \Omega_{ij}\Omega_{ij}\rangle = \tau_\eta^{-2}$.

The determination of the three parameters using the three constraints can be posed as a three-dimensional root-finding problem. The appropriate values for the parameters were found empirically by numerical solutions of the model (see §6.2.1 below for details) using Broyden's method.[219] The procedure involved iteratively adjusting D_s, D_a, and τ and evaluating sufficiently converged statistics of $\langle S_{ij}S_{ij}\rangle$, $\langle \Omega_{ij}\Omega_{ij}\rangle$ and $\langle R\rangle$ from the numerical solutions of the model until the constraints were satisfied with the desired accuracy (four decimal places). The iterative method for

determining the correct model parameters converges toward,

$$D_s = 0.1014/\tau_\eta^3, \qquad D_a = 0.0505/\tau_\eta^3, \qquad \tau = 0.1302\tau_\eta. \tag{6.17}$$

The mapping time is considerably shorter than that of RFD closure because the additional deviatoric part of the pressure Hessian was added to the RFD model, which, as shown by the RFD approach, was by itself already strong enough to counter the singularity with $\tau \approx 0.5\tau_\eta$.

6.2 Numerical Methods

6.2.1 Stochastic Differential Equation Solver

The three models introduced in the previous sections (RFD, EGF and RDGF) can be advanced numerically as a system of stochastic ODEs. A second-order predictor-corrector method is used for time advancement. Time steps of size $dt/\tau_\eta = 0.04$, 0.02, and 0.01 are compared to verify discretization convergence. Ensembles of 2^{16} trajectories are advanced for $1000\tau_\eta$ to achieve convergence of desired statistical quantities (up to fourth-order moments). Without loss of generality, $\tau_\eta = 1$ was used for all runs. The Fortran simulations are performed in serial and run on a desktop machine, taking a few hours to complete.

Table 6.1: Numerical details for simulations used in this chapter.

N	Re_λ	ϵ	ν	η	τ_η	Δt	$k_{max}\eta$
256^3	160	0.112	1.2e-03	1.11e-02	0.104	5e-04	1.34
1024^3	430	0.093	1.85e-04	2.87e-03	0.045	2e-04	1.39

6.2.2 Direct Numerical Simulation Database

The Johns Hopkins Turbulence Databases (JHTDB) isotropic dataset[77,185] provided the DNS statistics used for most of the comparisons in this chapter, see §2.5. In a few cases, the comparisons are supplemented with another DNS at $Re_\lambda = 160$ using the same simulation code. Important parameters for the simulations are compared in Table 6.1. It is worth noting that the RFD model with $\frac{\tau_K}{T} = 0.1$ has been equated with $Re_\lambda = 150$.[146] Reaching $Re_\lambda = 430$ requires $\frac{\tau_K}{T} \approx 0.035$, which is outside the range for which the RFD model produces results with reasonable accuracy. Therefore, in this chapter, we use $\frac{\tau_K}{T} = 0.1$ for the RFD simulations, the value at which the RFD model seems to perform the best.

6.3 Results

6.3.1 Longitudinal and Transverse Components

Figure 6.2 illustrates the output of the RDGF mapping closure by plotting sample trajectories of longitudinal and transverse velocity components over an interval of $20\tau_\eta$. Because of the stochastic forcing, the paths appear rough, even at the scale of

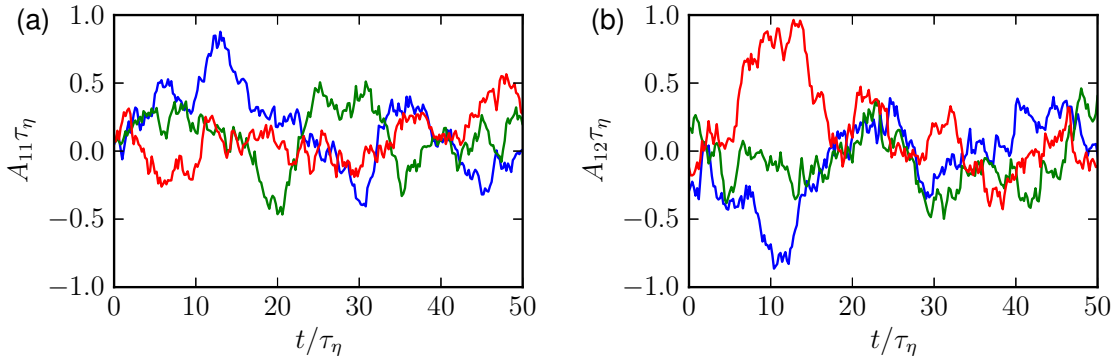

Figure 6.2: Sample trajectories of (a) longitudinal and (b) transverse velocity gradient components from the RDGF mapping closure. Three different trajectories are shown, represented by three different colours.

the Kolmogorov timescale. Nonetheless, such stochastic models can be useful when their statistical behavior provides a good model for Lagrangian velocity gradient statistics in isotropic turbulence.

The probability density functions for the longitudinal velocity derivative, A_{11}, and transverse velocity derivative, A_{12}, are shown in Figure 6.3. The RFD, EGF, and RDGF closures are compared with DNS results at the two different Reynolds numbers. The negative skewness expected for A_{11} and the symmetry expected for A_{12} are reflected by all three models. The RFD results appear much too close to Gaussian when compared with DNS results. The longitudinal velocity gradient distributions (top row of figure) from the EGF and RDGF models are better than that of RFD in terms of deviation from Gaussian behavior. For the transverse component, the RFD and EGF results appear similar, being between Gaussian and the DNS results. The RDGF mapping closure provides a much better match for the A_{12} PDF. The

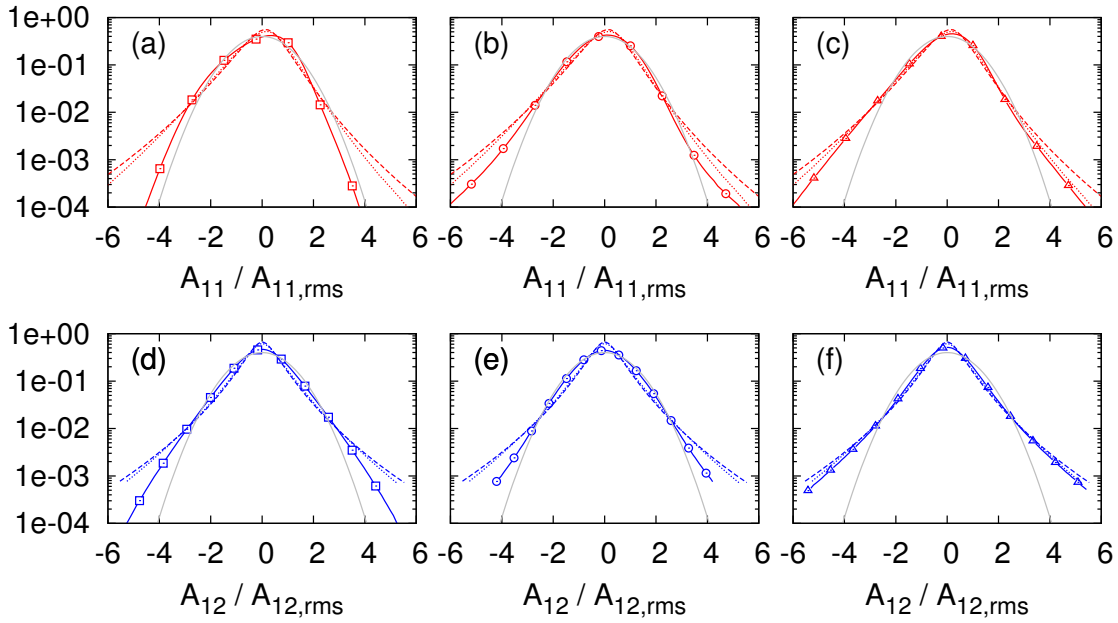

Figure 6.3: Single component PDFs for longitudinal (a-c) and transverse (d-f) velocity components. Three models are compared: (a,d) RFD, (b,e) EGF, (c,f) RDGF mapping closure. Solid gray line denotes Gaussian, dashed line shows DNS results at $Re_\lambda = 430$, dotted line shows DNS at $Re_\lambda = 160$, and solid line with markers shows the model result.

trends suggest that the RDGF model may provide an even better fit for DNS data at slightly lower Re_λ, but we refrain from any iterative matching with any particular precise value of Re_λ as we are mostly interested in overall trends.

As a compact comparison, Table 6.2 records the skewness and flatness factors of the above PDFs. All three models significantly under-predict the magnitude of the negative skewness for A_{11}, though the RFD and RDGF mapping closures are much closer than the EGF closure. The flatness factors for the longitudinal and transverse components help quantify the tendency of the model to reproduce the fattened tails of the PDFs in figure 6.3. For the longitudinal component, the EGF

Table 6.2: Skewness and kurtosis values for longitudinal and transverse velocity gradient components from each model compared with DNS.

	$\frac{\langle A_{11}^3\rangle}{\langle A_{11}^2\rangle^{3/2}}$	$\frac{\langle A_{12}^3\rangle}{\langle A_{12}^2\rangle^{3/2}}$	$\frac{\langle A_{11}^4\rangle}{\langle A_{11}^2\rangle^{2}}$	$\frac{\langle A_{12}^4\rangle}{\langle A_{12}^2\rangle^{2}}$
RFD	-0.44	0.0	3.2	4.3
EGF	-0.31	0.0	6.5	6.3
RDGF	-0.45	0.0	4.7	6.8
$Re_\lambda = 160$	-0.52	0.0	5.9	9.4
$Re_\lambda = 430$	-0.60	0.0	8.5	13.2

model appears to give the closest match, while the RDGF prediction is slightly closer for the transverse component. In each case, the flatness factors are too low, as was probably already evident in the above figures. It appears that the *trend* in the RFD and RDGF mapping closures that the longitudinal component has lower flatness than the transverse component better reflects the DNS trend. Indeed, as was discussed above, these results for RDGF could be seen as somewhat more appropriate for matching the DNS results at even lower Reynolds number.

6.3.2 Isotropic Relations

Table 6.3 compares the extent to which each of the models is able to reproduce important isotropy relations. Each ratio is equal to unity for isotropic turbulence. The first ratio, $\frac{\langle S_{ij}S_{ij}\rangle}{\langle \Omega_{ij}\Omega_{ij}\rangle}$, represents the ratio of strain-rate magnitude to vorticity magnitude produced by the model and is equal to unity since by construction (adjustment of forcing parameters), $\langle Q\rangle = 0$. The second ratio, $\frac{-\frac{1}{3}\langle S_{ij}S_{jk}S_{ki}\rangle}{\frac{1}{4}\langle \omega_i S_{ij}\omega_j\rangle}$, represents the balance between strain production and vorticity production and is equal to unity if $\langle R\rangle = 0$,

Table 6.3: Results for competing models in terms of reproducing known isotropic relations.

	$\frac{\langle S_{ij}S_{ij}\rangle}{\langle\Omega_{ij}\Omega_{ij}\rangle}$	$\frac{-\frac{1}{3}\langle S_{ij}S_{jk}S_{ki}\rangle}{\frac{1}{4}\langle\omega_i S_{ij}\omega_j\rangle}$	$\frac{15\langle A_{11}^2\rangle}{2\langle S_{ij}S_{ij}\rangle}$	$\frac{-\frac{35}{2}\langle A_{11}^3\rangle}{\langle\omega_i S_{ij}\omega_j\rangle}$
RFD	1.143	1.76	1.00	1.76
EGF	0.486	0.52	1.00	0.46
RDGF	1.000	1.00	1.00	1.00

also expected due to the adjustment of forcing parameters. The identities are all satisfied within numerical error showing that the numerical tuning of the three parameters (D_s,D_a, and τ) is very accurate. This represents a significant advantage of the RDGF mapping closure, seeing that the earlier RFD model slightly over-emphasizes strain-dominant and strain-production-dominant regions while the EGF model significantly over-emphasizes rotation-dominant and rotation-production-dominant regions. All three models satisfy the relation between dissipation and the longitudinal velocity derivative variance. It should be noted that the values in Table 6.3 from the RFD and EGF models could be improved if their $D_s = D_a$ constraint was removed and the two forcing coefficients tuned separately. This would allow one extra degree of freedom in tuning, which could be used to satisfy one, but not both, of the Betchov relations.

6.3.3 Enstrophy and Dissipation

The probability density distributions (PDFs) of enstrophy and dissipation in isotropic turbulence[33, 132, 133] provide another useful test for comparing Lagrangian

velocity gradient models. Figure 6.4 compares the dissipation (top) and enstrophy (bottom) PDFs of the RFD (left), EGF (middle), and RDGF (right) models with the DNS results at two Re_λ values. The RFD model appears to produce exponential tails (straight lines on the log-linear plot) rather than stretched exponential. The EGF model is much improved for the dissipation and enstrophy PDF, appearing somewhat closer to the characteristic stretched exponential shape. The RDGF model provides the best agreement with both dissipation and enstrophy distributions, displaying the stretched-exponential shape for both. It should be kept in mind that the EGF and RDGF do not have explicit Reynolds number dependence. Again, as a qualitative observation, the RDGF model gives results that may appear even more realistic for lower Re_λ.

6.3.4 Vorticity and Strain-Rate

One of the well-known features of velocity gradient statistics in turbulent flows is the non-trivial alignment of the vorticity vector with respect to the three eigenvectors of the strain-rate tensor.[111] The vorticity tends to align more closely with the strain-rate eigenvector associated with the intermediate eigenvalue. Meanwhile, the vorticity tends to be more perpendicular with respect to the strain-rate eigenvector of the smallest eigenvalue. The alignment distribution between the vorticity and the eigenvector of the largest strain-rate eigenvalue tends to be fairly uniform in comparison.

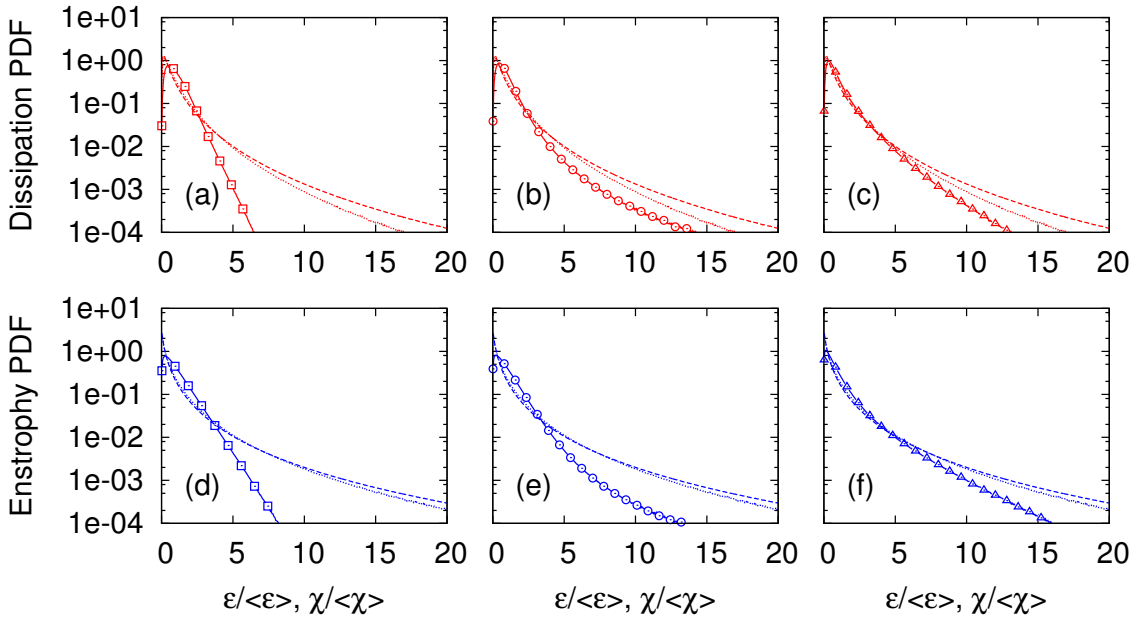

Figure 6.4: PDFs of dissipation (a-c) and enstrophy (d-f) normalized by their mean values for RFD (a,d), EGF (b,e), RDGF (c,f). Solid lines with symbols indicate model results, and DNS results are shown with dashed ($Re_\lambda = 430$) and dotted ($Re_\lambda = 160$) lines.

Figure 6.5a-c shows the PDFs for the cosines of the angles between vorticity and strain-rate eigenvectors. The DNS results at $Re_\lambda = 430$ are used for comparison here; these statistics show virtually no dependence on Re_λ. All three models mimic the well-known trend outlined above. The RFD model slightly underpredicts the anti-alignment of vorticity with the smallest strain-rate eigenvalue, while displaying a slight preference toward anti-alignment for the largest eigenvalue. The EGF consistently under-predicts the alignment biases seen in the DNS results. It appears that the RDGF model obtains the best agreement overall.

Lund and Rogers[197] introduced the measure $-1 \leq s^* \leq 1$ using the eigenvalues of

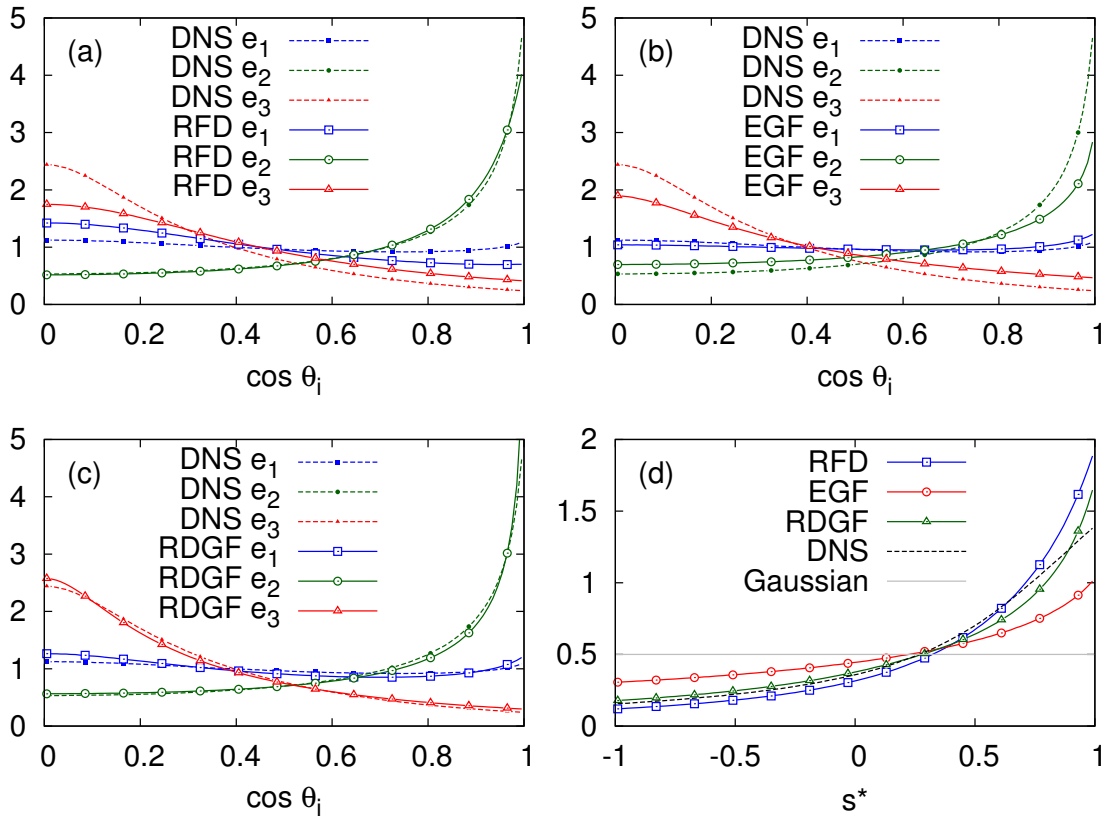

Figure 6.5: Probability distribution functions for the cosine of the angle between vorticity and the strain-rate eigenvectors: (a) RFD, (b) EGF, (c) RDGF. (d) Probability density functions for s^*, as defined in (6.18), for the three models compared with DNS results and Gaussian field statistics.

the strain-rate tensor,

$$s^* = -\frac{3\sqrt{6}\Lambda_1\Lambda_2\Lambda_3}{(\Lambda_1^2+\Lambda_2^2+\Lambda_3^2)^{3/2}}, \tag{6.18}$$

which compares the relative magnitudes of each of the three strain-rate eigenvalues taking into account that they must add up to zero. Figure 6.5(d) reports the PDFs for the three models considered here, shown in comparison to DNS results ($Re_\lambda = 430$). It is well-known that turbulent velocity gradients are biased toward $s^* > 0$, i.e. more

Table 6.4: Various mean values for strain-rate and vorticity measures.

	$\langle s^* \rangle$	$\langle \Lambda_1 \rangle \tau_\eta$	$\frac{\langle \Lambda_2 \rangle}{\langle \Lambda_1 \rangle}$	$\langle \cos(\theta_1) \rangle$	$\langle \cos(\theta_2) \rangle$	$\langle \cos(\theta_3) \rangle$
RFD	0.441	0.400	0.270	0.428	0.663	0.374
EGF	0.190	0.421	0.123	0.500	0.597	0.377
RDGF	0.347	0.392	0.224	0.473	0.656	0.317
DNS	0.371	0.366	0.231	0.484	0.659	0.311

distortion toward disk-like fluid elements.[69,197] All three models reflect this trend. The RFD model over-predicts the bias toward positive s^*, while the EGF model under-predicts it. The RDGF model appears to produce results in closest comparison with DNS.

Table 6.4 compares ensemble averages for some of these vorticity and strain-rate statistics, helping quantify the above discussion. Additionally available from this table is the ratio of average strain-rate eigenvalues, for which the RDGF models also provides good predictions.

6.3.5 Dynamics in the Q-R Plane

Another salient feature of turbulent velocity gradient statistics is the teardrop shaped contours of the joint-probability density function for the Q and R invariants.[141,220–222] Figure 6.6 compares such joint PDFs from the three models with DNS results ($Re_\lambda = 430$). Each model reproduces to some extent the features in the DNS results, most notably the teardrop shape.

The RFD results are too compact, lacking sufficient excursions far from the mean,

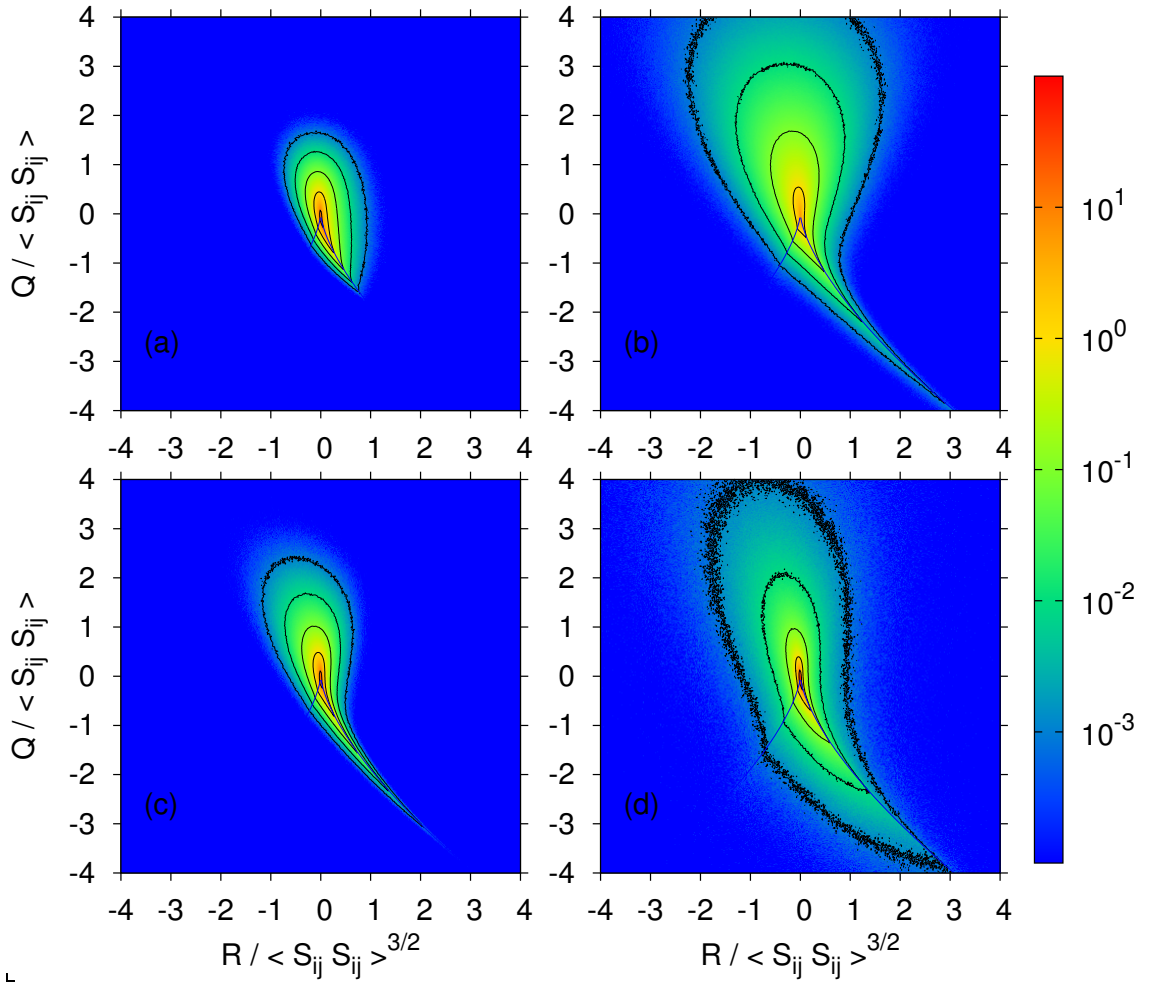

Figure 6.6: Logarithmically scaled joint-probability density function for the invariants Q and R as given by (a) RFD, (b) EGF, (c) RDGF, and (d) DNS.

as also seen previously for the single component PDFs in figure 6.3. One also observes a less prominent high-probability filament descending down the positive R branch of the Viellefosse line. The EGF model results are more accurate in their depiction of the high probability region along the Viellefosse line but a less realistic aspect of the EGF results is the exaggerated higher-probability in the positive Q region compared to the negative Q region. This feature is evidently responsible for the EGF model's

departure from $\langle Q \rangle = 0$ (the EGF also does not reproduce $\langle R \rangle = 0$). As mentioned previously, adapting the RDGF forcing scheme (tuning D_s and D_a separately) to the EGF could be used to satisfy one, but not both, of the Betchov relations.

The results from the RDGF mapping closure share some of the strengths and weaknesses of the RFD and EGF closures. For the RDGF, the low probability contours remain too compact, though less so than in the case of the RFD model. The shape of the high-probability regions closely mirrors those for the DNS. Additionally, there is some promising spread for the low-probability contours into the high positive Q regions. However, overall, the details of the low-probability contours (the tails of the joint distribution) still represents a challenge for all three models.

Neglecting the stochastic forcing for the moment, the dynamical equations for Q and R are,[141]

$$\frac{dQ}{dt} = -3R + A_{ij}P^{(d)}_{ji} - \nu A_{ij}\nabla^2 A_{ji}, \qquad \frac{dR}{dt} = \frac{2}{3}Q^2 + A_{ij}A_{jk}P^{(d)}_{ki} - \nu A_{ij}A_{jk}\nabla^2 A_{ki}. \tag{6.19}$$

The dynamics in probability space can be recovered thus from conditional averaging,

$$\left\langle \frac{dQ}{dt} \middle| Q, R \right\rangle = -3R + \left\langle A_{ij}P^{(d)}_{ji} \middle| Q, R \right\rangle - \nu \left\langle A_{ij}\nabla^2 A_{ji} \middle| Q, R \right\rangle, \tag{6.20}$$

$$\left\langle \frac{dR}{dt} \middle| Q, R \right\rangle = \frac{2}{3}Q^2 + \left\langle A_{ij}A_{jk}P^{(d)}_{ki} \middle| Q, R \right\rangle - \nu \left\langle A_{ij}A_{jk}\nabla^2 A_{ki} \middle| Q, R \right\rangle. \tag{6.21}$$

These equations represent average velocities in the QR probability space which, when

multiplied with the local probability density, represent fluxes in probability space. They are evaluated based on DNS as well as from the three models. In order to compare them under similar conditions, averages are evaluated as an *a priori* test, by evaluating the model results from an ensemble of DNS trajectories. In practice, we found that the most significant effect of this approach (as opposed to sample the statistics along model evaluations) was to increase the domain in QR space where the average velocities could be obtained.

Figure 6.7 shows the QR-space velocities attributed to the pressure Hessian term for the three models compared with DNS results ($Re_\lambda = 430$). The primary action of the RFD pressure Hessian is to oppose the restricted Euler motion along the Vieillefosse tail. In fact, the magnitude of the pressure Hessian opposing the restricted Euler singularity along the Vieillefosse tail is too strong in comparison with the DNS data. As previously noted,[146] the RFD pressure Hessian lacks the right-to-left motion seen in the DNS and the other two models. This elucidates the shortcoming of the upstream isotropic assumption for the pressure Hessian tensor. In fact, it is a significant contribution of the Gaussian form of the pressure Hessian that it adds this right-to-left tendency due to the deviatoric component of the tensor.

The EGF pressure Hessian tends to oppose the singularity with smaller magnitude than the DNS results indicate, while the RDGF opposes with slightly larger magnitude than DNS. While the right-to-left motion is captured by the EGF and RDGF closures, a few more subtle features of the DNS results are not. First, the relatively

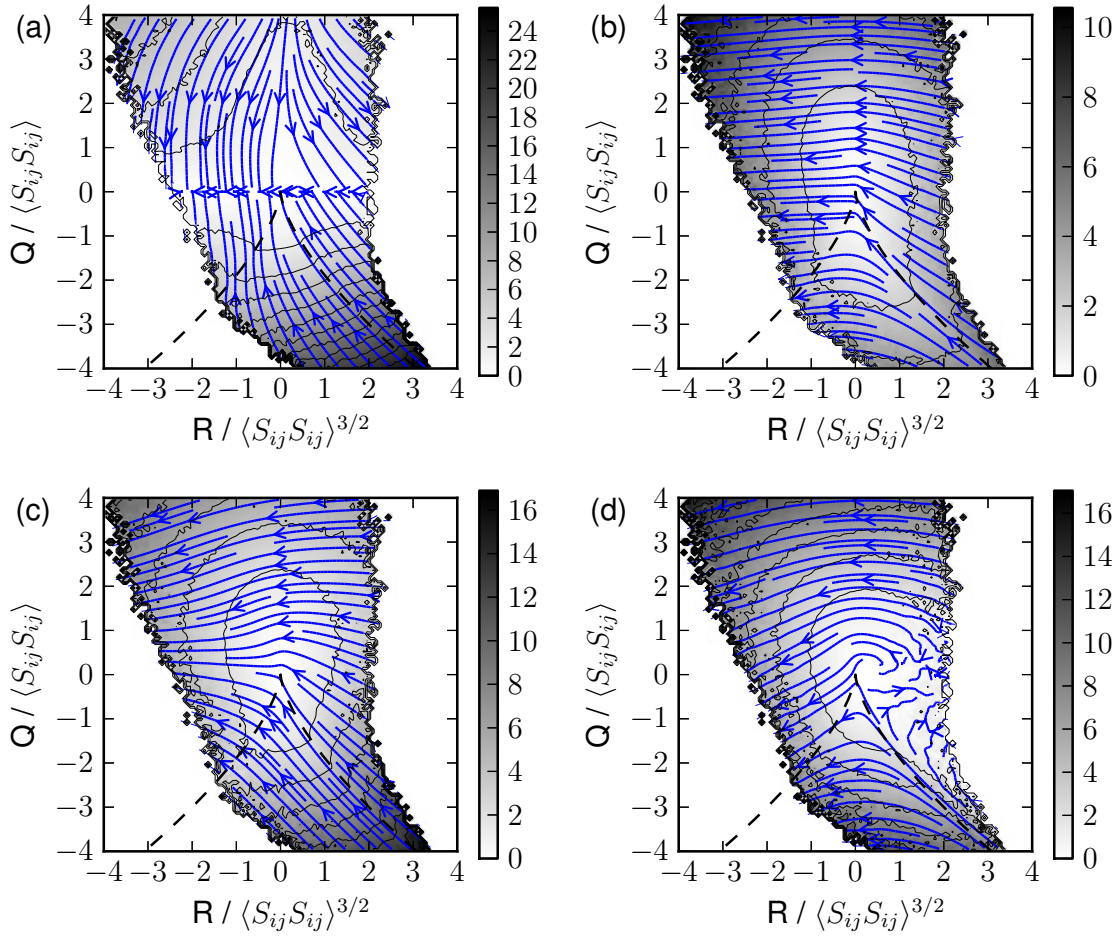

Figure 6.7: Thick lines with arrows represent "streamlines" in the QR-plane due to the deviatoric part of the pressure Hessian. Thin lines represent contours for the velocity magnitude in the QR-plane. Results are as given by (a) RFD, (b) EGF, (c) RDGF mapping closure, and (d) DNS.

ambient region of positive R near $Q = 0$ has an unphysically active right-to-left motion in the EGF and RDGF closures. Secondly, the DNS results indicate opposition to restricted Euler along the left side of the Vieillefosse line, which is not replicated by the EGF or RDGF closures. Other subtle differences and similarities may be noted, but the above discussion summarizes the most important trends noticeable.

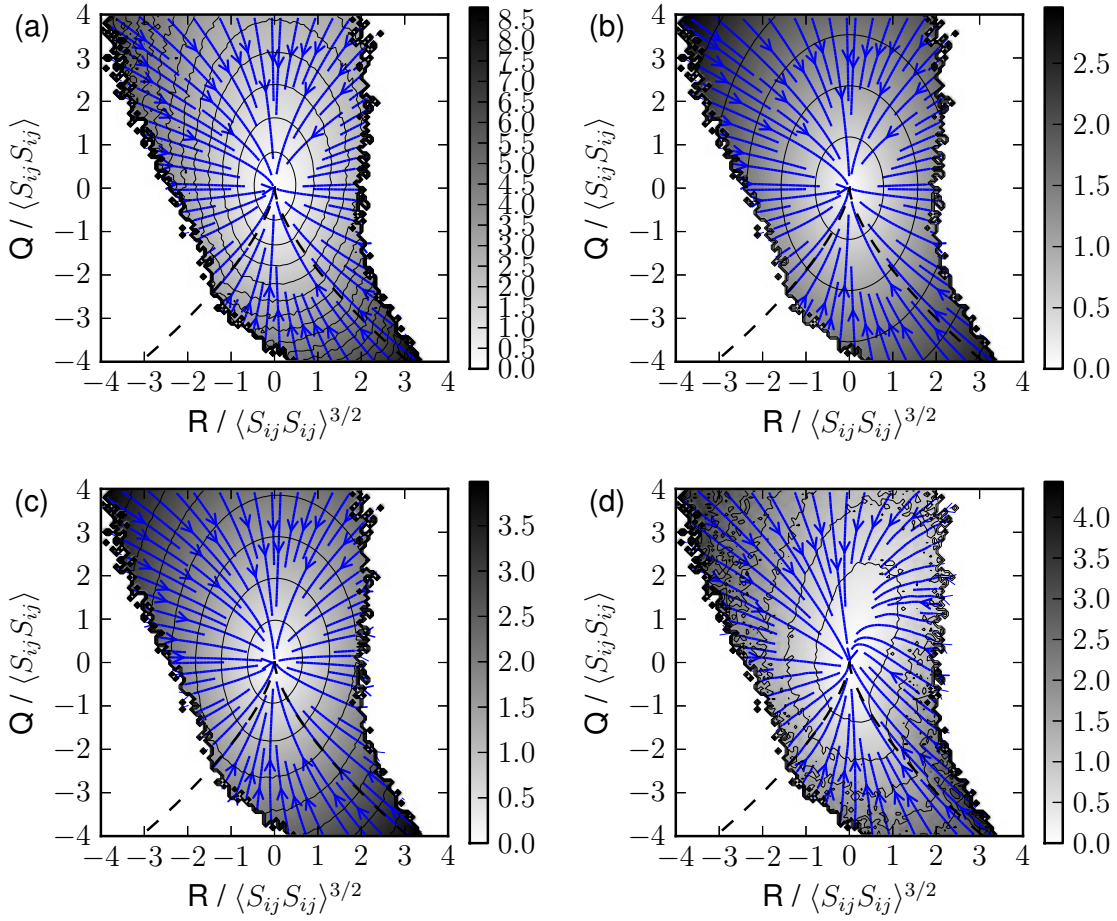

Figure 6.8: Thick lines with arrows represent streamlines in the QR-plane due to the viscous Laplacian. Thin lines represent contours for the velocity magnitude in the QR-plane, non-dimensionalized by powers of $\langle S_{ij}S_{ij}\rangle$. Results are as given by (a) RFD, (b) EGF, (c) RDGF, and (d) DNS.

The velocities in QR-space from the viscous Laplacian are shown in figure 6.8 for each of the models compared with DNS. All the models produce the same structure: the viscous Laplacian damps the velocity gradient, thus trajectories are pushed toward the origin in QR-space. Note that the DNS results show some slight deviation from pure damping structure. For example, near $Q = 0$ for $R > 0$, there is an upward

trend in the streamlines instead of proceeding straight toward the origin. Each of the models fail to capture this effect. Thus, updating the upstream conditions of the conditional viscous Hessian produces minimal changes in the behavior of the closure. It appears that the upstream isotropic assumption of RFD model for the viscous term produces relatively more accurate results than was the case for the pressure Hessian.

In terms of magnitude, the RFD model is too strong. The EGF model produces good agreement with DNS in magnitude for the $Q < 0$, $R > 0$ region near the Vieillefosse tail, while it is too weak in the $Q > 0$, $R < 0$ region. The RDG model has magnitudes in good agreement with DNS for $Q > 0$, $R < 0$ but is too strong in the $Q < 0$, $R > 0$ along the Viellefosse tail.

The above QR-space analysis shows advantages of the EGF and RDGF closures over the RFD closure. Of particular importance is that the RFD pressure Hessian does not have a strong tendency to decrease R. The structure of the deviatoric pressure Hessian from the Gaussian fields provides this effect. Furthermore, the RFD model's over-prediction of magnitude for both of the unclosed terms results in the overly compact joint-PDF contours seen in figure 6.6.

6.3.6 Correlation Coefficients

It is interesting to compare the *a priori* success of each model in terms of correlation coefficients for the deviatoric part of the pressure Hessian and the viscous Laplacian. For the deviatoric part of the pressure Hessian, the correlation coefficient

is defined as,

$$\rho_{\mathbf{P}^{(d)}} = \frac{\left\langle P_{ij}^{(d),\mathrm{DNS}} P_{ij}^{(d),\mathrm{model}} \right\rangle}{\sqrt{\left\langle P_{ij}^{(d),\mathrm{DNS}} P_{ij}^{(d),\mathrm{DNS}} \right\rangle \left\langle P_{ij}^{(d),\mathrm{model}} P_{ij}^{(d),\mathrm{model}} \right\rangle}}. \tag{6.22}$$

A similar correlation coefficient is also defined for the viscous Laplacian. These are computed using 8^{th}-order finite differencing from an ensemble of 10 million points in the DNS results.

Table 6.5 shows the resulting correlation coefficients. Included also is the original Gaussian Fields (GF) closure of Ref. 147, which did not provide a statistically stationary solution but rather succumbs to the finite-time singularity similar to the restricted Euler. Overall, the viscous Laplacian models are more successful than the pressure Hessian models. The RFD model has the lowest *a-priori* correlation coefficients for both closures. The difference between the GF and EGF model in Table 6.5 is minimal.

The RDGF model actually shows slightly lower correlation for its pressure Hessian model, indicating that the effect of the recent deformation on the Gaussian structure is perhaps not as helpful as one might have hoped. Perhaps the real advantage of the recent deformation is that the magnitude is increased without abandoning the analytical coefficients (i.e. $\alpha = -\frac{2}{7}$, $\beta = \frac{2}{5}$). The effect is that the singularity is avoided without recourse to DNS-tuned coefficients.

Table 6.5: Correlation coefficients for three models with DNS results at $Re_\lambda = 430$.

	$\rho_{\mathbf{P}^{(d)}}$	$\rho_{\nabla^2\mathbf{A}}$
RFD	0.23	0.41
GF	0.43	0.60
EGF	0.43	0.60
RDGF	0.37	0.61

6.3.7 Computational Cost

It is useful to mention that these three models are not equal in terms of computational cost. The above results were computed using a Fortran 90 code executed on a single processor. A minimal code involving only time advancement of the velocity gradient tensor without any statistical calculations was timed for the three models. It was found that, per time step, the RFD model requires about 1.5 times longer than the EGF model, while the RDGF model takes about 2.5 times longer. It is worth noting, however, that the RFD and RDGF models were found to run smoothly and accurately with a time step of about $dt = 0.04\tau_\eta$, while the EGF model required a time step of $dt = 0.01\tau_\eta$ to avoid singularity. Even with such a small time step, the stochastic system exhibited rare rogue trajectories that had an overwhelming effect on the flatness factors, preventing convergence in a reasonable amount of time (e.g. trajectories advanced for $1000\tau_\eta$). We note that Ref. 147 used an even smaller time step of $dt = 0.001\tau_\eta$. Therefore, the computational cost advantage of EGF model is not realized. The RFD model does have a computation cost per time step approximately 40% smaller than that of the RDGF model.

6.4 Conclusions

In this chapter, a new closure, the Recent Deformation of Gaussian Fields (RDGF) mapping closure, for the pressure Hessian and viscous Laplacian along Lagrangian trajectories in turbulent flow is introduced. The new closure benefits from the insights of both the Recent Fluid Deformation (RFD) and Gaussian Field (GF) closures. The GF closure calculations are applied for the initial upstream conditions of the conditional pressure Hessian and viscous Laplacian, before performing a recent fluid deformation mapping to complete the closure. The coefficients for Gaussian fields can be used and three remaining free parameters related to forcing and time-scale are constrained so that the model reproduces known exact statistical relations. The stochastic forcing for this model is also generalized from that used for the previous models so that the magnitude of the symmetric and anti-symmetric forcings can be applied independently.

A priori evaluation of the models in terms of correlation coefficients and QR-space velocities reveals the shortcomings of RFD closure: the magnitudes of the unclosed terms are significantly over-estimated, and the role of the pressure Hessian in decreasing the R invariant is absent. These shortcomings are much improved using the conditional pressure Hessian from Gaussian fields. On the other hand, the exponential non-linearity of the recent deformation tensor allows for more effective prevention of singularities. As a result, the RDGF model does not require DNS-tuned coefficients in order to prevent the singularity. In this way, the RDGF model has the

robustness and analytical closedness of RFD model while providing a more realistic structure of the pressure Hessian from the GF closure.

A comparison of various single-time statistics suggests that the RDGF model can provide excellent results in comparison to the two previous models. However, by comparison with DNS at $Re_\lambda = 430$, the quantitative results reveal remaining shortcomings such as lack of increasing long tails and intermittency. The RDGF results seem more consistent with lower Reynolds number DNS results. This highlights one of the major limitations of the current model, that it does not include a robust way of changing the Reynolds number whereas velocity gradient statistics are known to depend strongly on Reynolds number. The RFD model does include a mechanism for increasing the Reynolds number, but only in a very limited range. In fact, RFD applied for $Re_\lambda \approx 430$ is already outside the range where it performs well. The RDGF mapping closure suffers these same drawbacks as RFD, even if the skewness factor is adjusted to reflect its (weak) dependence on Reynolds number.

In summary, this chapter builds a new closure framework for the conditional pressure Hessian and viscous Laplacian which leverages insights of previous approaches. It provides, therefore, a promising direction for future investigations of velocity gradient statistics in isotropic turbulence. At sufficiently high Reynolds numbers, where approximate isotropy of small scales is a safe assumption, models for isotropic turbulence can be applicable for a more general class of turbulent flows, for which some applications may find efficient access to velocity gradient statistics useful.

Chapter 7

High Reynolds Numbers and Intermittency in a Stochastic Model for Lagrangian Velocity Gradients

The refined similarity hypotheses[29,30] and the multifractal formalism[34,202,223] have provided a conceptual framework for understanding intermittency, and various types of phenomenological descriptions such as cascade models,[34,223,224] shell models,[225] and stochastic Markov processes for velocity increments across scales[226] have been constructed to be consistent with the energy cascade mechanism. Using adjustable parameters, these models can describe empirical intermittency exponents. However,

connecting these models and their intermittency exponents with the incompressible Navier-Stokes equations through a systematic derivation has proved to be an elusive goal. The only *ab initio* intermittency predictions are for Burgers turbulence[227] and for the Kraichnan model for passive scalars in a random (prescribed) velocity field.[228] In this chapter, we explore the intermittency of small-scale turbulence from the perspective of the velocity gradient tensor. To do this, the stochastic RDGF model from the previous chapter is expanded to include Re_λ effects.

Intermittency at the small scales of turbulence can be described using the scaling of velocity gradient moments with Reynolds number, such as $\langle|\partial u/\partial x|^m\rangle \sim (\langle\epsilon\rangle/\nu)^{m/2} Re_\lambda^{\alpha(m)}$, where $Re_\lambda = \sqrt{15}u'^2/\sqrt{\nu\langle\epsilon\rangle}$ is the Taylor-scale Reynolds number, u' the turbulent root-mean-square velocity (turbulent kinetic energy is $\frac{3}{2}u'^2$), ν the fluid's kinematic viscosity and $\langle\epsilon\rangle$ the flow's mean dissipation rate. Intermittency can be observed as deviations from $\alpha(m) = 0$. We remark that Re_λ represents a ratio of time scales between the slowest and fastest motions of the turbulent flow, $Re_\lambda \sim T/\tau_\eta$, where $T \sim u'^2/\langle\epsilon\rangle$ is the large-eddy turnover time and $\tau_\eta = \sqrt{\nu/\langle\epsilon\rangle}$ is the Kolmogorov time.[108]

The construction of the model is described in §7.1 starting with the stochastic model of chapter 6. After the details of the numerical implementation are briefly given in §7.2, the results are shown and discussed in §7.3. Finally, conclusions are drawn in §7.4. This chapter's material can also be found in Ref. 63.

7.1 Constructing a Stochastic Model for High Reynolds Numbers

7.1.1 Relevant Background

As mentioned previously, Lagrangian models for the velocity gradient tensor have only been successful for low-to-moderate Reynolds numbers ($Re_\lambda \leq 150$) and fail to reproduce realistic build-up of intermittency at arbitrarily high Re_λ.[150] A velocity gradient shell model[229] was a first attempt to extend this type of modeling to high Reynolds numbers, but it was based on a generic non-linear energy-preserving inter-shell coupling term without clear basis in the underlying dynamical equations. In this chapter, we propose a new low-dimensional model of turbulence that can describe intermittency growth at arbitrarily high Reynolds numbers.

7.1.2 Single-level Model

In this subsection, we review the modeling approach of chapter 6 which applies to relatively low Re_λ dynamics and provides the background for developing the new model for arbitrarily high Re_λ explained afterward. As detailed in §2.2.3, the dynamics of the velocity gradient tensor, (2.31), can be modeled by the stochastic differential

equation,[147] (2.35), which can be written in the form,

$$dA_{ij} = \left[-\left(A_{ik}A_{kj} - \tfrac{1}{3}A_{pq}A_{qp}\delta_{ij} \right) + h_{ij} \right] dt + dF_{ij}, \tag{7.1}$$

where $h_{ij} = -\langle P^{(d)}_{ij} | \mathbf{A} \rangle + \nu \langle \nabla^2 A_{ij} | \mathbf{A} \rangle$ includes all the unclosed terms and $dF_{ij} = b_{ijk\ell} dW_{k\ell}$ is the stochastic forcing built on the tensorial Wiener process with $\langle dW_{ij} \rangle = 0$ and $\langle dW_{ij} dW_{k\ell} \rangle = \delta_{ik}\delta_{j\ell}$. Modeling is required to specify h_{ij} and $b_{ijk\ell}$ in terms of known local quantities. We proceed in this chapter using the recent deformation of Gaussian fields (RDGF) approach from chapter 6 for representing the conditional averages of the pressure Hessian and viscous Laplacian needed for h_{ij} in (7.1).

We briefly summarize the main points of the closure here, while chapter 6 contains a more detailed discussion, for what we will call a 'single-level' model to be extended in this chapter. Recall that this model assumes that pressure p and $\mathbf{A}$ are slowly varying along Lagrangian fluid trajectories (i.e. constant for a short time τ) while their spatial gradients (Hessians and Laplacian) can be related to the deformation of the surrounding fluid, itself determined by the velocity gradient tensor. Gaussian field statistics are assumed for the initial ensemble on which the deformation during a short time τ is performed. With these assumptions, the conditional averages were evaluated in chapter 6 analytically, resulting in expressions which depend only on the deformation time scale τ and the dissipation time scale τ_η. Furthermore, prescribing the stochastic forcing dF_{ij} requires specification of two diffusion coefficients D_s and

D_a, for the symmetric and antisymmetric parts, respectively. Three basic constraints are enforced. The first is the consistency of the model, requiring $\langle |S|^2 \rangle = \tau_\eta^{-2}$ (where $|S|^2 = 2S_{ij}S_{ij}$). Also, homogeneous turbulence must satisfy $\langle Q \rangle = 0$ and $\langle R \rangle = 0$[218] (where $Q = -\frac{1}{2}\mathrm{tr}\mathbf{A}^2$ and $R = -\frac{1}{3}\mathrm{tr}\mathbf{A}^3$). These conditions uniquely determine the three parameters as follows: $\tau = 0.1302\tau_\eta$, $D_s = 0.1014\tau_\eta^{-3}$, $D_a = 0.0505\tau_\eta^{-3}$. The resulting mathematical model is stated succinctly in §6.1.3.

7.1.3 Coarse-Grained (Two-level) Model

To reach higher Re_λ, we interpret the results of the RDGF model described above as if it represented a filtered velocity gradient $\langle A \rangle_{\mathrm{filt}} = \widetilde{A}$ at a higher Reynolds number ($\langle .. \rangle_{\mathrm{filt}}$ and the *tilde* denote spatial filtering at some length-scale). The similarity between velocity gradients at a low Re_λ and filtered gradients at a larger Re_λ can be motivated by considering the gradient of the filtered Navier-Stokes equations,

$$\frac{\widetilde{d}}{dt}\widetilde{A}_{ij} = -(\widetilde{A}_{ik}\widetilde{A}_{kj} - \tfrac{1}{3}\widetilde{A}_{pq}\widetilde{A}_{qp}\delta_{ij}) - \widetilde{P}_{ij}^{(d)} + \nu\nabla^2\widetilde{A}_{ij} - \Sigma_{ij}, \tag{7.2}$$

where $\Sigma_{ij} = -\partial_j\partial_k\sigma_{ik}$ represents the effect of the sub-scale stress $\sigma_{ik} = \widetilde{u_i u_k} - \widetilde{u}_i\widetilde{u}_k$ typically modeled in large-eddy simulations and $\frac{\widetilde{d}}{dt}$ represents rate of change along trajectories following the coarse-grained velocity field. With a constant eddy viscosity model for the sub-scale stresses, the filtered gradient dynamics reduce to (2.35) with an enhanced viscosity. Similar modeling steps lead to the original RDGF model

but for coarse-grained velocity gradients and with a (larger) time scale $\beta\tau_\eta$, where $\beta = \sqrt{\langle|S|^2\rangle/\langle|\widetilde{S}|^2\rangle} \gg 1$ is a free parameter of the model specifying the extent of the coarse-graining. In other words, at the large scales one solves (6.11)-(6.17) but the model uses $\tau_1 = \beta\tau_\eta$ as the time scale instead of τ_η.

This model for $\widetilde{A}_{ij}$ provides crucial information for modeling the unfiltered velocity gradient tensor at high Re_λ, namely, the local rate at which energy is passed to smaller scales, $\Pi = -\sigma_{ij}\widetilde{S}_{ij} \approx \nu_e|\widetilde{S}|^2$, where ν_e is the effective eddy viscosity for the filtered dynamics (the value of ν_e can be specified in relation to β as shown below). The rate Π must be matched by the locally averaged rate at which energy is dissipated by the unfiltered velocity gradients within a region of scale comparable to the filter scale, i.e. $\nu_e|\widetilde{S}|^2 = \widetilde{\epsilon} = \nu\langle|S|^2\rangle_{\text{filt}}$. Matching these rates for each trajectory and assuming a constant ν_e leads to $\langle|S|^2\rangle_{\text{filt}} = (\nu_e/\nu)|\widetilde{S}|^2$. This step shows that the local variance of the inverse time-scale of the small-scale motions is slaved locally to that of the larger-scale motions. Thus, the characteristic time scale for the small scales should not be a single constant value, τ_η, but should be modulated by the characteristic time scales of the larger scale motions. Specifically, a fluctuating time scale $\tau_2(t) = \beta^{-1}|\widetilde{S}|^{-1}$ should be used for the full velocity gradient dynamics (2.35). Therefore, the time-dependent $\tau_2(t)$ replaces the constant τ_η in the RDGF closure for the unfiltered dynamics (7.1) for this two-time scale model. Here, β is a fixed ratio of time scales, which can be thought of as ensuring global balance of energy dissipation rates. Consistency with the model's weak coupling of small-scale $\mathbf{A}$ with coarse-grained $\widetilde{\mathbf{A}}$ requires $\beta \gg 1$,

i.e. a large separation between time scales.

7.1.4 Extension to Arbitrary Number of Levels

To reach even higher values of Re_λ, this second level ($n = 2$) can itself be thought of as a coarse-grained velocity gradient with the introduction of a third level evolving at even smaller and faster scales still to be described. In this way, the procedure outlined above can be iterated an arbitrary number of times to construct a multiple-time scale model with N levels and $Re_\lambda \approx Re_{\lambda,0}\beta^{N-1}$, where $Re_{\lambda,0}$ represents the effective Reynolds number of the single-level model ($Re_{\lambda,0} \approx 60$ will be seen to describe the data well). Therefore, the parameters β and $Re_{\lambda,0}$ determine the Reynolds number represented by a given number of levels by setting how quickly the effective Reynolds number grows with each additional level. The general multiple-time scale model thus consists of a series of 3×3 tensors $\mathbf{A}^{(n)}$ with time scales $\tau_n(t)$ for $n = 1, ..., N$. The first level evolves with the modeling and forcing using a constant time scale of $\tau_1 = \beta^{N-1}\tau_\eta \sim \beta^{-1}T$, where T is the time-scale of eddies at the integral scale of turbulence. All faster levels obtain their instantaneous, trajectory-specific time scale from the next coarser level using $\tau_n(t) = \beta^{-1}|S^{(n-1)}|^{-1}$.

7.1.5 Unsteady Dissipation Constraint

An additional drift term must be added to the equation to account for the fact that the single-level model was calibrated for an imposed constant time scale τ_η. Because each $n \geq 2$ level has a fluctuating time scale, $\tau_n(t)$, which takes the place of τ_η, we must ensure that the consistency constraint $\langle |S^{(n)}|^2 \rangle = \tau_n^{-2} = \beta^{-2} |S^{(n-1)}|^2$ holds. This can be accomplished by introducing a term $-\frac{1}{\tau_n}\frac{d\tau_n}{dt}\mathbf{A}$. To see this, the single-level RDGF system with constant-in-time τ_η can be written in the dimensionless form:

$$\tfrac{d}{dt^*} A^*_{ij} = f^*_{ij}(\mathbf{A}^*), \quad \text{where} \quad A^*_{ij} = A_{ij}\tau_\eta, \quad dt^* = dt/\tau_\eta, \tag{7.3}$$

and

$$f^*_{ij}(\mathbf{A}^*) = -(A^*_{ik}A^*_{kj} - \tfrac{1}{3}A^*_{k\ell}A^*_{\ell k}) + h^*_{ij}(\mathbf{A}^*) + dF^*_{ij}/dt^*. \tag{7.4}$$

This dimensionless system satisfies $\langle |S^*|^2 \rangle = 1$ by design. Replacing τ_η with $\tau_n(t)$, using the product rule to expand $\frac{d}{dt^*}(A^*_{ij}) = \tau_n \frac{d}{dt}(A_{ij}\tau_n) = \tau_n^2 \frac{d}{dt}A_{ij} + A_{ij}\tau_n \frac{d\tau_n}{dt}$, and substituting for the time derivatives, it is straightforward to obtain

$$f_{ij}(\mathbf{A}, \tau_n) = \tfrac{1}{\tau_n^2} f^*_{ij}(\mathbf{A}^*) - \tfrac{1}{\tau_n}\tfrac{d\tau_n}{dt} A_{ij}. \tag{7.5}$$

Thus the RDGF model follows an imposed arbitrary $\tau_n(t)$ signal by by introducing the unsteady constraint term $-\frac{1}{\tau_n}\frac{d\tau_n}{dt}\mathbf{A}$ in the equation.

7.1.6 Final Form of the Proposed Model

Finally, the proposed multiple-time scale Lagrangian RDGF model for the velocity gradient tensor reads

$$dA_{ij}^{(n)} = \Big[-\left(A_{ik}^{(n)} A_{kj}^{(n)} - \tfrac{1}{3} A_{pq}^{(n)} A_{qp}^{(n)} \delta_{ij} \right) - \tfrac{1}{\tau_n} \tfrac{d\tau_n}{dt} A_{ij}^{(n)} \tag{7.6}$$

$$+ h_{ij}^{(n)}(\mathbf{A}^{(n)}, \tau_n) \Big] \, dt + dF_{ij}^{(n)}(\tau_n), \quad n = 1, 2, 3..N,$$

where the local (fluctuating) time scale is $\tau_n(t) = \beta^{-1} |S^{(n-1)}|^{-1}$ for $n \geq 2$, but for the first level the time scale does not fluctuate: $\tau_1 = \beta^{N-1} \tau_\eta$ (e.g., $\tau_1 = \beta \tau_\eta$ for $N = 2$ as described in §7.1.3). The deformation map, $D_{ij} = [\exp(\mathbf{A}^{(n)} \tau)]_{ij}$, is used for each level, but the duration $\tau = 0.1302 \tau_n(t)$ depends on the local time scale. Each level is given by (6.11) with equations (6.12) and (6.13) giving the conditional average statistical closures. The gradient tensor at each level, $\mathbf{A}^{(n)}$, then has the input $\tau_n(t)$ replacing τ_η in the definition of the viscous coefficient $\delta = \frac{-7}{10\sqrt{15}} \frac{C_{kk}}{3} \tau_n^{-1}(t)$ as well as in the time lag $\tau = 0.1302 \tau_n(t)$ for the short-time deformation map. Finally, (6.16) is used with $D_s = 0.1014 \tau_n^{-3}(t)$, $D_a = 0.0505 \tau_n^{-3}(t)$. The result, which can be written in the form of (7.6), is a system of stochastic differential equations, representing the dynamics of coarse-grained ($1 \leq n < N$) and fully-resolved ($n = N$) velocity gradients, with only $9N$ components yet having its roots in the Navier-Stokes dynamics.

7.2 Numerical Implementation

For the numerical results shown in this chapter, the stochastic differential equations are advanced numerically for 10^4 Kolmogorov times using a second-order predictor-corrector method with adaptive time step set by a tolerance of 10^{-3} relative difference between first and second order schemes at each time step. Each level of each trajectory is advanced with its own unique time step size. Linear temporal interpolation and central differencing in time was used to compute $\tau_n(t)$ and $d\tau_n/dt$ information passed between levels, respectively.

7.3 Results

We begin by showing results from a three-level simulation with $\beta = 10$. Figure 7.1 shows sample time signals for $A_{11}^{(n)}$ for $n = 1, 2, 3$. This tensor component is the longitudinal gradient $\partial u/\partial x$ commonly studied experimentally. The coarse-grained velocity gradients vary on longer time scales and act to modulate the amplitude of the finer scale ones which change rapidly. This generates more extreme events in the faster levels.

Next, we evaluate statistical and scaling properties of the model, and integrate up to $N = 5$ levels. The PDFs for A_{11} and A_{12} are shown in figure 7.2 for number of levels from $N = 1$ to $N = 5$. The distributions become increasingly heavy-tailed as more levels are added. The PDF from DNS data[77] with $Re_\lambda = 430$ is also shown, with its

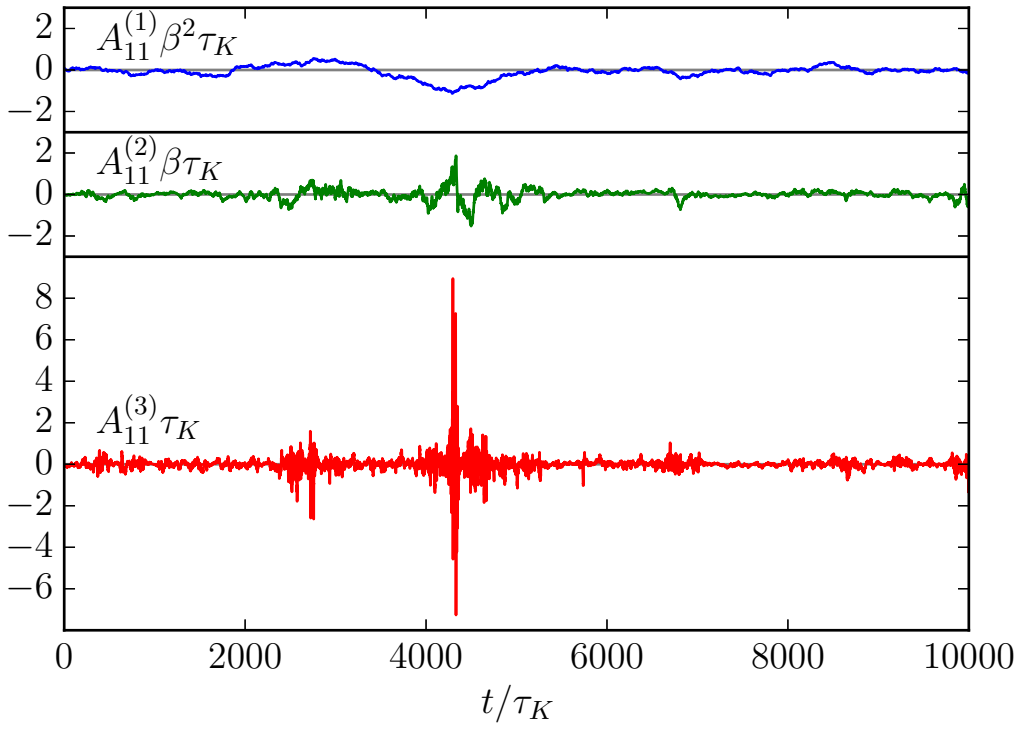

Figure 7.1: A sample A_{11} signal from three adjacent levels of the same trajectory in a three-level model. Top: coarsest level, $n = 1$; middle: next-coarsest level, $n = 2$; Bottom: fully resolved velocity gradient, $n = N = 3$.

level of intermittency falling between the results for $N = 1$ and $N = 2$. The skewness factor of the longitudinal component, defined as $S_k = \langle {A_{11}^{(N)}}^3 \rangle / \langle {A_{11}^{(N)}}^2 \rangle^{3/2}$, and flatness factors $F_1 = \langle {A_{11}^{(N)}}^4 \rangle / \rangle / \langle {A_{11}^{(N)}}^2 \rangle^2$ (and similarly for $A_{12}^{(N)}$) of the longitudinal and transverse components are evaluated from numerical integration of the model for various N. Results are shown and compared against DNS and experimental results in figure 7.3 using $Re_\lambda = 60\beta^{N-1}$ where $\beta = 10$ is chosen by matching the increase in flatness of the longitudinal components (A_{11}) between the one-level and two-level systems with the trends of DNS and experiments, as seen in figure 7.3 on the right. Thus, $Re_\lambda \approx 6 \times 10^5$ is reached with only 5 levels. Note that in figure 7.3 the

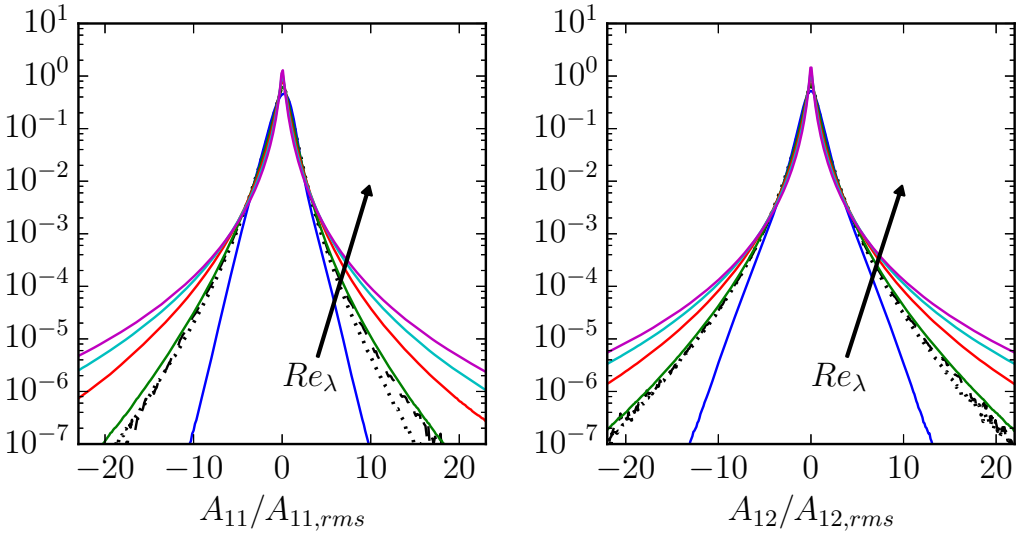

Figure 7.2: Probability density functions of A_{11} (left) and A_{12} (right) for $N = 1$, 2, 3, 4, and 5 (colored solid lines) compared with DNS data at $Re_\lambda = 430$ (dotted line). Also shown is a model with $N_{\text{eff}} = 1.85$ (dashed line).

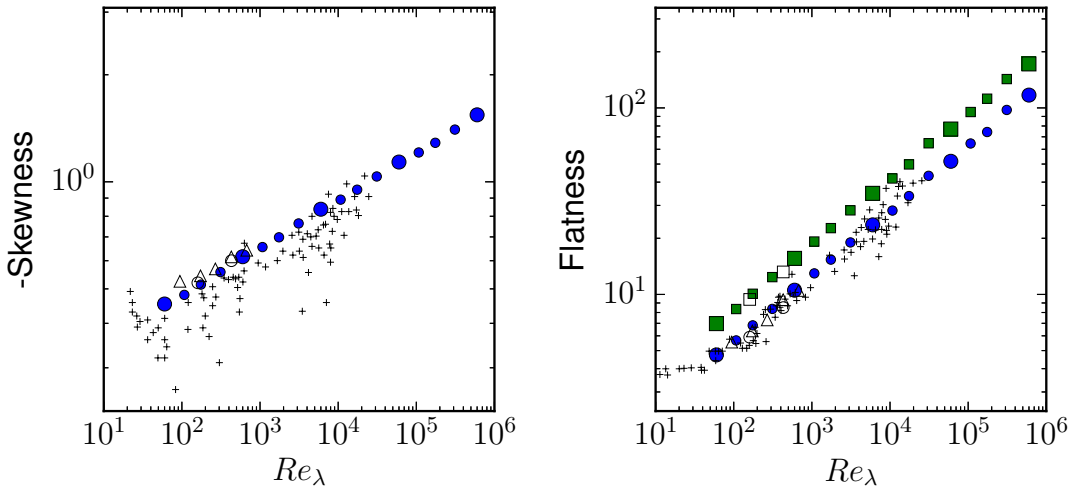

Figure 7.3: Skewness (left) and flatness (right) factor of velocity gradient components as a function of Re_λ compared with DNS data. Filled circles (A_{11} skewness and flatness) and squares (A_{12} flatness) represent the results of the multi-level model. DNS data from chapter 6 (□,○); 230 (△); and a compilation of experimental data from Ref. 1 (+). Smaller filled symbols represent the multi-level model with non-integer N_{eff}.

negative of the skewness is shown, proving that the model predicts negative skewness consistent with the energy cascade. Values near $S_k \approx -0.5$ are obtained for moderate $Re_\lambda \sim 10^2$ and rising in magnitude at higher Re_λ.

To use the model for any desired value of Re_λ in-between those given by integer N, one may obtain an effective (non-integer) number of levels $N_{\text{eff}} = 1 + \log_\beta(Re_\lambda/60)$. Then, using $\lceil N_{\text{eff}} \rceil$ levels ($\lceil .. \rceil$ is the ceiling function), one can effectively shrink the time-scale ratio between the first and second levels. This is accomplished by writing the dissipation at the second level as a mixture with fraction γ from the fluctuations of the first level, while a fraction $1-\gamma$ is contributed by a non-fluctuating dissipation rate (Figure 7.4). This leads to a dissipation timescale, $\tau_2(t)$, depending on γ as:

$$\tau_2(t) = \left[\gamma\beta^2|S^{(1)}|^2 + (1-\gamma)\beta^{-2(N-2)}\tau_\eta^{-2}\right]^{-1/2}. \tag{7.7}$$

Note that this mixing of time scales is only done between the first and second levels, while subsequent levels proceed as normal with $\tau_n(t) = \beta^{-1}|S^{(n-1)}|^{-1}$ for $n = 3, ..., N$. To relate the mixture fraction $0 < \gamma \leq 1$ to N_{eff}, we have found the following scaling to work well: $\gamma = [N_{\text{eff}} - (N-1)]^{2/3}$. This is simply an empirical relation from running the model with many different values of γ and adjusting until the plotted results in figure 7.3 line up on a straight line. This relation does not impact the predicted scaling of the model, but only allows the model to extend its predicted scaling to any arbitrary Reynolds number. Furthermore, the appropriateness of this correspondence

between Reynolds number and levels in the multiple-time scale description is verified by running the model for a desired $Re_\lambda = 430$ to compare with DNS. For this case we find $N_{\text{eff}} = 1 + \log_{10}(430/60) = 1.85$ and thus must choose $N = \lceil N_{\text{eff}} \rceil = 2$ levels and $\gamma = 0.85^{2/3} = 0.90$. The dashed line PDF in figure 7.2 shows excellent agreement with the DNS data at that Reynolds number.

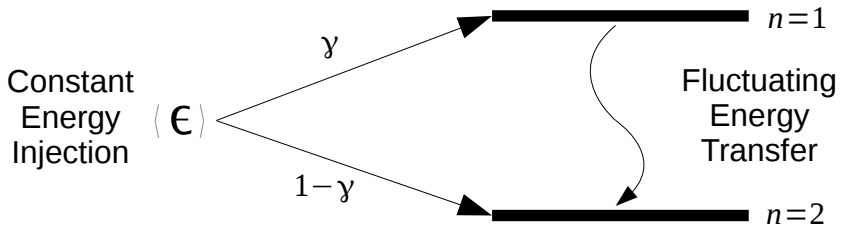

Figure 7.4: Schematic showing the phenomenological construction of the dissipation mixing leading to the equation (7.7). The dissipation rate at the second level used for defining $\tau_2(t)$ is mixed between a fraction γ of the total energy dissipation rate transferred from the first level (and fluctuating in time on each individual trajectory) and a fraction $1-\gamma$ of the total energy dissipation rate from 'direct' injection (constant in time and over all trajectories) which lowers the effective intermittency.

The anomalous scaling (i.e., intermittency) properties of the model results can be explored via the higher-order standardized moments, $\mu_m = \langle |A_{11}|^m \rangle / \langle A_{11}^2 \rangle^{m/2} \sim Re_\lambda^{\alpha(m)}$. These moments are evaluated from the model up to $m = 10$ yielding log-log plots with excellent scaling, as those shown in figure 7.3(b) (that corresponds to $m = 4$). The slopes can be measured, leading to $\alpha(m)$ shown in figure 7.5 as filled circles. Results clearly deviate from the non-intermittent case $\alpha(m) = 0$. In order to compare with earlier cascade models, $\alpha(m)$ can be related to existing velocity increment scaling exponents, ζ_p, using Nelkin's transformation,[34,170] i.e. $\alpha(m) = 2p(m) - 3m$, where $p(m)$ is the unique solution to $\zeta_p + p = 2m$. The measured $\alpha(m)$ up to $m = 10$

corresponds to about $p \approx 16$. For $\beta = 10$, the multiple-time scale RDGF model gives similar scaling exponents as those of the She-Leveque model,[224] the p-model,[223] and the lognormal model with $\mu = 0.2$ for smaller m. Choosing a lower ratio of time scales, $\beta = 6$, effectively increases the intermittency in the model away from the She-Leveque and p-models, but closer to the $\mu = 0.25$ lognormal curve for $m \leq 6$ and still within the variations in scaling exponents from the various DNS studies that are observed especially at the higher moments.

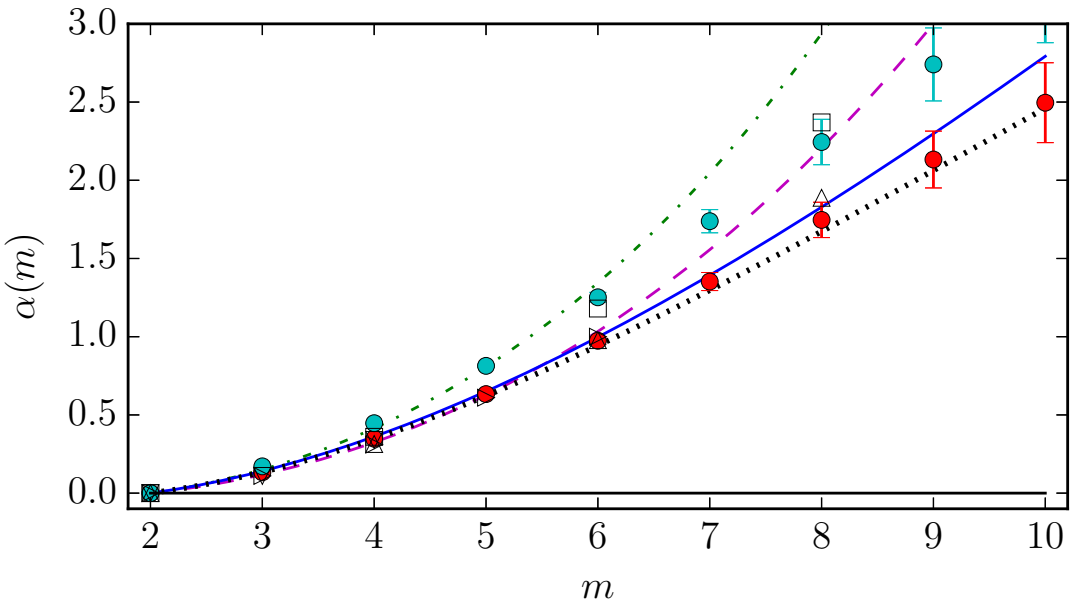

Figure 7.5: Scaling exponents $\alpha(m)$ from the multiple-time scale RDGF model with ratio $\beta = 10$ (filled red circles with error bars), compared with lognormal $\mu = 0.2$ (dashed magenta line) and $\mu = 0.25$ (dot-dashed green line), She-Leveque[224] (continuous blue line), p-model[223] with $p_1 = 0.7$ (black dotted line), and DNS data from Refs. 230 ($\triangledown$), 38 ($\triangle$), and 231 ($\square$), as well as experimental data from Ref. 232 ($\triangleright$). The RDGF model with $\beta = 6$ is shown as well (filled green circles with error bars), illustrating the effect of changing β on the predicted scaling exponents.

In extending the models to higher Re_λ by adding more levels, the statistical properties of local topology are maintained from the original (single-level) model. For

instance, figure 7.6 on the left shows the PDFs for alignment between the vorticity vector and the strain-rate eigenvectors ordered by decreasing eigenvalue, Λ_i. The vorticity's preferential alignment parallel to the intermediate strain-rate eigenvalue direction and orthogonal to the minimal eigenvalue direction is reproduced. On the right of figure 7.6, the PDF of $s^* = -3\sqrt{6}\Lambda_1\Lambda_2\Lambda_3/(\Lambda_1^2 + \Lambda_2^2 + \Lambda_3^2)^{3/2}$ (Ref. 197) is shown. The model produces these same PDFs for any arbitrary number of levels. Furthermore, figure 7.7 compares the joint PDF of Q and R for $N = 2$ with DNS at $Re_\lambda = 430$. The model predicts this joint PDF well. As the number of levels increases, the outer iso-contours expand as rare events become more likely, while the signature teardrop shape is maintained.

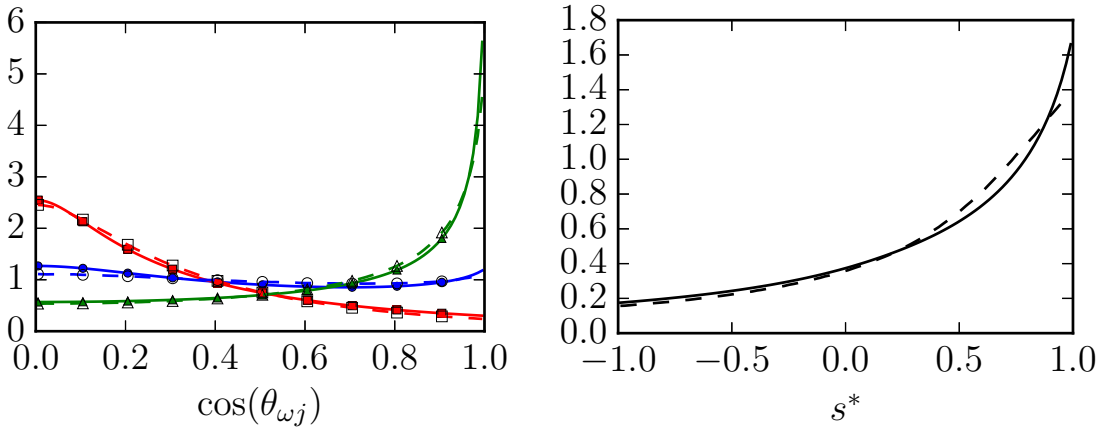

Figure 7.6: Probability density functions of alignment of vorticity vector with the j^{th} strain-rate eigenvector ordered by decreasing eigenvalues (left): Λ_1, circles; Λ_2, triangles; Λ_3, squares; and of s^* (right). Dashed lines indicate DNS results from Ref. 77 at $Re_\lambda = 430$ and solid lines indicate model results that are the same for any N.

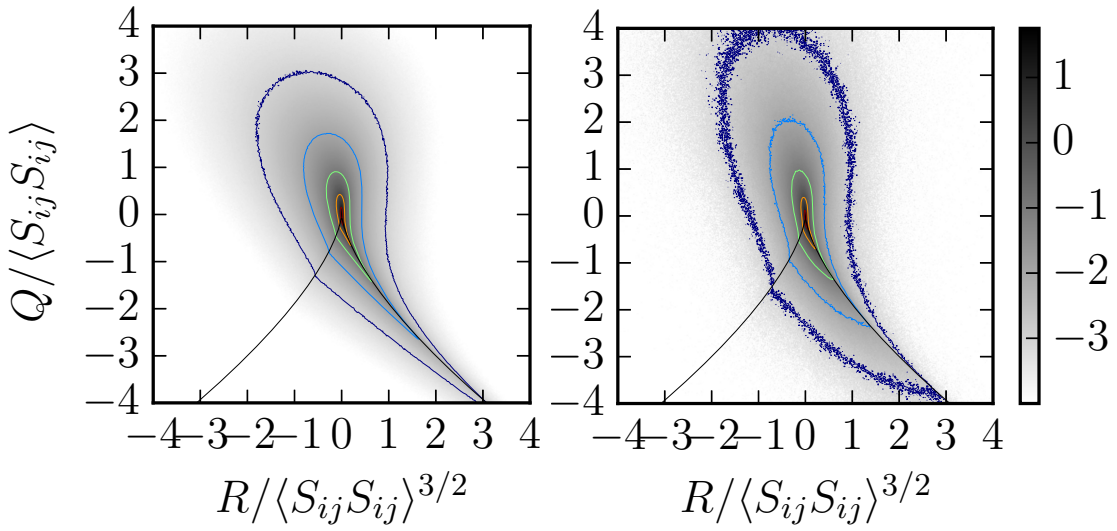

Figure 7.7: Joint PDFs in RQ invariant space from the multilevel RDGF stochastic model with $\beta = 10$ and $N_{\text{eff}} = 1.85$ (left) and from DNS of Ref. 77 at $Re_\lambda = 430$ (right). Logarithmically-spaced iso-contours shown are: 10^1, 10^0, 10^{-1}, 10^{-2}, 10^{-3}.

7.4 Conclusions

In summary, a low-dimensional multiple time scale model for Lagrangian time evolution of the velocity gradient tensor in fluid turbulence has been proposed. The stochastic model is based on the RDGF closure scheme from chapter 6, but includes a multiple time scale extension which introduces a way to adjust Re_λ. This model differs fundamentally from prior shell models and other empirically-motivated models of intermittency because the gradient self-stretching and rotation $\mathbf{A}^2$ term vital to the energy cascade and intermittency development is derived directly from Navier-Stokes. In the new approach, each level effectively contains a wide band of dynamical frequencies ($\beta = 10$ compared to $2^{2/3}$ in Ref. 229 and typical of other shell models). The exact representation of the nonlinear term captures local-in-scale interactions

naturally within each level, eliminating the need for strong, ad hoc coupling between levels. The model yields realistic predictions of intermittency dependence on Re_λ and describes the full tensorial structure of the velocity gradient, reflecting unique signatures and geometric alignments of velocity gradients in Navier-Stokes turbulence.

Chapter 8

Coupling Stochastic Models for Lagrangian Velocity Gradients with Large-eddy Simulations

The detailed dynamics of small-scale turbulence are not directly accessible in large-eddy simulations (LES), posing a modeling challenge, because many micro-physical processes such as deformation of aggregates, drops, bubbles and polymers dynamics depend strongly on the velocity gradient tensor which is dominated by the turbulence structure in the viscous range. In this chapter, we introduce a method for coupling existing stochastic models for the Lagrangian evolution of the velocity gradient tensor with coarse-grained fluid simulations to recover small-scale physics in flows with arbitrary large-scale geometrical complexity without resorting to direct numerical

simulations (DNS). In particular, we extend the stochastic model of chapters 6 and 7 to predict velocity gradients in inhomogeneous turbulence by coupling the model to an LES solution of the large-scale flow.

The proposed approach is implemented in LES of turbulent channel flow and detailed comparisons with DNS are carried out. An application to modeling the fate of deformable, small (sub-Kolmogorov) droplets at negligible Stokes number and low volume fraction with one-way coupling is carried out and results are again compared to DNS results. Results illustrate the ability of the proposed model to predict the influence of small scale turbulence on droplet micro-physics in the context of LES. This modeling approach opens up the possibility for simulating velocity gradient effects across the wide range of natural and man-made turbulent flows for which inhomogeneity is an important feature.

The structure of the chapter is as follows. The models used in this chapter are given in §8.1. The details of the various numerical simulations are provided in §8.2 and results are shown in §8.3. A summary of results and conclusions are drawn in §8.4. The work in this chapter is also presented in Ref. 64.

8.1 Modeling Framework

In this chapter, we consider the incompressible Navier-Stokes (INS) equations, (2.3). The INS equations form the basis for the modeling and analysis of veloc-

ity gradients discussed below. In terms of statistical descriptions of the small-scale structure of turbulence and gradients, the hypothesis of local isotropy for small-scale turbulence, which can be traced back to Ref. 37, is very prominent and has garnered considerable empirical support (see e.g.[1,61,233]). This hypothesis provides a rationale for modeling the dynamics of small-scale quantities such as velocity gradients in the canonical flow of isotropic turbulence.

This section provides modeling details for the chapter. The status of energy dissipation and velocity gradients in the context of LES is reviewed in §2.3, particularly emphasizing what small-scale information is and is not present in an LES representation of the flow. §8.1.1 develops the method for (one-way) coupling to LES. This coupling requires tracking the particle trajectories in LES, which is done using a modeling framework reviewed in §8.1.2 along with a theoretical derivation for one of the model coefficients. Finally, to facilitate a demonstration of micro-physics which are strongly influenced by the velocity gradient, a simple model for droplet deformation and relaxation dynamics is presented in §8.1.3.

8.1.1 Lagrangian Velocity Gradients

In this chapter, we use the Recent Deformation of Gaussian Fields (RDGF) model of chapters 6 and 7 in conjunction with LES. Because the test case described in §8.2 will be at a relatively low Reynolds number, the single-level model of chapter 6 will suffice. The dissipation rate, or equivalently the dissipation time scale $\tau_\eta = \sqrt{\nu/\langle\epsilon\rangle}$,

was assumed constant in time in the development of the original RDGF model for homogeneous isotropic turbulence (at low Re_λ). In an inhomogeneous flow, the RDGF model may obtain from the LES solution a local (time-dependent) dissipation rate, $\hat{\epsilon}(\mathbf{x}, t)$. In theory, we can think of $\hat{\epsilon}(\mathbf{x}, t)$ as the mean dissipation rate at a point in the flow given the entire space-time field of filtered velocity, $\hat{\epsilon}(\mathbf{x}, t) = \langle 2\nu S_{ij} S_{ij}(\mathbf{x}, t) | \widetilde{\mathbf{u}} \rangle$. That is, if we simulated an ensemble of particles in the filtered flow field all at a given point $\mathbf{x}$ and time t, their expected dissipation rate would be $\hat{\epsilon}$. It is quite natural to balance the dissipation rate from LES (Π) with this expected dissipation $\hat{\epsilon}$ for the small scales. In order to build in a cascade time delay[48,234] between production and dissipation of energy, we propose the following model,

$$\frac{d\hat{\epsilon}}{dt} = \frac{\Pi - \hat{\epsilon}}{\tau_\epsilon}, \tag{8.1}$$

with $\tau_\epsilon^{-1} = C_\epsilon \hat{\epsilon}^{1/3} \Delta^{-2/3}$ being the energy cascade time lag and $C_\epsilon = 1.5$ is seen to provide good results in §8.3. At small Reynolds numbers, one can use $\Pi + \nu |\widetilde{S}|^2$ instead of just Π in (8.1) to include the resolved dissipation rate from LES as well, though this correction will be negligible at high Reynolds numbers. For this chapter, given that the DNS cases used are at relatively low Reynolds numbers, we implement this correction.

When $\tau_\eta(t)$ fluctuates in time, as shown in §7.1.5 an added constraint term must be added to the model. This constraint is added for this chapter in the context of LES,

but only a single-level RDGF is considered, where the single RDGF level functions somewhat like the second level of a two-level RDGF in chapter 7. In this way, the LES-RDGF work done in this chapter resembles a two-level RDGF model where the first level is given by the LES solution and only the second level behaves according to the RDGF stochastic equations.

8.1.2 Lagrangian Trajectories

Lagrangian trajectories are computed by using the fluid velocity at the particle location,

$$\frac{dX_i}{dt} = u_i(X_i(t), t). \tag{8.2}$$

In LES, however, the velocity is not fully resolved, and advancing particles using the resolved component of velocity $\widetilde{u}_i$ leads to an under-prediction of dispersion. While other approaches have been developed,[164,165] in this chapter we consider a stochastic model for the unresolved velocity component, $u_i' = u_i - \widetilde{u}_i$, by Ref. 162, which is an adaptation to LES of the Langevin model of Ref. 235 for isotropic turbulence,

$$du_i' = \frac{\partial \tau_{ij}}{\partial x_j}dt - u_j'\frac{\partial \widetilde{u}_i}{\partial x_j}dt - \left(\frac{1}{2} + \frac{3}{4}C_0\right)\frac{\Pi}{k_r}u_i'dt + \sqrt{C_0\Pi}dW_i. \tag{8.3}$$

Here, dW_i is a vector Wiener process with $\langle dW_i \rangle = 0$ and $\langle dW_i dW_j \rangle = \delta_{ij}dt$. The first term is the sub-scale force acting equally and opposite to its role in (2.54). The second term is a "production" term for sub-grid kinetic energy resulting from the

sub-grid velocity acting on the resolved velocity gradient. The third and fourth terms represent the simplified Langevin model of Ref. 235 for decaying isotropic turbulence using $\Pi = (C_s\Delta)^2|\widetilde{S}|^3$ from the LES model as the dissipation rate. The third term also depends on the residual (or unresolved) kinetic energy k_r.[162] To specify k_r, we follow Ref. 162 and use the Yoshizawa model,[236]

$$k_r = 2C_y\Delta^2|\widetilde{S}|^2, \tag{8.4}$$

where C_y is the Yoshizawa constant, which results in

$$\frac{\Pi}{k_r} = C'|\widetilde{S}| \tag{8.5}$$

where $C' = C_s^2/(2C_y)$. The C_s coefficient can be computed from a dynamic procedure, but we set a constant C' (i.e. $C_y = C_s^2/(2C')$ with dynamic C_s but fixed C') from theoretical considerations as,

$$C' = \frac{1}{\mathcal{S}_s}\left(\frac{2}{3C_k}\right)^{3/2}, \tag{8.6}$$

where $\mathcal{S}_s = \langle|\widetilde{S}|^3\rangle/\langle|\widetilde{S}|^2\rangle^{3/2}$ is the skewness of the resolved strain-rate magnitude and C_k is the Kolmogorov constant for the energy spectrum of isotropic turbulence, $E(k) = C_k\langle\epsilon\rangle^{2/3}k^{-5/3}$. This result, with detailed derivation given in Appendix J, is computed similarly to Ref. 153 using a spectral cut-off filter, where Ref. 153 assumed

$\mathcal{S}_s = 1.0$. However, we find from the LES in this chapter that $\mathcal{S}_s \approx 1.3$, and so we use that value with (8.6) to obtain k_r. The commonly accepted value of the Kolmogorov constant $C_k = 1.6$ is used, resulting in $C' \approx 0.21$. Also, the value $C_0 = 2.1$ from Ref. 235 is used. The results of this model for dispersion in the channel flow LES are shown later, in §8.3.1.

8.1.3 Sub-Kolmogorov Droplet Model

As a sample application of the model to describing small-scale physics, we consider sub-Kolmogorov scale, deformable droplets sparsely distributed in a turbulent flow. Further, for our purposes here, the inertia of the droplets is neglected assuming small Stokes number. Also, only one-way coupling is considered. Ref. 183 introduced a simple ellipsoidal model which describes the droplet with a symmetric morphology tensor, M_{ij}. The eigenvectors of $\mathbf{M}$ indicate the direction of the three semi-axes and (the square root of) their associated eigenvalues indicate the semi-axis lengths. The evolution of the morphology tensor includes rotation by the vorticity, deformation by the strain-rate, and relaxation towards a spherical shape ($M_{ij} = \delta_{ij}$),

$$\frac{dM_{ij}}{dt} = \Omega_{ik}M_{kj} - M_{ik}\Omega_{kj} + f_2(\hat{\mu})\left(S_{ik}M_{kj} - M_{ik}S_{kj}\right) - \frac{f_1(\hat{\mu})}{\tau_d}\left(M_{ij} - \tfrac{3\mathrm{III}}{\mathrm{II}}\delta_{ij}\right). \quad (8.7)$$

where II and III are the second and third invariants of the morphology tensor, f_1 and f_2 are modeled functions of the viscosity ratio $\hat{\mu} = \mu_d/\mu_0$ between droplet and

surrounding fluid, and $\tau_d = \mu_0 R/\sigma$ is the relaxation time scale for a droplet with (undeformed) radius R and interfacial tension σ.

For this chapter, we note that (8.7) can be rewritten in terms of a deformation tensor $\mathcal{D}_{ij}$, which is related to the morphology tensor by $\mathbf{M} = \mathcal{D}\mathcal{D}^T$,

$$\frac{d\mathcal{D}_{ij}}{dt} = \Omega_{ik}\mathcal{D}_{kj} + f_2(\hat{\mu})S_{ik}\mathcal{D}_{kj} - \frac{f_1(\hat{\mu})}{2\tau_d}\left(\mathcal{D}_{ij} - \tfrac{3\mathrm{III}}{\mathrm{II}}\mathcal{D}_{ji}^{-1}\right). \tag{8.8}$$

It is straightforward to show the equivalence of (8.7) and (8.8) by substituting $M_{ij} = \mathcal{D}_{ik}\mathcal{D}_{jk}$. The same information about the semi-axes can be extracted from the deformation using a singular value decomposition, $\mathcal{D} = \mathbf{U}\mathbf{\Sigma}\mathbf{V}^T$, where $\mathbf{U}$ is a unitary matrix comprised of the singular vectors indicating the semi-axis directions and $\mathbf{\Sigma}$ is a diagonal matrix whose elements are the associate singular values $\sigma_1 \geq \sigma_2 \geq \sigma_3$, i.e., the length of the semi-axes. The total extent of deformation away from a spherical droplet is commonly measured using a deformation parameter, $D = (\sigma_1 - \sigma_3)/(\sigma_1 + \sigma_3)$.

The viscosity ratio functions are given by,[183]

$$f_1(\hat{\mu}) = \frac{40(\hat{\mu}+1)}{(2\hat{\mu}+3)(19\hat{\mu}+16)}, \qquad f_2(\hat{\mu}) = \frac{5}{2\hat{\mu}+3}. \tag{8.9}$$

Note that in the case of zero surface tension with unity viscosity ratio, $f_2 = 1$ and the fluid material deformation tensor evolution equation,[59] $\frac{d\mathcal{D}_{ij}}{dt} = A_{ik}\mathcal{D}_{kj}$, is recovered from (8.8), where $\mathcal{D}_{ij} = \partial X_i/\partial X_{0,j}$, is the sensitivity of final Lagrangian position $\mathbf{X}$ to initial condition $\mathbf{X}_0$. The model of Ref. 183, i.e. (8.7), has been successfully

implemented with one-way coupling in DNS for both isotropic[9] and Taylor-Couette flows.[11] Here, we implement the same model in LES, but use the formulation given by (8.8).

The magnitudes of $\mathbf{\Omega}$ and $\mathbf{S}$ being set by the dissipation time scale, the dynamics described by (8.8) are influenced by two dimensionless parameters: the viscosity ratio already introduced and the capillary number Ca,

$$Ca = \frac{\mu_0 R}{\sigma \tau_{\eta,\text{bulk}}}, \tag{8.10}$$

where $\tau_{\eta,\text{bulk}}$ is a single characteristic (or 'bulk') dissipation time scale of the flow. For $Ca = \mathcal{O}(1)$, the deforming force of the turbulent velocity gradients fluctuates around the same magnitude as the restorative force of surface tension. The surface tension dominates when $Ca \ll 1$ and the particles remain very close to spherical, while for $Ca \gg 1$ the droplet deformation begins to be unbounded and other physical mechanisms (e.g. droplet break-up) become important. The simple ellipsoidal model used here is less accurate for highly deformed droplets near break-up.[183] In this chapter, we do not use this model to perform a detailed study of droplet behavior in turbulence, but rather as a simple model to demonstrate the effectiveness of the velocity gradient model introduced above for evaluating the impact of turbulence on micro-physics within the flow.

8.2 Computational Setup

8.2.1 Problem Statement

Lagrangian particles in a turbulent channel flow at $Re_\tau = u_\tau h/\nu = 1000$ are considered as a test case for the proposed modeling technique for inhomogeneous turbulent flows. The friction velocity, u_τ, is prescribed by the imposed pressure drop, while $h = L_y/2$ is the channel half-height and ν is the molecular viscosity. The parameters for the particular turbulent channel flow considered here are given in Table 8.1. The channel has unit half-height and the bulk velocity is near unity, so the unit timescale is the time to traverse a half channel height traveling according to the mean flow rate. Under statistically stationary conditions, we consider an ensemble of particles released from random positions along the centerline of the channel ($y^+ = 1000$) at $t = 0$. The particles disperse from the centerline according to (8.2) until $t = L_t$ while the velocity and pressure fields evolve according to (2.3). The duration of the flow, $L_t = 26$, is approximately one flow-through time in the periodic domain. The notation $\langle\cdot\rangle_E$ is used to denote Eulerian averaging (in time and homogeneous space directions x and z) while $\langle\cdot\rangle_L$ is used to denote averaging over the ensemble of Lagrangian trajectories which sample the flow in a biased, time-dependent manner after being released from the centerline at $t = 0$. As the particles disperse away from the centerline of the channel, where there is minimum dissipation rate on average, the particles tend to experience more intense velocity gradients.

$L_x \times L_y \times L_z$	L_t	ν	u_τ	Re_τ
$8\pi \times 2 \times 3\pi$	26	$5e$-5	$5e$-2	$1e3$

Table 8.1: Parameters for the turbulent channel flow case considered in this chapter.

In addition to velocity gradient statistics, we consider the deformation of sub-Kolmogorov scale droplets according to the simple ellipsoidal model[183] described in §8.1.3. The droplets are initialized as spherical at $t = 0$ and are deformed by the velocity gradient tensor according to (8.8). The 'bulk' dissipation timescale used here to define Ca for the channel flow,[61]

$$\tau_{\eta,\text{bulk}} = \sqrt{\frac{\nu}{\langle\epsilon\rangle_{\text{space}}}} = \sqrt{\frac{\nu h}{u_\tau^2 U_{\text{bulk}}}}, \tag{8.11}$$

is constructed from the kinematic viscosity and the pumping power required the drive the flow at a volumetric rate of $U_{\text{bulk}}A_\perp$ through a cross-sectional area of $A_\perp$. This timescale gives a single, convenient value for the average velocity gradient magnitude across the channel, although as will be shown, velocity gradient magnitudes vary significantly with distance from the wall.

Table 8.2 summarizes the four cases considered in this chapter. A DNS dataset of turbulent channel flow from the Johns Hopkins Turbulence Databases (JHTDB),[190] with details given in §8.2.2, is used as the baseline for judging the performance of the model. The particle trajectories and velocity gradients were calculated from the DNS data using built-in database functions.[61,187,212] In order to provide insight into the

Case	Abbr.	$X_i(t)$	$\Pi(\mathbf{x}, t)$	$A_{ij}(t)$
baseline	DNS	DNS	(N/A)	DNS
a priori	fDNS-RDGF	DNS	fDNS/Smagorinsky	RDGF
a posteriori	LES-RDGF	LES+Fede	LES	RDGF
no model	LES-NM	LES+Fede	(N/A)	LES

Table 8.2: Methods used for calculating trajectories $\mathbf{X}$, sub-grid production Π, and velocity gradients $\mathbf{A}$ for the four cases considered in this chapter.

accuracy of the RDGF velocity gradient model isolated from LES SGS modeling accuracy concerns, an *a priori* case is constructed by filtering the DNS dataset (fDNS), which can be treated as a 'perfect' LES result. The next case consists of actually running an *a posteriori* LES with no input from the DNS, which can be argued to provide the most relevant results on the performance of the model in simulations. For this reason, the comparison of the *a posteriori* case with DNS results will be explored in the most detail. Finally, in order to highlight clearly the contribution provided by the velocity gradient modeling, it is sometimes useful to compare results with a 'no model' case in which the velocity gradients from the LES are used, i.e. neglecting entirely the SGS range of scales that are known to dominate the velocity gradient statistics. It should be kept in mind that the relative performance of LES velocity gradients (i.e., 'no model') in mimicking DNS results is sensitive to the resolution of the LES and the Reynolds number of the flow, i.e., given by the scaling arguments in §2.3.3 – even if the LES sub-grid model is 'perfect'. Furthermore, the accuracy LES-RDGF approach will depend on the accuracy of the LES closure (i.e. C_s and wall model), particularly in determining accurate local dissipation rates.

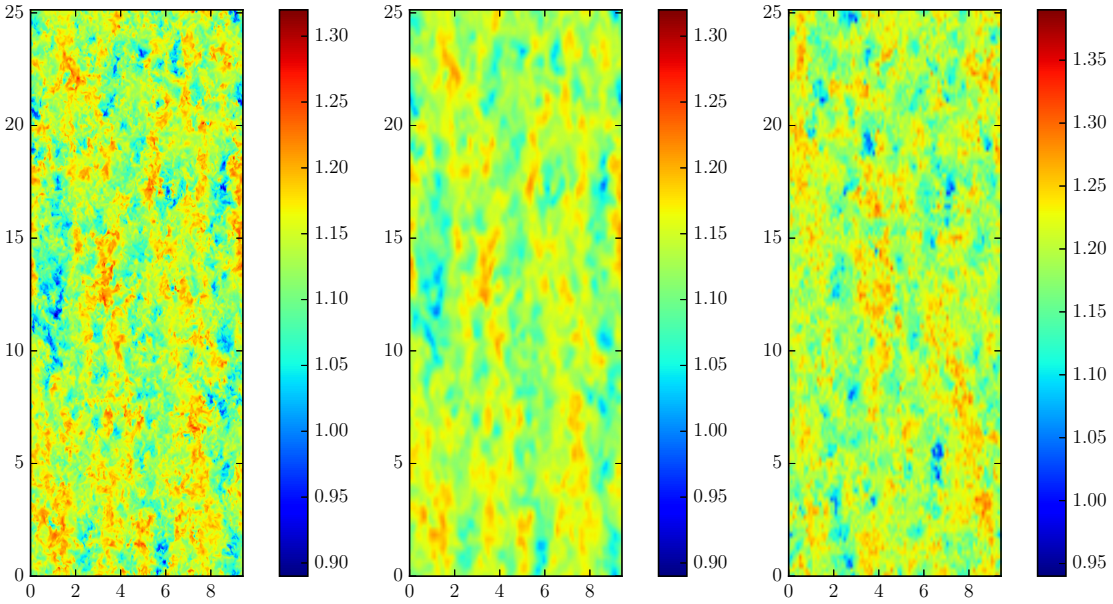

Figure 8.1: Snapshots of streamwise velocity on a plane parallel to the wall at the center of the channel from the DNS (left), fDNS (center), LES (right).

Figure 8.1 presents a visualization of the streamwise velocity along the centerline of the channel for the DNS, fDNS, and LES datasets. Note that the DNS and fDNS are from the same time step, so the corresponding regions of high and low velocity can be seen. The LES, of course, is from a completely different realization, so the correspondence is only qualitative with the other two. Also, as will be seen later in a more quantitative sense, the LES corresponds to a slightly smaller filter scale as compared to the fDNS.

8.2.2 Direct Numerical Simulation

The baseline DNS data is taken from the publicly-available JHTDB,[77] specifically, the channel flow dataset from[190] described in §2.5.2 and previously used in chapter 5. For this dataset, the numerical resolution in terms of effective Kolmogorov scale $\eta(y) = \sqrt{\nu/\langle\epsilon|y\rangle_E}$ remains near $k_{max}\eta \sim 1$ which, while typical for isotropic simulations, may not be sufficiently fine for capturing the most extreme velocity gradient events in the flow.[133]

The DNS particle trajectories for the baseline and *a priori* cases were tracked through the database using the built-in *getPosition* function. This function solves (8.2) using a second-order predictor-corrector method with sixth-order Lagrange interpolation for the velocity at the particle location (fourth- and eighth-order interpolation is also available). For more details on the parallel implementation of the particle tracking in the database, see Ref. 61, 212 and chapter 5. Similarly, the velocity gradients at the particle locations were computed from the database using the built-in *getVelocityGradient* function with fourth-order finite differencing and fourth-order Lagrange interpolation.

For the *a priori* test case, every sixteenth snapshot was downloaded and filtered using a non-isotropic box filter. The box filter was implemented by averaging over 32 grid points with trapezoidal rule integration in each direction and storing the value on a new grid point at the centroid of the averaged region. The filtered DNS (fDNS) dataset is computed for every sixteenth grid point, so that there is a factor

Case	$\frac{\Delta_x}{dx} = \frac{\Delta_z}{dz}$	$N_x \times N_y \times N_z$	N_t	dt_{sim}	dt_{DB}	U_{bulk}	$\tau_{\eta,\text{bulk}}$
DNS	1	$2048 \times 512 \times 1536$	4000	0.0013	0.0065	1.00	0.141
fDNS	32	$128 \times 32 \times 96$	250	(N/A)	0.104	1.00	(N/A)
LES	16	$128 \times 32 \times 96$	250	0.0104	0.104	1.04	0.139

Table 8.3: Parameters for the DNS, filtered DNS, and LES simulation databases used in this chapter.

of two overlap between neighboring points on the filtered grid. In this way, the grid for the fDNS is also non-uniform in the wall normal direction with $y^+ \approx 8$ for the first grid point. It should be noted that such a grid would not be optimal for an actual LES simulation since the boundary conditions would be difficult to set, but is unproblematic for present purposes. The numerical details of the fDNS dataset are given in Table 8.3.

The results for Eulerian-averaged velocity profile and Reynolds stress components for the DNS and fDNS datasets are shown in Figure 8.2. The mean velocity profile displays the expected log-law behavior $\langle u \rangle^+ \approx \frac{1}{\kappa} \ln(y^+) + B$ with $\kappa \approx 0.41$ and $B \approx 5.2$. The filtered dataset matches this mean velocity profile well except for the first two grid points in the buffer region, where spatial smoothing in the wall-normal direction causes the mismatch. The velocity variances, however, are significantly impacted by the filtering procedure and roughly half of the turbulent kinetic energy is unresolved.

In the first fDNS tests, trajectories computed from the fully resolved DNS dataset are used for the *a priori* test so as to avoid introducing errors from the sub-grid dispersion model of §8.1.2. Care is also taken in establishing dissipation rates from

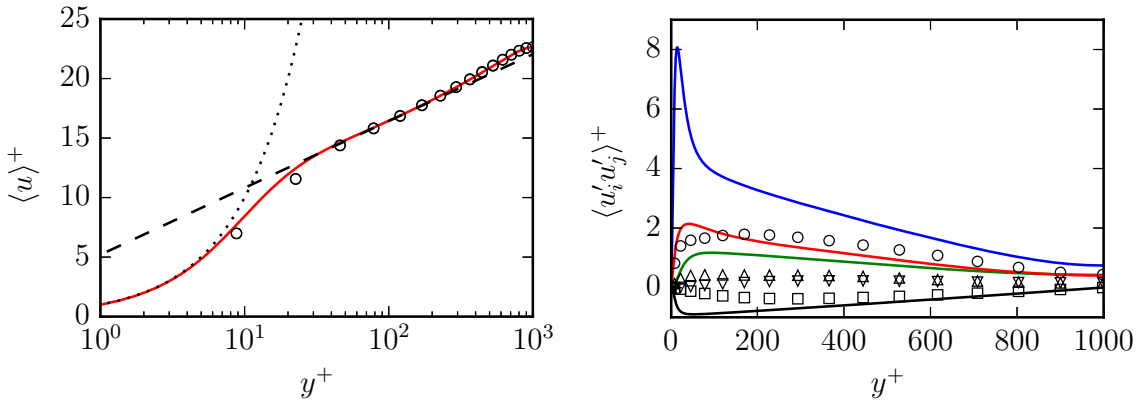

Figure 8.2: Mean velocity (left) and Reynolds stress tensor component (right) profiles for DNS (continuous lines) and filtered DNS (symbols). For the Reynolds stress components: $\langle u'^2 \rangle_E$ ($\circ$), $\langle v'^2 \rangle_E$ ($\triangledown$), $\langle w'^2 \rangle_E$ ($\triangle$), and $\langle u'v' \rangle_E$ ($\square$).

the fDNS so as to match DNS dissipation rates in the sense of the mean profile $\langle \epsilon | y \rangle_E$. The details of the fDNS dissipation rate are given in Appendix K. Using DNS information to carefully construct the fDNS data allows the *a priori* case to focus on the particular errors of the RDGF model without introducing other modeling errors involved in coarse-grained simulations. In this way, even though the filter for the fDNS is evidently somewhat severe compared with standard LES (as evidenced by Figure 8.2b), the careful treatment of the dissipation rates creates the necessary conditions for the RDGF model to flourish. The LES simulation described next then provides an a posteriori view on the model's effectiveness in the context of other modeling errors such as particle trajectory errors and LES SGS model errors.

8.2.3 Large-eddy Simulation

A wall-modeled large-eddy simulation of the same turbulent channel flow provides the main (*a posteriori*) test case for the velocity gradient model. As with the DNS simulation, the parameters of the LES are given in Table 8.1. The in-house LESGO code[1] was used to generate a dataset with a time sequence of snapshots mimicking those from the fDNS. This code is pseudo-spectral in the wall-parallel directions with 2/3 dealiasing with second-order finite-differencing on a staggered grid in the wall-normal direction. The wall-normal grid spacing is constrained to be uniform. With 32 grid points across the channel, $\Delta y^+ = 62.5$, and the first grid point for wall-parallel velocity components resides at $y^+ = 31.25$, at the inner edge of the log-law region. The equilibrium specification of Ref. 237 is used to set the boundary condition at the wall along with a no-penetration condition. Time is advanced with a second-order Adams-Bashforth method and the pressure Poisson equation is used to maintain a solenoidal velocity field to within machine precision. The scale-dependent Lagrangian dynamic Smagorinsky model[238] is used for the sub-grid stresses. This model is also used to compute $\Pi = (C_s\Delta)^2|\widetilde{S}|^3$ for input to (8.1) to determine the dissipation rate for the velocity gradient model. While the LES resides on a grid having the same dimensions as the fDNS, the wall-normal spacing is different (uniform vs. non-uniform) and the filter width is chosen using the grid spacing (rather than twice the grid spacing as in the fDNS case). The result is that the LES results are more finely

[1]LESGO: A parallel pseudo-spectral large-eddy simulation code. https://lesgo-jhu.github.io/lesgo (2017)

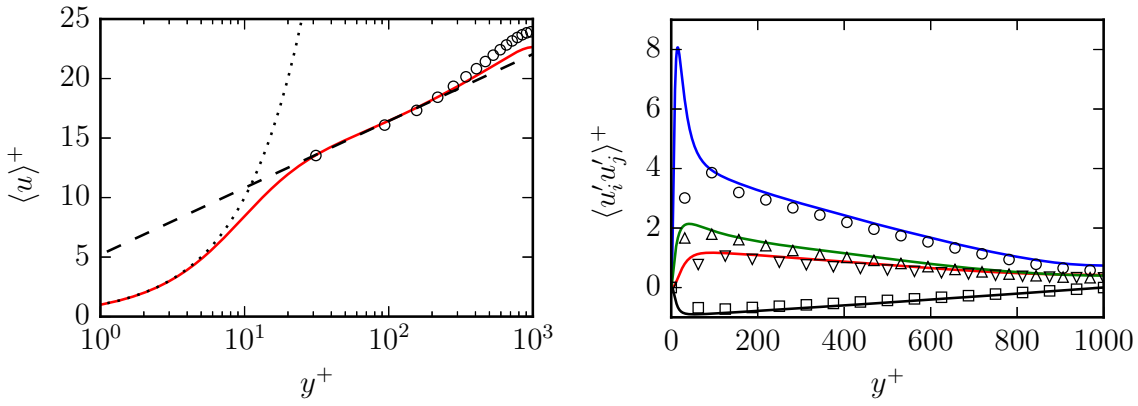

Figure 8.3: Mean velocity (left) and Reynolds stress tensor component (right) profiles for DNS (continuous lines) and LES (symbols). For the Reynolds stress components: $\langle u'^2 \rangle$ ($\circ$), $\langle v'^2 \rangle$ ($\triangledown$), $\langle w'^2 \rangle$ ($\triangle$), and $\langle u'v' \rangle$ ($\square$).

resolved than the fDNS, as is apparent in figure 8.1. The numerical details of the LES dataset is given in Table 8.3.

The LES results provide quite accurate mean velocity and Reynolds stress profiles, as shown in Figure 8.3. The first few grid points show excellent agreement with the DNS log-law, consistent with the prescribed equilibrium wall model boundary conditions. The wake region correction, however, appears to be over-predicted, which leads to the over-prediction of bulk velocity (flow rate) seen in Table 8.3, i.e., an under-prediction of the friction coefficient. The over-prediction of bulk velocity at a prescribed pressure drop leads to an under-prediction of volume-averaged dissipation rate (pumping power) and hence a slight over-prediction of $\tau_{\eta,\text{bulk}}$. The majority of the turbulent kinetic energy is resolved by the LES, in keeping with general heuristics for LES resolution,[108] which highlights the smaller effective filter width in the LES results compared with fDNS in §8.2.2.

Of even more relevance to the modeling effort at hand is the prediction of wall-normal dependence of dissipation rates. For the LES, we do not allow for any use of information from the DNS. The dissipation rate in the LES is determined by adding the resolved dissipation rate $\nu|\widetilde{S}|^2$ to the sub-grid production rate Π. The resulting Kolmogorov scale as a function wall distance is shown in Figure 8.4 on the left compared with DNS. Overall, the prediction is quite acceptable, although there is a noticeable over-prediction of dissipation rate throughout most of the channel (the equilibrium model under-predicts the dissipation in the near-wall region, but as shown in Table 8.3, the volume-averaged dissipation is over-predicted). To provide some perspective to the level of differences between LES and DNS, the left of Figure 8.4 shows the Kolmogorov scale using only the resolved dissipation rate (i.e. if no model for unresolved velocity gradients is used). A significant error is committed in this case because velocity gradients are dominated by the smallest scales which are unresolved in the LES even when most of the velocity fluctuations are resolved. This error in velocity gradient magnitude will only increase with increasing Reynolds number as discussed in §2.3.3. On the right side of Figure 8.4, the average Smagorinsky coefficient determined in the LES is shown against the assumed Smagorinsky coefficient used for the fDNS in §8.2.2. While the turbulence is more finely resolved in the LES compared to the fDNS, the Smagorinsky coefficient is also quite different between the two cases, since C_s can also depend on resolution, type of filtering, etc.

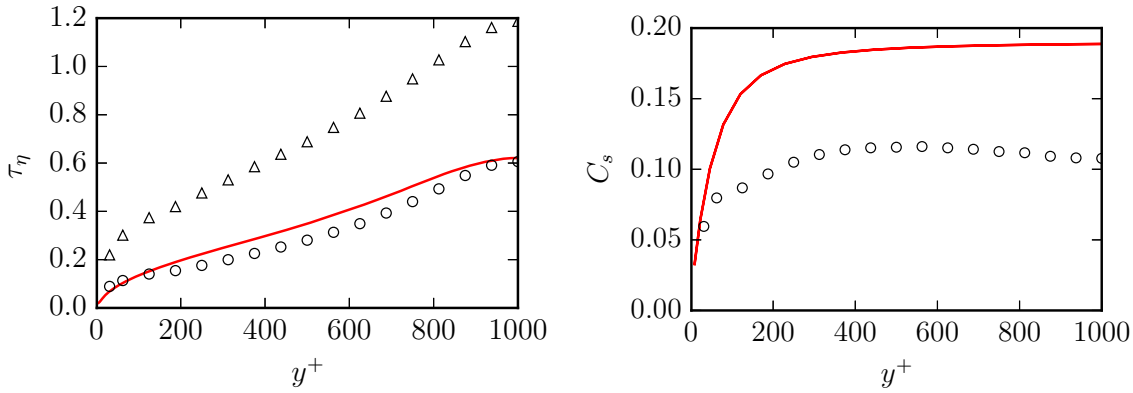

Figure 8.4: On the left, Kolmogorov timescales $\tau_\eta = \sqrt{\nu/\langle\epsilon|y\rangle_E}$ from DNS ($-$), LES-RDGF ($\circ$), and LES-NM ($\triangle$). On the right, the Smagorinsky coefficient prescribed for fDNS-RDGF ($-$), i.e. (K.1), and $\langle C_s|y\rangle_E$ as computed by the LES with the scale-dependent Lagrangian dynamic formulation ($\circ$).

8.2.4 Stochastic Differential Equations

For each case enumerated in Table 8.2, an ensemble of 172800 particles are initialized on the centerline of the channel with location in x and z determined in the following way. The domain in x and z is split into 24×9 square regions of size $\pi/3 \times \pi/3$ and the particles are divided evenly into 800 per sub-domain. Each particle is given a random x and z location within its sub-domain from a uniform distribution. While the baseline and *a priori* cases use the built-in interpolation, differentiation, and particle advancement from the JHTDB database, the *a posteriori* and *no model* cases use second-order finite-differencing, trilinear interpolation, and a second-order predictor-corrector time advancement. The particles are advanced in the LES using the resolved velocity plus the stochastic model for the unresolved velocity, (8.3), which itself is updated with a second-order predictor-corrector method for stochastic

differential equations. The same predictor-corrector method is used to update (6.11) – with the added unsteady constraint term – for the velocity gradients and (8.8) for the droplet morphologies.

The stochastic ODEs for velocity and velocity gradient are initialized by starting with a random Gaussian condition and running the stochastic model for each particle frozen at its initial location for a start-up time until transients subside. Then that result is used to initialize the velocity and velocity gradient in the particle dispersion simulation. The droplet morphology tensors are initialized to the identity tensor (indicating a spherical droplet). When the particles travel below the first grid point in the LES ($y^+ < 31.25$) the velocity gradient model is turned off and arbitrarily set to $A_{ij} = 0$, because the RDGF model was constructed for isotropic turbulence and is not expected to produce realistic gradients in the buffer and viscous sublayers. Accordingly, when statistics are taken over the ensemble of particles, those closer to the wall than $y^+ = 100$ are not included in the ensemble, so as to focus the comparison on the region of the channel flow displaying isotropic turbulence-like velocity gradient statistics.[61] This controls the model comparison to focus on the region of the flow where the model is expected to be valid. Finally, for the droplet deformation, it is possible for regions of strong velocity gradient for high-Ca droplet to undergo unbounded deformation. In that case, numerical round-off errors become more significant when the disparity between singular values (ellipsoid semi-axes) becomes large. To prevent this, droplets with $D > 0.9999$ at any time step are removed from the

ensemble at the time step and are not replaced.

8.3 Results

In this section, the results for particle trajectories (§8.3.1), velocity gradients (§8.3.2), and droplet deformation (§8.3.3) are shown. We primarily focus on the comparison of the LES-RDGF results with DNS, although the other cases in table 8.2 are used at times to shed further light on the accuracy of the various models used. Figure 8.5 shows sample time histories for wall-normal location, transverse velocity gradient, and droplet deformation for six trajectories chosen at random. As the particles approach closer to the boundaries of the channel at $y = -1$ and $y = 1$, they tend to experience higher velocity gradient magnitudes which fluctuate at higher frequencies.

8.3.1 Particle Dispersion Statistics

It is important to first validate the dispersion of particles in LES away from the centerline by the combination of resolved velocity and the stochastic model for sub-grid velocity contributions, §8.1.2. Such a validation is presented in Figure 8.6 by comparing particle location PDFs as a function of time from the LES and DNS cases. The distributions of particles at eight different times are shown, four early times on the left ($0.26 \leq t \leq 2.34$) and four later times on the right ($2.6 \leq t \leq 23.4$). The LES

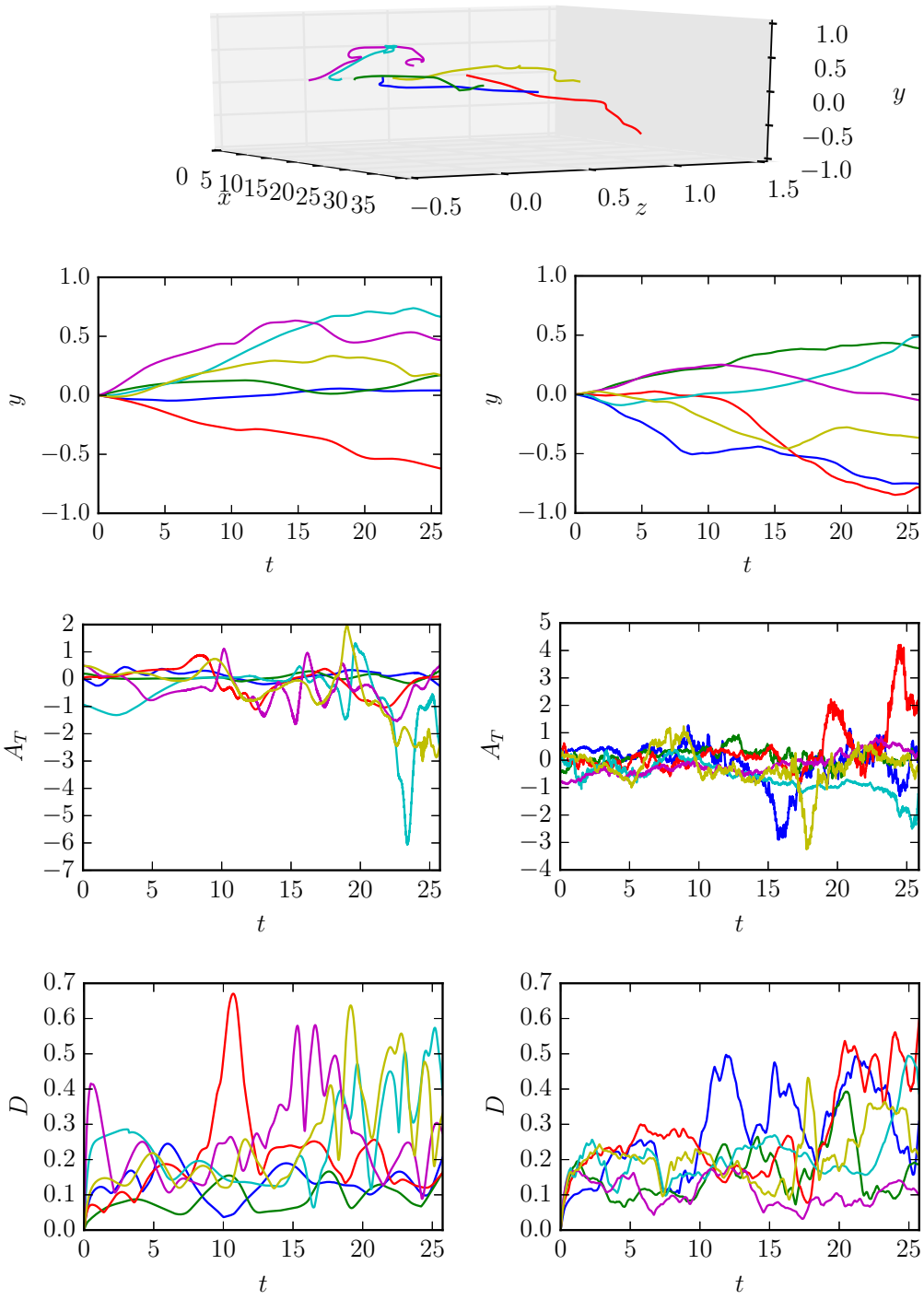

Figure 8.5: Sample time histories of wall-normal location (top) and transverse velocity component (middle) and deformation magnitude parameter D (bottom) from the DNS (left) and LES-RDGF (right) results for 6 independent Lagrangian trajectories. The droplets shown are have $Ca = 1.0$ and $\hat{\mu} = 1.0$.

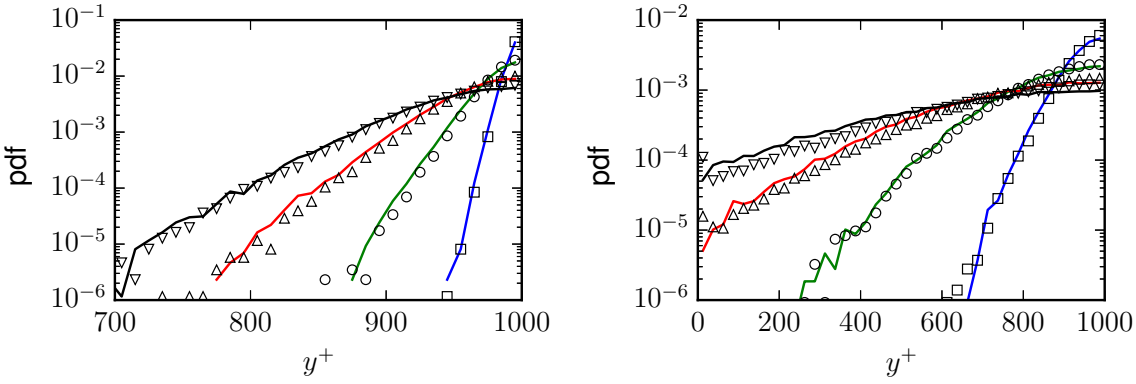

Figure 8.6: Distribution of particles at different times after being released from the centerline at $t = 0$. Continuous lines show the distributions from DNS while symbols show the results from LES with stochastic model for sub-grid velocity. Left: $t = 0.26$ ($\square$), $t = 0.78$ ($\circ$), $t = 1.56$ ($\triangle$), $t = 2.34$ ($\triangledown$). Right: $t = 2.6$ ($\square$), $t = 7.8$ ($\circ$), $t = 15.6$ ($\triangle$), $t = 23.4$ ($\triangledown$).

with the stochastic model provides excellent agreement with the dispersion seen in the DNS, with some small differences arising at later times. The first particles begin to interact with the wall around $t \approx 10$. After that, there is a small but noticeable under-prediction of the uniformity of the particle location PDF given by the LES results. The overall results are, however, quite good.

8.3.2 Velocity Gradient Statistics

We now compare the results of the LES-RDGF model with DNS results in terms of the magnitude and tensorial structure of the velocity gradient along particle paths. The magnitude of velocity gradients determines the dissipation rate and thus establishes the ability of turbulence to rotate, deform, and otherwise affect small objects in a flow. Meanwhile, the statistical topology of velocity gradients are also important

for accurately capturing how various micro-physical parameters, such as the aspect ratio of rigid particles in Jeffrey's equation[239,240] or the capillary number of small droplets in (8.8), impact the efficiency of velocity gradients in imposing their effects. Following a presentation of results for general velocity gradient statistics, we pursue further validation for the particular case of small droplets in §8.3.3.

Figure 8.7 considers the distribution of dissipation and enstrophy ($\chi = \frac{1}{2}\omega_i\omega_i$), characterizing the fluctuations in velocity gradient magnitudes in the flow. These distributions are computed by averaging over the particle ensembles and averaging in time. As a result, these PDFs contain both internal fluctuations of the RDGF velocity gradient model, as well as fluctuations due to the spatial-temporal behavior of Π from LES. In this figure, the results of the *a posteriori* case compare quite favorably with the DNS results, indicating the accuracy of the fluctuations within the RDGF model which generate stretched exponential tails in the dissipation and enstrophy PDFs. The dotted lines in this figure indicate the distribution of resolved dissipation rate in the LES (i.e., the 'no model' case), which severely under-predicts the intermittency of dissipation and enstrophy – in addition to significantly under-predicting the mean dissipation. Thus, Figure 8.7 highlights the importance of the sub-grid velocity gradient model in generating accurate intermittency levels for extreme fluctuations in the velocity gradient magnitude.

Turbulence dynamics is known to generate a non-trivial signature in the structure of the velocity gradient tensor. For instance, the vorticity vector tends to align most

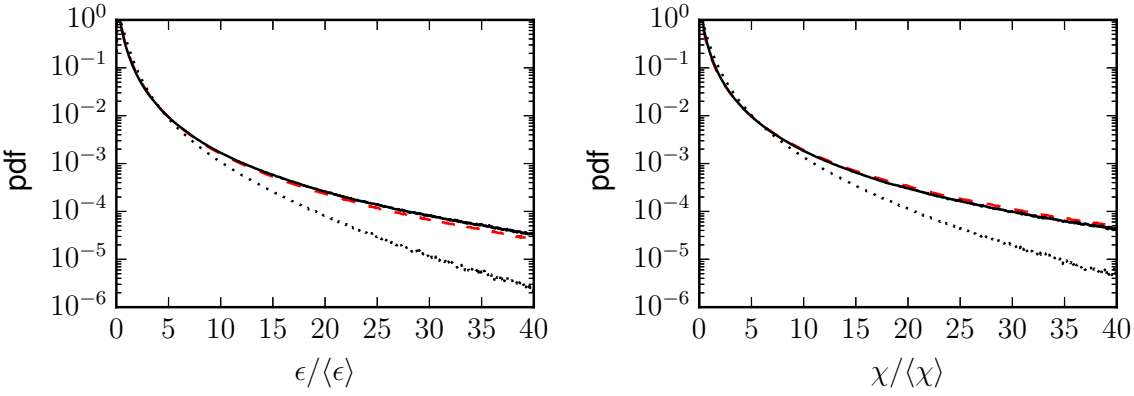

Figure 8.7: Probability distribution functions for dissipation (left) and enstrophy (right) using an ensemble of all particle locations at each time for $0 < t < L_t$, excluding $y^+ < 100$. The continuous black line indicates LES-RDGF results compared with DNS (red dashed line) and LES-NM results (black dotted line).

prevalently with the strain-rate eigenvector associated with its intermediate eigenvalue, Λ_2, while noticeably avoiding alignment with the compressive eigenvector with eigenvalue $\Lambda_3 < 0$.[111] The RDGF model, by faithfully capturing the non-linear self-stretching term in the governing equations, has been shown to capture this tendency well.[62] Indeed, the results for this alignment tendency are quite accurate in LES-RDGF as shown on the left of Figure 8.8. Without using any model for unresolved velocity gradients, the LES particularly under-predicts the tendency of vorticity to align perpendicularly with the Λ_3 eigenvector. Additionally, the s^* parameter, introduced by Ref. 197 for quantifying the tendency of the strain-rate tensor to deform spherical material elements toward prolate ($s^* < 0$) or oblate ($s^* > 0$) ellipsoids, has its own unique signature in turbulence. Shown on the right of Figure 8.8, the PDF of s^* is also predicted quite successfully by the LES-RDGF model, while the LES-NM

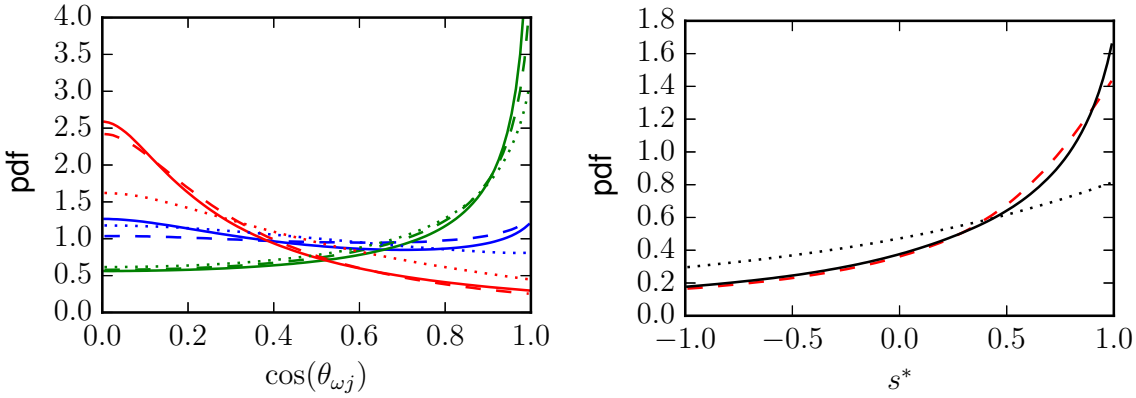

Figure 8.8: Probability distribution functions for alignment cosine between vorticity and strain-rate eigenvectors (left) and topology indicator $s^* = -3\sqrt{6}\Lambda_1\Lambda_2\Lambda_3/(\Lambda_1^2 + \Lambda_2^2 + \Lambda_3^2)^{3/2}$ (right) using an ensemble of all particle locations at each time for $0 < t < L_t$, excluding $y^+ < 100$. The continuous lines indicate LES-RDGF results compared with DNS (dashed lines) and LES-NM results (dotted lines). On the left, colors indicate the eigenvectors associated with largest eigenvalue (blue), intermediate eigenvalue (green), smallest eigenvalue (red).

results under-predict the bias toward oblate topologies. The coarse-grained velocity gradient evolution equations share the same self-stretching term with the fully resolved equation, therefore the results in Figure 8.8 for LES-NM are qualitatively the same as DNS, even though the LES-RDGF is quantitatively more accurate.

Finally, in Figure 8.9, the joint-PDF of invariants $Q = -\frac{1}{2}\text{tr}\mathbf{A}^2$ and $R = -\frac{1}{3}\text{tr}(\mathbf{A}^3)$ are considered from the DNS and the LES-RDGF results. It is well-known that turbulence dynamics generates a signature feature in this joint-PDF, namely, the increased probability for rare fluctuations along the right-hand side of the so-called Vieillefosse tail in the fourth quadrant. This feature is intimately connected with the non-linear dynamics of the $\mathbf{A}^2$ term in (2.29), and hence is naturally captured in the RDGF and other similar models.[62,146,147] Figure 8.9 highlights the accuracy of the

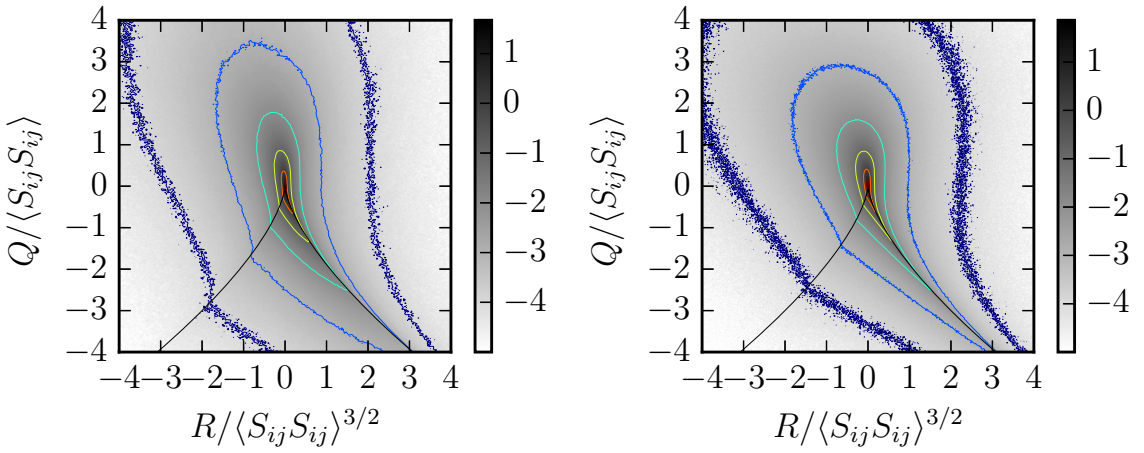

Figure 8.9: Logarithmically-spaced contours of the joint probability density function for the second and third invariants of the velocity gradient tensor along the particle trajectories, excluding $y^+ < 100$. The results of DNS (left) are compared with LES-RDGF model results (right).

RDGF model in reproducing the key features of the PDF in QR invariant space.

The discussion of velocity gradient accuracy in this section so far has centered on the benefits of the stochastic model, namely, the tensorial structure and intermittent fluctuations of the velocity gradient. We now turn our attention to predictions of the mean dissipation rates (velocity gradient magnitudes). As will be seen, inherent difficulties exist for providing accurate inputs to the RDGF model (i.e. accurate trajectory-specific dissipation rates) from the LES. The ensemble of Lagrangian particles is initialized at the center of the channel, where there is a minimum of dissipation rate from and Eulerian perspective. However, as illustrated by the DNS results in Figure 8.10, the average dissipation rate over the whole ensemble initially decreases (i.e., the dissipation timescale increases), even as the particles spread to locations nearer the wall where there is more dissipation in terms of Eulerian averages. Furthermore,

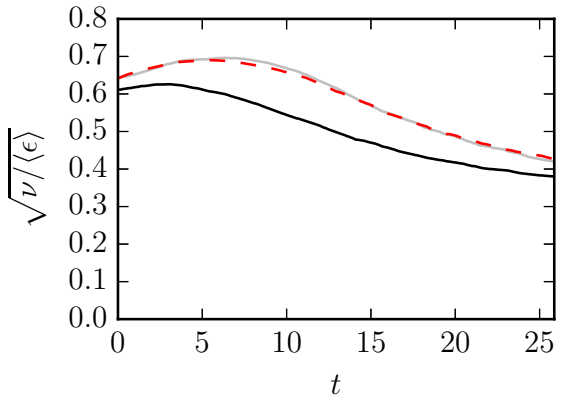

Figure 8.10: Kolmogorov timescale $\tau_\eta = \sqrt{\nu/\langle\epsilon\rangle_L}$ with averaging over the particle ensemble as a function of time after release from the centerline. The DNS results (dashed red) are compared with fDNS-RDGF (continuous gray) and LES-RDGF (continuous black).

in Figure 8.11, it can be seen from DNS by comparing the red and gray continuous lines (or from the model comparing black and gray circles), that Lagrangian particles which begin in the centerline tend to sample regions with lower dissipation than given by Eulerian averaging.

This effect can be understood as follows. While it is true that Eulerian-averaged dissipation is minimum at the center of the channel, a more extreme minimum at the centerline is found in the SGS production results, see Figure K.1. In fact, from a RANS perspective, the production of turbulent kinetic energy from mean flow energy is exactly zero (by symmetry) at the centerline. The following picture emerges as a simplification of the physics. While no kinetic energy is produced at the centerline, as the energy cascade proceeds to small scales, turbulent diffusion tends to move turbulent energy from high production regions nearer to the wall toward the centerline,

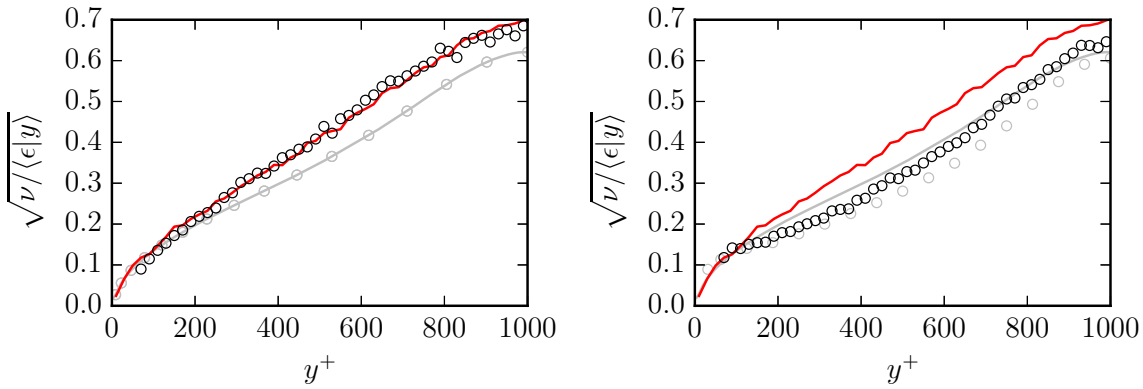

Figure 8.11: Kolmogorov timescales as a function of wall distance for Eulerian averaging (gray) and particle ensemble averaging at time $t = 23.4$ (black). Continuous lines indicate DNS results and symbols ($\circ$) indicate RDGF results. Left: fDNS-RDGF (*a priori*) compared with DNS. Right: LES-RDGF (*a posteriori*) compared with DNS.

resulting in a more uniform profile for large-scale energy dissipation as the filter width is decreased. Still, even at the smallest scales (i.e. viscous dissipation in unfiltered equations), the profile of dissipation rate is not perfectly uniform.

Some evidence has been shown in isotropic turbulence that the energy cascade has a distinct Lagrangian characteristic,[48,234] and that fluctuations in SGS production are correlated with molecular dissipation fluctuations with a time lag *along Lagrangian trajectories*, an effect which motivates the use of (8.1). This suggests that while particles starting on the centerline tend to have the least dissipation rate compared to starting elsewhere, at a slightly later time, their dissipation rate is strongly affected by their SGS production rate from when they were on the centerline. The initial phase of increasing dissipation timescale in Figure 8.10 suggests that this Lagrangian cascade effect is, at least initially, stronger than the effect of particle dispersion to

higher dissipation regions (in an Eulerian-averaged sense) nearer the wall. As the particle ensemble continues to spread toward the walls and the memory of initial conditions continues to fade, the average dissipation rate over the particle ensemble increases as expected from the Eulerian observations. However, as shown by Figure 8.11, this Lagrangian effect can still be seen even at much later times by conditional averaging based on y.

In the *a priori* test case, shown as a gray line in Figure 8.10, the actual DNS trajectories are used and a non-equilibrium correction (explained in §8.2.2) ensures an accurate wall-normal profile of Eulerian-averaged dissipation rates in the fDNS. The result is that this initial "bump" in the ensemble timescale is captured and the time history of particle ensemble dissipation rate is quite accurately reproduced. In fact, the time lag model between Π and $\hat{\epsilon}$ given in (8.1) has been introduced and the coefficient $C_\epsilon = 1.5$ has been chosen precisely to accurately capture this effect which can be important in non-homogeneous flows. Similarly, Figure 8.11 shows that dissipation rates conditioned on wall distance are also captured well in the *a priori* (fDNS-RDGF) case due the combination of accurate Eulerian averaged dissipation profiles and Lagrangian trajectories. However, the results for the *a posteriori* (LES-RDGF) test case are not as accurate, owing both to a deterioration in accuracy of the trajectories themselves due to the limitations of the stochastic dispersion model described in §8.1.2 and to the over-prediction of Eulerian-averaged dissipation rate by the LES, as shown in Figure 8.4. These errors are largely independent of the

details of the RDGF velocity gradient model, and improvements in velocity gradient magnitude would need to be accomplished primarily through a more accurate model for $\hat{\epsilon}$ in LES, for example, by including turbulent diffusion effects in the spirit of RANS modeling of the ϵ equation.[108,241] Improved accuracy of sub-grid dispersion modeling could also be helpful here. It is important to recall from Figure 8.4, and more generally from the scaling arguments of §8.1.1, that the LES with no model will more severely under-predict the dissipation rates, and the LES-RDGF model still represents a significant improvement which is even more important as Reynolds number increases, as emphasized in §8.1.1.

The results shown in this section (and the following one) have neglected data from any particle closer to the wall than 100 viscous units, so as to compare only data from regions which roughly follow local isotropy behavior at small scales in this flow.[61] A clear limitation to the LES-RDGF model as presented here is that the RDGF model is designed for isotropic (or approximately isotropic) turbulence at small-scales. Near the wall, this type of behavior is no longer seen, and capturing velocity gradient statistics in the near-wall region (as well as at higher Reynolds number flows) will require more detailed future modeling efforts.

8.3.3 Droplet Deformation Statistics

To illustrate the benefits and predictive properties of the velocity gradient modeling technique proposed in this chapter, we choose one particular application for which

velocity gradient information is necessary, namely predicting deformation statistics of sub-Kolmogorov scale droplets. The droplets are evolved numerically according to (8.8) using a 2nd order predictor-corrector method. They are deformed by the velocity gradients from the stochastic model (one-way coupling). The main parameter used to quantify the magnitude of deformation for a droplet is

$$D = \frac{\sigma_1 - \sigma_3}{\sigma_1 + \sigma_3}, \tag{8.12}$$

where σ_i is the i^{th} singular value of the deformation tensor $\mathcal{D}$. These three singular values, representing the lengths of the three semi-axes of the ellipsoid, are computed using a singular value decomposition routine from LAPACK. The deformation parameter $0 \leq D < 1$ takes on the value $D = 0$ when the droplet is spherical (as in the initial condition) and asymptotically approaches $D = 1$ for strongly deformed droplet ($\sigma_1 \gg \sigma_3$). In this way, the temporal history of D (and other droplet measures) is computed along each trajectory.

For $Ca = 1$, Figure 8.12 compares the PDF of D for the ensemble of droplets at a time late in the simulation. It is clear that the LES-NM results significantly under-predict the extent of deformation, which is a straightforward result of the lower velocity gradient magnitudes. Meanwhile, the results of the *a posteriori* (LES-RDGF) test reveal results that are much closer to the DNS results. A slight over-prediction of D can be observed, which is related to the small over-prediction of dissipation rates.

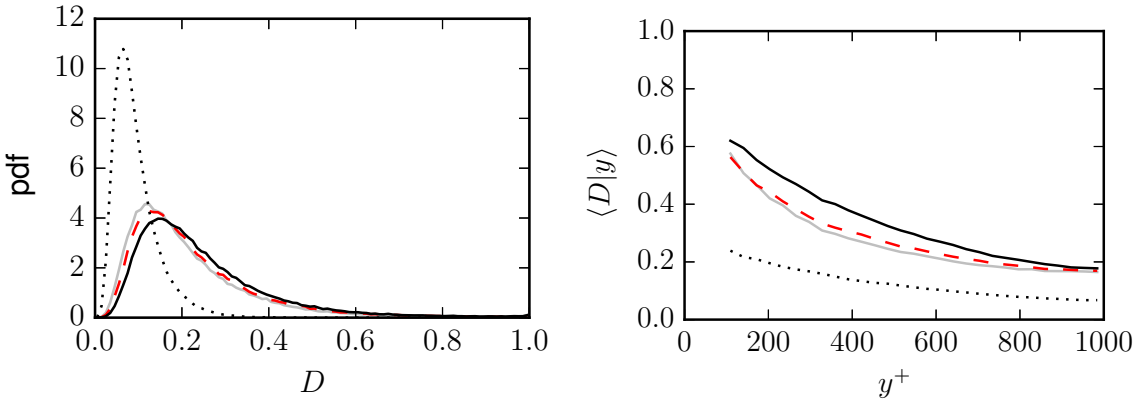

Figure 8.12: At $t = 23.4$, the PDF of D (left) and conditional average $\langle D|y\rangle_L$ (right) for the droplet ensemble. Droplet with location $y^+ < 100$ are removed from the ensemble for these plots. The DNS results (red dashed lines) are compared with fDNS-RDGF (gray lines), LES-RDGF (black lines), and LES-NM (black dotted lines).

The *a priori* test shows the best accuracy compared with DNS, but does slightly under-predict the deformations. This is most likely attributable to minor inaccuracies in the RDGF model itself, for example, in the Lagrangian auto-correlation of strain.

In addition to D, we introduce the shape parameter,

$$s_d^* = -\frac{3\sqrt{6}\ln\sigma_1\ln\sigma_2\ln\sigma_3}{\left(\ln^2\sigma_1+\ln^2\sigma_2+\ln^2\sigma_3\right)^{3/2}}, \tag{8.13}$$

which helps differentiate between prolate and oblate droplet shapes. A droplet having the shape of a prolate spheroid assumes the value $s_d^* = -1$ while an oblate shape has $s_d^* = 1$. The value $s_d^* = 0$ signifies that the intermediate semi-axis has its original (undeformed length) while $\sigma_3 = -\sigma_1$. For short times starting from an initial sphere, $\ln\sigma_i \approx \Lambda_i$, where Λ_i is the i^{th} eigenvalue of the strain-rate tensor. This means that, for arbitrarily short time, $s_d^* = s^*$ where s^* is the original parameter defined by Ref.

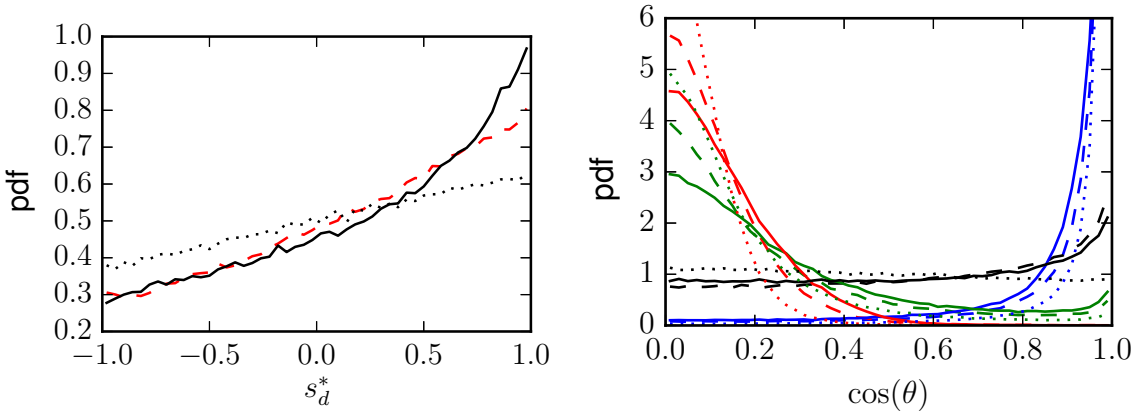

Figure 8.13: Left: the PDF of the shape parameter s_d^* at $t = 23.4$ for the ensemble of droplets, exclude those with $y^+ < 100$. Right: the PDFs of alignment cosines between the σ_1 singular vector of the droplet deformation tensor and the three eigenvectors of the strain rate tensor (blue: Λ_1, green: Λ_2, red:Λ_3) as well as the vorticity vector (black). In both, the continuous lines indicate LES-RDGF results, the dashed lines show DNS results, and the dotted lines are results from the LES-NM case.

197 for the strain-rate tensor. Therefore, $s_d^* \approx s^*$ for nearly-spherical droplets, and the PDF of s_d^* approaches that of s^* for $Ca \ll 1$. The PDF of s_d^* at $Ca = 1$ is shown in Figure 8.13 for the different cases. At this capillary number, a bias toward oblate droplets is seen in the DNS and is well matched by both fDNS-RDGF and LES-RDGF cases. The LES-NM results under-predict the bias toward $s_d^* > 0$.

Also shown in Figure 8.13 are the PDFs of alignment between the singular vector of the deformation tensor associated with its largest singular value with the three strain-rate eigenvalues as well as with vorticity. Here, LES-RDGF and LES-NM are compared with DNS. The main qualitative features are similar: a strong tendency toward parallel alignment with the largest strain-rate eigenvalue and perpendicular alignment with the other two, especially the smallest strain-rate eigenvalue. The slight

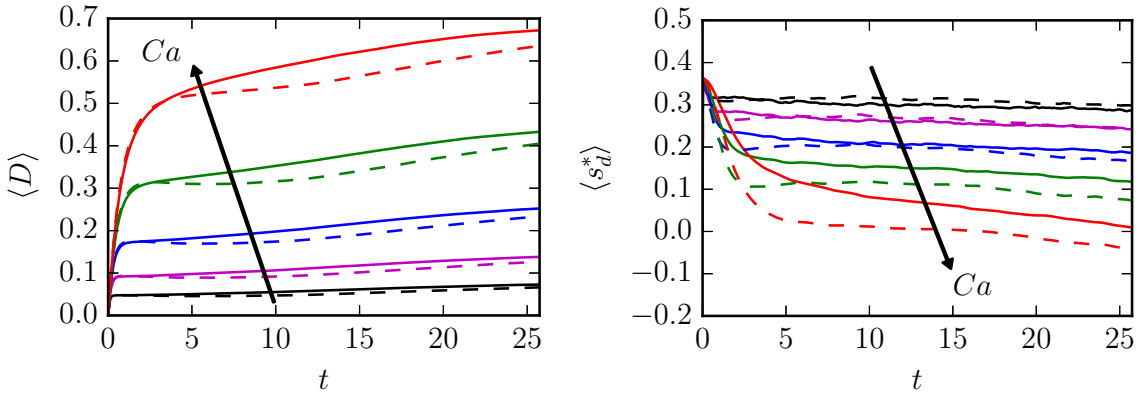

Figure 8.14: The deformation magnitude ($0 < D < 1$) and shape parameter ($-1 < s_d^* < 1$) averaged over the particle ensemble as a function of time for $Ca = 0.25$ (black), 0.5 (magenta), 1.0 (blue), 2.0 (green), 4.0 (red). Dashed lines show DNS results while continuous lines show results from the *a posteriori* LES simulation. Arrows indicate the direction of increasing Ca.

bias toward parallel alignment with the vorticity seen in the DNS results is mimicked by the LES-RDGF model but not by LES-NM. The most notable advantage gained by the LES-RDGF velocity gradient model over simply using the velocity gradients from LES without a model is the magnitude of deformation (Figure 8.12), but some improvements in droplet shape and alignment with flow features are also seen. The importance of the RDGF model is expected to become even more important for higher Reynolds numbers.

We now consider a more detailed comparison directly between the DNS and the *a posteriori* LES-RDGF model. To this end, droplets with $0.25 < Ca < 4.0$ were simulated to characterize the ability of the models developed in this chapter to capture dependence of droplet deformation on relative surface tension strength. For simplicity, a viscosity ratio of $\mu_d/\mu_0 = 1.0$ is assumed. Again, inertial effects due to density

differences are neglected.

Figure 8.14 shows the temporal evolution of particle ensemble averages after spherical droplets are released from the centerline of the channel at $t = 0$ and allowed to deform as they are advected by the flow. There is a rapid adjustment from initially spherical droplets ($D = 0$) to a quasi-equilibrium in which velocity gradient stretching is approximately balanced by surface tension in the sense of ensemble averages. This rapid adjustment period is followed by a slow variation dictated by the magnitude of velocity gradients experienced as the droplets spread away from the center of the channel and toward the walls where they experience higher velocity gradient magnitudes. The droplets' initial departure from sphericity follows the local strain-rate at $t = 0$, so $s_d^* = s^*$ for short times. As observed by Ref. 62, $\langle s^* \rangle \approx 0.37$ in isotropic turbulence and the same value is observed here for $\langle s_d^* \rangle$ at $t = 0$.

At any given time, the average deformation increases as surface tension forces are decreased (increasing Ca). Less trivially, the average shape parameter decreases as Ca is increased, signaling a decreasing bias toward disk-shaped (oblate) droplets. In fact, near the very end of the simulation ($t > 20$), the $Ca = 4.0$ DNS results show a slightly negative s_d^* average, indicating a slight bias toward cigar-shaped (prolate) droplets. The full distributions of D and s^* for a single time near the end of the simulation are shown in Figure 8.15. For the deformation magnitude, the PDF shifts from most droplets slightly deformed ($D < 0.2$) at $Ca = 0.25$ to a situation in which most droplets become highly deformed for $Ca = 4.0$. Meanwhile, as Ca increases, the

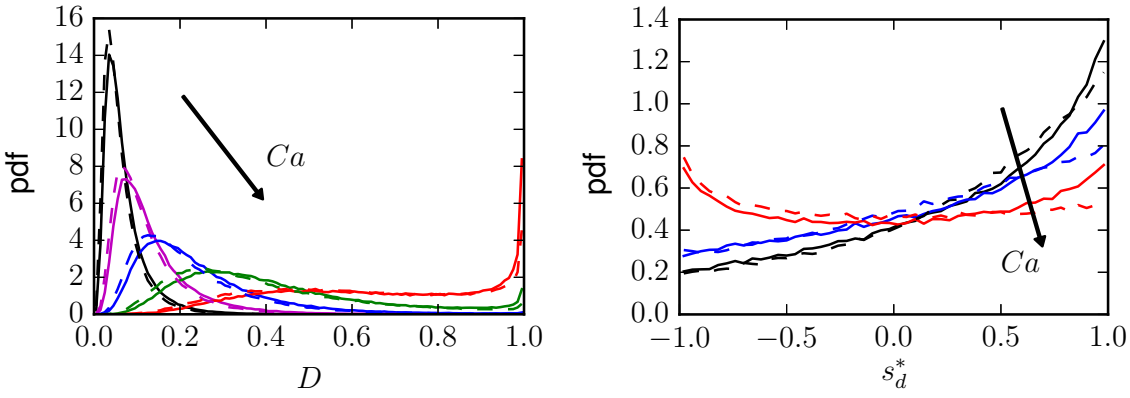

Figure 8.15: Probability density functions for droplet deformation magnitude (left) and shape parameter (right) near the end of the simulation, $t = 23.4$. On the left, the range of Ca in Figure 8.14 is shown, while on the right, a reduced set $Ca = 0.25$, 1.0, 4.0 is shown. Continuous lines indicate LES-RDGF results while dashed lines show DNS results. Arrows indicate the direction of increasing Ca.

bias toward oblate droplets decreases. One of the more noticeable differences between the PDFs for DNS and LES-RDGF results is the consistent over-prediction of $s_d^* \approx 1$ droplets.

Figure 8.16 further elaborates on these trends. The deformation magnitude as a function of wall-normal distance shows that the trend with Ca is captured very well, but the slight over-prediction of deformation is consistent at any Ca. The conditional average of s_d^* as a function of D shows the dependence of shape on the extent to which droplets are deformed. At all Ca, the maximum $\langle s_d^* | D \rangle$ (most bias toward prolate shapes) occurs near the peak of the PDF. The LES-RDGF model appears to over-predict the bias toward oblate shapes for highly-deformed droplets, whereas DNS even shows a prolate bias for very high D. This discrepancy helps explain the growing error for $\langle s_d^* \rangle$ in Figure 8.14 as Ca increases. Taken together with Figure

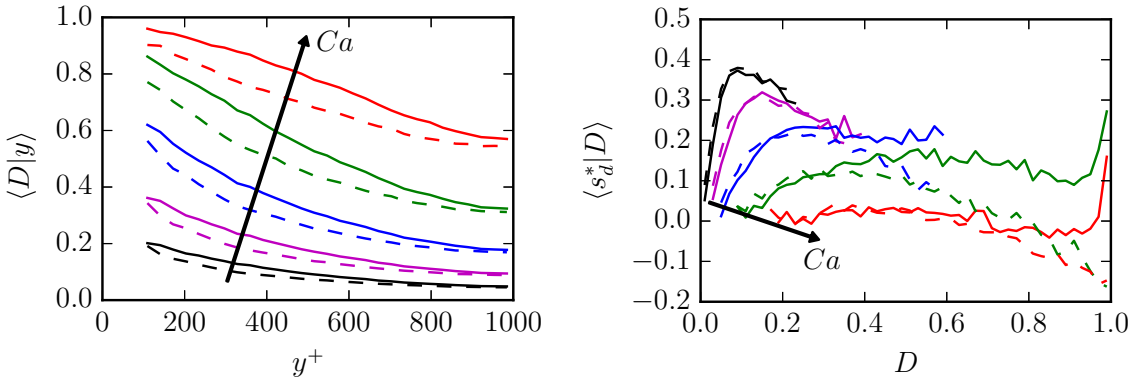

Figure 8.16: Conditional means for deformation magnitude conditioned on wall-normal distance (left) and shape parameter conditioned on deformation magnitude near the end of the simulation, $t = 23.4$. The same range of Ca from Figure 8.15 is shown. Arrows indicate the direction of increasing Ca.

8.15, this shows that the velocity gradient model over-predicts the amount of highly deformed oblate droplets compared with the DNS. Otherwise, the agreement between the LES-RDGF model and DNS is very good.

Finally, while the above simulations have demonstrated the relative accuracy of the LES-RDGF model compared with DNS, we close by considering a more physically-motivated choice of parameters (Ca and $\hat{\mu}$) to mimic oil droplet behavior in a turbulent environment. The following parameter choices are rough estimates for the purpose of demonstration only, and not necessarily meant to directly match any particular flow experiment or simulation. We consider oil droplets in water (μ_0 = 1e-3 Pa-s, ρ_0 = 1e3 kg/m^3) with estimated surface tension of about σ = 2e-2 N/m and viscosity μ_d = 4e-3 Pa-s without added dispersants[242] and σ = 5e-5 N/m with a dispersant-to-oil ratio of 50.[243] We use a dissipation rate of $\langle \epsilon \rangle$ = 5 m^2/s^3,[244] which yields $\eta \approx$ 2e-5 m, $\tau_\eta \approx$ 4e-4 s, $\upsilon_\eta \approx$ 5e-2 m/s, for estimated Kolmogorov length, time,

and velocity scales respectively. These values result in $\hat{\mu} = 4$ and $Ca =$ 5e-3 (without dispersants) and 2 (with dispersants) for droplets with radius $R \approx 2\eta$, which would be on the upper end of droplet sizes which can be described well by (8.8), namely $R \ll 10\eta$, since most of the dissipation occurs at scales near $\sim 10\eta$.[108]

Figure 8.17 shows results for droplets with viscosity ratio $\hat{\mu} = 4$ in the turbulent channel flow using DNS and LES-RDGF with $Ca =$ 5e-3 ('without dispersants') and $Ca = 2$ ('with dispersants'). Given the dramatic reduction in surface tension caused by the dispersants, the behavior of the droplets also changes dramatically. The droplets without dispersants deform negligibly and remain very close to spherical while the $Ca = 2$ case shows significant deformation. Qualitatively the results in Figure 8.17 are similar to those of previous figures in this section, so that same conclusions about droplet behavior and model accuracy also apply to this case.

8.4 Summary and Conclusions

In this chapter, we have demonstrated that, while direct use of coarse-grained velocity gradients in a large-scale flow simulation leads to significant errors (which increase with Re), the stochastic modeling techniques for the velocity gradient tensor in isotropic turbulence can be successfully coupled to LES to provide small-scale information along trajectories. In this way, the effect of large scale features captured in the LES is transmitted to the small-scale dynamics and flow inhomogeneity from

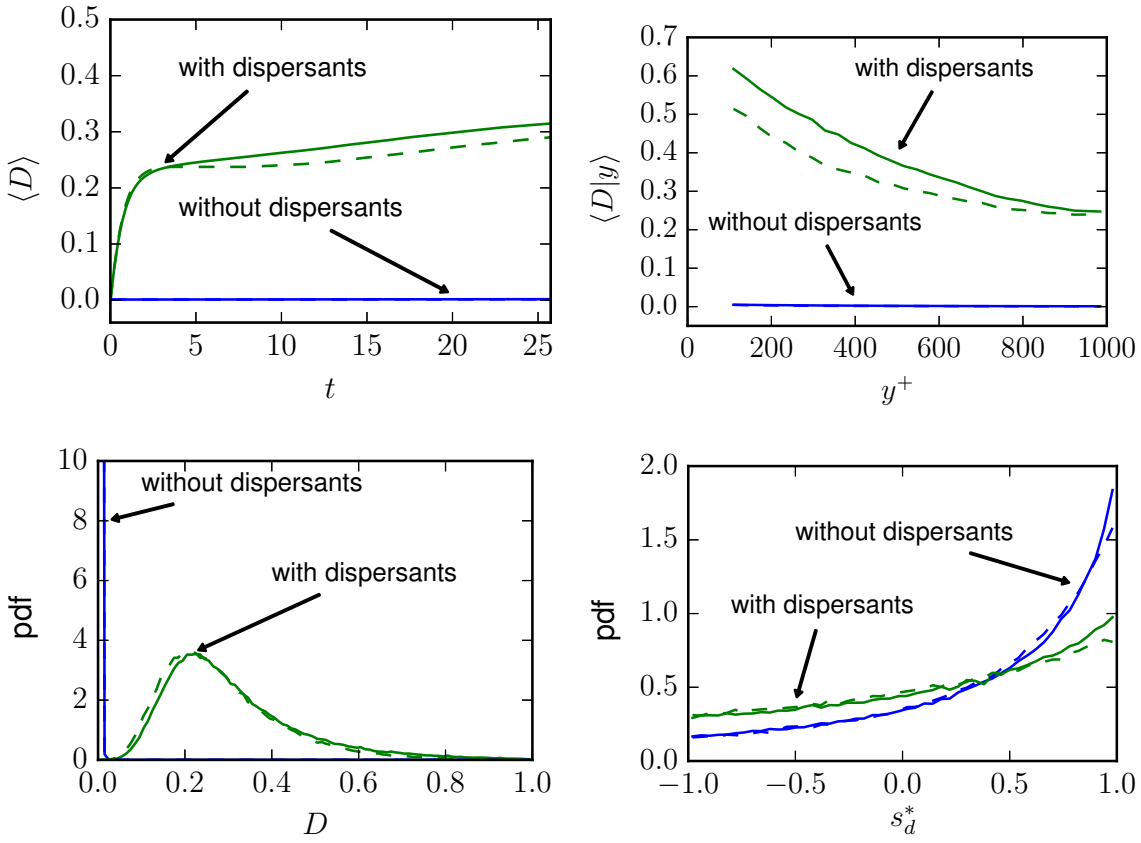

Figure 8.17: Comparison of deformation for oil droplet cases for Ca = 5e-3 (without dispersants) and $Ca = 2$ (with dispersants). Top left: time history of ensemble averaged deformation magnitude after release from channel centerline at $t = 0$. Top right: Average deformation magnitude conditioned on wall distance at $t = 23.4$. Bottom left: PDF of deformation magnitude at $t = 23.4$. Bottom right: PDF of droplet shape parameter at $t = 23.4$.

LES is naturally incorporated into stochastic model previously used only for isotropic turbulence.

The stochastic model provides an accurate level of intermittency for the dissipation and enstrophy fluctuations, matching the stretched-exponential tails of the PDFs. By taking into account the non-linear dynamics of the velocity gradient in the viscous range, the tensorial structure is captured with remarkable accuracy by the stochastic model. This includes the various alignment trends of vorticity with strain-rate eigenvectors as well as the relative probability of prolate and oblate deformation events in the strain-rate eigenvalues. Further, the velocity gradient models provide a rich description of the local flow conditions and can be coupled to micro-physical models to predict the effect of inhomogeneous turbulence on small-scale physics. In particular, this was demonstrated for small droplets using a phenomenological model relating their deformation and rotational behavior to the velocity gradient. In addition to capturing deformation magnitude trends with Ca and accurate PDF shapes, the stochastic model results were also able to represent shape distributions with good accuracy, although there was a tendency to slightly over-predict highly-deformed oblate droplets.

While the LES-RDGF model shown here enjoys a good amount of success, a few discrepancies with DNS results have been identified, such as the over-prediction of dissipation rate by the LES in the core of the channel and the over-prediction by the RDGF model of the bias toward creating oblate droplet morphologies for highly

deformed droplets. Further improvement on these shortcomings would rely on (i) improved modeling of dissipation rate statistics from LES and (ii) improved multi-time statistics in the RDGF stochastic model or similar modeling approach.

The scope of the velocity gradient model could also be quite usefully extended if near-wall deviations from approximate isotropy could be taken into account. We recall that the application of the RDGF model to the channel flow case studied in this chapter was predicated on the ability of isotropic turbulence to capture the main small-scale effects in this non-homogeneous flow. This prevents the current methodology from capturing some effects. For instance, it is known that the peak of the $\partial u/\partial y$ PDF in channel flow occurs for negative gradients,[245] an observation that cannot be explained by a local isotropy assumption. In fact, in our proposed formulation, the tensorial structure of the resolved velocity gradient $\widetilde{A}$ is not used when computing the total velocity gradient. However, in wall-bounded applications, even at high Reynolds numbers, the local Reynolds number decreases near the wall and consideration of the resolved velocity gradient, $\widetilde{\mathbf{A}}$, becomes more important. Also, the pressure Hessian and viscous Laplacian closures developed for unbounded isotropic turbulence may also need modification to capture important near wall effects in the buffer region and viscous sublayer. For realistic modeling of droplet behavior, inertial effects caused by mismatched density between the droplet and surrounding fluid ($\rho_d \neq \rho_0$) could also become important, e.g. in the case of oil droplets in §8.3.3 above where the droplets are lighter than the surrounding fluid. While preliminary steps

have been taken toward including inertial effects in both dispersion[162] and velocity gradient models,[65] a fully functional version of RDGF does not yet exist for inertial trajectories. Lighter particles tend to sample more rotationally dominant regions of the flow while heavy particles tend toward strain dominated regions, which could have an important impact on droplet deformation rates for large enough particles.

In conclusion, the proposed method for coupling stochastic ODE models for the velocity gradient tensor with LES provides an alternative to expensive DNS simulations for capturing the effect of turbulence on the detailed dynamics of important (approximately) passive micro-physics such as droplet deformation, rigid particle rotation/orientation, or scalar dissipation and mass transfer, to name a few. While most of the dissipation (velocity gradient magnitude) is not directly resolved in LES, we have demonstrated a fairly simple way to estimate local dissipation rates from the LES solution (at least for the channel flow considered here) and thus set expected velocity gradient magnitudes, leaving the detailed evolution of the complex tensorial structure of the velocity gradient tensor to the stochastic model. The recent advances in physics-based modeling of the Lagrangian velocity gradient serves as a basis for the success of this approach.

Chapter 9

A Restricted Euler Model for Velocity Gradients on Inertial Trajectories

In the previous three chapters, models for the velocity gradient along Lagrangian (inertia-free) particle paths were considered. In various applications, however, the inertia of a particle has a vital impact on its trajectory and hence the velocity gradients that it experiences in turbulence. In this chapter, the effect of inertia on velocity gradient history is considered in the context of the restricted Euler model, i.e., without including the closure models for pressure Hessian and viscous Laplacian but insteady focusing on terms which can be captured exactly in the limit of low St number.

As reviewed in §2.2.2, Ref. 137, 138 and Ref. 139 developed and studied the so-

called restricted Euler system along inertial-less trajectories. This model is obtained by taking the spatial gradient of the Navier Stokes equations and neglecting the viscous and anisotropic pressure Hessian contributions. The model consists of a system of 3×3 nonlinear coupled ordinary differential equations for velocity gradient tensor elements, (2.34). Without the neglected, unclosed terms, however, the restricted Euler system eventually yields finite time singularities for almost all initial conditions. The restricted Euler system played an important role in motivating subsequent work on modeling the unclosed terms[62,145–149,229] and related work on the perceived velocity gradient[26,28] at various scales, which has resulted in models capable of reproducing certain turbulent statistics with good quantitative accuracy, although extension to arbitrarily high Reynolds numbers remains an open challenge.[69,150]

In this chapter, we derive an extension to the restricted Euler system that considers the effect of inertia on the velocity gradient dynamics when following an inertial particle, yet can likewise be projected into a dynamical system with just two degrees of freedom, namely, the two tensor invariants $Q = -\frac{1}{2}\mathrm{Tr}(\mathbf{A}^2)$ and $R = -\frac{1}{3}\mathrm{Tr}(\mathbf{A}^3)$. We explore whether the behavior in the full RQ plane observed in DNS[246] can be explained by the new model. The model is developed from governing equations in §9.1 followed by an exploration of its behavior compared with DNS in §9.2. Model properties such as fixed points and stability are investigated analytically in §9.3 before conclusions are drawn in §9.4. The content of this chapter is also published in Ref. 65.

9.1 Model Construction

In this chapter, we consider the evolution of the fluid velocity gradient, $A_{ij} = \partial u_i/\partial x_j$, along the particle trajectory, as sketched in Figure 2.2. Considering a particle velocity field $v_i(\mathbf{x}, t)$, the evolution equation for the velocity gradient can be related to the Lagrangian evolution by $dA_{ij}/dt = DA_{ij}/Dt + (v_k - u_k)\,\partial A_{ij}/\partial x_k$, where $D/Dt = \partial/\partial t + u_k \partial/\partial x_k$ is the Lagrangian or tracer particle time derivative. Upon substitution of the gradient of Navier-Stokes, (2.29),

$$\frac{dA_{ij}}{dt} = -A_{ik}A_{kj} - \frac{\partial^2 p}{\partial x_i \partial x_j} - \frac{\partial v_k}{\partial x_k}A_{ij} - \frac{\partial T_{ijk}}{\partial x_k}, \tag{9.1}$$

where p is the pressure divided by density and T_{ijk} represents spatial fluxes of velocity gradient due to viscosity and inertial effects according to $T_{ijk} = -\nu \partial A_{ij}/\partial x_k + A_{ij}(1-\beta)\tau_p Du_k/Dt$. A key step is to evaluate the divergence of the particle velocity field using Eq. (2.58) for a divergence-free fluid velocity field,[95] i.e. $\partial v_k/\partial x_k = (1-\beta)\tau_p A_{k\ell}A_{\ell k}$. The final steps in deriving the new inertial restricted Euler system are, similarly as in the classical restricted Euler model, (a) to replace the pressure Hessian $\partial_i \partial_j p$ by its isotropic part $\nabla^2 p\,(\delta_{ij}/3)$ and to invoke the pressure Poisson equation $\nabla^2 p = -A_{k\ell}A_{\ell k}$, and (b) to neglect any spatial fluxes, i.e. setting $T_{ijk} = 0$ where we make the strong assumption of neglecting fluxes due to viscosity and inertia effects.

The resulting system reads as follows,

$$\frac{dA_{ij}}{dt} = -A_{ik}A_{kj} + \frac{1}{3}A_{k\ell}A_{\ell k}\delta_{ij} + (1-\beta)\tau_p A_{k\ell}A_{\ell k}A_{ij}, \tag{9.2}$$

thus extending the restricted Euler system of equations, (2.34), to include inertial trajectory effects through the addition of the final term: $(1-\beta)\tau_p A_{k\ell}A_{\ell k}A_{ij}$. The original restricted Euler equation is recovered by considering tracer particles with equal density to the surrounding fluid, $\rho_p = \rho_f$, hence $\beta = 1$. Equation (9.2) thus shows, within the limitations of the restricted Euler assumptions, how a particle's inertia impacts the rate of change for each of the velocity gradient components it experiences along its trajectory. It is important to note that the effect of viscosity essential to studying inertial particles, Stokes drag, *is* represented in (9.2) while the less crucial effect of spatial diffusion of fluid velocity gradient is neglected. These simplifications enable us to focus on the terms which can be represented exactly in a low-dimensional dynamical system.

The inertial restricted Euler dynamics given by (9.2) can be projected into the two-dimensional space of tensor invariants Q and R, and yields the following two-dimensional dynamical system:

$$\frac{dQ}{dt} = -3R - \frac{2}{3}\alpha Q^2, \qquad \frac{dR}{dt} = \frac{2}{3}Q^2 - \alpha QR, \tag{9.3}$$

where $\alpha = 6(1-\beta)\tau_p$ is the timescale representing inertial effects. The second invari-

ant, $Q = \frac{1}{2}(\Omega_{ij}\Omega_{ij} - S_{ij}S_{ij})$, represents the relative balance between local rotation, $\Omega_{ij} = \frac{1}{2}(A_{ij} - A_{ji}) = -\frac{1}{2}\epsilon_{ijk}\omega_k$, and straining, $S_{ij} = \frac{1}{2}(A_{ij} + A_{ji})$. The third invariant, $R = -\frac{1}{3}S_{ij}S_{jk}S_{ki} - \frac{1}{4}\omega_i S_{ij}\omega_j$, represents the balance between strain production and enstrophy production.[146] The QR dynamics of the original restricted Euler system are recovered by setting $\alpha = 0$, which physically can happen either for $\rho_p = \rho_f$ hence $\beta = 1$ or for infinitesimally small particles $a \to 0$.

For particles that are heavier than the surrounding fluid, $0 < \beta < 1$ and $\alpha > 0$. For particles lighter than the surrounding fluid, $1 < \beta < 3$ and $\alpha < 0$. For heavy particles ($\alpha > 0$), the inertial term in the evolution equation for Q tends to oppose rotation-dominant states ($Q > 0$) and reinforce strain-dominant states ($Q < 0$). The exact opposite is true for light particles, where the inertial term opposes highly straining states and favors highly rotating states. In this way, heavy particles cluster in straining regions ($Q < 0$) and lighter particles cluster in rotating regions ($Q > 0$), qualitatively mimicking well-known preferential concentration trends. In homogeneous turbulence, $\langle Q \rangle = 0$ and $\langle R \rangle = 0$, where angle brackets denote ensemble averaging,[218] but when averaging over inertial trajectory ensembles, one observes that $\langle Q \rangle < 0$ for heavy particles and $\langle Q \rangle > 0$ for light particles.[247] The qualitative features of RQ space are sketched in Figure 9.1, including this qualitative effect of inertia on $\langle Q \rangle$, which is valid for any random velocity field, but in (9.3) is combined with turbulence-like dynamics in a manner consistent with first principles.

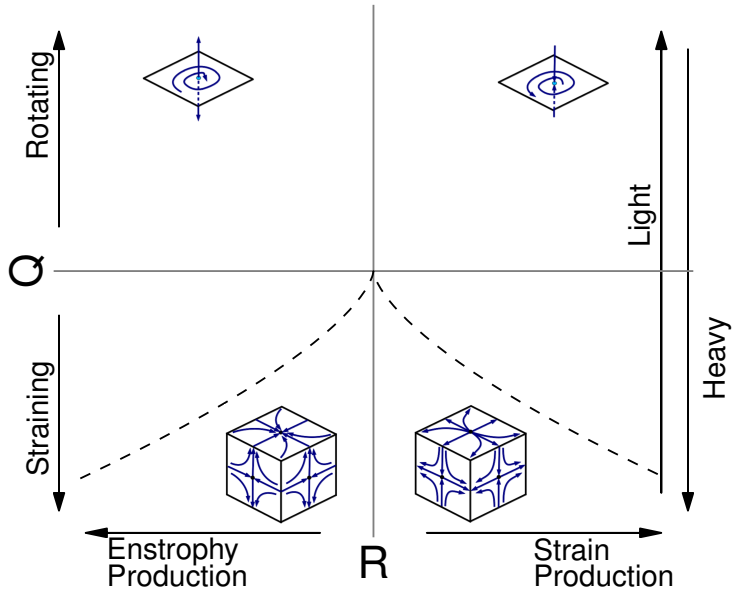

Figure 9.1: Sketch outlining the features of the RQ invariant space, including representative local flow topology cubes. The Vieillefosse tail (dashed line) represents the boundary between real and complex eigenvalues of the velocity gradient tensor.

9.2 Results

We now pursue a more detailed exploration of inertial effects in Navier-Stokes turbulence according to the restricted Euler model developed in the §9.1. Figure 9.2 shows the RQ phase-space portrait for non-inertial (fluid tracer), heavy, and light particles computed numerically from (9.3). Also shown is the stationary joint-PDF of Q and R computed from DNS at $Re_\lambda = 185$.[188] Although statistical stationarity (and hence direct comparison of the joint-PDF) cannot be achieved in the system of Eq. 9.3 without introducing models for the neglected terms, the qualitative comparison of streamlines with the joint-PDF in RQ space for heavy particles from DNS is informative. In particular, on the top left is the original restricted Euler system

($\alpha = 0$), for which trajectories move left to right along lines of constant $Q^3 + \frac{27}{4}R^2$, eventually proceeding toward the finite-time singularity in the fourth quadrant.[137–139] The sheared tear-drop shape in the joint-PDF on the top right highlights the dynamical significance of the Vieillefosse tail for the full (Navier-Stokes) dynamics of the velocity gradient tensor.[141,220–222]

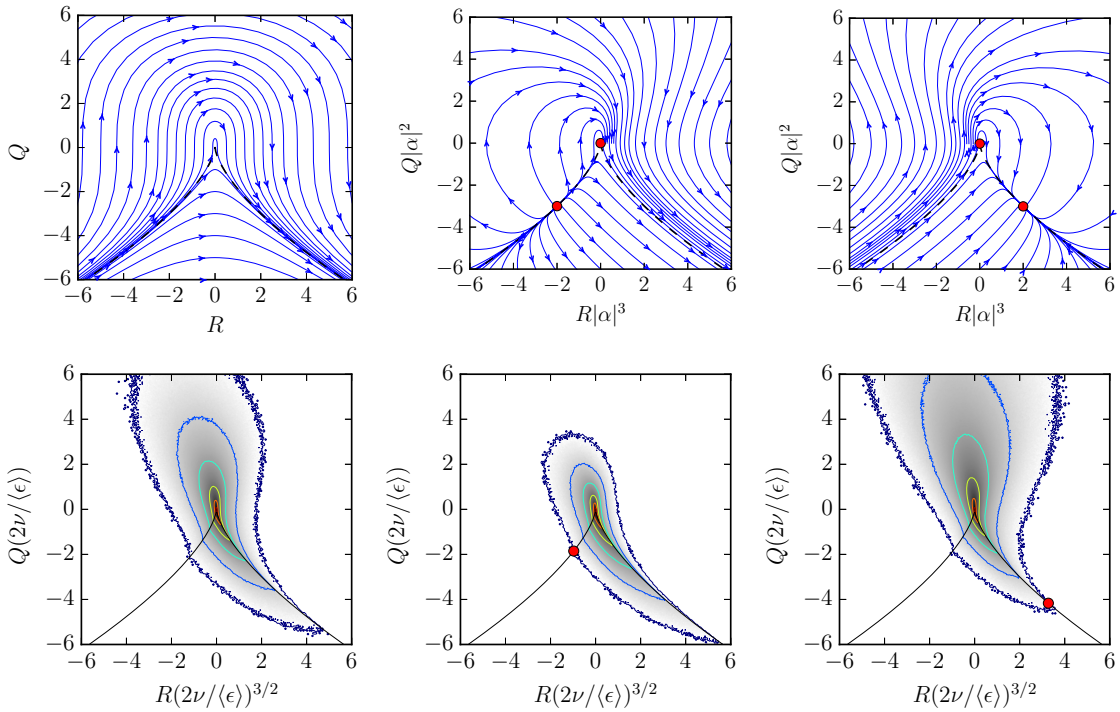

Figure 9.2: Restricted Euler streamlines (top) and DNS-computed joint-PDF iso-contours (bottom) for Lagrangian trajectories (left), heavy particle trajectories with $\beta = 0$, $St = 0.3, \alpha = 1.8\sqrt{\nu/\langle\epsilon\rangle}$ (center), and light particle trajectories with $\beta = 3$, $St = 0.1, \alpha = -1.2\sqrt{\nu/\langle\epsilon\rangle}$ (right). The timescale $|\alpha|$ is used to normalize the axes on the streamline plots, while $\sqrt{2\nu/\langle\epsilon\rangle}$ is used to normalize the axes for the DNS results, where $\langle\epsilon\rangle$ is the average turbulent dissipation rate from the simulation. The red circles show fixed points of the RQ dynamics, providing a visual connection between the two normalizations. The DNS data is from a pseudo-spectral simulation performed at $Re_\lambda = 185$ with a grid resolution of 512^3.[188] The PDF iso-contours are spaced logarithmically with levels 10^z, $z = 1, 0, -1, -2, -3, -4$.

In the middle row of Figure 9.2, the inertial restricted Euler phase-space portrait is shown for the case of heavy particles ($\alpha > 0$). The finite-time singularity down the Vieillefosse line in the fourth quadrant remains and is strengthened. In addition, some initial conditions proceed to a finite-time singularity down the other branch of the Vieillefosse line in the third quadrant, however it is a very unstable manifold in the third quadrant, meaning that any noise in the system will prevent particles from proceeding to that singularity. In the first quadrant, the downward "flow" of particles is enhanced while the left-to-right "flow" is suppressed. The DNS results for heavy particles indeed show the tendency down the Vieillefosse tail in the fourth quadrant, as well as reduced probabilities in the upper half ($Q > 0$).

Finally, the phase-space trajectories for light particles ($\alpha < 0$) are shown on the bottom row of Figure 9.2. The restricted Euler trajectories tend to proceed toward the fixed point in the fourth quadrant. There, a rapid collapse towards Vieillefosse tail is followed by slower evolution along it towards the fixed point. The restricted Euler dynamics impose more resistance to (e.g. noise-driven) movement away from the tail than movement along the tail. Trajectories no longer exhibit a finite-time singularity down the Vieillefosse tail. However, some trajectories in the second and third quadrants (e.g. $R(0)|\alpha|^3 < -3.2$ with $Q(0)|\alpha|^2 = 0$) do blow up in finite time with $Q > 0$ along inverted Vieillefosse-like manifolds with $Q \sim R^{2/3}$. The joint-PDF from DNS data indeed suggests that the Viellefosse tail is still dynamically important for light particles, but that light particles do not tend to reach extreme states as far

down the Viellefosse tail compared with neutral and heavy particles, an effect that may be qualitatively linked to the fixed point in the restricted Euler dynamics. The fixed point here takes on a clear physical interpretation, that inertial effects prevent light particles from sampling regions of the flow with more extreme values down the Vieillefosse tail. In general, the lower probabilities in the $Q < 0$ region are offset by higher probabilities in the $Q > 0$ region. Additionally, the upward and left-to-right movement in the first quadrant (toward $R \gg 0$) of the inertial restricted Euler streamlines is consistent with the enhanced probabilities observed in the DNS results.

While the qualitative comparisons between streamlines of the inertial restricted Euler system and joint-PDFs from DNS are encouraging for both heavy and light particles, quantitative comparison of stationary statistics cannot be accomplished without models for the neglected unclosed terms, as was also the case for the original restricted Euler system.[69] Besides the pressure Hessian and viscous Laplacian, additional modeling work is likely necessary for the additional terms introduced for inertial trajectories, namely $\partial \left[\left(v_i - u_i \right) A_{ij} \right] / \partial x_k$. It is important to note that the finite-time singularities in the original and inertial restricted Euler are not physical and exist only because of the absence of the neglected terms.

The St numbers used in Figure 9.2 are evidently low enough for good qualitative agreement and increasing accuracy of the linear perturbation solution with further decreasing St could be further investigated with the careful development of reliable statistical closure schemes for the neglected terms to enable quantitative comparisons.

For larger St (or larger $|\alpha|$) the model predicts that the equilibrium points will move ever closer to the origin, thus increasing the deviations of the joint PDF with those along tracer particles. This can be appreciated by comparing with the DNS of Ref. 246, which were for larger St than the present results.

9.3 Analysis

Due to its inherent simplicity, many of the features of the inertial restricted Euler system can be investigated analytically. A salient feature of the original restricted Euler equation ($\alpha = 0$) is the invariant $Q^3 + \frac{27}{4}R^2$.[137,139] For the extended system given by (9.3),

$$\frac{d}{dt}\left(Q^3 + \frac{27}{4}R^2\right) = -2\alpha Q\left(Q^3 + \frac{27}{4}R^2\right), \tag{9.4}$$

so that for the particular choice $Q^3 + \frac{27}{4}R^2 = 0$, this remains an invariant of the dynamics. Strikingly, this means that the Vieillefosse tail, $Q_v(R) = -\left(\frac{27}{4}\right)^{1/3} R^{2/3}$, is an invariant manifold for all values of α, an important observation clearly supported by the DNS evidence in Figure 9.2.

It is straightforward to show that (9.3) has two fixed points, one at the origin and another at $R_0 = -2/\alpha^3$, $Q_0 = -3/\alpha^2$, which lies on the Vieillefosse tail, i.e., $Q_0^3 + \frac{27}{4}R_0^2 = 0$ as clearly seen in Figure 9.2. Linear stability analysis of this fixed point reveals eigenvalues of $\lambda_1 = 6/\alpha$ and $\lambda_2 = 1/\alpha$ with (unnormalized) eigenvectors $\mathbf{e}^{(1)} = \left(1, -\frac{3}{2}\alpha\right)^T$ and $\mathbf{e}^{(2)} = (1, \alpha)^T$. The fixed point is unstable for heavy particles

and stable for light particles, as seen in Figure 9.2. The slope of the Vieillefosse tail at the fixed point is $dQ_v/dR|_{Q_0} = \alpha$, so that the eigenvector associated with the more weakly stable/unstable eigenvector points along the Vieillefosse manifold.

Along the Vieillefosse manifold, the dynamics are given by $dR/dt = \frac{3}{2^{1/3}}R^{4/3} + \frac{3}{2^{2/3}}\alpha R^{5/3}$, which for $\alpha \neq 0$ can be written as

$$\frac{dR}{dt} = \frac{6}{\alpha^4}\left[\left(\frac{R}{R_0}\right)^{4/3} - \left(\frac{R}{R_0}\right)^{5/3}\right]. \tag{9.5}$$

This shows the reinforcement of the original finite-time singularity behavior in the fourth quadrant for heavy particles as well as a similar path to singularity in the third quadrant, for $R < R_0 < 0$. It also shows that there is no longer a finite-time singularity along the Vieillefosse manifold for light particles due to the stable fixed point. This stable fixed point for light particles highlights the role of inertia in counteracting the tendency toward more heavily strain-dominated regions down the Vieillefosse tail. This tendency, meanwhile, is strengthened for heavy particles.

The linear stability of the Vieillefosse manifold is examined by considering the trajectory $Q(R) = Q_v(R) + \epsilon(R)$. Using $d\ln\epsilon/dt = d\ln\epsilon/dR\ dR/dt$, the linearized behavior of ϵ can be shown to be

$$\frac{d\ln\epsilon}{dt} = 2^{1/3}\alpha R^{1/3}\left(R^{1/3} - \left(\frac{16}{\alpha^3}\right)^{1/3}\right). \tag{9.6}$$

When $d\ln\epsilon/dt > 0$, the Vieillefosse line is an unstable manifold. When $d\ln\epsilon/dt < 0$

it is a stable manifold. The stability of the manifold changes sign twice: once at the origin, and also at the point

$$(R_s, Q_s) = \left(\frac{16}{\alpha^3}, -\frac{12}{\alpha^2}\right). \tag{9.7}$$

For $\alpha > 0$ (heavy particles), the Vieillefosse manifold is stable for $0 < R < R_s$ while unstable if $R < 0$ or $R > R_s$. Meanwhile, for $\alpha < 0$ (light particles), it is stable for $R < R_s$ or $R > 0$ and unstable for $R_s < R < 0$. The point of neutral stability, R_s, has an opposite sign to the fixed point, R_0, and is also eight times larger in magnitude. Thus, it is unlikely to be of much relevance to the stationary statistics at low St number, as shown in Figure 9.2.

9.4 Conclusions

With only two degrees of freedom, the extension of the restricted Euler system for inertial particle paths yields qualitative agreement with basic trends seen from DNS in the RQ plane. The trends observed follow directly from first principles, i.e from the "self-stretching" properties of the nonlinear term in the Navier-Stokes and particle transport equations whose effects are elucidated here by neglecting all of the "non-local" spatial flux terms. While the restricted Euler system cannot itself offer quantitative predictions in most cases, the qualitative success in representing basic inertial effects suggests that it can be a good starting point for developing more

complete models for velocity gradients along particle trajectories for applications such as preferential (fractal) concentration[79,177,248] of heavy and light anisotropic particles[14,44] and deformation of liquid droplets[9] or bubbles when inertial trajectory effects are important.

Chapter 10

Summary and Conclusions

The research presented in this dissertation centers on the behavior of the velocity gradient tensor in turbulent flows and its stretching and rotating qualities following particle trajectories. The first part, chapters 3 through 5, explore cumulative stretching and deformation statistics in isotropic turbulence and turbulent channel flow using DNS. Following that, chapters 6 through 9 dealt with modeling challenges for constructing low-dimensional dynamical systems which mimic the evolution of the velocity gradient tensor along Lagrangian and inertial paths. The insights obtained in these works lay a foundation for physical understanding and efficient computational modeling of velocity gradients in turbulence, particularly following particle trajectories.

By considering the large deviation principle for joint FTLE statistics, chapter 3 explored the geometry of infinitesimal material volume deformation using the full

Lyapunov spectrum, which plays a role in important dynamics such as surface area stretching relevant to flamelet combustion[157] or the deformation of three-dimensional objects in a flow. This analysis showed a tendency toward $\gamma_2 > 0$, that is, material surface area stretching rates exceeding those of material lines. The joint Cramér function revealed that both weakly and strongly deformed trajectories experience this bias toward $\gamma_2 > 0$. In addition, chapter 3 explored the impact of rotation by vorticity and non-persistent straining on these stretching rates. Both of these processes play a roughly equal role in decreasing the stretching rates by about a factor of 3 below their potential value (the scenario with perfect alignment between cumulative deformation eigenvectors and strain-rate eigenvectors). This means that embedded particles which have higher or lower sensitivity to vorticity, e.g. droplets with viscosity different from the surrounding fluid, will experience a decrease or increase in efficiency of geometrical alignment with the strain-rate tensor, respectively. Future work could explore this effect in more detail by weighting strain and vorticity at various levels to mimic this viscosity ratio effect. It was also shown that much of the asymmetry in the marginal Cramér functions can be explained by the incompressibility constraint with Gaussian variables, without the need to invoke intermittency effects.

Chapter 4 introduced an analogue to the FTLE for vorticity stretching and showed that it has a large deviation principle. The Cramér function for cumulative vorticity stretching was introduced, allowing for direct comparison between material lines stretching and vorticity stretching in terms of their large-deviation statistics. It is

well-known that, while vorticity stretching shares some similarity with material line stretching, important differences exist, such as viscous tilting and two-way coupling with the strain-rate. As a result the mean vorticity stretching is slightly lower than mean material line stretching, but with overall quite similar statistics.

The mean vorticity stretching (Lyapunov exponent analog), $\lambda_\omega = \langle \widehat{\omega}_i S_{ij} \widehat{\omega}_j \rangle \approx 0.10 \tau_\eta^{-1}$, bears some resemblance to the average enstrophy production, which has an analytically-derived value of $\langle \omega_i S_{ij} \omega_j \rangle = -\frac{7}{6\sqrt{15}} \mathcal{S} \tau_\eta^{-3} \approx 0.18 \tau_\eta^{-3}$, where $\mathcal{S} \approx -0.6$ is the longitudinal velocity derivative skewness with value given from the $Re_\lambda \approx 430$ DNS. Batchelor even confuses these two averages in equation (6.1) of Ref. 16, writing in effect, $\langle \widehat{\omega}_i S_{ij} \widehat{\omega}_j \rangle = -\frac{7}{6\sqrt{15}} \mathcal{S} \tau_\eta^{-1} \approx 0.18 \tau_\eta^{-1}$, which can be corrected by the values obtained in this dissertation (almost a factor of 2 different). This impacts Batchelor's model for heat (or mass) transfer with diffusion coefficient κ to a small sphere of radius a in turbulence – equation (4.4) of Ref. 16,

$$Nu_t \approx 0.968 \left(\frac{a^2 \langle \widehat{\omega}_i S_{ij} \widehat{\omega}_j \rangle}{\kappa} \right)^{1/3}, \tag{10.1}$$

where $Nu_t = \frac{h_t a}{\kappa}$ is the Nusselt number and h_t is the heat transfer coefficient. He uses this to obtain in equation (7.1) of Ref. 16,

$$Nu_t \approx 0.55 Pe_t^{1/3}, \tag{10.2}$$

where $Pe_t = \frac{a^2}{\kappa \tau_\eta}$ is the turbulent Peclet number based on the Kolmogorov scales. The

values observed in this work from DNS, $\langle \widehat{\omega}_i S_{ij} \widehat{\omega}_j \rangle \approx 0.10 \tau_\eta^{-1}$ (note the 0.10 instead of Batchelor's 0.18) instead lead to

$$Nu_t \approx 0.45 Pe_t^{1/3}, \tag{10.3}$$

which represents a decrease of about 20% in the predicted heat (or mass) transfer rate. This is important, e.g., for modeling nutrient uptake rates for phytoplankton,[15] where Batchelor's model is directly used.

While the results of chapters 3 and 4 are from isotropic turbulence, it is shown in chapter 5 that these quantities have very similar statistics in a turbulent channel flow DNS for $y^+ > 100$. This underscores the basic insight of Kolmorogov[37] that turbulence at small-scales far enough from solid boundaries will be well approximated by isotropic turbulence. The influence of vorticity and non-persistence of strain-rate in decreasing the stretching efficiency (stretching per unit dissipation) of turbulence becomes even stronger in the buffer and viscous sublayers of the channel flow. The competing effects of increasing dissipation rate (available strain-rate) and decreasing alignment efficiency between material lines and strain-rate eigenvectors results in a maximum stretching in the buffer layer, $10 \leq y^+ \leq 20$. The physics of material line stretching near the wall is important for applications such as polymer drag reduction,[3,4] where the stretching of polymers near the wall and the relaxation to a coiled configuration further away leads to a dramatic change in the mean velocity profile

and viscous drag. The movement of fluid particles toward and away from the wall is highlighted by the much wider Cramér functions in the channel flow compared with isotropic turbulence. Interesting future work could explore the Cramér function and other stretching statistics in wall bounded flows when the two-way coupling of polymer elasticity with flow is included.

Chapter 6 shifts from the focus on DNS observations in the former chapters to the development of predictive models for velocity gradient dynamics along fluid particle trajectories. These models have very few numerical degrees of freedom compared with DNS and offer a dramatic reduction in cost. The price for this dramatic reduction in computational cost is the requirement for closure models for the pressure Hessian and viscous Laplacian. A novel closure for these terms was developed in chapter 6 using a short-time Lagrangian deformation map applied to Gaussian field statistical calculations. The model is named the Recent Deformation of Gaussian Fields (RDGF) model and bears some resemblance to previous closure ideas such as the mapping closures of Kraichnan and co-workers,[213,214] though the context and details are obviously different. This new closure permits the simulation of Lagrangian velocity gradient time histories at a tiny fraction of the cost of DNS and shows remarkable agreement for a wide range of statistical quantities. The closures are carefully developed from well-controlled and physically motivated approximations which capture the essential physics of the pressure Hessian in QR space, yet do not require parameters to be adjusted to match DNS values (the EGF model[147]). One difficulty in the RDGF model

(and other similar models) is that the formulation is constructed for consistency with the Fokker-Planck equation for the single-time PDF. This means that even a perfect model for the conditional averages which gives agreement for single-time statistics may still not match DNS for multi-time statistics such as autocorrelations and higher order quantities. One important effect which is difficult to capture is the disparity between strain and vorticity autocorrelation timescales, which could be very important for Lagrangian-integrated physics such as particle rotation and deformation. An important question for future research is whether a more general formulation can be developed to capture these multi-time statistics accurately in a low-cost model.

While the RDGF model developed in chapter 6 matches DNS statistics well for isotropic turbulence at low Re_λ, it does not contain a mechanism for increasing the Reynolds number. Chapter 7 provides such a mechanism using a multiple time scale approach. This approach takes advantage of the similarity between fully-resolved and coarse-grained velocity gradient dynamics, particularly in terms of the closed $\mathbf{A}^2$ term, which is important for energy cascade dynamics. A very simple constant turbulent viscosity closure for the sub-grid Hessian is used and energy dissipation rates are balanced between adjacent levels, though more complex ones could certainly be developed. This approach effectively provides a way to 'localize' the RDGF closure, i.e., to close the conditional averages based on a local dissipation rate rather than a global one. The resulting model matches known intermittency effects, such as the power-law growth of skewness and flatness factors, with remarkable accuracy, un-

derscoring the advantages of exploring the intermittency phenomenon (an important one in turbulence theory) from the perspective of Lagrangian velocity gradients. The multiple time scale RDGF model does require setting one tunable parameter: the ratio of time scales between levels, $\beta = 10$. Future work may be able to eliminate or constrain this parameter with physical considerations, resulting in parameter-free intermittency predictions. One possible way forward is to increase the fidelity of the sub-grid Hessian closure beyond the simple model used here. Such models may also be able to reproduce effects such as the dramatic increase of skewness and flatness for $\widetilde{\mathbf{A}}$ when the filter width enters the dissipation range – an effect possibly tied to the fluctuating Kolmogorov length scale in Nelkin's theory.[170] It may also be insightful to study this modeling approach in higher dimensions,[249] such as four-dimensional turbulence.[250]

The focus of chapters 6 and 7 is homogeneous isotropic turbulence. While local isotropy of the velocity gradient is shown to hold quite well in chapter 5 for inhomogeneous flows, large-scale inhomogeneity can play an important role in Lagrangian velocity gradient dynamics more complex flows. The main idea of chapter 7 for coupling a coarse-grained and fine-grained representation through dissipation rate balances naturally carries over to LES, where the coarse-grained field is resolved using standard LES techniques instead of a dynamical model for $\widetilde{\mathbf{A}}$. This development, demonstrated in chapter 8, provides an economical way to simulate Lagrangian velocity gradient dynamics (e.g. droplet deformation) in high Reynolds number tur-

bulent flows, bypassing the requirements of DNS for directly resolving the smallest scales of turbulence. The RDGF-LES model is tested against DNS of a turbulent channel flow at $Re_\tau = 1000$ and provides quite favorable comparisons, using a grid 16 times coarser in each direction. The computational savings can be even more significant for larger Reynolds number turbulent flows. This demonstrates the extent to which models such as the RDGF closure can have on practical situations with complex turbulent flow geometries. The model does rely on the LES providing accurate dissipation rates, Π, something not always considered in the development of SGS models. Further, the RDGF model being developed under the assumption of local isotropy, significant modeling error is expected near solid boundaries and further work is needed for developing wall models for this approach.

Finally, the inertia of a particle can profoundly influence its path in turbulence, causing it to deviate from fluid or inertia-free trajectories. Capturing this effect could be quite important in many applications, because heavier particle tend to sample more strain-dominated regions while lighter particles tend to move toward more vorticity-dominated regions. The success of chapters 6 through 8 is rooted in the fact that the Lagrangian velocity gradient formulation captures the self-stretching nonlinear term ($\mathbf{A}^2$) exactly from the Navier-Stokes equations. Chapter 9 introduces an inertial particle correction to the original restricted Euler system, which considered Lagrangian trajectories. In so doing, key qualitative aspects of velocity gradient behavior along inertial trajectories (such as the preferential concentration effect men-

tioned above) are qualitatively mimicked in a dynamical system reduced to 2 degrees of freedom. The inertial restricted Euler system created provides a very simple model with analytically-derivable features in which some basic aspects of inertial particles are captured. Furthermore, the qualitative success opens the door to more quantitative models, which must be constructed to avoid finite-time singularities by statistical modeling of unclosed terms. Such modeling efforts, left to future work, could provide an extension of the modeling approaches in chapters 6 through 8 to inertial particles. This could provide a new approach to quantifying turbulence-induced preferential concentration as well as other velocity gradient-related physics, such as deformation and rotation of embedded particles, when density mismatch plays an important role.

Appendix A

Comparison of the Cramér Function for FTLEs Using Two Alternate Definitions

In this appendix, we consider the two definitions for the Lyapunov exponents introduced in Section 2.1.1. First, using the singular values of the deformation tensor, we have

$$\gamma_i(\mathbf{X}, t) = \frac{1}{t - t_0} \ln(\sigma_i(\mathbf{X}, t)), \tag{A.1}$$

and using the length of an infinitesimal line element, we have,

$$\gamma(\mathbf{X}, t) = \frac{1}{t - t_0} \ln\left(\frac{|\mathbf{r}(\mathbf{X}, t)|}{|\mathbf{r}(\mathbf{X}, t_0)|}\right), \tag{A.2}$$

which approaches γ_1 at long integration times. In the following, we explore the statistics of this second definition in comparison to the first.

A.1 Two-Dimensions

For simplicity, we complete the following illustration in two-dimensions, which is qualitatively instructive also for the three-dimension scenario considered in chapter 3. Consider an infinitesimal line element $\mathbf{r}$ in two dimensions stretched (or compressed) by the velocity gradient. For a given integration time T, let us denote the direction of the largest stretching by $\mathbf{e}_1$, which is the eigenvector of the Cauchy-Green tensor associated with the largest eigenvalue. Perpendicular to that vector, we have $\mathbf{e}_2$, the eigenvector associated with the other (smaller) eigenvalue. The length of the material line is given by

$$|\mathbf{r}(t)|^2 = e^{2\gamma_1 t}(\mathbf{r}(0)\cdot\mathbf{e}_1)^2 + e^{2\gamma_2 t}(\mathbf{r}(0)\cdot\mathbf{e}_2)^2, \tag{A.3}$$

and introducing the angles

$$\cos\theta_i = \frac{\mathbf{r}(0)\cdot\mathbf{e}_i}{|\mathbf{r}(0)|}, \qquad i = 1, 2, \tag{A.4}$$

we can write

$$\gamma = \frac{1}{2T}\ln\left(e^{2\gamma_1 t}\cos^2\theta_1 + e^{2\gamma_2 t}\cos^2\theta_2\right) = \frac{1}{2T}\ln\left(e^{2\gamma_1 t}\sin^2\theta_2 + e^{2\gamma_2 t}\cos^2\theta_2\right). \tag{A.5}$$

The probability density function for γ is then

$$p(\gamma, T) = \iiint p_{12\theta}(\gamma_1, \gamma_2, \theta_2, T)\delta\left(\gamma - \frac{1}{2T}\ln\left(e^{2\gamma_1 T}\sin^2\theta_2 + e^{2\gamma_2 T}\cos^2\theta_2\right)\right)d\gamma_1 d\gamma_2 d\theta_2, \quad \text{(A.6)}$$

where $p_{12\theta}$ is the joint-probability density function of the two FTLEs as well as the angle of the initial perturbation vector with the eigenvectors associated to γ_2. Upon assuming an isotropic distribution of initial material lines, the distribution of θ_2 is uniform on the interval $[0, \pi/2]$ and independent of γ_1 and γ_2,

$$p_{12\theta}(\gamma_1, \gamma_2, \theta_2, T) = \frac{2}{\pi}p_{12}(\gamma_1, \gamma_2, T). \quad \text{(A.7)}$$

For an approximation at long times, we split the integral into two parts, one for which the γ_1 dominates and one for which γ_2 dominates, with the delineation made at

$$e^{2\gamma_1 T}\sin^2\theta_2^{cr} = e^{2\gamma_2 T}\cos^2\theta_2^{cr}, \qquad \text{i.e. } \theta_2^{cr} = \tan^{-1}\left(e^{(\gamma_2-\gamma_1)T}\right). \quad \text{(A.8)}$$

This results in

$$p(\gamma, T) = \frac{2}{\pi}\iint p_{12}(\gamma_1, \gamma_2, T)\left(\int_0^{\theta_2^{cr}}\delta(\gamma-\gamma_2)d\theta_2 + \int_{\theta_2^{cr}}^{\pi/2}\delta(\gamma-\gamma_1)d\theta_2\right)d\gamma_1 d\gamma_2. \quad \text{(A.9)}$$

Carrying out the sifting property of the Dirac delta-functions, we are left with

$$p(\gamma,T)=\int\frac{2\theta_2^{cr}}{\pi}p_{12}(\gamma_1,\gamma,T)d\gamma_1+\int\left(1-\frac{2\theta_2^{cr}}{\pi}\right)p_{12}(\gamma,\gamma_2,T)d\gamma_2. \tag{A.10}$$

For long time, with $\gamma_2<\gamma_1$, it is easy to verify that $\theta_2^{cr}\ll 1$, and using $\tan^{-1}(x)\approx x$ for small x, then

$$p(\gamma,T)=\int\frac{2}{\pi}e^{(\gamma-\gamma_1)T}p_{12}(\gamma_1,\gamma,T)d\gamma_1+\int p_{12}(\gamma,\gamma_2,T)d\gamma_2. \tag{A.11}$$

The second term simply gives the marginal pdf,

$$p(\gamma,T)=\int\frac{2}{\pi}e^{(\gamma-\gamma_1)T}p_{12}(\gamma_1,\gamma,T)d\gamma_1+p_1(\gamma,T). \tag{A.12}$$

Substituting the large-deviation form for the marginal and joint-pdf,

$$p(\gamma,T)=\int C_{12}\exp\left[-T\left(S_{12}(\gamma_1,\gamma)+\gamma_1-\gamma\right)\right]d\gamma_1+C_1\exp\left(-TS_1(\gamma)\right). \tag{A.13}$$

and using the steepest-descent method for the first term,

$$p(\gamma,T)=C'_{12}\exp\left[-T\inf_{\gamma_1}\left(S_{12}(\gamma_1,\gamma)+\gamma_1-\gamma\right)\right]+C_1\exp\left(-TS_1(\gamma)\right). \tag{A.14}$$

The Cramér function is then

$$S(\gamma) = \lim_{T\to\infty} \frac{1}{T} \ln\left(p(\gamma, T)\right) = \min\left\{ S_1(\gamma), \inf_{\gamma_1} \left(S_{12}(\gamma_1, \gamma) + \gamma_1 - \gamma\right) \right\}. \tag{A.15}$$

Thus, we see a subtle difference in the Cramér function considering material elements $S(\gamma)$, with that obtained from the singular value decomposition, $S_1(\gamma)$. One primary conclusion for the three-dimensional system is that while $S_1(\gamma)$ requires positive γ_1, the same cannot be said of $S(\gamma)$ for the material lines, where negative γ is possible. To correct this qualitatively in the Gram-Schmidt numerical method in chapter 3, the stretching rates given by each renormalization are re-ordered so that γ_1 is always positive.

A.2 Three-Dimensions, Volume-Preserving

Now we extend the above analysis to three dimensions so as to get a result for which we can utilize the joint-Cramér functions found in chapter 3. In three dimensions, the infinitesimal material line has length

$$|\mathbf{r}(t)|^2 = e^{2\gamma_1 T}(\mathbf{r}(0)\cdot\mathbf{e}_1)^2 + e^{2\gamma_2 T}(\mathbf{r}(0)\cdot\mathbf{e}_2)^2 + e^{2\gamma_3 T}(\mathbf{r}(0)\cdot\mathbf{e}_3)^2, \tag{A.16}$$

with the constraint $\gamma_1 + \gamma_2 + \gamma_3 = 0$. For integrating over all possible alignments, we need to angles (spherical coordinates), ϕ and θ, such that

$$\begin{gathered}\mathbf{r}(0)\cdot\mathbf{e}_1 = |\mathbf{r}(0)|\sin\phi, \qquad \mathbf{r}(0)\cdot\mathbf{e}_2 = |\mathbf{r}(0)|\cos\phi\sin\theta, \\ \mathbf{r}(0)\cdot\mathbf{e}_3 = |\mathbf{r}(0)|\cos\phi\cos\theta,\end{gathered} \tag{A.17}$$

which gives

$$\begin{aligned}\gamma &= \frac{1}{T}\ln\left(\frac{|\mathbf{r}(T)|}{|\mathbf{r}(0)|}\right) \\ &= \frac{1}{2T}\ln\left(e^{2\gamma_1 T}\sin^2\phi + e^{2\gamma_2 T}\cos^2\phi\sin^2\theta + e^{2\gamma_3 T}\cos^2\phi\cos^2\theta\right).\end{aligned} \tag{A.18}$$

The probability density for γ is then

$$\begin{aligned}p(\gamma,T) = \iiiint p_{13\phi\theta}(\gamma_1,\gamma_3,\phi,\theta,T)\cos\phi \\ \delta\left(\gamma - \frac{1}{2T}\ln\left(e^{2\gamma_1 T}\sin^2\phi + e^{2\gamma_2 T}\cos^2\phi\sin^2\theta + e^{2\gamma_3 T}\cos^2\phi\cos^2\theta\right)\right) d\phi d\theta d\gamma_1 d\gamma_3.\end{aligned} \tag{A.19}$$

Assuming independence of the FTLEs from the initial angle and an isotropic distribution of material lines over initial angles, we write

$$p_{13\phi\theta}(\gamma_1,\gamma_3,\phi,\theta) = \frac{2}{\pi}p_{13}(\gamma_1,\gamma_3). \tag{A.20}$$

Further, we approximate the integral for long times by splitting the unit sphere of initial solid angles in the positive octant in 3D space into three regions where each of

the three terms in the expression for γ dominate separately. We create these regions by defining critical angles from

$$e^{2\gamma_1 t}\sin^2\phi^{(cr)} = e^{2\gamma_2 t}\cos^2\phi^{(cr)}\sin^2\theta,$$
$$\text{with} \quad \sin^2\theta \sim 1, \qquad \phi^{cr} = \tan^{-1}\left(e^{(\gamma_2-\gamma_1)T}\right) \approx e^{(\gamma_2-\gamma_1)T}, \quad \text{(A.21)}$$

with the approximation made for $\gamma_2 < \gamma_1$ and long time hence $e^{(\gamma_2-\gamma_1)T} \ll 1$ (i.e. $\tan^{-1}(x) \approx x$ for $x \ll 1$). Additionally,

$$e^{2\gamma_2 T}\cos^2\phi\sin^2\theta^{(cr)} = e^{2\gamma_3 T}\cos^2\phi\cos^2\theta^{(cr)},$$
$$\text{i.e.} \quad \theta^{(cr)} = \tan^{-1}\left(e^{(\gamma_3-\gamma_2)T}\right) \approx e^{(\gamma_3-\gamma_2)T}. \quad \text{(A.22)}$$

In this approximation, we break the Dirac delta function as follows,

$$\delta\left(\gamma - \frac{1}{2T}\ln\left(e^{2\gamma_1 T}\sin^2\phi + e^{2\gamma_2 T}\cos^2\phi\sin^2\theta + e^{2\gamma_3 T}\cos^2\phi\cos^2\theta\right)\right)$$
$$= \begin{cases} \delta(\gamma-\gamma_1) & , \ \phi > \phi^{(cr)} \\ \delta(\gamma-\gamma_2) & , \ \phi < \phi^{(cr)} \wedge \theta > \theta^{(cr)} \\ \delta(\gamma-\gamma_3) & , \ \phi < \phi^{(cr)} \wedge \theta < \theta^{(cr)} \end{cases} \quad \text{(A.23)}$$

With the above substitutions, we get

$$p(\gamma,T)=\frac{2}{\pi}\iint p_{13}(\gamma_1,\gamma_3,T)\left[\left(\delta(\gamma-\gamma_1)\int_0^{\pi/2}\int_{\phi^{(cr)}}^{\pi/2}\cos\phi d\phi d\theta\right)\right.$$
$$\left.+\left(\delta(\gamma-\gamma_2)\int_{\theta^{(cr)}}^{\pi/2}\int_0^{\phi^{(cr)}}\cos\phi d\phi d\theta\right)+\left(\delta(\gamma-\gamma_3)\int_0^{\theta^{(cr)}}\int_0^{\phi^{(cr)}}\cos\phi d\phi d\theta\right)\right]d\gamma_1 d\gamma_3, \tag{A.24}$$

carrying out the integrals, with appropriate approximations in the limits $\phi^{(cr)}\ll 1$, $\theta^{(cr)}\ll 1$,

$$p(\gamma,T)=\iint p_{13}(\gamma_1,\gamma_3,T)$$
$$\left[\delta(\gamma-\gamma_1)+\phi^{(cr)}\delta(\gamma-\gamma_2)+\frac{2\theta^{(cr)}}{\pi}\phi^{(cr)}\delta(\gamma-\gamma_3)\right]d\gamma_1 d\gamma_3, \tag{A.25}$$

and substituting for the critical angles, with $\delta(\gamma-\gamma_2)=\delta(\gamma+\gamma_1+\gamma_3)$,

$$p(\gamma,T)=p_1(\gamma,T)+\int p_{13}(\gamma_1,-\gamma_1-\gamma,T)e^{(\gamma-\gamma_1)T}d\gamma_1$$
$$+\frac{2}{\pi}\int p_{13}(\gamma_1,\gamma,T)e^{(\gamma-\gamma_1)T}d\gamma_1. \tag{A.26}$$

For each of the PDFs in this expression, we substitute the large-deviation form,

$$p(\gamma,T)=C_1\exp\left(-TS_1(\gamma)\right)+C_{12}\int\exp\left(-T\left[S_{13}(\gamma_1,-\gamma_1-\gamma)-\gamma+\gamma_1\right]\right)d\gamma_1$$
$$+C_{13}\int\exp\left(-T\left[S_{13}(\gamma_1,\gamma)-\gamma+\gamma_1\right]\right)d\gamma_1. \tag{A.27}$$

Finally, evaluating the Cramér function for the left hand side using steepest-descent,

$$S(\gamma) = -\frac{1}{T}\ln\left(p(\gamma,T)\right) \tag{A.28}$$
$$= \min\left\{S_1(\gamma), \inf_{\gamma_1}\left[S_{13}(\gamma_1,-\gamma_1-\gamma)-\gamma+\gamma_1\right], \inf_{\gamma_1}\left[S_{13}(\gamma_1,\gamma)-\gamma+\gamma_1\right]\right\}.$$

We stress that this is an *approximate* formulation for the Cramér function based on infinitesimal material line stretching in terms of the Cramér function based on the Cauchy-Green tensor. Nonetheless, it provides an interesting application for the joint-Cramér function calculated in chapter 3. Each of the three terms on the right hand side of Eq. (A.28) are plotted in Fig. A.1 along with the left hand side.

Note from Fig. A.1 that the two correction terms on the right-hand side of Eq. (A.28) open the possibility of negative γ for material line stretching in finite time. In terms of numerical calculations, the difference between the left-hand side function and the first term on the right-hand side of Eq. (A.28) is that the left-hand side is calculated directly from the Gram-Schmidt stretching factor results (specifically, from the element that is never projected), while for the right-hand side we re-order the total stretching after the Gram-Schmidt calculation so that we enforce that $\gamma_1 \geq \gamma_2 \geq \gamma_3$. This re-ordering is done for all the calculations in chapter 3 to enforce the inequality.

The approximation based on the joint-Cramér function and the results in Eq. (A.28) perform well. The difference in considering the two forms of the FTLE (material line vs. Cauchy-Green eigenvalue) is primarily at very small (and possibly

negative) FTLE values.

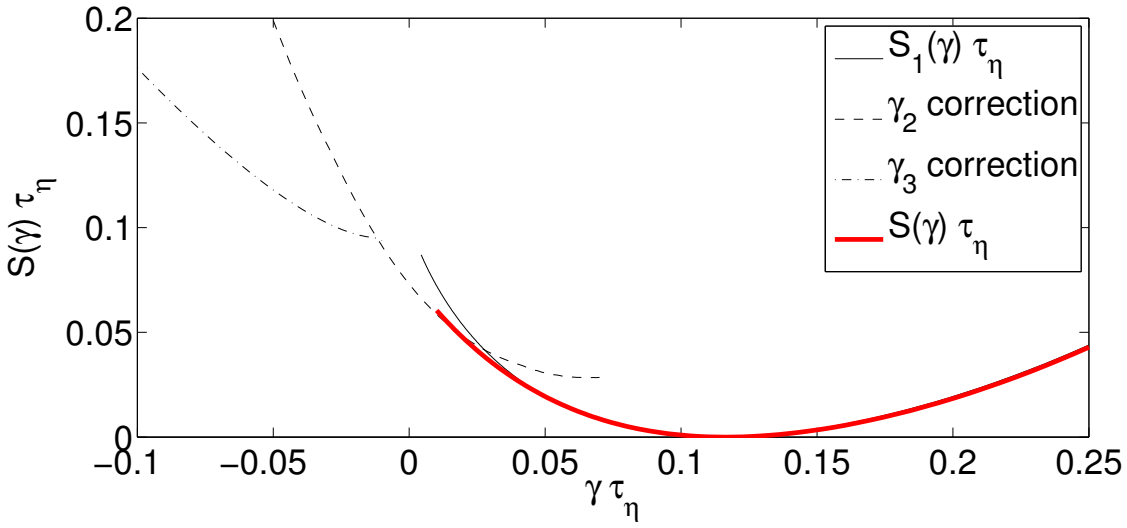

Figure A.1: The Cramér function $S(\gamma)$ for the infinitessimal material line FTLE, $\gamma = \frac{1}{T}\ln\left(\frac{|\mathbf{r}(T)|}{|\mathbf{r}(0)|}\right)$, solid thick (red) line, along with the three terms on the right hand side of Eq. (A.28): $S_1\gamma$, the Cramér function from the largest eigenvalue of the Cauchy-Green tensor, $\gamma_1 = \frac{1}{T}\ln(\sigma_1)$, solid thin (black) line; the correction due to material line stretching dominated by γ_2, $\inf_{\gamma_1}[S_{13}(\gamma_1, -\gamma_1 - \gamma) - \gamma + \gamma_1]$, dashed (black) line; and the correction due to material line stretching dominated by γ_3, $\inf_{\gamma_1}[S_{13}(\gamma_1, \gamma) - \gamma + \gamma_1]$, dashed-dot (black) line.

Appendix B

Code Validation and Error Estimations for Lyapunov Exponents

In this appendix, we apply the numerical routines developed for computing the Cramér function for three-dimensional Lagrangian particles in isotropic turbulence to a model system for validation. Specifically, we compare the minimum point of the Cramér function constructed via the Legendre transform method (§3.2.2). By examining the dependence of the measure LEs for this model system on the integration time of the FTLEs used to construct the Cramér function, the convergence of the technique to the true asymptotic values is explored. We also use trajectory data from another simulation database for exploring the convergence of the method for

the turbulence particle trajectories. With this in hand, we make estimates of the error incurred from finite time effects inherent in the use of the JHTDB database with only 45 Kolmogorov times.

B.1 Validation: Lorenz System

For validation, we use the Lorenz system, introduced in 1963 by Lorenz[251] and studied widely since then. The Lorenz system is a three-dimensional deterministic set of ODEs, with the evolution of state variables x, y, and z given by

$$\begin{cases} \dot{x} = -\sigma x + \sigma y \\ \dot{y} = \rho x - y - xz \\ \dot{z} = xy - \beta z \end{cases} . \tag{B.1}$$

An ensemble of $20,000$ trajectories are integrated using a 4^{th}-order Runge-Kutta scheme, with initial conditions randomly selected in a uniform manner over $1,000$ subregions of the phase space near the attractor. Along each trajectory, the Jacobian,

$$\mathbf{J} = \begin{pmatrix} -\sigma & \sigma & 0 \\ \rho - z & -1 & -x \\ y & x & -\beta \end{pmatrix}, \tag{B.2}$$

is used in place of the velocity gradient tensor in Eq. (2.4) to advance the deformation tensor. For the calculation of the Cramér function, the numerical techniques described in §3.1.2 and §3.2.2 are used.

The minimum point of the Cramér function is the Lyapunov exponents. From the Legendre transform method, it is given by

$$\lambda_i = \left.\frac{dL_i}{dq}\right|_{q=0}. \tag{B.3}$$

Values for Lyapunov exponents are compared against values reported in literature for previous numerical results with three different sets of parameters, shown in Table B.1. Each of these sets result in at least one positive Lyapunov exponent so that the behavior of the trajectories is chaotic.

Table B.1: Three sets of parameters for which comparison is made with previous numerical results for Lyapunov exponents.

	σ	β	ρ
1	10	$\frac{8}{3}$	28
2	16	4	45.92
3	16	4	40

In order to facilitate comparison with the results from turbulent trajectories, a representative time scale for the fastest motions is estimated for each set of parameters. The estimation is based on the clear oscillatory behavior of the state variables in the Lorenz system, with relatively well defined frequency, ω. The representative time scale is then chosen to be $\tau = \omega^{-1}$. This allows for scaling of the results analogous to

the Kolmogorov time scale, τ_η, used for the turbulent trajectories. The trajectories were first advanced for $t = 200\tau$ to reach statistical stationarity, before initializing the deformation tensors and computing the FTLEs for an additional $t = 200\tau$.

The results of these three validation cases are summarized in Table B.2. It should be noted that the Lorenz system is not volume-preserving like the turbulent trajectories considered in this dissertation. In fact, the third set of parameters shows that the minimal LE is very negative in comparison to the slightly positive maximal LE. The middle LE is zero. The values shown are calculated from curve fits applied to the data for $150\tau < t < 200\tau$. For the first set of parameters, the calculation was repeated three times and each of the three values are reported. For all three parameter sets, the numerical procedure used throughout chapter 3 gives results in excellent agreement with previously reported results.

Table B.2: Validation results for the Lyapunov exponents of the Lorenz system.

1: $\sigma = 10$, $\beta = \frac{8}{3}$, $\rho = 28$	λ_1	λ_2	λ_3
Kim and Choe 2010[252])	0.8989	–	–
Alligood et al.[253])	0.905	–	–
Present results	0.8965, 0.9041, 0.9033	–	–
2: $\sigma = 16$, $\beta = 4$, $\rho = 45.92$	λ_1	λ_2	λ_3
Kim & Choe 2010[252])	1.498	–	–
Rosenstein et al. 1993[254])	1.5	–	–
Wolf et al. 1985[255])	1.50	–	-22.5
Present results	1.504	–	-22.5
3: $\sigma = 16$, $\beta = 4$, $\rho = 40$	λ_1	λ_2	λ_3
Sano & Sawada 1985[256])	1.37	-0.02	-15.2
Shimada and Nagashima 1979[257])	1.37	0.00	-22.37
Present results	1.376	1.3×10^{-5}	-22.38

B.2 Convergence of Lyapunov Exponents

First, we investigate the convergence of Lyapunov exponents in time for the Lorenz system. We choose the first set of parameters for further study. For the $\ln\langle\exp(q\gamma_i t)\rangle$ vs t plots, the center of the curve fits range was varied from 50τ to 175τ, with the range including 25τ on either side of marked time. For each curve fit range, the GLEs are constructed and the LE is computed. The results are shown in Fig. B.1. For increasing time, the Lyapunov exponent is clearly approaching an asymptotic value in close agreement with the results reported in the literature. For a fourth simulation, only 2000 trajectories were integrated up to 2000τ and the plateau was confirmed to continue through that time.

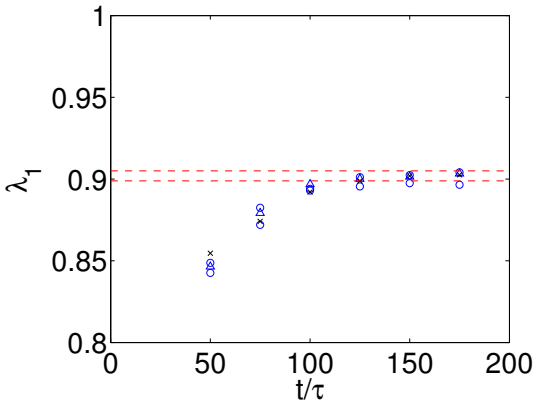

Figure B.1: Variation of computed Lyapunov exponent of the Lorenz system ($\sigma = 10$, $\beta = \frac{8}{3}$, $\rho = 28$) with the curve fit range used for the generalized Lyapunov exponent. Open symbols represent the three identical runs with $20,000$ trajectories and the 'x' markers represent one of the run with only 2000 trajectories. The last symbols (at $t = 175\tau$) represent the results reported in Table B.2 compared to literature (dotted lines).

For the turbulent trajectories, the iCFD database simulation[188] with $Re_\tau = 420$

is used to explore the behavior of the Lyapunov exponent at longer times. This simulation uses a pseudo-spectral method in space with a 2^{nd}-order Adams-Bashforth method for time advancement. The Reynolds number was very close to that of the JHTDB data, allowing for close comparison between the two datasets. Particle trajectories and velocity gradients were calculated during the simulation, having the advantages of spectral differentiation methods for the velocity gradient calculations rather than finite differencing. The velocity gradient data are stored with a time step of about $\Delta t \approx \tau_\eta/17$ over a time interval of about $270\tau_\eta$ for 3184 trajectories. The details of the underlying simulation for the iCFD database are given in Ref. 188 and compared to the JHTDB parameters in Table 2.1.

The maximal LE results for the iCFD data are shown in Fig. B.2. As with the Lorenz system, the Lyapunov exponents appear to be slowly reaching an asymptote, but it is not clear this has been reached, even by $t = 225\tau_\eta$. When the width of the time range used for the curve fit is reduced, the noise is increased in the convergence plots but the overall trend is maintained. Because of the lower number of trajectories, the moments used for the curve fit are more susceptible to statistical noise and hence it is recommended that the curve fits be taken over a long enough range to smooth out the noise.

It is clear that, given enough time, the LEs will converge to a time invariant value. The time needed appears to be at least on the order of $200\tau_\eta$, but the percent error induced by using a shorter time can be estimated from this figure. Furthermore,

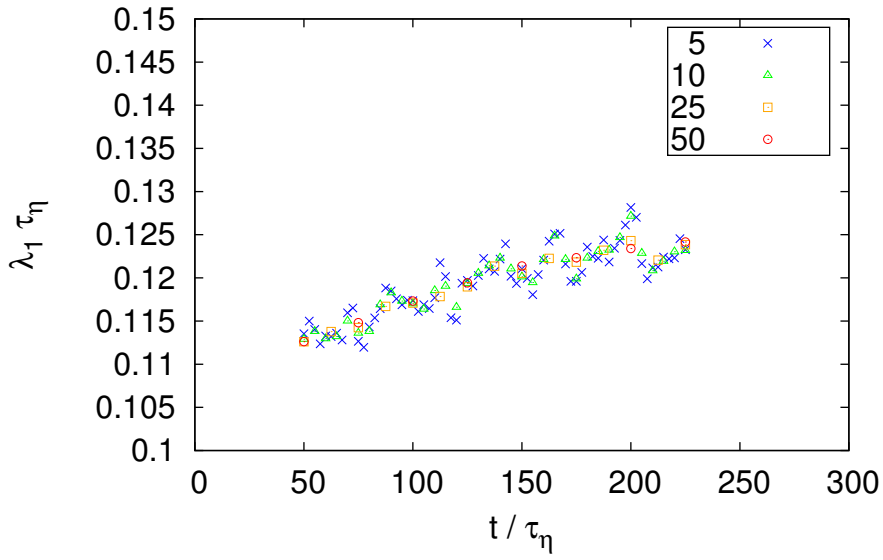

Figure B.2: The trend of maximal LE with increasing time of curve fit range from the iCFD Lagrangian database. The length of the time used for each curve fit range is varied from $5\tau_\eta < t < 50\tau_\eta$.

we expect that other points of the Cramér function will also converge but may take an even longer time. In general, for those shown in Fig. 3.5, we expect that the Cramér function for γ_1 will shift to the left and the Cramér function for γ_3 will shift to the right for increasing integration times. The error induced in the JHTDB results because only $45\tau_\eta$ is available from the database appears to be about 10%. With the help of the iCFD data, the estimate of the Lyapunov spectrum is $\{\lambda_1, \lambda_2, \lambda_3\}\tau_\eta \approx \{0.123, 0.032, -0.155\}$.

Appendix C

Derivation of Finite-Size Effects for Histogram-based Computation of Cramér Functions

C.1 Marginal PDFs

From the large deviation formalism, we expect that the PDF of the FTLE behaves as

$$p(\gamma, t) = N(t) \exp(-tS(\gamma)), \tag{C.1}$$

or

$$S(\gamma) = \lim_{t\to\infty} -\frac{1}{t}[\ln(p(\gamma, t)) - \ln(N(t))], \tag{C.2}$$

where $S(\gamma)$ is the Cramér function characterizing extreme events in the separation of two neighboring particle trajectories. The pre-factor $N(t)$ is a normalization constant so that at any given time t

$$\int_{-\infty}^{\infty} p(\gamma, t) d\gamma = N(t) \int_{-\infty}^{\infty} \exp(-tS(\gamma)) d\gamma = 1. \tag{C.3}$$

For long time t, this integral will only receive non-negligible contributions near the minimum of $S(\gamma)$, so that Laplace's method can be used for integration. This method uses the second-order Taylor series expansion near the minimum

$$S(\gamma) \approx \frac{1}{2}(\gamma - \gamma_0)^2 S''(\gamma_0), \tag{C.4}$$

because

$$S(\gamma_0) = S'(\gamma_0) = 0, \qquad S''(\gamma_0) > 0. \tag{C.5}$$

The resulting integration yields a normalization constant equal to that of a 'Gaussianized' PDF:

$$N(t) = \sqrt{\frac{S''(\gamma_0)t}{2\pi}}. \tag{C.6}$$

The Cramer function is therefore

$$S(\gamma) = -\frac{1}{t} \ln(p(\gamma, t)) + \frac{1}{2t} \ln\left(\frac{tS''(\gamma_0)}{2\pi}\right). \tag{C.7}$$

The curvature of the Cramér function at its minimum contributes a time dependent shift that decays as $t^{-1}\ln(t)$, which is the first order correction for measuring the Cramér function using data with finite time. For numerically evaluating the Cramér function at a finite time, the first term of Eq. (C.7) can be evaluated from the normalized PDF (histogram), then the curvature at the minimum can be measured by curve fitting a parabola through points near the minimum. The curvature can then be used to evaluate the second term of Eq. (C.7), which completes the calculation of the Cramér function.

C.2 Joint PDFs

The same procedure can be repeated to account for finite-time effects in the histogram method for the joint-Cramér function, which has the form

$$p(\gamma_1, \gamma_3, t) = N(t)\exp(-tS(\gamma_1, \gamma_3)). \tag{C.8}$$

The normalization constant of the PDF gives

$$\int_{-\infty}^{\infty}\!\!\int p(\gamma_1, \gamma_3, t)d\gamma_1 d\gamma_3 = N(t)\int_{-\infty}^{\infty}\!\!\int \exp(-tS(\gamma_1, \gamma_3))d\gamma_1 d\gamma_3 = 1, \tag{C.9}$$

which, for long time, will have contribution only from the neighborhood of the minimum where $S(\gamma_{1_0}, \gamma_{3_0}) = 0$. Here we are expecting the Cramér functions to be convex

at the minimum, hence

$$\left.\frac{\partial S}{\partial \gamma_1}\right|_{\gamma_{1_0},\gamma_{3_0}} = 0, \quad \left.\frac{\partial S}{\partial \gamma_3}\right|_{\gamma_{1_0},\gamma_{3_0}} = 0, \quad \left.\frac{\partial^2 S}{\partial \gamma_1^2}\right|_{\gamma_{1_0},\gamma_{3_0}} > 0, \quad \left.\frac{\partial^2 S}{\partial \gamma_3^2}\right|_{\gamma_{1_0},\gamma_{3_0}} > 0. \tag{C.10}$$

The Taylor series truncated after second-order derivatives is the

$$S(\gamma_1,\gamma_3) \approx \frac{1}{2}(\gamma_1-\gamma_{1_0})^2 \left.\frac{\partial^2 S}{\partial \gamma_1^2}\right|_{\gamma_{1_0},\gamma_{3_0}} + (\gamma_1-\gamma_{1_0})(\gamma_3-\gamma_{3_0}) \left.\frac{\partial^2 S}{\partial \gamma_1 \partial \gamma_3}\right|_{\gamma_{1_0},\gamma_{3_0}} + \frac{1}{2}(\gamma_3-\gamma_{3_0})^2 \left.\frac{\partial^2 S}{\partial \gamma_3^2}\right|_{\gamma_{1_0},\gamma_{3_0}}. \tag{C.11}$$

When the Taylor series is used to approximate the integral by steepest descent, the PDF used for normalization is a joint-Gaussian with inverse covariance matrix

$$\mathbf{C}^{-1} = \begin{bmatrix} t\frac{\partial^2 S}{\partial \gamma_1^2} & t\frac{\partial^2 S}{\partial \gamma_1 \partial \gamma_3} \\ t\frac{\partial^2 S}{\partial \gamma_1 \partial \gamma_3} & t\frac{\partial^2 S}{\partial \gamma_3^2} \end{bmatrix}. \tag{C.12}$$

The covariance matrix of the 'Gaussianized' PDF is then

$$\mathbf{C} = \begin{bmatrix} \frac{\frac{\partial^2 S}{\partial \gamma_3^2}}{t\left(\frac{\partial^2 S}{\partial \gamma_1^2}\frac{\partial^2 S}{\partial \gamma_3^2} - \left(\frac{\partial^2 S}{\partial \gamma_1 \partial \gamma_3}\right)^2\right)} & \frac{-\frac{\partial^2 S}{\partial \gamma_1 \partial \gamma_3}}{t\left(\frac{\partial^2 S}{\partial \gamma_1^2}\frac{\partial^2 S}{\partial \gamma_3^2} - \left(\frac{\partial^2 S}{\partial \gamma_1 \partial \gamma_3}\right)^2\right)} \\ \frac{-\frac{\partial^2 S}{\partial \gamma_1 \partial \gamma_3}}{t\left(\frac{\partial^2 S}{\partial \gamma_1^2}\frac{\partial^2 S}{\partial \gamma_3^2} - \left(\frac{\partial^2 S}{\partial \gamma_1 \partial \gamma_3}\right)^2\right)} & \frac{\frac{\partial^2 S}{\partial \gamma_1^2}}{t\left(\frac{\partial^2 S}{\partial \gamma_1^2}\frac{\partial^2 S}{\partial \gamma_3^2} - \left(\frac{\partial^2 S}{\partial \gamma_1 \partial \gamma_3}\right)^2\right)} \end{bmatrix}, \tag{C.13}$$

so we have variances

$$\sigma_{\gamma_1}^2 = \frac{\frac{\partial^2 S}{\partial \gamma_3^2}}{t\left(\frac{\partial^2 S}{\partial \gamma_1^2}\frac{\partial^2 S}{\partial \gamma_3^2} - \left(\frac{\partial^2 S}{\partial \gamma_1 \partial \gamma_3}\right)^2\right)}, \qquad \sigma_{\gamma_3}^2 = \frac{\frac{\partial^2 S}{\partial \gamma_1^2}}{t\left(\frac{\partial^2 S}{\partial \gamma_1^2}\frac{\partial^2 S}{\partial \gamma_3^2} - \left(\frac{\partial^2 S}{\partial \gamma_1 \partial \gamma_3}\right)^2\right)}, \tag{C.14}$$

and correlation coefficient

$$\rho_{13} = \frac{-\frac{\partial^2 S}{\partial \gamma_1 \partial \gamma_3}}{\sqrt{\frac{\partial^2 S}{\partial \gamma_1^2}\frac{\partial^2 S}{\partial \gamma_3^2}}}. \tag{C.15}$$

which satisfies the Cauchy-Schwarz inequality provided

$$\left.\frac{\partial^2 S}{\partial \gamma_1^2}\right|_{\gamma_{1_0},\gamma_{3_0}} \left.\frac{\partial^2 S}{\partial \gamma_3^2}\right|_{\gamma_{1_0},\gamma_{3_0}} - \left(\left.\frac{\partial^2 S}{\partial \gamma_1 \partial \gamma_3}\right|_{\gamma_{1_0},\gamma_{3_0}}\right)^2 > 0. \tag{C.16}$$

Finally, the normalization constant of the 'Gaussianized' PDF is

$$N(t) = \frac{1}{2\pi\sqrt{\det(\mathbf{C})}} = \frac{\sqrt{\det(\mathbf{C}^{-1})}}{2\pi} = \frac{t\sqrt{\frac{\partial^2 S}{\partial \gamma_1^2}\frac{\partial^2 S}{\partial \gamma_3^2} - \left(\frac{\partial^2 S}{\partial \gamma_1 \partial \gamma_3}\right)^2}}{2\pi}, \tag{C.17}$$

so the Cramér function can be found from the PDF by

$$S(\gamma_1, \gamma_3) = -\frac{1}{t}\ln[p(\gamma_1, \gamma_3, t)] + \frac{1}{t}\ln\left[\frac{t}{2\pi}\sqrt{\frac{\partial^2 S}{\partial \gamma_1^2}\frac{\partial^2 S}{\partial \gamma_3^2} - \left(\frac{\partial^2 S}{\partial \gamma_1 \partial \gamma_3}\right)^2}\right], \tag{C.18}$$

where the partial derivatives are evaluated at the minimum of the Cramér function $S(\gamma_{1_0}, \gamma_{3_0}) = 0$. As with the case of the marginal Cramér function, when calculating for finite time, the normalization correction fades as $\sim t^{-1}\ln(t)$.

Appendix D

Derivation of the Cramér Function for the Ratio of FTLEs

Defining the ratio of FTLEs as

$$r^* = \frac{\gamma_2}{\gamma_1}, \tag{D.1}$$

the PDF of this measure is

$$p(r^*, t) = \int_0^\infty d\gamma_1 \int_{-2\gamma_1}^{-\frac{1}{2}\gamma_1} d\gamma_3 \;\; p(\gamma_1, \gamma_3, t) \;\; \delta\left(\frac{-\gamma_3}{\gamma_1} - 1 - r^*\right). \tag{D.2}$$

Evaluating the Dirac delta distribution gives

$$p(r^*,t) = \int_0^\infty \gamma_1 p(\gamma_1, -\gamma_1(1+r^*), t) d\gamma_1, \tag{D.3}$$

and substitution of the large deviation form further yields

$$p(r^*,t) = \int_0^\infty \gamma_1 N(t) e^{-tS(\gamma_1, -\gamma_1(1+r^*))} d\gamma_1. \tag{D.4}$$

Seeking a new Cramér function such that for long time

$$p(r^*,t) = N^*(t) \exp\left(-tS(r^*)\right), \tag{D.5}$$

we have

$$S(r^*) = \lim_{t\to\infty} -\frac{1}{t}\ln[p(r^*,t)] + \frac{1}{t}\ln[N^*(t)], \tag{D.6}$$

$$S(r^*) = \lim_{t\to\infty} -\frac{1}{t}\ln\left[N(t)\int_0^\infty \gamma_1 e^{-tS(\gamma_1,-\gamma_1(1+r^*))} d\gamma_1\right] + \frac{1}{t}\ln[N^*(t)], \tag{D.7}$$

$$S(r^*) = \lim_{t\to\infty} -\frac{1}{t}\ln\left[\int_0^\infty \gamma_1 e^{-tS(\gamma_1,-\gamma_1(1+r^*))} d\gamma_1\right] - \frac{1}{t}\ln[N(t)] + \frac{1}{t}\ln[N^*(t)], \tag{D.8}$$

in the spirit of steepest descent integration, this integral will be dominated, for large t near the minimum of $S(\gamma_1, -\gamma_1(1+r^*))$, which we denote at $\overline{\gamma}_1$

$$\frac{\partial}{\partial\gamma_1}\Big(S(\gamma_1, -\gamma_1(1+r^*))\Big)_{\overline{\gamma}_1} = 0, \tag{D.9}$$

then locally, a Taylor series expansion gives a parabolic form

$$S(\gamma_1, -\gamma_1(1+r^*)) \approx S(\overline{\gamma}_1, -\overline{\gamma}_1(1+r^*)) + \frac{1}{2}(\gamma_1 - \overline{\gamma}_1)^2 \frac{\partial^2}{\partial \gamma_1^2} \left(S(\gamma_1, -\gamma_1(1+r^*)) \right)_{\overline{\gamma}_1}. \tag{D.10}$$

Substituting this and integrating leads to

$$S^*(r^*) = \lim_{t\to\infty} S(\overline{\gamma}_1, -\overline{\gamma}_1(1+r^*)) - \frac{1}{t}\ln\left[\overline{\gamma}_1 \sqrt{\frac{2\pi}{\frac{\partial^2}{\partial \gamma_1^2}\left(S(\gamma_1, -\gamma_1(1+r^*)) \right)_{\overline{\gamma}_1} t}}\right] - \frac{1}{t}\ln[N(t)] + \frac{1}{t}\ln[N^*(t)] \tag{D.11}$$

with the new normalization constant being calculated as before

$$N^*(t) = \sqrt{\frac{S''(r^*)t}{2\pi}}. \tag{D.12}$$

combining all of the normalization terms

$$S^*(r^*) = \lim_{t\to\infty} S(\overline{\gamma}_1, -\overline{\gamma}_1(1+r^*)) + \frac{1}{t}\ln\left[\frac{1}{\overline{\gamma}_1}\sqrt{\frac{S''(r^*)\frac{\partial^2}{\partial \gamma_1^2}\left(S(\gamma_1, -\gamma_1(1+r^*)) \right)_{\overline{\gamma}_1}}{\frac{\partial^2 S}{\partial \gamma_1^2}\frac{\partial^2 S}{\partial \gamma_3^2} - \left(\frac{\partial^2 S}{\partial \gamma_1 \partial \gamma_3}\right)^2}}\right] \tag{D.13}$$

but these vanish in the long time limit as $\sim t^{-1}$, leaving

$$S^*(r^*) = S(\overline{\gamma}_1, -(1+r^*)\overline{\gamma}_1) \tag{D.14}$$

This result is essentially an application of the contraction principle for large deviations theory.[80]

Appendix E

Kramers-Moyal Solution for Linear Relaxation

We briefly demonstrate a solution to the Kramers-Moyal model for the stationary PDF by considering linear relaxation, i.e., when the viscous term in Eq. (4.2) is linear ($n = 1$) in vorticity magnitude with a relaxation time $\tau = \frac{1}{A}$,

$$f(\omega) = -\nu\widehat{\omega}_i \frac{\partial^2 \omega_i}{\partial x_j \partial x_j} = \frac{\omega}{\tau}. \tag{E.1}$$

As a result, the evolution of $\ln \omega$ becomes,

$$\frac{d \ln \omega}{dt} = \widehat{\omega}_i S_{ij} \widehat{\omega}_j - \frac{1}{\tau}, \tag{E.2}$$

that is, the relaxation function is a constant, $\widetilde{f}(\ln\omega) = \frac{1}{\tau}$. This scenario was considered by Ref.[5] in the context of polymer stretching.

Under this assumption, the Kramers-Moyal model for the stationary PDF, Eq. (4.44), yields a constant-coefficient ordinary differential equation in χ of infinite order. The relaxation can be absorbed into the generalized Lyapunov exponents by defining,

$$\widetilde{L}(q) = L(q) - \frac{q}{\tau}, \tag{E.3}$$

which is the Legendre transform of a shifted Cramér function,

$$\widetilde{S}(g) = \sup_q \left[gq - \widetilde{L}(q)\right] = \sup_q \left[\left(g + \frac{1}{\tau}\right) q - L(q)\right] = S\left(g + \frac{1}{\tau}\right). \tag{E.4}$$

With this modified generalized Lyapunov exponent, the equation for the stationary distribution becomes,

$$0 = \sum_{m=1}^{\infty} \frac{(-1)^m}{m!} \widetilde{L}^{(m)}(0) \frac{d^m p_{\ln\omega}}{d\chi^m}. \tag{E.5}$$

We can solve this differential equation on a semi-infinite domain (i.e. for the right-hand side 'tail' region of the PDF) using a Laplace transform. Utilizing the properties of derivatives under Laplace transformation, the equation for the stationary distribution in Laplace space becomes,

$$C(s) = \widehat{p}_{\ln\omega}(s) \sum_{m=1}^{\infty} \frac{(-s)^m}{m!} \widetilde{L}^{(m)}(0), \tag{E.6}$$

where $C(s)$ is an analytic function arising from the necessity to specify boundary conditions in probability space. In this form, the summation is seen to be a Taylor expansion of the generalized Lyapunov exponent about zero, so

$$C(s) = \widehat{p}_{\ln\omega}(s)\widetilde{L}(-s). \tag{E.7}$$

The stationary distribution can be constructed by solving for $\widehat{p}_{\ln\omega}(s)$ and performing the inverse Laplace transform via contour integration in the complex plane. Because $C(s)$ is an analytic function, the only poles contributing to this inverse transform come from the zeros of $\widetilde{L}(-s)$.

Constraints on the generalized Lyapunov exponent, namely that $\widetilde{L}(0) = 0$ and $L''(q) \geq 0$, require that there be at most two first-order zeros with one being at $q = 0$ and the other being at $q = q^*$ (or one second-order zero at $q = 0$). The form of the stationary distribution is thus,

$$p_{\ln\omega}(\chi) = A_1 + A_2 \exp(-q^*\chi). \tag{E.8}$$

The decay of the PDF to zero at infinity requires $A_1 = 0$. By changing variables from $\ln\omega$ to ω, the PDF for the vorticity magnitude becomes a power-law,

$$p_\omega(w) = A_2 w^{-1-q^*}, \tag{E.9}$$

in agreement with the results of Ref.[5]

As a caveat, the conditional statistics in Fig. 4.6 clearly show that the viscous destruction of vorticity increases super-linearly ($n > 1$) with increasing vorticity magnitude, and therefore a linear model is ill-equipped to describe the vorticity statistics. Nonetheless, this appendix shows that the Kramers-Moyal model constructed here produces a known result for the case of linear relaxation.

Appendix F

Isotropic Tensorial Stochastic Forcing for Symmetric and Anti-Symmetric Components

In this appendix, the form of the stochastic forcing in (2.35) is established. As identified in the text, the forcing should have the form $dF_{ij} = b_{ijk\ell}dW_{k\ell}$, and can be thought of as a sum of symmetric and anti-symmetric forcing, $dF_{ij} = dF_{ij}^{(s)} + dF_{ij}^{(a)}$, where $dF_{ij}^{(s)} = \frac{1}{2}(dF_{ij} + dF_{ji})$ and $dF_{ij}^{(a)} = \frac{1}{2}(dF_{ij} - dF_{ji})$. Since dW_{ij} represents a tensorial Wiener process, i.e. $\langle W_{ij}\rangle = 0$ and $\langle dW_{ij}dW_{k\ell}\rangle = \delta_{ik}\delta_{j\ell}dt$, then

$$\langle dF_{ij}dF_{k\ell}\rangle = b_{ijmn}b_{k\ell mn}dt = d_{ijk\ell}dt. \tag{F.1}$$

Therefore, the forcing contributes a variance growth rate of

$$d\left\langle F_{ij}F_{ij}\right\rangle = \left\langle dF_{ij}dF_{ij}\right\rangle = d_{ijij}dt \tag{F.2}$$

and furthermore, the symmetric and anti-symmetric variance growth rates are,

$$d\left\langle F_{ij}^{(s)}F_{ij}^{(s)}\right\rangle = \left\langle dF_{ij}^{(s)}dF_{ij}^{(s)}\right\rangle = \frac{1}{2}\left(d_{ijij}+d_{ijji}\right)dt \equiv D_s dt. \tag{F.3}$$

$$d\left\langle F_{ij}^{(a)}F_{ij}^{(a)}\right\rangle = \left\langle dF_{ij}^{(a)}dF_{ij}^{(a)}\right\rangle = \frac{1}{2}\left(d_{ijij}-d_{ijji}\right)dt = D_a dt. \tag{F.4}$$

Here, by definition, D_s and D_a represent the growth rate of the variance of symmetric and anti-symmetric parts of the forcing.

To model isotropic turbulence, the stochastic forcing should be statistically isotropic. The most general isotropic form for the diffusion tensor is

$$d_{ijk\ell} = d_1\delta_{ij}\delta_{k\ell} + d_2\delta_{ik}\delta_{j\ell} + d_3\delta_{i\ell}\delta_{jk}. \tag{F.5}$$

Requiring also that the forcing be trace-free (incompresibility), then

$$d_{iik\ell} = \left(3d_1 + d_2 + d_3\right)\delta_{k\ell} = 0. \tag{F.6}$$

Combining this constraint with the two definitions of D_s and D_a given above,

$$D_s = \frac{1}{2}\left(d_{ijij} + d_{ijji}\right) = 3d_1 + 6d_2 + 6d_3, \tag{F.7}$$

$$D_a = \frac{1}{2}\left(d_{ijij} - d_{ijji}\right) = 3d_2 - 3d_3, \tag{F.8}$$

then the system of 3 equations and 3 unknowns can be solved for

$$d_{ijk\ell} = -\frac{D_s}{15}\delta_{ij}\delta_{k\ell} + \left(\frac{D_s}{10} + \frac{D_a}{6}\right)\delta_{ik}\delta_{j\ell} + \left(\frac{D_s}{10} - \frac{D_a}{6}\right)\delta_{i\ell}\delta_{jk}. \tag{F.9}$$

The choice of $D_s = D_a = 15$ reduces to the form of Chevillard and Meneveau[146] used for the RFD model,

$$D_{ijk\ell} = -\delta_{ij}\delta_{k\ell} + 4\delta_{ik}\delta_{j\ell} - \delta_{i\ell}\delta_{jk}. \tag{F.10}$$

To implement this forcing, however, the tensor $b_{ijk\ell}$ is necessary, thus the equation $b_{ijmn}b_{k\ell mn} = d_{ijk\ell}$ must be solved. Using the general isotropic form

$$b_{ijk\ell} = b_1\delta_{ij}\delta_{k\ell} + b_2\delta_{ik}\delta_{j\ell} + b_3\delta_{i\ell}\delta_{jk}, \tag{F.11}$$

the tensor contractions yield the following system of equations,

$$d_1 = 3b_1^2 + 2b_1b_2 + 2b_1b_3 = -\frac{D_s}{15}, \tag{F.12}$$

$$d_2 = b_2^2 + b_3^2 = \frac{D_s}{10} + \frac{D_a}{6}, \tag{F.13}$$

$$d_3 = 2b_2 b_3 = \frac{D_s}{10} - \frac{D_a}{6}. \tag{F.14}$$

Solution to this system of equations yields,

$$b_{ijk\ell} = -\frac{1}{3}\sqrt{\frac{D_s}{5}}\delta_{ij}\delta_{k\ell} + \frac{1}{2}\left(\sqrt{\frac{D_s}{5}} + \sqrt{\frac{D_a}{3}}\right)\delta_{ik}\delta_{j\ell} + \frac{1}{2}\left(\sqrt{\frac{D_s}{5}} - \sqrt{\frac{D_a}{3}}\right)\delta_{i\ell}\delta_{jk}, \tag{F.15}$$

which reduces to the form of Ref. 146 with the choice $D_s = D_a = 15$. Meanwhile, Ref. 147 tuned $D_s = D_a$ such that the definition of τ_η was consistent between model and numerics.

As shown by Ref. 147, the $D_s = D_a$ constraint can be derived by considering the gradient of homogeneous forcing. However, as pointed out in §2.2.3, this stochastic forcing term must represent both the gradient of the large-scale forcing and the fluctuations of the unclosed terms about their conditional means, the latter of which is not subject to the above constraint. In the authors' current view, e.g. considering (2.36) and (2.37), there is no a-priori reason that the strain-rate and vorticity should be forced stochastically with the same amplitude, therefore, the present model considers D_s and D_a to be two independent tuning parameters. In fact, given that the fluctuations of the pressure Hessian about its conditional mean, P'_{ij}, must be a symmetric tensor, it is somewhat realistic to expect $D_s > D_a$.

Appendix G

Analytical Calculation of γ for the Gaussian Fields Representation of the Conditional Pressure Hessian

A key component to both the Enhanced Gaussian closure and the recent-deformation of Gaussian fields mapping closure is the representation of a conditional pressure Hessian using (2.49). While the coefficients α and β were directly evaluated from the Gaussian fields closure, the last coefficient is determined by the details of the longitudinal correlation function, (2.50). Calculations are easier using the longitudinal structure function $D_{LL}(r) = 2\overline{u^2}(1 - f(r))$.

$$\gamma = \frac{6}{25} + \frac{16}{75 D''_{LL}(0)^2} \int_0^\infty \frac{D'_{LL}(r) D'''_{LL}(r)}{r} dr, \tag{G.1}$$

where $D''_{LL}(0) = \frac{2\epsilon}{15\nu}$ according to the proper viscous range behavior. Using the approach of Ref. 217, the viscous and inertial range behavior of the structure function can be preserved using a blending function,

$$D_{LL}(r) = C_2\epsilon^{2/3}r^{2/3}F\left(\frac{r}{\gamma_2\eta}\right). \tag{G.2}$$

Here, we assume K41 scaling for the inertial range with Kolmogorov coefficient $C_2 \approx 2.0$.[108] The blending function of Ref. 217 is

$$F\left(\frac{r}{\gamma_2\eta}\right) = \left[1 + \left(\frac{r}{\gamma_2\eta}\right)^{-2}\right]^{-2/3}, \tag{G.3}$$

where $\gamma_2 = (15C_2)^{3/4} \approx 13$ sets the cross-over point between viscous and inertial behavior, recovering the correct viscous range behavior. With the application of product rule differentiation, we can write

$$D'_{LL}(r) = C_2\epsilon^{2/3}r^{-1/3}F_1\left(\frac{r}{\gamma_2\eta}\right), \tag{G.4}$$

$$D'''_{LL}(r) = C_2\epsilon^{2/3}r^{-7/3}F_3\left(\frac{r}{\gamma_2\eta}\right), \tag{G.5}$$

and thus the integral simplifies under the change of variable $\hat{r} = \frac{r}{\gamma_2\eta}$,

$$\gamma = \frac{6}{25} + \frac{12}{225}I, \tag{G.6}$$

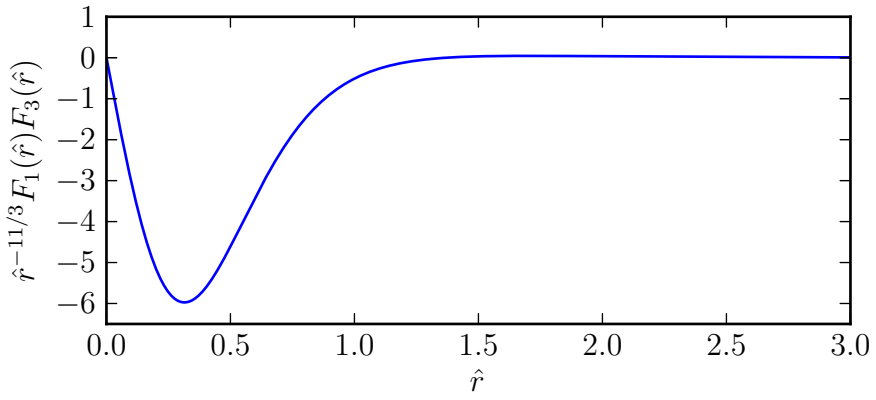

Figure G.1: Integrand in (G.7) plotted in normalized variables $\hat{r} = \frac{r}{\gamma_2 \eta}$ with $\gamma_2 \approx 13$.

where

$$I = \int_0^\infty \hat{r}^{-11/3} F_1(\hat{r}) F_3(\hat{r}) d\hat{r}, \tag{G.7}$$

with the derivative functions

$$F_1(\hat{r}) = \frac{2}{3} F(\hat{r}) + \hat{r} F'(\hat{r}), \tag{G.8}$$

$$F_3(\hat{r}) = \frac{8}{27} F(\hat{r}) - \frac{2}{3} \hat{r} F'(\hat{r}) + 2\hat{r}^2 F''(\hat{r}) + \hat{r}^3 F'''(\hat{r}). \tag{G.9}$$

This integrand is plotted in figure G.1, from which it is apparent that the integral is dominated by contributions from the viscous range, i.e. $r < 13\eta$. Without considering the details of the integration, the manipulation so far shows that γ is (approximately) independent of Re_λ (neglecting weak Re_λ-effects on the cutoff scale), and its precise value is difficult to determine because it will depend heavily on the details of the blending function used.

The integral can be written fully as

$$I = \int_0^\infty \left[\frac{16}{81} \left(1+\hat{r}^2\right)^{-4/3} + \frac{416}{81} \left(1+\hat{r}^2\right)^{-7/3} - \frac{304}{27} \left(1+\hat{r}^2\right)^{-10/3} - \frac{2080}{81} \left(1+\hat{r}^2\right)^{-13/3} + \frac{2560}{81} \left(1+\hat{r}^2\right)^{-16/3} \right] \frac{d\hat{r}}{\hat{r}}. \tag{G.10}$$

To integrate, add

$$\left(\frac{16}{81} + \frac{416}{81} - \frac{304}{27} - \frac{2080}{81} + \frac{2560}{81} \right) \frac{\left(1+\hat{r}^2\right)^{-1/3}}{\hat{r}} = 0, \tag{G.11}$$

to the integrand and use the change of variables,

$$\zeta = 1 + \hat{r}^2, \qquad \frac{d\zeta}{2\left(\zeta - 1\right)} = \frac{d\hat{r}}{\hat{r}}. \tag{G.12}$$

As a result, the integral becomes,

$$I = \frac{1}{2} \int_1^\infty \left[-\frac{16}{81}\zeta^{-4/3} - \frac{416}{81}\zeta^{-7/3}\left(\zeta+1\right) + \frac{304}{27}\zeta^{-10/3}\left(\zeta^2+\zeta+1\right) + \frac{2080}{81}\zeta^{-13/3}\left(\zeta^3+\zeta^2+\zeta+1\right) - \frac{2560}{81}\zeta^{-16/3}\left(\zeta^4+\zeta^3+\zeta^2+\zeta+1\right) \right] d\zeta. \tag{G.13}$$

Then algebraic simplification

$$I = \frac{1}{2} \int_1^\infty \left[\frac{16}{81}\zeta^{-7/3} + \frac{432}{81}\zeta^{-10/3} - \frac{480}{81}\zeta^{-13/3} - \frac{2560}{81}\zeta^{-16/3} \right] d\zeta, \tag{G.14}$$

and completing the power-law integrations results in

$$I = -\frac{302}{91}. \tag{G.15}$$

Substitution of this results leads to

$$\gamma = \frac{86}{1365} \approx 0.063. \tag{G.16}$$

Appendix H

Gaussian Fields Approximation for the Conditional Hessian of the Velocity Gradient

This appendix details the derivation of (6.3) in the main text, following the method outlined in Ref. 147. The characteristic function of the turbulent velocity field,

$$\phi^u\left[\lambda(\mathbf{x})\right] = \left\langle \exp\left(i \int \lambda_i(\mathbf{x}) u_i(\mathbf{x}) d\mathbf{x} \right) \right\rangle, \tag{H.1}$$

contains all the statistical information necessary to compute the desired conditional mean, namely $\left\langle \frac{\partial^2 A_{ij}}{\partial x_p \partial x_q} \middle| \mathcal{A} \right\rangle$. To make progress analytically, the turbulent velocity field

is taken to be Gaussian, meaning that all n-point pdfs are joint-Gaussian,

$$\phi^u\left[\lambda(\mathbf{x})\right] = \exp\left(-\frac{1}{2}\int\int \lambda_i(\mathbf{x})B_{ij}(\mathbf{x},\mathbf{x}')\lambda_j(\mathbf{x}')d\mathbf{x}d\mathbf{x}'\right), \tag{H.2}$$

where B_{ij} is the two-point covariance tensor, which for homogeneous isotropic turbulence depends only on the separation vector, $\mathbf{r} = \mathbf{x} - \mathbf{x}'$, and has the form

$$B_{ij}(\mathbf{x},\mathbf{x}') = B_{ij}(\mathbf{r}) = \langle u_1^2\rangle\left[f(r)\delta_{ij} + \frac{1}{2}rf'(r)\left(\delta_{ij} - \hat{r}_i\hat{r}_j\right)\right], \tag{H.3}$$

where $r = |\mathbf{r}|$ and $\hat{r}_i = \frac{r_i}{r}$. In this way the characteristic functional, when assumed Gaussian for isotropic turbulence, is uniquely specified by the longitudinal velocity correlation function,

$$f(r) = \frac{\langle u_1(\mathbf{x})u_1(\mathbf{x}+r\mathbf{e}_1)\rangle}{\langle u_1^2\rangle}. \tag{H.4}$$

With integration by parts, the relationship between the characteristic functional for the velocity field and that of the velocity gradient field can be shown to be

$$\phi^A\left[\mathbf{\Lambda}\right] = \phi^u\left[-\nabla\cdot\mathbf{\Lambda}\right]. \tag{H.5}$$

Again, with integration by parts, substituting this relationship into the Gaussian characteristic functional for the velocity field,

$$\phi^A\left[\mathbf{\Lambda}(\mathbf{x})\right] = \exp\left(-\frac{1}{2}\int\int \Lambda_{ik}(\mathbf{x})C_{ijk\ell}(\mathbf{x},\mathbf{x}')\Lambda_{j\ell}(\mathbf{x}')d\mathbf{x}d\mathbf{x}'\right), \tag{H.6}$$

where

$$C_{ijk\ell}(\mathbf{x},\mathbf{x}') = \frac{\partial^2 B_{ij}}{\partial x_k \partial x'_\ell}(\mathbf{x},\mathbf{x}') = \langle A_{ik}(\mathbf{x}) A_{j\ell}(\mathbf{x}')\rangle \,, \tag{H.7}$$

is the covariance tensor for the velocity gradient, which only depends on $\mathbf{r} = \mathbf{x} - \mathbf{x}'$. It is computed from the Hessian of the velocity covariance tensor,

$$\begin{aligned} C_{ijk\ell}(\mathbf{r}) = -\frac{\partial^2 B_{ij}}{\partial r_k \partial r_\ell} = \langle u_1^2\rangle \Bigg[&\left(-\frac{3}{2}\frac{f'(r)}{r} - \frac{1}{2}f''(r)\right)(\delta_{ij}\delta_{k\ell}) + \left(\frac{1}{2}\frac{f'(r)}{r}\right)(\delta_{ik}\delta_{j\ell} + \delta_{i\ell}\delta_{jk}) \\ &+ \left(\frac{3}{2}\frac{f'(r)}{r} - \frac{3}{2}f''(r) - \frac{1}{2}rf'''(r)\right)(\delta_{ij}\hat{r}_k\hat{r}_\ell) \\ &+ \left(-\frac{1}{2}\frac{f'(r)}{r} + \frac{1}{2}f''(r)\right)(\delta_{i\ell}\hat{r}_j\hat{r}_k + \delta_{k\ell}\hat{r}_i\hat{r}_j + \delta_{j\ell}\hat{r}_i\hat{r}_k + \delta_{ik}\hat{r}_j\hat{r}_\ell + \delta_{jk}\hat{r}_i\hat{r}_\ell) \\ &+ \left(\frac{3}{2}\frac{f'(r)}{r} - \frac{3}{2}f''(r) + \frac{1}{2}rf'''(r)\right)(\hat{r}_i\hat{r}_j\hat{r}_k\hat{r}_\ell)\Bigg] . \end{aligned} \tag{H.8}$$

The desired statistical quantity in this exercise is

$$\nu\left\langle \frac{\partial^2 A_{ij}}{\partial x_k \partial x_\ell}\middle| \mathcal{A}\right\rangle = \nu \lim_{r\to 0}\frac{\partial^2}{\partial r_k \partial r_\ell}\langle A_{ij}(\mathbf{x}+\mathbf{r})|\mathcal{A}(\mathbf{x})\rangle \,. \tag{H.9}$$

Following exactly the steps outlined in Appendix B2 of Ref. 147,

$$\langle A_{ij}(\mathbf{x}+\mathbf{r})|\mathcal{A}(\mathbf{x})\rangle = C_{ikj\ell}(\mathbf{r})C^{-1}_{km\ell n}(\mathbf{0})\mathcal{A}_{mn}, \tag{H.10}$$

where equality at the origin means

$$C^{-1}_{km\ell n}(\mathbf{0}) = \frac{2}{15\langle u_1^2\rangle f''(0)}\left(-4\delta_{km}\delta_{\ell n} - \delta_{kn}\delta_{m\ell}\right), \tag{H.11}$$

see Appendix B1 of Ref. 147 for details. Combining expressions,

$$\nu \left\langle \frac{\partial^2 A_{ij}}{\partial x_p \partial x_q} \middle| \mathcal{A} \right\rangle = \nu \lim_{r\to 0} \frac{\partial^2 C_{ikj\ell}}{\partial r_p \partial r_q} C^{-1}_{km\ell n}(\mathbf{0}) \mathcal{A}_{mn}. \tag{H.12}$$

A tedious calculation by twice taking the gradient of (H.8) results in,

$$\begin{aligned} \lim_{r\to 0} \frac{\partial^2 C_{ikj\ell}}{\partial r_p \partial r_q} = \langle u_1^2 \rangle f^{(4)}(0) \, [& - (\delta_{ik}\delta_{j\ell}\delta_{pq} + \delta_{ik}\delta_{jp}\delta_{\ell q} + \delta_{ik}\delta_{jq}\delta_{\ell p}) \\ & + \tfrac{1}{6} (\delta_{ij}\delta_{k\ell}\delta_{pq} + \delta_{i\ell}\delta_{kj}\delta_{pq} + \delta_{i\ell}\delta_{kp}\delta_{jq} + \delta_{i\ell}\delta_{jp}\delta_{kq} + \delta_{ip}\delta_{k\ell}\delta_{jq} + \delta_{iq}\delta_{k\ell}\delta_{jp} \\ & + \delta_{j\ell}\delta_{kp}\delta_{iq} + \delta_{j\ell}\delta_{ip}\delta_{kq} + \delta_{ij}\delta_{kp}\delta_{\ell q} + \delta_{ij}\delta_{\ell p}\delta_{kq} + \delta_{kj}\delta_{ip}\delta_{\ell q} + \delta_{kj}\delta_{\ell p}\delta_{iq})] \end{aligned} \tag{H.13}$$

Substitution of (H.11) and (H.13) into (H.12), followed by a tedious calculation of tensor contractions yields,

$$\begin{aligned} \nu \left\langle \frac{\partial^2 A_{ij}}{\partial x_p \partial x_q} \middle| \mathcal{A} \right\rangle = \frac{2\nu f^{(4)}(0)}{15 f''(0)} \Bigg[& \left(\frac{23}{6}\mathcal{A}_{ij} + \frac{1}{3}\mathcal{A}_{ji} \right) \delta_{pq} + \left(\frac{23}{6}\mathcal{A}_{iq} + \frac{1}{3}\mathcal{A}_{qi} \right) \delta_{jp} \\ & + \left(\frac{23}{6}\mathcal{A}_{ip} + \frac{1}{3}\mathcal{A}_{pi} \right) \delta_{jq} - \left(\frac{5}{6}\mathcal{A}_{jq} + \frac{5}{6}\mathcal{A}_{qj} \right) \delta_{ip} \\ & - \left(\frac{5}{6}\mathcal{A}_{jp} + \frac{5}{6}\mathcal{A}_{pj} \right) \delta_{iq} - \left(\frac{5}{6}\mathcal{A}_{pq} + \frac{5}{6}\mathcal{A}_{qp} \right) \delta_{ij} \Bigg], \end{aligned} \tag{H.14}$$

which can be written in the form of (6.3) with (6.4).

Appendix I

Determination of δ for the RDGF Model Using the Enstrophy Balance

Using the result of Appendix H, the back-in-time velocity gradient Hessian is given by

$$\nu \left\langle \frac{\partial^2 A_{ij}}{\partial X_p \partial X_q} \middle| \mathcal{A} \right\rangle = \delta \left(T_{ij}\delta_{pq} + T_{iq}\delta_{jp} + T_{ip}\delta_{jq} - \frac{2}{21} S_{jq}\delta_{ip} - \frac{2}{21} S_{jp}\delta_{iq} - \frac{2}{21} S_{pq}\delta_{ij} \right), \tag{I.1}$$

where the coefficient δ can be written in terms of the enstrophy dissipation,

$$\delta = \nu \frac{7}{3} \frac{f^{(4)}(0)}{f''(0)} = -\tau_\eta^2 \nu \left\langle \frac{\partial \omega_i}{\partial X_j} \frac{\partial \omega_i}{\partial X_j} \right\rangle. \tag{I.2}$$

APPENDIX I. DETERMINATION OF δ FOR RDGF

Note that since the Gaussian fields evaluation is back-in-time, so this can be interpreted as the back-in-time enstrophy dissipation. By definition, the RFD-style mapping used to generate the approximate back-in-time values keeps velocity gradients constant, but not velocity Hessians. Therefore, the enstrophy production $\langle \omega_i S_{ij} \omega_j \rangle$ is constant under the mapping but the enstrophy dissipation is not constant. Two choices are thus available: apply the enstrophy balance for the back-in-time enstrophy dissipation, or try to invert the mapping effect on the enstrophy dissipation to apply the balance at the present time. It is the opinion of the authors that the second option is desirable, since it leads to the application of the enstrophy balance at the present time rather than back-in-time.

Thus, by modeling choice, the relevant enstrophy balance is

$$\langle \omega_i S_{ij} \omega_j \rangle = \nu \left\langle \frac{\partial \omega_i}{\partial x_j} \frac{\partial \omega_i}{\partial x_j} \right\rangle . \tag{I.3}$$

To map the enstrophy dissipation forward in time,

$$\left\langle \frac{\partial \omega_i}{\partial X_j} \frac{\partial \omega_i}{\partial X_j} \right\rangle = \left\langle \frac{\partial x_k}{\partial X_j} \frac{\partial \omega_i}{\partial x_k} \frac{\partial \omega_i}{\partial x_\ell} \frac{\partial x_\ell}{\partial X_j} \right\rangle = \left\langle C_{k\ell} \frac{\partial \omega_i}{\partial x_k} \frac{\partial \omega_i}{\partial x_\ell} \right\rangle \approx C_{k\ell} \left\langle \frac{\partial \omega_i}{\partial x_k} \frac{\partial \omega_i}{\partial x_\ell} \right\rangle . \tag{I.4}$$

In the last step, the value of $C_{k\ell}$ is localized by approximation, so that no ensemble averages are needed to advance the model stochastic equations. Finally, the enstrophy

dissipation tensor is assumed isotropic,

$$\left\langle \frac{\partial \omega_i}{\partial x_k} \frac{\partial \omega_i}{\partial x_\ell} \right\rangle \approx \frac{1}{3} \left\langle \frac{\partial \omega_i}{\partial x_j} \frac{\partial \omega_i}{\partial x_j} \right\rangle \delta_{k\ell}. \tag{I.5}$$

Substituting, the resulting enstrophy balance is

$$\langle \omega_i S_{ij} \omega_j \rangle = \frac{3\nu}{C_{kk}} \left\langle \frac{\partial \omega_i}{\partial X_j} \frac{\partial \omega_i}{\partial X_j} \right\rangle. \tag{I.6}$$

Using the isotropic relation $\langle \omega_i S_{ij} \omega_j \rangle = -\frac{7\mathcal{S}}{6\sqrt{15}\tau_\eta^3}$ on the left side and the definition of δ in terms of enstrophy dissipation on the right side, the result is

$$\delta = \frac{C_{kk}}{3} \frac{7}{6\sqrt{15}} \frac{\mathcal{S}}{\tau_\eta}. \tag{I.7}$$

The result given by Ref. 147 is recovered when the mapping is removed, $D_{ij} = \delta_{ij}$, so that $C_{kk} = 3$. In this way, the δ coefficient itself depends on the recent deformation. This provides the convenience of an additional non-linearity in the viscous term to prevent unwanted singularities while advancing the stochastic differential equation.

As a final note, the scaling of $\delta \sim \tau_\eta^{-1}$ contradicts the RFD model for the viscous Laplacian, which used the integral timescale and thus introduced a Re_λ^{-1} scaling for the viscous term. While Re_λ dependence can be introduced in the present model through the skewness coefficient, the similar difficulties as encountered by the RFD model are seen when going to large Reynolds numbers. It is the authors' view that a

fixed skewness coefficient, $\mathcal{S} = -0.6$, is appropriate for the present model's the level of fidelity.

Appendix J

Derivation of Yoshizawa and Smagorinsky Coefficients

In this derivation, we assume a spectral cutoff filter $\widehat{G}(\kappa) = H(\kappa_c - \kappa)$ for wavenumber magnitude κ where H is the Heaviside step function and $\kappa_c = \pi/\Delta$ is the cutoff wavenumber. An infinitely long inertial range with spectrum $E(\kappa) = C_k \epsilon^{2/3} \kappa^{-5/3}$ valid from $k = 0$ to $k = \infty$ is assumed to simplify the calculations.

In order to estimate C_y and C_s in the expressions

$$k_r = 2C_y \Delta^2 |\widetilde{S}|^2, \tag{J.1}$$

and

$$\Pi = C_s^2 \Delta^2 |\widetilde{S}|^3, \tag{J.2}$$

it is first necessary to estimate the strain-rate magnitude, $|\widetilde{S}| = \sqrt{2\widetilde{S}_{ij}\widetilde{S}_{ij}}$, as follows,[153]

$$\langle|\widetilde{S}|^2\rangle = \int_0^\infty \hat{G}^2(\kappa)\left[2\kappa^2 E(\kappa)\right]. \tag{J.3}$$

Substituting the above expressions for the filter kernel and assumed energy spectrum,

$$\langle|\widetilde{S}|^2\rangle = 2C_k\langle\epsilon\rangle^{2/3}\int_0^{\pi/\Delta}\kappa^{1/3}d\kappa = \frac{3C_k\pi^{4/3}}{2}\langle\epsilon\rangle^{2/3}\Delta^{-4/3}. \tag{J.4}$$

The ensemble average of (J.1) is

$$\langle k_r\rangle = 2C_y\Delta^2\langle|\widetilde{S}|^2\rangle, \tag{J.5}$$

The residual kinetic energy per mass is given by,[108]

$$\langle k_r\rangle = \int_0^\infty (1-\hat{G}^2(\kappa))E(\kappa)d\kappa. \tag{J.6}$$

Using the spectral cutoff filter kernel and inertial range spectrum assumed above, it is straightforward to compute

$$\langle k_r\rangle = C_k\langle\epsilon\rangle^{2/3}\int_{\pi/\Delta}^\infty \kappa^{-5/3}d\kappa = \frac{3C_k}{2\pi^{2/3}}\langle\epsilon\rangle^{2/3}\Delta^{2/3}. \tag{J.7}$$

Substituting (J.4) and (J.7) into (J.5), one finds for the Yoshizawa coefficient,

$$C_y = \frac{1}{2\pi^2}, \tag{J.8}$$

independent of Δ or $\langle\epsilon\rangle$.

Meanwhile, equating average SGS production (J.2) with the average dissipation rate,

$$\langle\Pi\rangle = \langle\epsilon\rangle = C_s^2\Delta^2\langle|\widetilde{S}|^3\rangle = \mathcal{S}_s C_s^2\Delta^2\langle|\widetilde{S}|^2\rangle^{3/2}, \tag{J.9}$$

where $\mathcal{S}_s = \langle|\widetilde{S}|^3\rangle/\langle|\widetilde{S}|^2\rangle^{3/2}$ is the strain-skewness, which Ref. 153 assumes equal to unity but we find $\mathcal{S}_s \approx 1.3$ in the channel flow simulation for chapter 8. Substituting (J.4) into (J.9), one obtains an estimate for the Smagorinsky coefficient,

$$C_s^2 = \frac{1}{\mathcal{S}_s\pi^2}\left(\frac{2}{3C_k}\right)^{3/2}. \tag{J.10}$$

Finally, for the drift term in (8.3), we can compute,

$$\frac{\Pi}{k_r} = C'|\widetilde{S}| = \frac{C_s^2}{2C_y}|\widetilde{S}| = \frac{1}{\mathcal{S}_s}\left(\frac{2}{3C_k}\right)^{3/2}|\widetilde{S}|, \tag{J.11}$$

which is the result reported in (8.6). Substituting $\mathcal{S}_s \approx 1.3$ as an empirical result from our LES with scale-dependent Lagrangian model,[238] along with $C_k \approx 1.6$, one

obtains

$$\frac{\Pi}{k_r} = C'|\widetilde{S}| \approx 0.207|\widetilde{S}|. \tag{J.12}$$

While we have used a prescribed constant for C' in chapter 8, a dynamic model based on (8.4) using a test filter could be constructed for ${C_y}^{258}$ and combined with the dynamic model for C_s to compute C'.

Appendix K

Dissipation Rates in the Filtered DNS

In this appendix, the specialized treatment of dissipation rates in the fDNS dataset is described. The main goal is to construct a dataset which isolates the modeling error of the velocity gradient stochastic model by removing other errors such a LES SGS modeling errors and particle trajectory errors. In particular, this appendix deals with how Π is computed in the fDNS for use in (8.1).

For the *a priori* case, $\Pi = -\sigma_{ij}\widetilde{S}_{ij}$ could have been computed directly from the database by computing the sub-grid stress in addition to the filtered velocity gradient, this would introduce the problem of dealing with significant backscatter which complicates the implementation of the velocity gradient model in §8.1.1. In practice, most LES models are designed to prevent backscatter, so we do not pursue this

difficulty further. Instead, for the fDNS data, we compute $\Pi = (C_s\Delta)^2|\widetilde{S}|^3$ using a Smagorinsky model with a fixed y-dependent C_s from Ref. 259,

$$C_s(y) = \left[C_{s,0}^{-n} + \left(\frac{\kappa y}{\Delta}\right)^{-n}\right]^{-1/n}, \tag{K.1}$$

where $C_{s,0} = 0.19$ and $n = 2$ are chosen because they give good results for Eulerian averaged quantities for this flow, see Figure K.1 on the left. Here, the coarse-grained velocity gradient necessary for computing Π for (8.1) along the trajectories, is computed using second-order finite differencing and trilinear interpolation.

Figure K.1 elucidates the dissipative behavior of the DNS and fDNS datasets. As indicated by the agreement between the $\triangle$ symbols and dashed line on the left, the average sub-grid production as a function of wall-normal distance is matched well by (K.1) when the values $C_s = 0.19$ and $n = 2$ are chosen. However, there is a significant mismatch between the average production and dissipation near the centerline of the channel (and near the wall). This mismatch is physical and related to the non-trivial dynamics of sub-grid kinetic energy and is exacerbated by the relatively large filter width used to construct the fDNS dataset. For the purposes of constructing an *a priori* test case, we simply use the DNS dissipation to provide a non-equilibrium correction, $\Pi_{corr} = C_{neq}(y)\Pi$, where the correction factor $C_{neq}(y) = \langle\epsilon|y\rangle_E/\langle\Pi|y\rangle_E$ enforces the agreement for average dissipation rate seen between $\circ$ symbols and the continuous line on the left of Figure K.1. This does not, in general, guarantee the

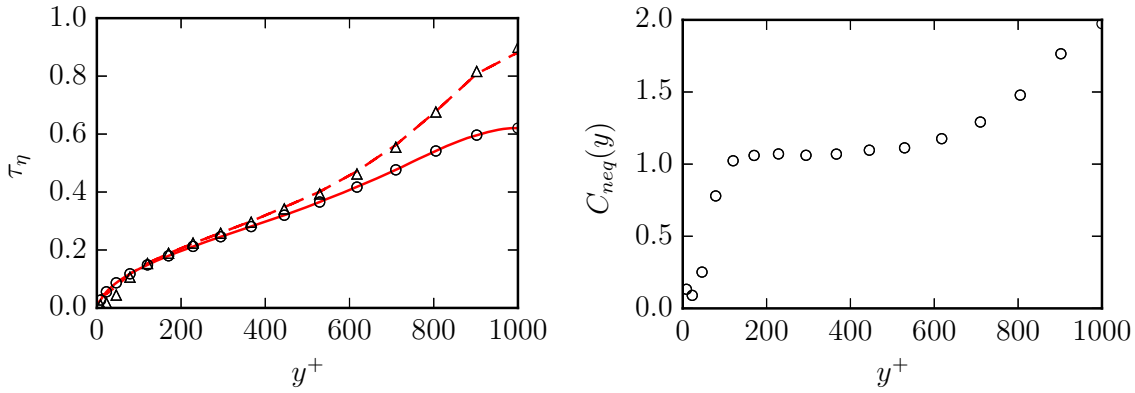

Figure K.1: On the left, Kolmogorov timescales from DNS (lines) and fDNS (symbols) constructed using sub-grid production $\tau_\eta = \sqrt{\nu/\langle\Pi|y\rangle_E}$ (- -,△) and using dissipation rate $\tau_\eta = \sqrt{\nu/\langle\epsilon|y\rangle_E}$ (−,○). On the right, the non-equilibrium correction used for matching the DNS dissipation rate in the fDNS case.

correct local dissipation rate and (8.1) is used with Π_{corr} to determine an approximate $\hat{\epsilon}$ for input to the RDGF model.

Bibliography

[1] K. R. Sreenivasan and R. A. Antonia, "The Phenomenology of Small-Scale Turbulence," *Annual Review of Fluid Mechanics*, vol. 29, no. 1, pp. 435–472, Jan. 1997.

[2] J. M. Wallace, "Twenty years of experimental and direct numerical simulation access to the velocity gradient tensor: What have we learned about turbulence?" *Physics of Fluids*, vol. 21, no. 2, p. 021301, 2009.

[3] C. M. White and M. G. Mungal, "Mechanics and Prediction of Turbulent Drag Reduction with Polymer Additives," *Annual Review of Fluid Mechanics*, vol. 40, no. 1, pp. 235–256, Jan. 2008.

[4] I. Procaccia, V. S. L'Vov, and R. Benzi, "Colloquium: Theory of drag reduction by polymers in wall-bounded turbulence," *Reviews of Modern Physics*, vol. 80, pp. 225–247, 2008.

[5] E. Balkovsky, A. Fouxon, and V. Lebedev, "Turbulent Dynamics of Polymer Solutions," *Physical Review Letters*, vol. 84, no. 20, pp. 4765–4768, May 2000.

[6] M. Chertkov, "Polymer Stretching by Turbulence," *Physical Review Letters*, vol. 84, no. 20, pp. 4761–4764, 2000.

[7] C. Marchioli and A. Soldati, "Turbulent breakage of ductile aggregates," *Physical Review E - Statistical, Nonlinear, and Soft Matter Physics*, vol. 91, no. 5, pp. 1–8, 2015.

[8] R. Maniero, O. Masbernat, E. Climent, and F. Risso, "Modeling and simulation of inertial drop break-up in a turbulent pipe flow downstream of a restriction," *International Journal of Multiphase Flow*, vol. 42, pp. 1–8, 2012.

[9] L. Biferale, C. Meneveau, and R. Verzicco, "Deformation statistics of sub-kolmogorov-scale ellipsoidal neutrally buoyant drops in isotropic turbulence," *Journal of Fluid Mechanics*, vol. 754, pp. 184–207, 2014.

[10] M. U. Babler, L. Biferale, L. Brandt, U. Feudel, K. Guseva, A. S. Lanotte, C. Marchioli, F. Picano, G. Sardina, A. Soldati, and F. Toschi, "Numerical simulations of aggregate breakup in bounded and unbounded turbulent flows," *Journal of Fluid Mechanics*, vol. 766, pp. 104–128, 2015.

[11] V. Spandan, R. Verzicco, and D. Lohse, "Deformation and orientation statistics of neutrally buoyant sub-Kolmogorov ellipsoidal droplets in turbulent Taylor-Couette flow," *Journal of Fluid Mechanics*, vol. 809, pp. 480–501, 2016.

[12] G. A. Voth and A. Soldati, "Anisotropic Particles in Turbulence," *Ann. Rev. Fluid Mech.*, 2017.

[13] A. Pumir and M. Wilkinson, "Orientation statistics of small particles in turbulence," *New Journal of Physics*, vol. 13, 2011.

[14] L. Chevillard and C. Meneveau, "Orientation dynamics of small , triaxial-ellipsoidal particles in isotropic turbulence," *Journal of Fluid Mechanics*, vol. 737, pp. 571–596, 2013.

[15] L. Karp-Boss, E. Boss, and P. A. Jumars, "Nutrient Fluxes to Planktonic Osmotrophs in the Presence of Fluid Motion," *Oceanography and Marine Biology: An Annual Review*, vol. 34, pp. 71–107, 1996.

[16] G. K. Batchelor, "Mass transfer from small particles suspended in turbulent fluid," *Journal of Fluid Mechanics*, vol. 98, p. 609, 1980.

[17] M. Behbahani, M. Behr, M. Hormes, U. Steinseifer, D. Arora, O. Coronado, and M. Pasquali, "A review of computational fluid dynamics analysis of blood pumps," *European Journal of Applied Mathematics*, vol. 20, p. 363, 2009.

[18] M. D. De Tullio, J. Nam, G. Pascazio, E. Balaras, and R. Verzicco, "Computational prediction of mechanical hemolysis in aortic valved prostheses," *European Journal of Mechanics, B/Fluids*, vol. 35, pp. 47–53, 2012.

[19] F. Vitale, J. Nam, L. Turchetti, M. Behr, R. Raphael, M. C. Annesini, and M. Pasquali, "A Multiscale, Biophysical Model of Flow-Induced Red Blood Cell Damage," *AIChE Journal*, vol. 60, no. 4, pp. 1509–1516, 2014.

[20] F. De Vita, M. D. de Tullio, and R. Verzicco, "Numerical simulation of the non-Newtonian blood flow through a mechanical aortic valve," *Theoretical and Computational Fluid Dynamics*, pp. 129–138, 2015.

[21] K. R. Sreenivasan, "Possible effects of small-scale intermittency in turbulent reacting flows," *Flow, Turbulence and Combustion*, vol. 72, no. 2-4 SPEC. ISS., pp. 115–131, 2004.

[22] C. Dopazo, L. Cifuentes, J. Martin, and C. Jimenez, "Strain rates normal to approaching iso-scalar surfaces in a turbulent premixed flame," *Combustion and Flame*, vol. 162, no. 5, pp. 1729–1736, 2015.

[23] M. R. Maxey, "The gravitational settling of aerosol particles in homogeneous turbulence and random flow fields," *J. Fluid Mech.*, vol. 174, p. 441, 1987.

[24] J. Eaton and J. Fessler, "Preferential concentration of particles by turbulence," *Int. J. Multiphase Flow*, vol. 20, pp. 169–209, Aug. 1994.

[25] V. Borue and S. A. Orszag, "Local energy flux and subgrid-scale statistics in three-dimensional turbulence," *Journal of Fluid Mechanics*, vol. 366, pp. 1–31, jul 1998.

[26] M. Chertkov, A. Pumir, and B. I. Shraiman, "Lagrangian tetrad dynamics and the phenomenology of turbulence," *Physics of Fluids*, vol. 11, no. 8, pp. 2394–2410, 1999.

[27] F. Van der Bos, B. Tao, C. Meneveau, and J. Katz, "Effects of small-scale turbulent motions on the filtered velocity gradient tensor as deduced from holographic particle image velocimetry measurements," *Physics of Fluids*, vol. 14, no. 7, pp. 2456–2474, 2002.

[28] A. Pumir, E. Bodenschatz, and H. Xu, "Tetrahedron deformation and alignment of perceived vorticity and strain in a turbulent flow," *Physics of Fluids*, vol. 25, no. 2013, 2013.

[29] A. N. Kolmogorov, "A refinement of previous hypotheses concerning the local structure of turbulence in a viscous incompressible fluid at high reynolds number," *Journal of Fluid Mechanics*, vol. 13, pp. 82–85, 5 1962.

[30] A. M. Oboukov, "Some specific features of atmospheric turbulence," *Journal of Fluid Mechanics*, vol. 13, no. 1, pp. 77–81, 1962.

[31] E. A. Novikov and R. Stewart, "The intermittency of turbulence and the spectrum of energy dissipation fluctuations," *Izv. Geophys. Ser*, vol. 3, pp. 408–413, 1964.

[32] G. Parisi and U. Frisch, "On the singularity structure of fully developed tur-

bulence," in *Turbulence and Predictability in Geophysical Fluid Dynamics*, M. Ghil, R. Benzi, and G. Parisi, Eds. North-Holland, New York, 1985.

[33] C. Meneveau and K. R. Sreenivasan, "The multifractal nature of turbulent energy dissipation," *Journal of Fluid Mechanics*, vol. 224, pp. 429–484, Apr. 1991.

[34] U. Frisch, *Turbulence: The Legacy of A. N. Kolmogorov*. Cambridge University Press, 1995.

[35] R. Benzi and L. Biferale, "Homogeneous and Isotropic Turbulence: A Short Survey on Recent Developments," *J. Stat. Phys.*, vol. 161, pp. 1351–1365, 2015.

[36] B. Zeff, D. Lanterman, R. McAllister, R. Roy, E. Kostelich, and D. Lathrop, "Measuring intense rotation and dissipation in turbulent flows," *Nature*, vol. 421, no. 6919, pp. 146–149, 2003.

[37] A. N. Kolmogorov, "The local structure of turbulence in incompressible viscous fluid for very large reynolds numbers," *Dokl. Akad. Nauk SSSR*, vol. 30, no. 4, pp. 299–303, 1941.

[38] J. Schumacher, J. D. Scheel, D. Krasnov, D. A. Donzis, V. Yakhot, and K. R. Sreenivasan, "Small-scale universality in fluid turbulence," *PNAS*, vol. 111, no. 30, pp. 10 961–10 965, 2014.

[39] G. Falkovich, K. Gawedski, and M. Vergassola, "Particles and fields in fluid turbulence," *Rev. Mod. Phys.*, vol. 73, no. October, pp. 913–975, 2001.

[40] F. Toschi and E. Bodenschatz, "Lagrangian Properties of Particles in Turbulence," *Annual Review of Fluid Mechanics*, vol. 41, no. 1, pp. 375–404, Jan. 2009.

[41] L. Biferale, A. Scagliarini, and F. Toschi, "On the measurement of vortex filament lifetime statistics in turbulence," *Physics of Fluids*, vol. 22, 2010, 065101.

[42] F. Bagheri, D. Mitra, P. Perlekar, and L. Brandt, "Statistics of polymer extensions in turbulent channel flow," *Physical Review E*, vol. 86, 2012, 056314.

[43] T. J. Pedley and J. Kessler, "Hydrodynamic Phenomena In Suspensions Of Swimming Microorganisms," *Annual Review of Fluid Mechanics*, vol. 24, pp. 313–358, 1992.

[44] S. Parsa, E. Calzavarini, F. Toschi, and G. a. Voth, "Rotation rate of rods in turbulent fluid flow," *Physical Review Letters*, vol. 109, no. September, pp. 1–4, 2012.

[45] D. Arora, M. Behr, and M. Pasquali, "A tensor-based measure for estimating blood damage," *Artificial Organs*, vol. 28, no. 11, pp. 1002–1015, 2004.

[46] L. Biferale, G. Boffetta, A. Celani, B. J. Devenish, A. Lanotte, and F. Toschi,

"Multifractal statistics of Lagrangian velocity and acceleration in turbulence," *Physical Review Letters*, vol. 93, no. 6, p. 064502, Aug. 2004.

[47] S. S. Girimaji and S. B. Pope, "Material-element deformation in isotropic turbulence," *Journal of Fluid Mechanics*, vol. 220, pp. 427–458, 1990.

[48] C. Meneveau and T. S. Lund, "On the Lagrangian nature of the turbulence energy cascade," *Physics of Fluids*, vol. 6, no. 8, pp. 2820–2825, 1994.

[49] H. Yu and C. Meneveau, "Lagrangian refined Kolmogorov similarity hypothesis for gradient time evolution and correlation in turbulent flows," *Physical Review Letters*, vol. 104, no. 8, 2010, 084502.

[50] G. Boffetta, F. De Lillo, and S. Musacchio, "Lagrangian statistics and temporal intermittency in a shell model of turbulence," *Physical Review E*, vol. 66, no. 6, p. 066307, Dec. 2002.

[51] L. Chevillard, S. G. Roux, E. Leveque, N. Mordant, J. Pinton, and A. Arneodo, "Lagrangian Velocity Statistics in Turbulent Flows: Effects of Dissipation," *Physical Review Letters*, vol. 91, no. 21, p. 214502, Nov. 2003.

[52] L. Biferale, E. Bodenschatz, M. Cencini, A. S. Lanotte, N. T. Ouellette, F. Toschi, and H. Xu, "Lagrangian structure functions in turbulence: A quantitative comparison between experiment and direct numerical simulation," *Physics of Fluids*, vol. 20, no. 6, p. 065103, Jun. 2008.

[53] A. Arnèodo, R. Benzi, J. Berg, L. Biferale, E. Bodenschatz, A. Busse, E. Calzavarini, B. Castaing, M. Cencini, L. Chevillard, R. T. Fisher, R. Grauer, H. Homann, D. Lamb, A. Lanotte, E. Lévèque, B. Lüthi, J. Mann, N. Mordant, W.-C. Müller, S. Ott, N. Ouellette, J.-F. Pinton, S. Pope, S. Roux, F. Toschi, H. Xu, and P. K. Yeung, "Universal Intermittent Properties of Particle Trajectories in Highly Turbulent Flows," *Physical Review Letters*, vol. 100, no. 25, p. 254504, Jun. 2008.

[54] J. M. Ottino, *The Kinematics of Mixing, Stretching, Chaos, and Transport*. Cambridge, UK: Cambridge University Press, 1989.

[55] G. Haller, "Finding finite-time invariant manifolds in two-dimensional velocity fields," *Chaos*, vol. 10, no. 1, pp. 99–108, 2000.

[56] G. Haller and G. Yuan, "Lagrangian coherent structures and mixing in two-dimensional turbulence," *Physica D*, vol. 147, pp. 352–370, 2000.

[57] M. A. Green, C. W. Rowley, and G. Haller, "Detection of lagrangian coherent structures in three-dimensional turbulence," *Journal of Fluid Mechanics*, vol. 572, pp. 111–120, 2007.

[58] G. Haller, "Langrangian Coherent Structures," *Annual Review of Fluid Mechanics*, vol. 47, no. 1, pp. 137–162, Jan. 2015.

[59] P. L. Johnson and C. Meneveau, "Large-deviation joint statistics of the finite-

time Lyapunov spectrum in isotropic turbulence," *Physics of Fluids*, vol. 27, no. 8, p. 085110, 2015.

[60] ——, "Large-deviation statistics of vorticity stretching in isotropic turbulence," *Physical Review E*, vol. 93, p. 033118, 2016.

[61] P. L. Johnson, S. S. Hamilton, R. Burns, and C. Meneveau, "Analysis of geometrical and statistical features of Lagrangian stretching in turbulent channel flow using a database task-parallel particle tracking algorithm," *Physical Review Fluids*, vol. 2, p. 014605, 2017.

[62] P. L. Johnson and C. Meneveau, "A closure for Lagrangian velocity gradient evolution in turbulence using recent deformation mapping of initially Gaussian fields," *J. Fluid Mech.*, vol. 804, pp. 387–419, 2016.

[63] ——, "Turbulence intermittency in a multiple-time scale, Navier-Stokes based reduced model," *under review for Physical Review Fluids*, 2017.

[64] ——, "Predicting viscous-range velocity gradient dynamics in large-eddy simulations of turbulence," *under review for Journal of Fluid Mechanics*, 2017.

[65] ——, "Restricted Euler dynamics along trajectories of small inertial particles in turbulence," *Journal of Fluid Mechanics*, vol. 816, p. R2, 2017.

[66] E. Ott, *Chaos in Dynamical Systems*. Cambridge, UK: Cambridge University Press, 1993.

[67] J.-P. Eckmann and I. Procaccia, "Fluctuations of Dynamical Scaling Indices in Nonlinear Systems," *Physical Review A*, vol. 34, no. 1, pp. 659–661, 1986.

[68] G. Paladin and A. Vulpiani, "Anomalous scaling laws in multifractal objects," *Physics Reports (Review Section of Physics Letters)*, vol. 156, no. 4, pp. 147–225, 1987.

[69] C. Meneveau, "Lagrangian dynamics and models of the velocity gradient tensor in turbulent flows," *Annual Review of Fluid Mechanics*, vol. 43, pp. 219–245, 2011.

[70] J. Jeong and F. Hussain, "On the identification of a vortex," *Journal of Fluid Mechanics*, vol. 285, pp. 69–94, 1995.

[71] G. Haller, "Distinguished material surfaces and coherent structures in three-dimensional fluid flows," *Physica D*, vol. 149, pp. 248–277, 2001.

[72] ——, "A variational theory of hyperbolic Lagrangian Coherent Structures," *Physica D: Nonlinear Phenomena*, vol. 240, no. 7, pp. 574–598, Mar. 2011.

[73] T. Peacock and J. Dabiri, "Introduction to focus issue: Lagrangian coherent structures," *Chaos*, vol. 20, 2010, 017501.

[74] S. C. Shadden, F. Lekien, and J. E. Marsden, "Definition and properties of lagrangian coherent structures from finite-time lyapunov exponents in two-dimensional aperiodic flows," *Physica D*, vol. 212, pp. 271–304, 2005.

[75] F. Lekien and N. Leonard, "Dynamically consistent lagrangian coherent structures," in *American Institute of Physics Conference Series*, ser. American Institute of Physics Conference Series, S. Boccaletti, B. J. Gluckman, J. Kurths, L. M. Pecora, R. Meucci, and O. Yordanov, Eds., vol. 742, Dec. 2004, pp. 132–139.

[76] M. Mathur, G. Haller, T. Peacock, J. E. Ruppert-Felsot, and H. L. Swinney, "Uncovering the lagrangian skeleton of turbulence," *Physical Review Letters*, vol. 98, 2007, 144502.

[77] Y. Li, E. Perlman, M. Wan, Y. Yang, C. Meneveau, R. Burns, S. Chen, S. A., and G. Eyink, "A public turbulence database cluster and applications to study lagrangian evolution of velocity increments in turbulence," *Journal of Turbulence*, vol. 9, no. 31, pp. 1–29, 2008.

[78] H. Cramer, "Sur un nouveau theoreme-limite de la theorie des probabilites," *Actualites Scientifiques et Industrielles*, vol. 736, pp. 5–23, 1938.

[79] J. Bec, L. Biferale, G. Boffetta, M. Cencini, S. Musacchio, and F. Toschi, "Lyapunov exponents of heavy particles in turbulence," *Physics of Fluids*, vol. 18, 2006, 091702.

[80] H. Touchette, "The large deviation approach to statistical mechanics." *Physics Reports*, vol. 478, pp. 1–69, 2009.

[81] J. Gartner, "On large deviations from the invariant measure," *Theory of Probability and Its Applications*, vol. 22, pp. 24–39, 1977.

[82] R. S. Ellis, "Large deviations for a general class of random vectors," *The Annals of Probability*, vol. 12, no. 1, pp. 1–12, 1984.

[83] M. Donsker and S. R. S. Varadhan, "Asymptotic Evaluation of Certain Markov Process Expectations for Large Time, I," *Communications on Pure and Applied Mathematics*, vol. XXVIII, pp. 1–47, 1975.

[84] ——, "Asymptotic Evaluation of Certain Markov Process Expectations for Large Time, II," *Communications on Pure and Applied Mathematics*, vol. XXVIII, pp. 279–301, 1975.

[85] ——, "Asymptotic evaluation of certain Markov process expectations for large time, III," *Communications on Pure and Applied Mathematics*, vol. XXIX, pp. 389–461, 1976.

[86] M. D. Donsker and S. R. S. Varadhan, "Asymptotic evaluation of certain markov process expectations for large time, IV," *Communications On Pure And Applied Mathematics*, vol. 36, pp. 183–212, 1983.

[87] B. B. Mandelbrot, "Intermittent turbulence i n self-similar cascades : divergence of high moments and dimension of the carrier," *Journal of Fluid Mechanics*, vol. 62, no. 2, pp. 331–358, 1974.

[88] C. Evertsz and B. Mandelbrot, "Multifractal measures," in *Chaos and Fractals*, H.-O. Peitgen, H. Jurgens, and D. Saupe, Eds. Berlin: Springer, 1992, pp. 921–953. [Online]. Available: http://lipenreferences.googlecode.com/svn/trunk/Papers/Multifractals/1992MultifractalMeasures.pdf

[89] T. Watanabe, Y. Nakayama, and H. Fujisaka, "Large deviation statistics of the energy-flux fluctuation in the shell model of turbulence," *Physical review. E, Statistical physics, plasmas, fluids, and related interdisciplinary topics*, vol. 61, no. 2, pp. R1024–1027, 2000.

[90] Y. Nakayama, T. Watanabe, and H. Fujisaka, "Self-similar fluctuation and large deviation statistics in the shell model of turbulence," *Physical Review E*, vol. 64, p. 056304, 2001.

[91] G. L. Eyink, "Action Principle in Nonequilibrium Statistical Dynamics," *Physical Review E - Statistical, Nonlinear, and Soft Matter Physics*, vol. 54, no. 4, pp. 3419–3435, 1996.

[92] G. L. Eyink and F. J. Alexander, "Turbulence Fluctuations and New Universal Realizability Conditions in Modelling," *Physical Review Letters*, vol. 78, no. 13, pp. 2563–2566, 1997.

[93] E. Balkovsky and A. Fouxon, "Universal long-time properties of Lagrangian statistics in the Batchelor regime and their application to the passive scalar

problem." *Physical review. E, Statistical physics, plasmas, fluids, and related interdisciplinary topics*, vol. 60, no. 4, pp. 4164–4174, 1999.

[94] M. Vucelja, K. S. Turitsyn, and M. Chertkov, "Extreme value statistics of work done in stretching a polymer in a gradient flow," *Physical Review E*, vol. 91, p. 022123, 2015.

[95] E. Balkovsky, G. Falkovich, and A. Fouxon, "Intermittent distribution of inertial particles in turbulent flows," *Physical Review Letters*, vol. 86, no. 13, pp. 2790–2793, 2001.

[96] J. Miller, "Statistical mechanics of Euler equations in two dimensions," *Physical review letters*, vol. 65, no. 17, pp. 2137–2140, 1990.

[97] R. Robert, "A maximum-entropy principle for two-dimensional perfect fluid dynamics," *Journal of Statistical Physics*, vol. 65, pp. 531–553, 1991.

[98] R. Robert and J. Sommeria, "Relaxation Towards a Statistical Equilibrium State in Two-Dimensional Perfect Fluid Dynamics," *Physical Review Letters*, vol. 69, no. 19, pp. 2776–2779, 1992.

[99] F. Bouchet and A. Venaille, "Statistical mechanics of two-dimensional and geophysical flows," *Physics Reports*, vol. 515, no. 5, pp. 227–295, 2012.

[100] G. Boffetta, A. Celani, S. Musacchio, and M. Vergassola, "Intermittency in

two-dimensional Ekman-Navier-Stokes turbulence," *Physical Review E*, vol. 66, p. 026304, 2002.

[101] F. Bouchet and E. Simonnet, "Random Changes of Flow Topology in Two-Dimensional and Geophysical Turbulence," *Physical Review Letters*, vol. 102, p. 094504, 2009.

[102] F. Bouchet, J. Laurie, and O. Zaboronski, "Langevin Dynamics, Large Deviations and Instantons for the Quasi-Geostrophic Model and Two-Dimensional Euler Equations," *Journal of Statistical Physics*, vol. 156, pp. 1066–1092, 2014.

[103] J. M. Greene and J.-S. Kim, "The calculation of lyapunov spectra," *Physica D: Nonlinear Phenomena*, vol. 24, no. 1-3, pp. 213–225, Jan. 1987.

[104] R. H. Kraichnan, "Small-Scale Structure of a Scalar Field Convected by Turbulence," *Physics of Fluids*, vol. 11, no. 5, p. 945, 1968.

[105] K. Gawedzki, *Non-equilibrium statistical mechanics and turbulence*, ser. London Mathematical Society Lecture Note Series. Cambridge, UK: Cambridge University Press, 2008, ch. Soluble models of turbulent transport, pp. 44–107.

[106] C. Meneveau, K. R. Sreenivasan, P. Kailasnath, and M. S. Fan, "Joint multifractal measures: Theory and applications to turbulence," *Physical Review A*, vol. 41, no. 2, pp. 894–913, Jan. 1990.

[107] H. Tennekes and J. L. Lumley, *A First Course in Turbulence*. Cambridge, MA: MIT Press, 1972.

[108] S. B. Pope, *Turbulent Flows*. Cambridge, UK: Cambridge University Press, 2000.

[109] R. M. Kerr, "Higher-order derivative correlations and the alignment of small-scale structures in isotropic numerical turbulence," *Journal of Fluid Mechanics*, vol. 153, pp. 31–58, Apr. 1985.

[110] R. Kerr, "Histograms of helicity and strain in numerical turbulence," *Physical Review Letters*, vol. 59, no. 7, pp. 783–786, Aug. 1987.

[111] W. T. Ashurst, A. R. Kerstein, R. M. Kerr, and C. H. Gibson, "Alignment of vorticity and scalar gradient with strain rate in simulated navier-stokes turbulence," *Physics of Fluids*, vol. 30, no. 8, pp. 2343–2353, 1987.

[112] S. Kida and K. Ohkitani, "Spatiotemporal intermittency and instability of a forced turbulence," *Physics of Fluids A: Fluid Dynamics*, vol. 4, no. 5, p. 1018, 1992.

[113] K. Ohkitani and S. Kishiba, "Nonlocal nature of vortex stretching in an inviscid fluid," *Physics of Fluids*, vol. 7, no. 2, p. 411, 1995.

[114] K. K. Nomura and G. K. Post, "The structure and dynamics of vorticity and

rate of strain in incompressible homogeneous turbulence," *Journal of Fluid Mechanics*, vol. 377, pp. 65–97, 1998.

[115] D. I. Pullin and P. G. Saffman, "Vortex Dynamics in Turbulence," *Annual Review of Fluid Mechanics*, vol. 30, pp. 31–51, Jan. 1998.

[116] M. Guala, B. Luthi, A. Liberzon, A. Tsinober, and W. Kinzelbach, "On the evolution of material lines and vorticity in homogeneous turbulence," *Journal of Fluid Mechanics*, vol. 533, pp. 339–359, Jun. 2005.

[117] B. Luthi, A. Tsinober, and W. Kinzelbach, "Lagrangian measurement of vorticity dynamics in turbulent flow," *Journal of Fluid Mechanics*, vol. 528, pp. 87–118, Apr. 2005.

[118] T. Ishihara, T. Gotoh, and Y. Kaneda, "Study of High Reynolds Number Isotropic Turbulence by Direct Numerical Simulation," *Annual Review of Fluid Mechanics*, vol. 41, pp. 165–180, Jan. 2009.

[119] M. Holzner, M. Guala, B. Luthi, A. Liberzon, N. Nikitin, W. Kinzelbach, and A. Tsinober, "Viscous tilting and production of vorticity in homogeneous turbulence," *Physics of Fluids*, vol. 22, no. 6, p. 061701, 2010.

[120] A. Vincent and M. Meneguzzi, "The spatial structure and statistical properties of homogeneous turbulence," *Journal of Fluid Mechanics*, vol. 225, pp. 1–20, Apr. 1991.

[121] Z.-S. She, E. Jackson, and S. A. Orszag, "Sturcture and dynamics of homogeneous turbulence: models and simulations," *Proceedings of the Royal Society of London A*, vol. 434, pp. 101–124, 1991.

[122] J. Jiménez, A. A. Wray, P. G. Saffman, and R. S. Rogallo, "The structure of intense vorticity in isotropic turbulence," *Journal of Fluid Mechanics*, vol. 255, pp. 65–90, Apr. 1993.

[123] J. Jiménez and A. A. Wray, "On the characteristics of vortex filaments in isotropic turbulence," *Journal of Fluid Mechanics*, vol. 373, pp. 255–285, Oct. 1998.

[124] A. Y.-S. Kuo and S. Corrsin, "Experiment on the geometry of the fine-structure regions in fully turbulent fluid," *Journal of Fluid Mechanics*, vol. 56, no. 03, pp. 447–479, Mar. 1972.

[125] K. Bürger, M. Treib, R. Westermann, S. Werner, C. C. Lalescu, A. Szalay, C. Meneveau, and G. L. Eyink, "Vortices within vortices: hierarchical nature of vortex tubes in turbulence," *arXiv*, Oct. 2013.

[126] A. A. Townsend, "On the Fine-Scale Structure of Turbulence," *Proceedings of the Royal Society of London A*, vol. 208, no. 1095, pp. 534–542, 1951.

[127] H. Tennekes, "Simple model for the small-scale structure of turbulence," *Phys. Fluids*, vol. 11, pp. 669–671, 1968.

[128] T. S. Lundgren, "Strained spiral vortex model for turbulent fine structure," *Physics of Fluids*, vol. 25, no. 12, pp. 2193–2203, 1982.

[129] A. J. Chorin, "Turbulence and vortex stretching on a lattice," *Communications on Pure and Applied Mathematics*, vol. 39, no. S1, pp. S47–S65, 1986.

[130] ——, "Scaling laws in the vortex lattice model of turbulence," *Communications in Mathematical Physics*, vol. 114, no. 1, pp. 167–176, Mar. 1988.

[131] D. I. Pullin and P. G. Saffman, "On the Lundgren-Townsend model of turbulent fine scales," *Physics of Fluids A: Fluid Dynamics*, vol. 5, no. 1, pp. 126–145, Jan. 1993.

[132] A. Bershadskii, E. Kit, and A. Tsinober, "On universality of geometrical invariants in turbulenceExperimental results," *Physics of Fluids A: Fluid Dynamics*, vol. 5, no. 1993, p. 1523, 1993.

[133] D. A. Donzis, P. K. Yeung, and K. R. Sreenivasan, "Dissipation and enstrophy in isotropic turbulence: Resolution effects and scaling in direct numerical simulations," *Physics of Fluids*, vol. 20, no. 4, p. 045108, 2008.

[134] G. I. Taylor, "Production and Dissipation of Vorticity in a Turbulent Fluid," *Proceedings of the Royal Society of London. Series A, Mathematical and Physical Sciences*, vol. 164, no. 916, pp. 15–23, 1938.

[135] A. Tsinober, *An Informal Conceptual Introduction to Turbulence*, 2nd ed., R. Madylam, Ed. Springer, 2009.

[136] M.-J. Huang, "Correlations of vorticity and material line elements with strain in decaying turbulence," *Physics of Fluids*, vol. 8, no. 8, p. 2203, 1996.

[137] P. Vieillefosse, "Local interaction between vorticity and shear in a perfect incompressible fluid," *Journal de Physique*, vol. 43, pp. 837–842, 1982.

[138] ——, "Internal motion of a small element of fluid in an inviscid flow," *Physica A: Statistical Mechanics and its Applications*, vol. 125, pp. 150–162, 1984.

[139] B. J. Cantwell, "Exact solution of a restricted Euler equation for the velocity gradient tensor," *Physics of Fluids*, vol. 4, no. 4, pp. 782–793, 1992.

[140] J. Martin, A. Ooi, M. S. Chong, and J. Soria, "Dynamics of the velocity gradient tensor invariants in isotropic turbulence," *Physics of Fluids*, vol. 10, p. 2336, 1998.

[141] A. Ooi, J. Martin, J. Soria, and M. S. Chong, "A study of the evolution and characteristics of the invariants of the velocity-gradient tensor in isotropic turbulence," *Journal of Fluid Mechanics*, vol. 381, pp. 141–174, 1999.

[142] B. Lüthi, M. Holzner, and A. Tsinober, "Expanding the Q-R space to three dimensions," *Journal of Fluid Mechanics*, vol. 641, pp. 497–507, 2009.

[143] J. Lawson and J. Dawson, "On velocity gradient dynamics and turbulent structure," *Journal of Fluid Mechanics*, vol. 780, pp. 60–98, 2015.

[144] J. Martin, C. Dopazo, and L. Valino, "Dynamics of velocity gradient invariants in turbulence: Restricted Euler and linear diffusion models," *Physics of Fluids*, vol. 10, no. 8, pp. 2012–2025, 1998.

[145] S. S. Girimaji and S. B. Pope, "A diffusion model for velocity gradients in turbulence," *Physics of Fluids*, vol. 2, no. 2, p. 242, 1990.

[146] L. Chevillard, C. Meneveau, L. Biferale, and F. Toschi, "Modeling the pressure Hessian and viscous Laplacian in turbulence: Comparisons with direct numerical simulation and implications on velocity gradient dynamics," *Physics of Fluids*, vol. 20, no. 10, p. 101504, 2008.

[147] M. Wilczek and C. Meneveau, "Pressure Hessian and viscous contributions to velocity gradient statistics based on Gaussian random fields," *Journal of Fluid Mechanics*, vol. 756, pp. 191–225, 2014.

[148] L. Chevillard and C. Meneveau, "Lagrangian dynamics and statistical geometric structure of turbulence," *Physical Review Letters*, vol. 97, no. 17, p. 174501, Oct. 2006.

[149] E. Jeong and S. S. Girimaji, "Velocity-gradient dynamics in turbulence: effect of

viscosity and forcing," *Theoretical and Computational Fluid Dynamics*, vol. 16, no. 6, pp. 421–432, 2003.

[150] M. Martins-Afonso and C. Meneveau, "Recent fluid deformation closure for velocity gradient tensor dynamics in turbulence: Timescale effects and expansions," *Physica D: Nonlinear Phenomena*, vol. 239, no. 14, pp. 1241–1250, Jul. 2010.

[151] L. Moriconi, R. M. Pereira, and L. S. Grigorio, "Velocity-gradient probability distribution functions in a lagrangian model of turbulence," *Journal of Statistical Mechanics: Theory and Experiment*, vol. 2014, p. P10015, 2014.

[152] P. Sagaut, *Large Eddy Simulation for Incompressible Flows*, 3rd ed. Springer-Verlag, 2006.

[153] D. K. Lilly, "The representation of small-scale turbulence in numerical simulation experiments," in *Proc. IBM Scientific Computing Symp. on Environmental Sciences*, H. H. Gladstone, Ed. Yorktown Heights, NY: IBM, 1967, pp. 195–210.

[154] C. Meneveau and J. Katz, "Scale-invariance and turbulence models for large-eddy simulation," *Annual Review of Fluid Mechanics*, vol. 32, pp. 1–32, 2000.

[155] B. Sawford, "Turbulent relativedispersion," *Annual Review of Fluid Mechanics*, vol. 33, pp. 289–317, 2001.

[156] J. S. Guasto, R. Rusconi, and R. Stocker, "Fluid Mechanics of Planktonic Microorganisms," *Annual Review of Fluid Mechanics*, vol. 44, pp. 373–400, 2012.

[157] C. Meneveau and T. Poinsot, "Stretching and quenching of flamelets in premixed turbulent combustion," *Combustion and Flame*, vol. 86, no. 4, pp. 311–332, Sep. 1991.

[158] M. Germano, "Turbulence: the filtering approach," *Journal of Fluid Mechanics*, vol. 238, pp. 325–336, apr 1992.

[159] J. Smagorinsky, "General Circulation Experiments With the Primitive Equations," *Monthly Weather Review*, vol. 91, no. 3, pp. 99–164, 1963.

[160] M. Germano, U. Piomelli, P. Moin, and W. H. Cabot, "A dynamic subgrid-scale eddy viscosity model," *Physics of Fluids*, vol. 3, no. 7, pp. 1760–1765, 1991.

[161] J. G. Kuerten and A. W. Vreman, "Can turbophoresis be predicted by large-eddy simulation?" *Physics of Fluids*, vol. 17, no. 1, p. 011701, 2005.

[162] P. Fede, O. Simonin, and P. Villedieu, "Stochastic modeling of the turbulent subgrid fluid velocity along inertial particle trajectories," *Proceedings of the ...*, 2006.

[163] I. M. Mazzitelli, F. Toschi, and A. S. Lanotte, "An accurate and efficient

Lagrangian sub-grid model," *Physics of Fluids*, vol. 26, no. 9, p. 095101, sep 2014.

[164] G. I. Park, M. Bassenne, J. Urzay, and P. Moin, "A simple dynamic subgrid-scale model for LES of particle-laden turbulence," *Physical Review Fluids*, vol. 044301, no. April, p. 044301, 2017.

[165] B. Ray and L. R. Collins, "A subgrid model for clustering of high-inertia particles in large-eddy simulations of turbulence," *Journal of Turbulence*, vol. 15, no. 6, pp. 366–385, 2014.

[166] J. P. Minier, S. Chibbaro, and S. B. Pope, "Guidelines for the formulation of Lagrangian stochastic models for particle simulations of single-phase and dispersed two-phase turbulent flows," *Physics of Fluids*, vol. 26, p. 113303, 2014.

[167] J. Chen, G. Jin, and J. Zhang, "Large eddy simulation of orientation and rotation of ellipsoidal particles in isotropic turbulent flows," *J. Turbul.*, vol. 5248, no. June, pp. 1–19, 2016.

[168] M. Wilczek and R. Friedrich, "Dynamical origins for non-Gaussian vorticity distributions in turbulent flows," *Physical Review E*, vol. 80, p. 016316, 2009.

[169] Y. Li and C. Meneveau, "Origin of non-Gaussian statistics in hydrodynamic turbulence," *Phys. Rev. Lett.*, vol. 95, no. 16, p. 164502, 2005.

[170] M. Nelkin, "Multifractal scaling of velocity derivatives in turbulence," *Phys. Rev. A*, vol. 42, no. 12, pp. 7226–7229, 1990.

[171] G. L. Eyink and H. Aluie, "Localness of energy cascade in hydrodynamic turbulence. I. smooth coarse graining," *Physics of Fluids*, vol. 21, no. 2009, pp. 1–9, 2009.

[172] L.-P. Wang and M. R. Maxey, "Settling velocity and concentration distribution of heavy particles in homogeneous isotropic turbulence," *J. Fluid Mech.*, vol. 256, pp. 27–68, 1993.

[173] R. Monchaux, M. Bourgoin, and A. Cartellier, "Analyzing preferential concentration and clustering of inertial particles in turbulence," *Int. J. Multiphase Flow*, vol. 40, pp. 1–18, 2012.

[174] L.-P. Wang and M. R. Maxey, "The motion of microbubbles in a forced isotropic and homogeneous turbulence," *Appl. Sci. Research*, vol. 51, pp. 291–296, 1993.

[175] E. Calzavarini, T. H. van den Berg, F. Toschi, and D. Lohse, "Quantifying microbubble clustering in turbulent flow from single-point measurements," *Phys. Fluids*, vol. 20, no. 2008, 2008.

[176] B. Gopalan, E. Malkiel, and J. Katz, "Experimental investigation of turbulent diffusion of slightly buoyant droplets in locally isotropic turbulence," *Phys. Fluids*, vol. 20, no. 9, p. 095102, 2008.

[177] J. Bec, "Fractal clustering of inertial particles in random flows," *Phys. Fluids*, vol. 15, no. 2003, 2003.

[178] S. Sundaram and L. R. Collins, "Collision statistics in an isotropic particle-laden turbulent suspension. Part 1. Direct numerical simulations," *J. Fluid Mech.*, vol. 335, pp. 75–109, 1997.

[179] W. C. Reade and L. R. Collins, "Effect of preferential concentration on turbulent collision rates," *Phys. Fluids*, vol. 12, no. 2000, pp. 2530–2540, 2000.

[180] L.-P. Wang, A. S. Wexler, and Y. Zhou, "Statistical mechanical description and modelling of turbulent collision of inertial particles," *J. Fluid Mech.*, vol. 415, pp. 117–153, 2000.

[181] G. Falkovich, A. Fouxon, and M. G. Stepanov, "Acceleration of rain initiation by cloud turbulence." *Nature*, vol. 419, pp. 151–154, 2002.

[182] G. P. Bewley, E. W. Saw, and E. Bodenschatz, "Observation of the sling effect," *New J. Phys.*, vol. 15, 2013.

[183] P. Maffettone and M. Minale, "Equation of change for ellipsoidal drops in viscous flow," *J. Non-Newtonian Fluid Mech.*, vol. 78, no. 2-3, pp. 227–241, Aug. 1998.

[184] M. R. Maxey and J. J. Riley, "Equation of motion for a small rigid sphere in a nonuniform flow," *Phys. Fluids*, vol. 26, no. 4, pp. 883–889, 1983.

[185] E. Perlman, R. Burns, Y. Li, and C. Meneveau, "Data exploration of turbulence simulations using a database cluster," in *Proceedings of the 2007 ACM/IEEE conference on Supercomputing*. ACM New York, NY, 2007.

[186] G. S. Patterson and S. A. Orszag, "Spectral Calculations of Isotropic Turbulence: Efficient Removal of Aliasing Interactions," *Physics of Fluids*, vol. 14, no. 11, pp. 2538–2541, 1971.

[187] H. Yu, K. Kanov, E. Perlman, J. Graham, E. Frederix, R. Burns, A. Szalay, G. Eyink, and C. Meneveau, "Studying Lagrangian dynamics of turbulence using on-demand fluid particle tracking in a public turbulence database," *Journal of Turbulence*, vol. 13, no. 12, pp. 1–29, 2012.

[188] J. Bec, L. Biferale, A. S. Lanotte, A. Scagliarini, and F. Toschi, "Turbulent pair dispersion of inertial particles," *Journal of Fluid Mechanics*, vol. 645, pp. 497–528, 2010.

[189] M. Lee, N. Malaya, and R. D. Moser, "Petascale direct numerical simulation of turbulent channel flow on up to 786K cores," in *International Conference for High Performance Computing*. New York, NY: ACM Press, 2013.

[190] J. Graham, K. Kanov, X. I. a. Yang, M. K. Lee, N. Malaya, R. Burns, G. Eyink, R. D. Moser, and C. Meneveau, "A Web Services-accessible database of turbulent channel flow and its use for testing a new integral wall model for LES DNS

Approach and Simulation Parameters," *Journal of Turbulence*, vol. 17, no. 2, pp. 181–215, 2016.

[191] J. Kim, P. Moin, and R. Moser, "Turbulence statistics in fully developed channel flow at low Reynolds number," *Journal of Fluid Mechanics*, vol. 177, pp. 133–166, 1987.

[192] S. A. Orszag, "On the elimination of aliasing in finite difference schemes by filtering high-wavenumber components," *Journal of the Atmospheric Sciences*, vol. 28, p. 1074, 1971.

[193] G. Benettin, L. Galgani, A. Giorgilli, and J.-M. Strelcyn, "Lyapunov characteristic exponents for smooth dynamical systems and for hamiltonian systems; a method for computing all of them. part 1: Theory," *Meccanica*, vol. 15, no. 1, pp. 9–20, 1980.

[194] A. Crisanti, A. Vulpiani, and G. Paladin, *Products of Random Matrices in Statistical Physics*. Springer-Verlag, 1993.

[195] C. Meneveau and K. Sreenivasan, "Measurement of $f(\alpha)$ from scaling of histograms, and applications to dynamical systems and fully developed turbulence," *Physics Letters A*, vol. 137, no. 3, pp. 103–112, 1989.

[196] A. Monin and A. Yaglom, *Statistical Fluid Mechanics: Mechanics of Turbulence Volume II*, J. L. Lumley, Ed. Mineola: Dover Publications, 1975.

[197] T. S. Lund and M. M. Rogers, "An improved measure of strain state probability in turbulent flows," *Physics of Fluids (1994-present)*, vol. 6, no. 5, pp. 1838–1847, 1994.

[198] H. Xu, A. Pumir, and E. Bodenschatz, "The pirouette effect in turbulent flows," *Nature Physics*, vol. 7, no. 9, pp. 709–712, Jun. 2011.

[199] L. Chevillard and C. Meneveau, "Lagrangian time correlations of vorticity alignments in isotropic turbulence: Observations and model predictions," *Physics of Fluids*, vol. 23, no. 10, p. 101704, 2011.

[200] J. Boschung, P. Schaefer, N. Peters, and C. Meneveau, "The local topology of stream- and vortex lines in turbulent flows," *Physics of Fluids*, vol. 26, no. 4, p. 045107, Apr. 2014.

[201] H. Yu and C. Meneveau, "Scaling of conditional Lagrangian time correlation functions of velocity and pressure gradient magnitudes in isotropic turbulence," *Flow, Turbulence and Combustion*, vol. 85, no. 3-4, pp. 457–472, Apr. 2010.

[202] R. Benzi, G. Paladin, G. Parisi, and A. Vulpiani, "Characterisation of intermittency in chaotic systems," *Journal of Physics A*, vol. 18, no. 12, pp. 2157–2165, Aug. 1985.

[203] E. Dresselhaus and M. Tabor, "The kinematics of stretching and alignment of

material elements in general flow fields," *Journal of Fluid Mechanics*, vol. 236, pp. 415–444, Apr. 1991.

[204] T. S. Lundgren, "Distribution Functions in the Statistical Theory of Turbulence," *Physics of Fluids*, vol. 10, no. 5, pp. 969–975, 1967.

[205] A. Monin, "Equations of turbulent motion," *Prikl. Mat. Mekh.*, vol. 31, no. 6, pp. 1057–1068, 1967.

[206] E. A. Novikov, "Kinetic equations for a vortex field," *Soviet Physics Doklady*, vol. 12, p. 1006, 1968.

[207] R. F. Pawula, "Approximation of the Linear Boltzmann Equation by the Fokker-Planck Equation," *Physical Review*, vol. 162, no. 1, pp. 186–188, 1967.

[208] Y. Li and C. Meneveau, "Material deformation in a restricted Euler model for turbulent flows: Analytic solution and numerical tests," *Physics of Fluids*, vol. 19, 2007.

[209] P. E. Hamlington, J. Schumacher, and W. J. A. Dahm, "Local and nonlocal strain rate fields and vorticity alignment in turbulent flows," *Physical Review E - Statistical, Nonlinear, and Soft Matter Physics*, vol. 77, pp. 1–8, 2008.

[210] S. Kramel, S. Tympel, F. Toschi, and G. A. Voth, "Preferential rotation of chiral dipoles in isotropic turbulence," *Physical Review Letters*, vol. 117, p. 154501, 2016.

[211] J. Jiménez, "Cascades in Wall-Bounded Turbulence," *Annual Review of Fluid Mechanics*, vol. 44, pp. 27–45, 2012.

[212] K. Kanov and R. Burns, "Particle Tracking in Open Simulation Laboratories," in *ACM/IEEE Conference on Supercomputing*. Austin, TX: ACM, 2015.

[213] H. Chen, S. Chen, and R. H. Kraichnan, "Probability Distribution of a Stochastically Advected Scalar Field," *Physical Review Letters*, vol. 63, no. 24, pp. 2657–2660, 1989.

[214] R. H. Kraichnan, "Models of Intermittency in Hydrodynamic Turbulence," *Physical Review Letters*, vol. 65, no. 5, pp. 575–578, 1990.

[215] S. B. Pope, "Mapping Closures for Turbulent Mixing and Reaction," *Theoretical and Computational Fluid Dynamics*, vol. 2, pp. 255–270, 1991.

[216] C. Rosales and C. Meneveau, "Anomalous scaling and intermittency in three-dimensional synthetic turbulence," *Physical Review E - Statistical, Nonlinear, and Soft Matter Physics*, vol. 78, pp. 1–18, 2008.

[217] G. K. Batchelor, "Pressure fluctuations in isotropic turbulence," *Mathematical Proceedings of the Cambridge Philosophical Society*, vol. 47, no. 2, pp. 359–374, 1951.

[218] R. Betchov, "An inequality concerning the production of vorticity in isotropic

turbulence," *Journal of Fluid Mechanics*, vol. 1, no. 05, pp. 497–504, Mar. 1956.

[219] W. H. Press, S. A. Teukolsky, W. T. Vetterling, and B. P. Flannery, *Numerical Recipes in Fortran 77*, 2nd ed. New York, NY: Cambridge University Press, 1992.

[220] J. Soria, R. Sondergaard, B. J. Cantwell, M. S. Chong, and a. E. Perry, "A study of the fine-scale motions of incompressible time-developing mixing layers," *Physics of Fluids*, vol. 6, no. 1994, p. 871, 1994.

[221] H. M. Blackburn, N. N. Mansour, and B. J. Cantwell, "Topology of fine-scale motions in turbulent channel flow," *Journal of Fluid Mechanics*, vol. 310, p. 269, 1996.

[222] M. S. Chong, J. Soria, a. E. Perry, J. Chacin, B. J. Cantwell, and Y. Na, "Turbulence structures of wall-bounded shear flows found using DNS data," *Journal of Fluid Mechanics*, vol. 357, pp. 225–247, 1998.

[223] C. Meneveau and K. R. Sreenivasan, "Simple multifractal cascade model for fully developed turbulence," *Phys. Rev. Lett.*, vol. 59, no. 13, pp. 1424–1427, 1987.

[224] Z.-S. She and E. Leveque, "Universal scaling laws in fully developed turbulence," *Phys. Rev. Lett.*, vol. 72, no. 3, pp. 336–339, 1994.

[225] L. Biferale, "Shell models of energy cascade in turbulence," *Ann. Rev. Fluid Mech.*, vol. 35, no. 1, pp. 441–468, 2003.

[226] R. Friedrich and J. Peinke, "Description of a turbulent cascade by a fokker-planck equation," *Physical Review Letters*, vol. 78, no. 5, p. 863, 1997.

[227] J. Bec and K. Khanin, "Burgers turbulence," *Physics Reports*, vol. 447, no. 1-2, pp. 1–66, 2007.

[228] K. Gawedzki and A. Kupiainen, "Anomalous scaling of the passive scalar," *Phys. Rev. Lett.*, vol. 75, pp. 3834–3837, 1995.

[229] L. Biferale, L. Chevillard, C. Meneveau, and F. Toschi, "Multiscale model of gradient evolution in turbulent flows," *Phys. Rev. Lett.*, vol. 98, no. May, pp. 25–28, 2007.

[230] T. Ishihara, Y. Kaneda, M. Yokokawa, K. Itakura, and A. Uno, "Small-scale statistics in high-resolution direct numerical simulation of turbulence: Reynolds number dependence of one-point velocity gradient statistics," *Journal of Fluid Mechanics*, vol. 592, pp. 335–366, Nov. 2007.

[231] J. Boschung, "Exact relations between the moments of dissipation and longitudinal velocity derivatives in turbulent flows," *Phys. Rev. E*, vol. 92, no. 4, pp. 1–5, 2015.

[232] R. A. Antonia, A. J. Chambers, and B. R. Satyaprakash, "Reynolds number

dependence of high-order moments of the streamwise turbulent velocity derivative," *Boundary-Layer Meteorology*, vol. 21, no. 2, pp. 159–171, 1981.

[233] S. G. Saddoughi and S. V. Veeravalli, "Local isotropy in turbulent boundary layers at high Reynolds number," *J . Fluid Mech.*, vol. 268, pp. 333–372, 1994.

[234] M. Wan, Z. Xiao, C. Meneveau, G. L. Eyink, and S. Chen, "Dissipation-energy flux correlations as evidence for the Lagrangian energy cascade in turbulence," *Physics of Fluids*, vol. 22, no. 6, p. 061702, 2010.

[235] S. Pope, "Lagrangian PDF Methods for Turbulent Flows," *Annu. Rev. Fluid Mech.*, vol. 26, no. 1, pp. 23–63, 1994.

[236] A. Yoshizawa, "A statistically-derived subgrid model for the large-eddy simulation of turbulence," *Physics of Fluids*, vol. 25, no. 9, p. 1532, 1982.

[237] C.-H. Moeng, "A Large-Eddy-Simulation Model for the Study of Planetary Boundary-Layer Turbulence," *Journal of the Atmospheric Sciences*, vol. 41, no. 13, pp. 2052–2062, 1984.

[238] E. Bou-Zeid, C. Meneveau, and M. Parlange, "A scale-dependent Lagrangian dynamic model for large eddy simulation of complex turbulent flows," *Physics of Fluids*, vol. 17, no. 2, pp. 1–18, 2005.

[239] G. B. Jeffery, "The Motion of Ellipsoidal Particles Immersed in a Viscous Fluid," *Proceedings of the Royal Society of London A*, vol. 102, pp. 161–179, 1922.

[240] M. Junk and R. Illner, "A New Derivation of Jeffery's Equation," *Journal of Mathematical Fluid Mechanics*, vol. 9, pp. 455–488, 2007.

[241] D. C. Wilcox, *Turbulence Modeling for CFD*, 3rd ed. La Canada, CA: DCW Industries, 2006.

[242] P. S. Daling, F. Leirvik, I. K. Almås, P. J. Brandvik, B. H. Hansen, A. Lewis, and M. Reed, "Surface weathering and dispersibility of MC252 crude oil," *Marine Pollution Bulletin*, vol. 87, no. 1, pp. 300–310, 2014.

[243] O. Johansen, P. J. Brandvik, and U. Farooq, "Droplet breakup in subsea oil releases - Part 2: Predictions of droplet size distributions with and without injection of chemical dispersants," *Marine Pollution Bulletin*, vol. 73, no. 1, pp. 327–335, 2013.

[244] M. Derakhti and J. T. Kirby, "Bubble entrainment and liquid-bubble interaction under unsteady breaking waves," *Journal of Fluid Mechanics*, vol. 761, pp. 464–506, 2014.

[245] A. Pumir, H. Xu, and E. D. Siggia, "Small-scale anisotropy in turbulent boundary layers," *Journal of Fluid Mechanics*, vol. 804, pp. 5–23, 2016.

[246] R. Benzi, L. Biferale, E. Calzavarini, D. Lohse, and F. Toschi, "Velocity-gradient statistics along particle trajectories in turbulent flows: The refined similarity hypothesis in the Lagrangian frame," *Phys. Rev. E*, vol. 80, pp. 1–6, 2009.

[247] P. J. Ireland, A. D. Bragg, and L. R. Collins, "The effect of Reynolds number on inertial particle dynamics in isotropic turbulence. Part I: Simulations without gravitational effects," *J. Fluid Mech.*, vol. 796, pp. 659–711, 2016.

[248] M. Esmaily-Moghadam and A. Mani, "Analysis of the clustering of inertial particles in turbulent flows," *Physical Review Fluids*, vol. 1, no. 8, p. 084202, 2016.

[249] G. L. Eyink, private communications, 2017.

[250] T. Gotoh, Y. Watanabe, Y. Shiga, T. Nakano, and E. Suzuki, "Statistical properties of four-dimensional turbulence," *Physical Review E*, vol. 75, p. 016310, 2007.

[251] E. N. Lorenz, "Deterministic nonperiodic flow," *Journal of the atmospheric sciences*, vol. 20, no. 2, pp. 130–141, 1963.

[252] B. J. Kim and G. H. Choe, "High precision numerical estimation of the largest lyapunov exponent," *Communications in Nonlinear Science and Numerical Simulation*, vol. 15, no. 5, pp. 1378 – 1384, 2010.

[253] K. T. Alligood, T. D. Sauer, J. A. Yorke, and J. Crawford, *Chaos: An introduction to dynamical systems*. Springer-Verlag, 2008.

[254] M. T. Rosenstein, J. J. Collins, and C. J. D. Luca, "A practical method

for calculating largest lyapunov exponents from small data sets," *Physica D: Nonlinear Phenomena*, vol. 65, no. 12, pp. 117 – 134, 1993.

[255] A. Wolf, J. B. Swift, H. L. Swinney, and J. A. Vastano, "Determining lyapunov exponents from a time series," *Physica D: Nonlinear Phenomena*, vol. 16, no. 3, pp. 285 – 317, 1985.

[256] M. Sano and Y. Sawada, "Measurement of the lyapunov spectrum from a chaotic time series," *Phys. Rev. Lett.*, vol. 55, pp. 1082–1085, Sep 1985.

[257] I. Shimada and T. Nagashima, "A numerical approach to ergodic problem of dissipative dynamical systems," *Progress of Theoretical Physics*, vol. 61, no. 6, pp. 1605–1616, 1979.

[258] P. Moin, K. Squires, W. Cabot, and S. Lee, "A dynamic subgrid scale model for compressible turbulence and scalar transport," *Physics of Fluids*, vol. 3, no. 11, pp. 2746–2757, 1991.

[259] F. Porté-Agel, C. Meneveau, and M. B. Parlange, "A scale-dependent dynamic model for large-eddy simulation: application to a neutral atmospheric boundary layer," *Journal of Fluid Mechanics*, vol. 415, no. 2000, pp. 261–284, 2000.

Vita

Perry L. Johnson received a B.S. in 2011 and M.S. in 2013 from University of Central Florida in Mechanical Engineering, where his research was awarded the First Place Outstanding Thesis in Science, Engineering, and Technology as well as the David Weaver Best Student Paper at the 2012 AIAA Thermophysics conference. After receiving a Graduate Research Fellowship from National Science Foundation, Perry joined the Mechanical Engineering Ph.D. program at Johns Hopkins University in 2013. His research interests include a wide range of topics within turbulence theory and modeling for high Reynolds number flows, including the impact of turbulence on particle-laden flows and other micro-physical phenomena. In September 2017, Perry will be joining the Center for Turbulence Research at Stanford University as a postdoctoral fellow.